Using Solar Radiation Pressure and Luni-Solar Resonances for Debris Mitigation

by

Marielle Minassian Pellegrino

B.S., University of Florida, 2015

M.S., University of Colorado Boulder, 2018

A thesis submitted to the

Faculty of the Graduate School of the

University of Colorado in partial fulfillment

of the requirements for the degree of

Doctor of Philosophy

Department of Aerospace Engineering Sciences

2021

Committee Members:

Daniel Scheeres, Chair

Brett Streetman

Jay McMahon

Penina Axelrad

James Meiss

Pellegrino, Marielle Minassian (Ph.D., Aerospace Engineering)

Using Solar Radiation Pressure and Luni-Solar Resonances for Debris Mitigation

Thesis directed by Prof. Daniel Scheeres

This research approaches the problem of debris mitigation at high altitudes by leveraging naturally occurring perturbations. These perturbations include effects due to solar radiation pressure and effects due to third body gravitation. Solar radiation pressure can be used for a variety of high altitude orbits beyond where atmospheric effects dominate. For third body effects, they impact the work discussed in medium Earth orbit where luni-solar resonances affect the stability of the region. These instabilities cause trajectories to increase in eccentricity on the order of decades to centuries.

This research is broken up into four main goals. The first goal studies the averaging tools used in this research. Doubly averaged solutions provide rapid computation power for studying orbits over long time-spans but can lead to a degradation of the solution. This goal characterizes the uncertainties of this model in the unstable regime they are used in. The second and third goals relate to the instability of medium Earth orbit. The second goal studies the graveyard orbit approach, placing satellites in a disposal orbit at their end-of-life, and the long-term behavior of debris in these orbits. The third goal deciphers whether it is feasible or not to target these regions of instability for an atmospheric reentry to depopulate the orbits. The final goal involves using solar sailing for end-of-life debris mitigation at high altitudes. Similar to how satellites in low Earth orbit use drag sails to depopulate the orbit, the solar sail could be deployed at end-of-life to change the orbit and achieve an atmospheric reentry for high altitude orbits.

Dedication

I dedicate this work to my parents, Elizabeth and Michael, whose love and support have helped make this possible.

Acknowledgements

Thank you to my advisor Dan Scheeres for his continued guidance throughout this PhD.

Thank you to my Draper fellowship advisor Brett Streetman for helping to keep my work in context.

Thank you to my entire committee: Jay Mcmahon, Penny Axelrad, and James Meiss whose unique perspectives have strengthened this work.

Thank you to my family for not only offering emotional support but sometimes providing me with working stations during the pandemic: my parents, Elizabeth and Michael; my brothers and sisters-in-law Brandon, Christian, Jolee, and Ann; my nieces and nephews who fill me with such warmth and happiness, Brody, Lucy, Layla, Tyler, and Luca. Second thank you to my mom for reading my research papers including this one; I know how much she loved using her expertise this way.

Thank you to my fellow graduate students who had stepped into the role as mentors and took me under their wing at the start, JoAnna and Ann.

Thank you to my fellow lab members in CSML but also the greater CU PhD community for creating an environment that made coming to work a good part of my day (especially Ramya, CK, Katherine, Dan, Ethan, and Katie).

Thank you to my fellow Smead scholars and Draper fellows for being a continuous support system.

Thank you to the Smead Scholarship and the Draper Fellowship whose programs and funding made this research possible and helped my personal growth in this period of my life.

Contents

Chapter

Tables

Table

Figures

Figure

Chapter 1

Motivation and Introduction

1.1 Debris Mitigation at High Altitudes

Overcrowding and debris in the Earth's orbital regime pose the greatest threat to our space faring capabilities. With every new satellite that orbits Earth, there is an increased chance of collision which can destroy the satellite and, depending how catastrophic it is, create a greater debris field in orbit and potentially initialize a "Kessler syndrome" like growth in debris [24, 49]. So far three major collisions have happened in low Earth orbit (LEO) increasing the number of avoidance maneuvers that functioning satellites like the International Space Station make each year [32].

The Earth's orbital environment has special zones that are unique and irreplaceable. Geosynchronous orbit (GEO) is crucial for military and commercial communications and medium Earth orbit (MEO) is home to the world's global navigation satellite systems (GNSSs) including the US's global position system (GPS). Unlike in LEO, in GEO and MEO, a satellite's location is the most important characteristic, and avoidance maneuvers can inhibit its functionality, making it of utmost consequence to mitigate these risks before collisions happen.

Another unique issue for these high altitude orbits is that they do not experience atmospheric drag perturbations. In LEO, drag can eventually degrade orbits, causing satellites to reduce altitude and thus burn up in the atmosphere and remove themselves from orbit. Satellites in GEO and MEO do not have drag's natural decaying return time and remain in or near their original orbits without planned action.

1.1.1 Geosynchronous Orbit

In 1997, US Space Command and later the Inter Agency Space Debris Coordination Committee (IADC) recommended a disposal orbit for retired satellites in GEO 300 km in altitude above the nominal orbit [46, 13]. This disposal orbit, often referred to as a graveyard orbit, was developed to ensure old satellites and pieces from old satellites would not interact with functioning satellites in GEO.

A NASA study of the following year found that only a quarter of satellites were able to achieve this orbit [1]. In more recent years, studies have shown that one third of retired satellites do not have enough fuel to reach this graveyard orbit [6, 51]. It is imperative that satellite operators take an active role in depopulating orbits after they have finished their missions. It would be more effective if they could use naturally occurring perturbations, such as solar radiation pressure (SRP), rather than rely on an end-of-life fuel reserve.

1.1.2 Medium Earth Orbit

Satellite orbits in the GNSS regime are subject to destabilizing resonances from the Moon and Sun which make finding stable graveyard orbits difficult. Over centuries, the satellites will drift along resonances and into chaotic orbital regions and surrounding operational constellations. Once in these regions, a common occurrence is for the satellite to eventually suffer a growth in eccentricity which drops its periapsis, causing it to reenter the Earth's atmosphere [83].

Early work on these resonances were analytically expressed by Ely and Howell [27] and were focused around station keeping of GPS orbits [26, 48]. Jenkin et al. discussed collision risks for disposed upper stages [44] and disposal orbits for Block IIF satellites [43]. Chao et al. pointed out that for orbit lifetimes as short as 40 years non-operational GLONASS satellites could migrate into the operational GPS zone [19]. Gick proposed that the targeting of argument of perigee might be essential to achieving stable orbits for GPS Satellite disposal [35]. This targeting of argument of perigee is a technique Alessi et al. studied for GNSS orbits in general [9]. This work has been

mainly to study how nominal satellites behave in this orbital regime. Long-term studies of how high area-to-mass ratio objects, like the work in GEO and the Laplace plane [29], are still needed.

In more recent years, European programs Stardust and RedShift mapped out and defined these destabilizing zones and identified them as possible reentry targets for satellites at the end-of-life [85, 23]. Rosengren et al. mapped out the resonances for the differing semi-major axes including an extensive study of proposed Galileo disposal orbits [86]. Alessi et al. performed extensive numerical simulations mapping out the dependence of long term orbit stability on a variety of orbital parameters, and, in so doing, identified the chaotic nature of these orbits [7].

1.2 Research Goals

1.2.1 Thesis Statement

This research aims to provide debris mitigation techniques for high altitude orbits. This includes using eccentricity growth due to luni-solar resonance structure to achieve atmospheric reentry, understanding the stability of potential graveyard orbits in medium Earth orbit, and using solar sailing for direct reentry or targeting a specified orbit to lower reliance on end-of-life fuel reserve.

1.2.2 Research Goal 1 - Validation and Formulation of Doubly Averaged Method

At the foundation of this research is using averaging methods to study long term behavior of objects in GNSS orbital regimes. The use of averaging techniques can significantly speed up integration times (on the order of one million times faster); however, these methods lead to degraded precision. This research goal is to understand how well the doubly averaged method can characterize the behavior in the unstable regime of MEO. We statistically analyze the performance of the doubly averaged solution in a short reentry case which will be a surrogate for the highly chaotic dynamics observed in the region.

1.2.3 Research Goal 2 - Stability of MEO

This research goal is to preemptively consider the effects due to SRP in the dynamics of high area-to-mass ratio (HAMR) objects that may inhabit MEO. Previous simulations of chaos in MEO focus on studying nominal satellite area-to-mass ratios. In reality, space debris can often be characterized as HAMRs. These objects can be produced by shedding events like the ones seen of mylar in GEO as well as battery explosions and satellite collisions that have been observed elsewhere. Thus, when considering the stability of the regime for a possible graveyard orbit, it is important to include analysis of varying area-to-mass ratio objects or varying effects due to solar radiation pressure. We seek to understand the effects combining luni-solar resonances and solar radiation pressure in medium Earth orbital regime, in comparison to work done in LEO and GEO on resonance structure with SRP [8, 16].

1.2.4 Research Goal 3 - Targeting Regions of Chaos

Because one of the hallmarks of chaos is sensitivity, it is important to understand how precisely one needs to target an orbit in these chaotic regimes to ensure impact at some point in the future [55]. If we are to target specific orbital parameters for reentry, we need to also understand its neighborhood and the likelihood of that satellite reentering or following a non reimpacting trajectory near to its initial conditions. In this goal, we study the sensitivity of these chaotic orbits due to changes in their initial conditions thus determining how accurately a satellite must hit a targeted orbit to achieve reentry, potentially decades in the future.

1.2.5 Research Goal 4 - Utilizing Solar Radiation Pressure

Technologies are being developed which can attach simple solar sails to defunct satellites or can deploy sails at end-of-life. Solar sails have been typically thought of as planar designs but as this application calls to the use of defunct satellites, we will explore current research on the spherical- or balloon-style sail as Lücking et al. have proposed [56] and Alessi et al. has incorporated in a GNSS debris mitigation architecture [9].

We focus on leveraging averaged solutions to satellites subject to strong SRP forces to take advantage of the secular effects in Earth's orbit. This goal utilizes the averaged rotating solution to derive general trends on how the perturbation effects change in eccentricity and inclination depending on the orientation between the Sun and Earth. We demonstrate how the control of the maximum plane change or eccentricity change can be realized just by the choice of sun-relative node when the sail is furled at high altitudes.

Chapter 2

Methodology and Background

2.1 Dynamical Model

The dynamical models used in this research are defined as follows. The three forms of equations we will be using are the full numerical solution, integrated using Cartesian coordinates, and singly- and doubly-averaged equations, integrated using Milankovitch elements.

2.1.1 Full Numerical Solution

The dynamics of this system are modeled using Newton's Equation with a point mass Earth and a perturbing force from solar radiation pressure (SRP), Earth's oblateness (J_2), and third body effects from the Sun and Moon. The accelerations due to these forces are defined as

$$\ddot{\boldsymbol{r}} = -\frac{\mu_e}{r^3}\boldsymbol{r} + \boldsymbol{a_{SRP}} + \boldsymbol{a_{J_2}} + \boldsymbol{a_{Moon}} + \boldsymbol{a_{Sun}} \tag{2.1}$$

where μ_e is the gravitational parameter of Earth (constants are listed in Table 2.1), $\boldsymbol{r}$ represents the position vector of the satellite from the Earth, and r is its magnitude.

2.1.1.1 Third Body Perturbation

The acceleration due to the gravitational forces of a perturbing body are exhibited by

$$\boldsymbol{a}_p = -\mu_p\Big(\frac{\boldsymbol{r}-\boldsymbol{d}_p}{|\boldsymbol{r}-\boldsymbol{d}_p|^3} + \frac{\boldsymbol{d}_p}{|\boldsymbol{d}_p|^3}\Big) \tag{2.2}$$

where μ_p is the perturbing body's gravitational parameter; in the case of this research, it is either the Sun or the Moon. The position relative to the perturbing bodies is denoted by $\boldsymbol{d_p}$. The Moon's and Sun's positions were taken from NASA SPICE ephemeris data[1] .

2.1.1.2 Earth's Oblateness

The perturbing acceleration due to the oblateness of the Earth is characterized by

$$\boldsymbol{a}_{J_2} = \frac{3\mu J_2 r_e^2}{2r^4}\{[1 - 5(\hat{\boldsymbol{r}} \cdot \hat{\boldsymbol{p}})^2]\hat{\boldsymbol{r}} + 2(\hat{\boldsymbol{r}} \cdot \hat{\boldsymbol{p}})\} \tag{2.3}$$

where J_2 is the second degree zonal gravitational coefficient and r_e is the radius of the Earth. The polar axis of the Earth is represented by $\hat{\boldsymbol{p}}$.

Previous work by Daquin et al. shows how including higher order harmonics, up to the fifth zonal harmonic, does not change the behavior of the region [23]. The influence due to higher order harmonics is small because of the limited lifetime of these trajectories at low periapsis radii. Through our own simulations, we found that numerical deviations due to higher order harmonics are less than the assumptions made by averaging and therefore are not included in the analysis for this thesis.

2.1.1.3 Solar Radiation Pressure

The perturbing acceleration due to solar radiation pressure is defined by

$$\boldsymbol{a}_{SRP} = -\frac{P_0 \eta (1+\rho)}{d_S^2}\hat{\boldsymbol{d}}_s \tag{2.4}$$

The solar pressure constant is described as P_0. The distance between the Sun and the satellite (or more roughly the Earth) is d_s, and $\hat{\boldsymbol{d}}_{\boldsymbol{s}}$ is the unit vector from Sun to Earth.

The other variables relate to the satellite's properties. The ratio of reflectivity, ρ, describes one of the material properties of the surface of the satellite, specifically how the Sun's light is

[1] Kernel DE430 and DE431

reflected and varies between 0 and 1. The area-to-mass ratio, η, also affects how strongly the satellite is influenced by SRP and is computed as $\eta = \frac{area}{mass}\frac{\mathrm{m}^2}{\mathrm{g}}$.

Table 2.1: Constants

μ_e	$398600.44\mathrm{km}^3/\mathrm{s}^2$
μ_m	$4902.799\mathrm{km}^3/\mathrm{s}^2$
μ_s	$132712440000\mathrm{km}^3/\mathrm{s}^2$
J_2	0.0010826269
r_e	6378.1370km
d_s	$149,568,020\mathrm{km}$
d_m	$384,400.00\mathrm{km}$
P_0	$10^8 \frac{\mathrm{kgkm}^3}{\mathrm{s}^2\mathrm{m}^2}$
η	m^2/kg

2.1.2 Orbit Averaging

Averaging in this paper will be discussed two ways: singly and doubly. Singly-averaged solutions are averaged over the satellite's or object studied's orbit. Doubly-averaged solutions are averaged over the orbit of the perturbing body in addition to the satellite. Thus, the perturbing forces that can be doubly-averaged in our study are solar radiation pressure and third body gravitation which are averaged over the Sun's and Moon's orbits.

2.1.2.1 Milankovitch Elements

The forms of the averaged solutions will be in terms of the scaled Milankovitch elements which are defined as

$$\boldsymbol{e} = \frac{1}{\mu}\tilde{\boldsymbol{v}}\boldsymbol{H} - \hat{\boldsymbol{r}} \tag{2.5}$$

$$\boldsymbol{h} = \frac{\tilde{\boldsymbol{r}}\boldsymbol{v}}{\sqrt{\mu a}} \tag{2.6}$$

We use dyadic notation which denotes the cross product in the form of a dyad [96]:

$$\tilde{a} = a_x(\hat{\boldsymbol{z}}\hat{\boldsymbol{y}} - \hat{\boldsymbol{y}}\hat{\boldsymbol{z}}) + a_y(\hat{\boldsymbol{x}}\hat{\boldsymbol{z}} - \hat{\boldsymbol{z}}\hat{\boldsymbol{x}}) + a_z(\hat{\boldsymbol{y}}\hat{\boldsymbol{x}} - \hat{\boldsymbol{x}}\hat{\boldsymbol{y}}) \tag{2.7}$$

The eccentricity vector is $\boldsymbol{e}$ and the scaled angular momentum vector is $\boldsymbol{h}$. Since we are focused on gravitational and SRP perturbations formulated as conservative forces, the semi-major axis will be constant on average in general, thus validating our use of the scaled Milankovitch elements. The velocity vector is denoted by $\boldsymbol{v}$, angular momentum by $\boldsymbol{H}$, position vector by $\boldsymbol{r}$, and semi-major axis by a. Together these vectors define eccentricity, inclination, argument of periapsis, and longitude of the ascending node. The scaled Milankovitch elements also exhibit two constraints $\boldsymbol{e} \cdot \boldsymbol{h} = 0$ and $\boldsymbol{e} \cdot \boldsymbol{e} + \boldsymbol{h} \cdot \boldsymbol{h} = 1$.

2.1.2.2 Singly-Averaged

Singly-averaged solutions are derived from the disturbing function of the perturbation and are averaged over the mean anomaly of the satellite. These results are put into terms of the Milankovitch elements through the Lagrange planetary equations, referenced in Appendix A. This thesis will only discuss the results which are written along with their derivations by Rosengren et al. [87].

Third Body The third body gravitational perturbations in terms of the Milankovitch elements are Equations 2.8 and 2.9.

$$\dot{\bar{\boldsymbol{h}}}_p = \frac{3\mu_p}{2nd_p^3}\hat{\boldsymbol{d}}_p \cdot (5\boldsymbol{e}\boldsymbol{e} - \boldsymbol{h}\boldsymbol{h}) \cdot \tilde{\bar{\boldsymbol{d}}}_p \tag{2.8}$$

$$\dot{\bar{\boldsymbol{e}}}_p = \frac{3\mu_p}{2nd_p^3}\left(\hat{\boldsymbol{d}}_p \cdot (5\boldsymbol{e}\boldsymbol{h} - \boldsymbol{h}\boldsymbol{e}) \cdot \tilde{\bar{\boldsymbol{d}}}_p - 2\tilde{\bar{\boldsymbol{h}}} \cdot \boldsymbol{e}\right) \tag{2.9}$$

Earth's Oblateness The oblateness of the Earth is characterized in terms of singly-averaged dynamics as Equations 2.10 and 2.11.

$$\dot{\boldsymbol{h}}_{20} = -\frac{3nC_{20}}{2a^2h^5}(\hat{\boldsymbol{p}}\cdot\boldsymbol{h})\tilde{\hat{\boldsymbol{p}}}\cdot\boldsymbol{h} \tag{2.10}$$

$$\dot{\tilde{\boldsymbol{e}}}_{20} = -\frac{3nC_{20}}{4a^2h^5}\left(\left(1-\frac{5}{h^2}(\hat{\boldsymbol{p}}\cdot\boldsymbol{h})^2\right)\tilde{\boldsymbol{h}} + 2(\hat{\boldsymbol{p}}\cdot\boldsymbol{h})\tilde{\hat{\boldsymbol{p}}}\right)\cdot\boldsymbol{e} \tag{2.11}$$

Solar Radiation Pressure Solar radiation pressure is expressed in singly-averaged dynamics in Equations 2.12 and 2.13.

$$\dot{\tilde{\boldsymbol{h}}}_{srp} = -\frac{3}{2}\sqrt{\frac{a}{\mu}}\frac{P_0\eta(1+\rho)}{d^2}\tilde{\hat{\boldsymbol{d}}}_{\boldsymbol{s}}\cdot\boldsymbol{e} \tag{2.12}$$

$$\dot{\tilde{\boldsymbol{e}}}_{srp} = -\frac{3}{2}\sqrt{\frac{a}{\mu}}\frac{P_0(1+\rho)\eta}{d^2}\tilde{\hat{\boldsymbol{d}}}_{\boldsymbol{s}}\cdot\boldsymbol{h} \tag{2.13}$$

2.1.2.3 Rotating Singly-Averaged Formulation for Solar Radiation Pressure

In addition to averaging over the mean anomaly of the satellite, the rotating solution changes frames. We use a rotating frame oriented along the Sun-body line, pointing from the Sun to the Earth. Therefore, the vector $\hat{\boldsymbol{d}}$ rotates about the Earth's orbit normal $\hat{\boldsymbol{z}}$ as the body revolves around the Sun at the rate of change of the true anomaly of the Earth about the Sun. The full derivation can be found in Appendix A.

Then the solution can be found as:

$$\begin{bmatrix}\boldsymbol{e}_r(\psi)\\ \boldsymbol{h}_r(\psi)\end{bmatrix} = \Phi_r(\psi-\psi_0)\begin{bmatrix}\boldsymbol{e}_{0r}\\ \boldsymbol{h}_{0r}\end{bmatrix} \tag{2.14}$$

$$\Phi_r = \cos\psi I_{6\times6} + (1-\cos\psi)\times \begin{bmatrix} \cos^2\Lambda\hat{\boldsymbol{z}}\hat{\boldsymbol{z}} + \sin^2\Lambda\hat{\boldsymbol{d}}\hat{\boldsymbol{d}} & -\sin\Lambda\cos\Lambda(\hat{\boldsymbol{z}}\hat{\boldsymbol{d}} + \hat{\boldsymbol{d}}\hat{\boldsymbol{z}}) \\ -\sin\Lambda\cos\Lambda(\hat{\boldsymbol{z}}\hat{\boldsymbol{d}} + \hat{\boldsymbol{d}}\hat{\boldsymbol{z}}) & \cos^2\Lambda\hat{\boldsymbol{z}}\hat{\boldsymbol{z}} + \sin^2\Lambda\hat{\boldsymbol{d}}\hat{\boldsymbol{d}} \end{bmatrix} + \sin\psi \begin{bmatrix} -\cos\Lambda\tilde{\hat{\boldsymbol{z}}} & \sin\Lambda\tilde{\hat{\boldsymbol{d}}} \\ \sin\Lambda\tilde{\hat{\boldsymbol{d}}} & -\cos\Lambda\tilde{\hat{\boldsymbol{z}}} \end{bmatrix} \tag{2.15}$$

where the SRP parameter is defined as

$$\tan\Lambda = \frac{3(1+\rho)P_0\eta}{2V_{lc}H_s} \tag{2.16}$$

or

$$\tan\Lambda = \frac{3\eta(1+\rho)P_0}{2}\sqrt{\frac{a}{\mu_E\mu_S a_S(1-e_S^2)}} \tag{2.17}$$

where V_{lc} is the local circular speed of the orbiter, H_s is the magnitude of the Sun's angular momentum, and T_s is the Earth's orbital period about the Sun.

This simpler propagation of the variation due to SRP follows the SRP period, ψ, from 0 to 2π radians. The value ψ is the true anomaly of the Earth's orbit about the Sun scaled by the SRP parameter, $\psi = \nu_S/\tan\Lambda$.

Here we note that the state transition matrix Φ_r is a 6×6 orthonormal matrix and thus $\Phi_r^T = \Phi_r^{-1}$. We note that the matrix Φ_r can be split into a block form $\begin{bmatrix} \Phi_{ee}\Phi_{eh} \\ \Phi_{he}\Phi_{hh} \end{bmatrix}$ that we will used in Chapter 6.

The SRP parameter, Λ, varies between 0 to $\pi/2$ radians. Therefore the solution has two limiting cases for both of the extremes, Equations 2.18 and 2.19.

For $\Lambda = 0$

$$\Phi_r = \cos\psi I_{6\times6} + (1-\cos\psi)\times \begin{bmatrix} \hat{z}\hat{z} & 0 \\ 0 & \hat{z}\hat{z} \end{bmatrix} + \sin\psi \begin{bmatrix} -\tilde{\hat{z}} & 0 \\ 0 & -\tilde{\hat{z}} \end{bmatrix} \tag{2.18}$$

For $\Lambda = \pi/2$

$$\Phi_r = \cos\psi I_{6\times 6} + (1-\cos\psi)\times \begin{bmatrix} \hat{d}\hat{d} & 0 \\ 0 & \hat{d}\hat{d} \end{bmatrix} + \sin\psi \begin{bmatrix} 0 & \tilde{\hat{d}} \\ \tilde{\hat{d}} & 0 \end{bmatrix} \tag{2.19}$$

2.1.2.4 Doubly-Averaged

Perturbing forces due to third body effects and SRP can be averaged over the perturbing body's orbit in addition to the satellite's in the singly-averaged solution. This is done by a similar method as the singly-averaged solution. However, instead of averaging over the satellite's mean anomaly, the functions are averaged over the Sun's and Moon's mean anomaly. The only perturbations that can be doubly-averaged are solar radiation pressure and third body gravitation.

Third Body The doubly-averaged third body gravitational perturbations in terms of the Milankovitch elements are Equations 2.20 and 2.21.

$$\dot{\bar{\boldsymbol{h}}} = -\frac{3\mu_p}{4na_p^3h_p^3}\hat{\boldsymbol{H}}_p \cdot (5\boldsymbol{ee} - \boldsymbol{hh}) \cdot \tilde{\hat{\boldsymbol{H}}}_p \tag{2.20}$$

$$\dot{\bar{\boldsymbol{e}}} = -\frac{3\mu_p}{4na_p^3h_p^3}\big(\hat{\boldsymbol{H}}_p \cdot (5\boldsymbol{eh} - \boldsymbol{he}) \cdot \tilde{\hat{\boldsymbol{H}}}_p - 2\tilde{\boldsymbol{h}} \cdot \boldsymbol{e}\big) \tag{2.21}$$

where a_p is the semi-major axis of the perturbing body, h_p is the scaled angular momentum of the perturbing body, and $\hat{\boldsymbol{H}}_p$ is the unit vector of the angular momentum of the perturbing body.

Solar Radiation pressure The doubly-averaged equations of solar radiation pressure used in this paper is the most recent model derived by Rosengren and Scheeres [88].

$$\dot{\bar{\boldsymbol{h}}}_{srp} = -\frac{2\pi(1-\cos\Lambda)}{T_s\cos\Lambda}\tilde{\hat{\boldsymbol{H}}}_{\boldsymbol{s}} \cdot \boldsymbol{h} \tag{2.22}$$

$$\dot{\bar{\boldsymbol{e}}}_{srp} = -\frac{2\pi(1-\cos\Lambda)}{T_s\cos\Lambda}\tilde{\hat{\boldsymbol{H}}}_{\boldsymbol{s}} \cdot \boldsymbol{e} \tag{2.23}$$

2.1.3 Short-Period Corrections

When using averaging theory, it is important to use the true average when integrating the orbital elements. In the singly-averaged case, the equations are all averaged over the satellite's mean anomaly or one orbit. Thus, when propagating the orbital elements, the simulations cannot use the initial elements as the full solution does but must use the average of the elements over one orbit as well, referred to as a short period correction. Figure 2.1 shows the variations of each of the orbital elements for an eccentric GPS orbit and how the short period correction adjusts the initial conditions.

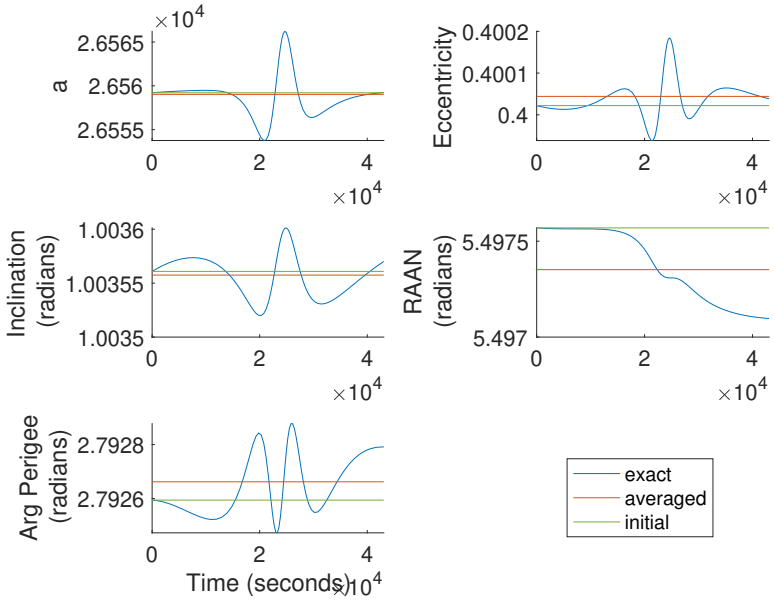

Figure 2.1: Orbital element variation of a highly eccentric GPS orbit over one orbital period compared to short period corrections.

Figure 2.1 shows that there are not large corrections for the short period effects over the satellite as they are all on the order of 10^{-4}. All of these variations are small and do not result in noticeable deviation from the final results.

In the doubly-averaged case, the equations of motion are averaged over not only the satellite's orbit but also the orbit of the perturbing bodies. Therefore, the solution is sensitive to variations

about the mean elements not only of the satellite, but of the perturbing bodies as well. Similar analysis to Figure 2.1, Figure 2.2 shows how large these variations are and whether they impact the solution enough to require a short period correction.

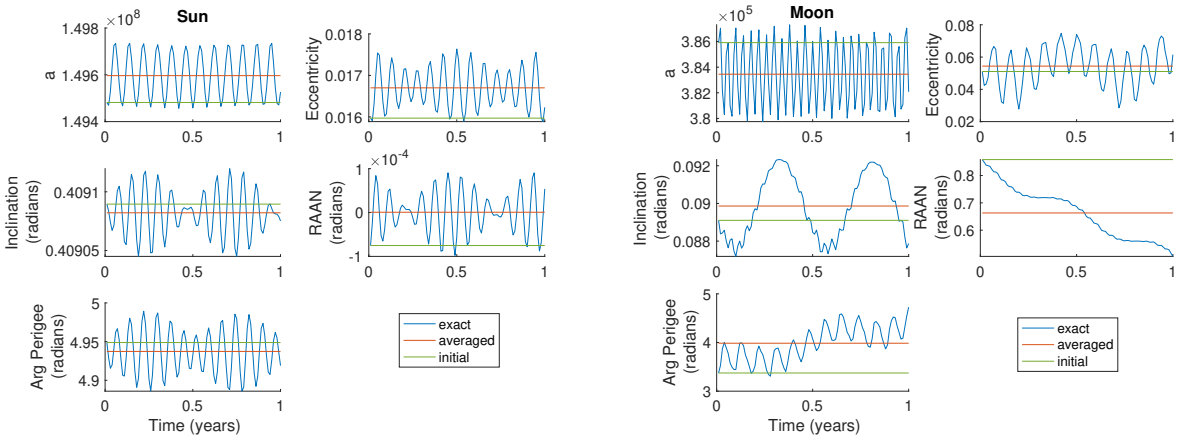

(a) Sun (b) Moon

Figure 2.2: Orbital element variation of the perturbing bodies compared to short term corrections.

Figure 2.2 shows large variations in the orbital elements of the perturbing bodies. These variations are about 2 orders of magnitude larger than the satellite's variations and can have a large impact on the solution if the perturbing bodies' orbits are not initialized from the true average over the orbit and rather the orbit's initial conditions at the epoch.

In addition to the periodic variation, a secular drift can be seen in Figure 2.2b which shows a trend in right ascension of the ascending node, RAAN. This is the regression of the lunar node which has a period of 18.6 years. This behavior is important when modeling the Moon's influence on the solution. Therefore, when calculating the angular momentum in Equations 2.20 and 2.21, the time variation of the Moon's RAAN is included as a constant rate of regression.

To perform the corrections of the perturbing bodies, we run a simulation similar to Figure 2.2 from the epoch until one year. We use this corrected orbital elements to then construct the angular momentum vectors of the Sun and inclination of the Moon. The RAAN of the Moon is taken to be the initial value and is varied by its period.

2.2 The Chaotic Dynamics of Medium Earth Orbit

The chaotic behavior of the medium Earth orbit region has been a topic of research for many years. Most recently, Rosengren et al. make the compelling argument for this behavior to be caused by luni-solar effects [83]. They outline how the region is too high for semi-secular effects caused by the apsidal precession rate from the Earth's oblateness and Sun's apparent mean motion resonance. The inclination-dependent critical inclination resonances have pendulum like behavior too "well-behaved" to be a marker of this chaos [21, 42]. Lastly, they argue tesseral resonances occur over too narrow a window of semi-major axes (tens of kilometers) to describe the behavior we see in MEO. Rosengren et al. argue that these effects must be the result of the regression of the lunar node.

2.2.1 Analytical Description

The full derivation for the analytical representation of these resonances can be found in previous work [83, 84, 37]. We will only highlight the final result for the construction of the resonance map and illustration of the behavior we are studying.

Resonances occur when the combination of secular precession frequencies is zero.

$$\dot{\psi}_{2-2p,m\pm s} = (2-2p)\dot{\omega} + m\dot{\Omega} \pm s\dot{\Omega}_2 \approx 0 \tag{2.24}$$

where $\dot{\Omega}_2$ is the regression of the lunar node and is equal to -0.053°/day and $\dot{\omega}$ and $\dot{\Omega}$ are the linear precession rates due to the Earth's oblateness and are equal to

$$\dot{\omega} = \frac{3}{4} J_2 n \left(\frac{r_e}{a}\right)^2 \frac{5\cos^2 i - 1}{(1-e^2)^2}, \quad \dot{\Omega} = -\frac{3}{2} J_2 n \left(\frac{r_e}{a}\right)^2 \frac{\cos i}{(1-e^2)^2} \tag{2.25}$$

where J_2 is the second zonal harmonic, n is the mean motion of the orbit, r_e is the radius of the Earth, e is the eccentricity of the orbit, i is the inclination of the orbit and a is the semi-major axis of the orbit. Therefore, these resonances are dependent on the orbital parameters, a, e, and i.

Figure 2.3 shows the resonance map for the GPS semi-major axis (the maps appear similarly for the other GNSS systems studied). The regions where the resonances cross are close to where instabilities can be found resulting in eccentricity growth. When the separation between the resonances is close to their libration widths, the critical angles of the resonances switch erratically between libration and circulation which results in chaotic behavior of the trajectory. It has been found that satellites in initially circular orbits would eventually drift to these regions, although the time scales involved can be centuries long [83].

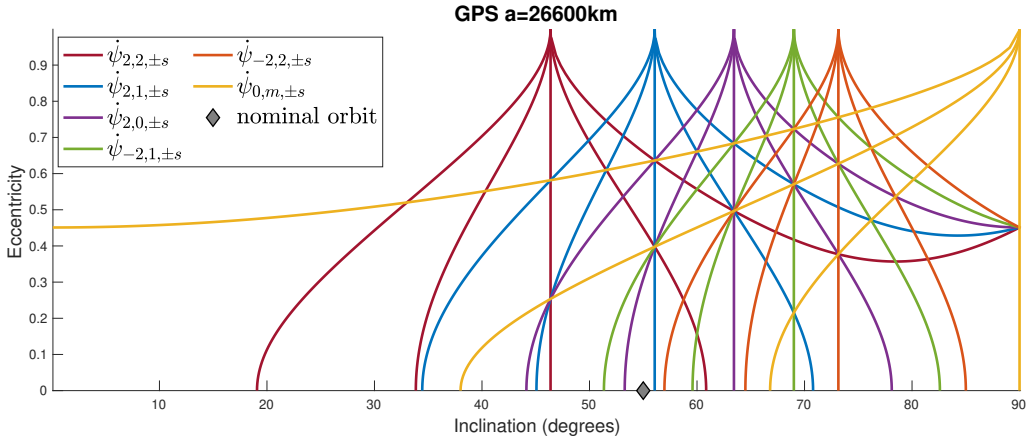

Figure 2.3: Map of luni-solar resonances for varying p, m, and s (integers that define the resonance between the different frequencies) of the GPS semi-major axis. The straight line is where $s = 0$.

2.2.2 Numerical Simulations

The analytical representation helps locate the chaotic regions we are studying and indicate the overall varying behavior of the satellite. However, when trying to describe the paths of specific orbits, it falls short. This is because the analytical description only accounts for semi-major axis, eccentricity, and inclination. In reality, there are more degrees of freedom to the problem including the initial epoch (or location of the third bodies), RAAN, and argument of perigee of the satellite. There is also the nature of chaotic trajectories' sensitivity to initial conditions. As time progresses, a trajectory can be confounded with a neighboring trajectory. This underscores the need for numerical studies for statistical analysis.

Figure 2.4 shows numerical simulations for varying inclinations and eccentricities at the GPS semi-major axis for an argument of perigee of 30° and a RAAN of 120° at the J2000 epoch. The mean anomaly in this orbital regime does not result in large fluctuations for the initial orbital elements (on the order of $\times 10^{-4}$), and therefore we do not institute a specific mean anomaly or any short period correction due to averaging. The time until Earth reentry, or time until collision, depicts how strong the secular growth in eccentricity is, with shorter times representing stronger eccentricity growth. It is shown with the resonance map in Figure 2.3 that the crossing resonances do not exactly line up with the chaotic regions. Although the crossing resonances are in the vicinity of the areas of instability and give a good general idea of the location, numerical simulations provide more concrete data on where the possible reentry orbits occur. This result emphasizes the need to study all the varying degrees of freedom of this problem, the orbital parameters, a, e, i, Ω, ω, and the epoch.

2.2.3 Sensitivity due to Ω and ω

Previous work by Alessi et al. illustrated how the chaotic behavior of this region changes with variables other than eccentricity and inclination [7]. This section is dedicated to understanding how the other orbital parameters affect changes in the instabilities of the regime.

Figure 2.5 shows how the argument of perigee and RAAN affect the chaotic behavior for a set inclination and eccentricity predicted to collide with Earth in 63 years by Figure 2.4. The chaotic dependency on (ω, Ω) is shown by the fractal structure of the eccentricity map. In this case of the GPS orbital regime, the eccentricity needs to be about 0.76 for the satellite to reenter the Earth's atmosphere.

The map illustrates how the growth in eccentricity is dependent on the two parameters. There are more stable orbits surrounding a RAAN of π. These inferences allow us to survey the space for instabilities later in this research.

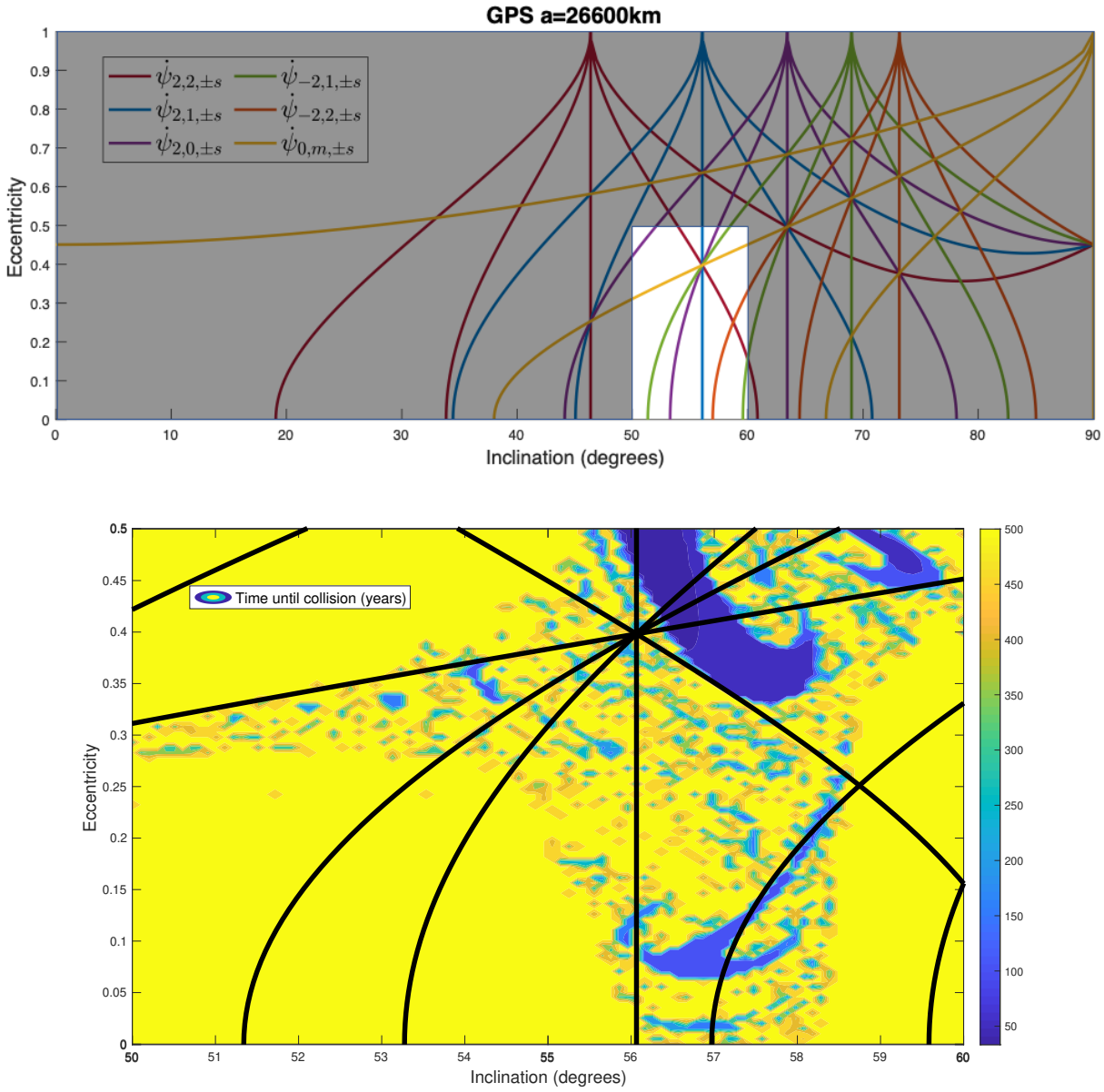

Figure 2.4: Numerical simulation of dynamics for varying inclination and eccentricity at the GPS semi-major axis with an overlay of the resonance map shown in Figure 2.3. The colorbar represents the reentry time of the satellite. The simulations were capped at 500 years so solutions showing that reentry time may have never reentered. Results are consistent with Daquin et al. [23]

.

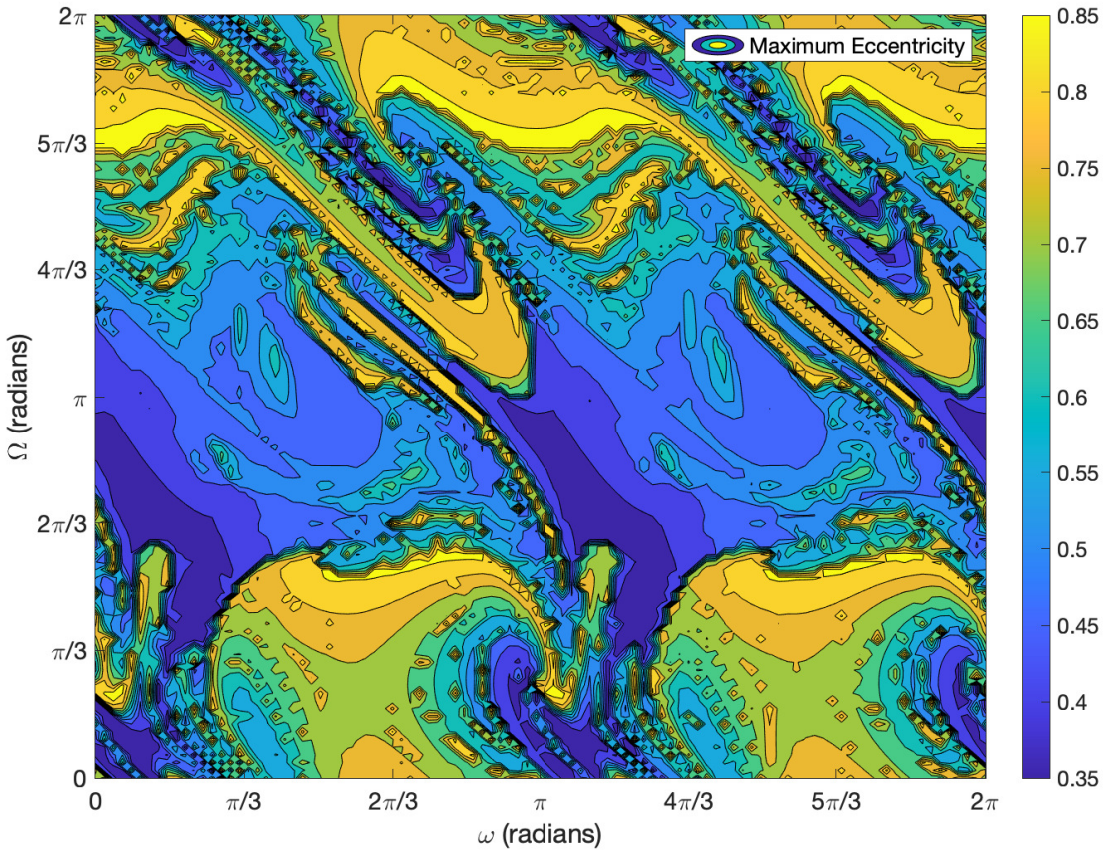

Figure 2.5: Maximum eccentricity achieved within 200 years from an initial condition of 0.35 eccentricity and inclination of 57.5°. The colorbar of the figure is the maximum eccentricity.

2.3 Lyapunov Exponents

Lyapunov exponents are often used as indicators of chaotic behavior as they measure the exponential growth of the deviation between neighboring solutions: a positive exponent indicating an unstable trajectory and a negative exponent indicating a stable one. These exponents are calculated using a modified Benettin algorithm [75].

Instead of letting the solution deviate from the initial point over the entire arc, the Benettin method for solving Lyapunov exponents normalizes the deviation after each time. This means that while the other methods find the supremum over the entire arc, the Benettin method has several smaller arcs; these values are calculated over which are all summed together to solve for the

Lyapunov exponent for the particular point. Figure 2.6 shows a schematic of the algorithm similar to Kuznetsov [54].

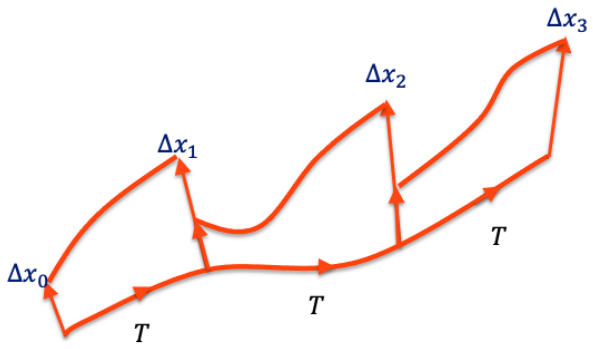

Figure 2.6: Normalization of the deviation using the Benettin algorithm.

The algorithm is defined as

$$\mu = \frac{1}{MT} \sum_{i=1}^{M} \ln \|\Delta x_i\| \tag{2.26}$$

where M is the number of intervals the deviation is normalized for. T is the time span for each interval.

We have slightly adjusted this equation to take the supremeum over the arc and normalize by that value.

$$\mu = \frac{1}{MT} \sum_{i=1}^{M} \sup \ln \frac{\|\Delta x_i\|}{\|\Delta x_{i0}\|} \tag{2.27}$$

This exponent will be used to quantify the chaotic nature of the trajectories in the subsequent chapters.

Chapter 3

Research Goal 1 - Validation of Doubly Averaged Method

Over long time-spans, we find that singly-averaged dynamics can follow the full solution well even in these highly chaotic regions while the doubly-averaged solution does not follow as precisely [74]. With our focus on long-term behavior, we are not concerned with the exact state, but rather the general trends in orbit evolution. This research seeks to understand the statistical significance in these deviations. We will examine how close neighboring solutions follow precise solutions of the dynamics. By determining if the doubly-averaged solution captures general trends in the chaos, we can validate it as a tool.

Averaging techniques have been used to study long time-span simulations in this region for decades. Chao et al. used a semi-analytic orbit propagator to investigate this region. Through older investigations of geosynchronous orbits (GEO) of 100 years, they validated this method against a full numerical orbit integration tool [18]. Chao et al. further validated that integrator in the GNSS regime by bounding the eccentricity growth and running the results with and without solar radiation pressure [19]. Celletti et al. validated their expanded semi-analytical model of luni-solar perturbations by comparing results with a Newtonian model for two cases with varying eccentricities. Those two cases were of one of a libration region and one of resonant island in which both cases mirrored the results of their averaged model [17]. Daquin et al. similarly studied the region using semi-analytical models of the perturbations [23]. The focus of their validation of the models was on the degree to which the perturbation was studied rather than the characterization of averaging itself.

None of the previous methods included doubly-averaged formulations. The use of the doubly-averaged solution enables a significant computational speed-up, about 1.6 million times faster than the full model (eight times faster than the singly-averaged model) and can characterize the chaotic trends in the GNSS region. However, there is some degradation of the solution as additional averaging is introduced into the model. The solution starts to wander from the secular behavior of the singly and full toward the end of the simulation. Therefore, it is important if we want to use doubly-averaged methods, that we rigorously analyze their performance and their degree of confidence.

The particular models used in this thesis are derived by Rosengren and Scheeres [87, 88] described in Chapter 2. These dynamical models were used to study HAMR objects in the Laplace plane in GEO and about small bodies. Previously, the results of these papers were compared to equations of motion for their validation. However, the degree of accuracy of the averaged models was never fully described. In this chapter, we will study how well these models compare to the other averaging methods and the Newtonian model, referred to as the full numerical solution.

To study the performance of the doubly-averaged model, we will utilize Monte Carlo analysis previously implemented by Park et al. [69, 70]. Park et al. used this statistical analysis to quantify uncertainty due to averaging techniques. These were only singly-averaged perturbations and used in hybrid with full numerical simulations to more rapidly study nonlinear environments. We will use the general principals of these papers in which the uncertainties are studied by perturbing a set of initial conditions around the true initial condition and using the expected values and standard deviations of the set to characterize the group.

This chapter is organized as follows. The chapter discusses two cases: one studying a satellite, a nominal area-to-mass ratio object, in a highly chaotic region and the other studying a piece of debris, a HAMR object, in a highly chaotic region. This will involve determining the highly chaotic region and analyzing it using a distribution of solutions. This analysis will include a way to characterize a single point and a way to characterize a set of points, providing differing levels of accuracy required to achieve each. Because HAMR objects are so heavily influenced by solar

radiation pressure, we will also provide additional analysis that we have conducted to help the previously derived doubly-averaged model perform better. Then, there is a brief discussion of HAMR objects beyond the area-to-mass ratio case we focus on, an outer layer of Multi-Layer Insulation (MLI). The chapter finishes with an example application of a Gaussian distribution with the limitations discussed in the results and illustrates how the final probability density functions compare.

3.1 Performance of Varying Area-to-Mass Ratio Types

This chapter will study two different cases of area-to-mass ratios. The first case examined is of a nominal satellite. The satellites in this region are relatively dense having area-to-mass ratios about 0.02 m^2/kg [31]. For this case, we use an average ratio of reflectivity of 0.5. In addition to studying how well a satellite representative of that region is propagated using averaged dynamics, we also study a HAMR object. HAMR objects can inhabit orbits from varying events including but not limited to a collision, an explosion, or mylar shedding. The area-to-mass ratio we study is representative of an outer layer of MLI, multi-layer insulation, and is 6 m^2/kg [30]. This area-to-mass ratio is high enough so that the SRP acceleration is of similar magnitude to the third body attractions which makes this case interesting for study in MEO. We will also include a brief discussion of some cases where an even higher area-to-mass ratio is used.

3.1.1 Nominal Area-to-Mass Performance

We computed a fifty year simulation using the full numerical model and the two averaged models. All the simulations were integrated using a RKF (Runge-Kutta-Fehlberg) order 7/order 8 method in Matlab on a Quad-Core Intel Core i5 processor [28]. Integrating using the full numerical equations took 135 hours for this trajectory compared to the singly-averaged equations which took 1.28 seconds and the doubly-averaged equations which took 0.16 seconds, Table 3.1. These results clearly indicate how orbit averaging is able to compute trajectories much more rapidly. They also show when computing many trajectories, the doubly-averaged solution provides even faster

computation times allowing for quick surveys of a large variation of initial conditions.

Table 3.1: Integration Time Comparison

	Full Numerical	Singly-Averaged	Doubly-Averaged	Doubly-Averaged with Singly SRP
Nominal Area-to-Mass	135 hr	1.28 sec	0.16 sec	-
High Area-to-Mass	143 hr	1.36 sec	0.08 sec	0.29 sec

The resulting averaged integrations track the simulation accurately until the 40 year mark as shown in Figure 3.1 where the doubly-averaged begins to deviate from the singly-averaged and full integration at the end of the simulation. The singly-averaged solution makes a good proxy for the full numerical model, and is used for that purpose in our analysis. The analysis of how well the doubly-averaged equations match the dynamics will be explored in Section 3.2.

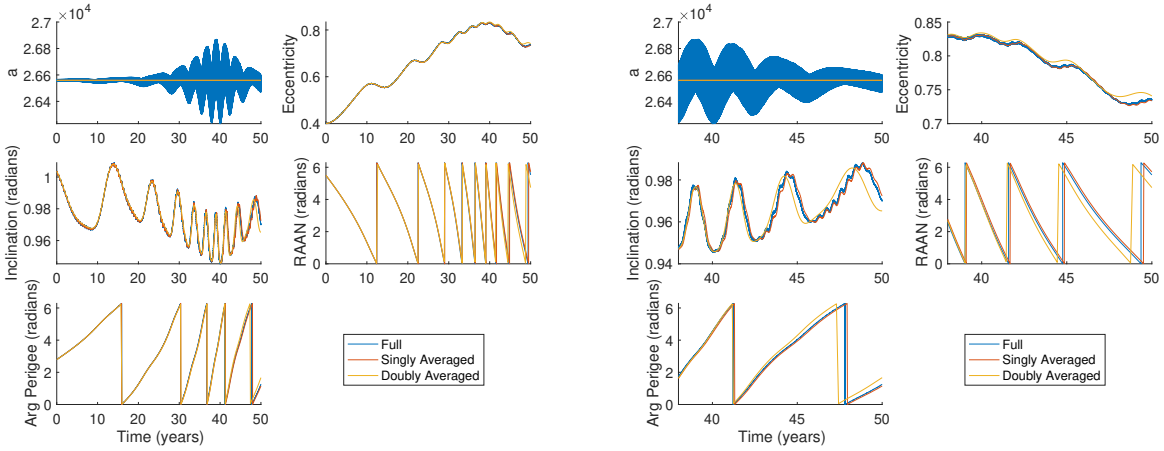

(a) Full time-span of the simulation

(b) Last 10 years of the simulation

Figure 3.1: Simulations of varying models for a nominal area-to-mass ratio

3.1.2 HAMR Performance

Similarly, a fifty year simulation of a HAMR object results in varying computation times per model. In this case, we use four different integration methods. Because SRP is a large contributing perturbation in HAMR objects, in addition to the fully doubly- and fully singly-averaged methods, we include a fourth method, a doubly-averaged third body computation with a singly SRP computation. Like all the integrations in this chapter, the simulations were integrated using a RKF (Runge-Kutta-Fehlberg) order 7/order 8 method [28]. Integrating using the full numerical equations took 143 hours for this trajectory compared to the fully singly-averaged which took 1.36 seconds, the fully doubly-averaged which took 0.08 seconds, and the doubly with singly SRP which took 0.29 seconds, Table 3.1.

The resulting integration does well at tracking the simulation until the 20 year mark as shown in Figure 3.2.

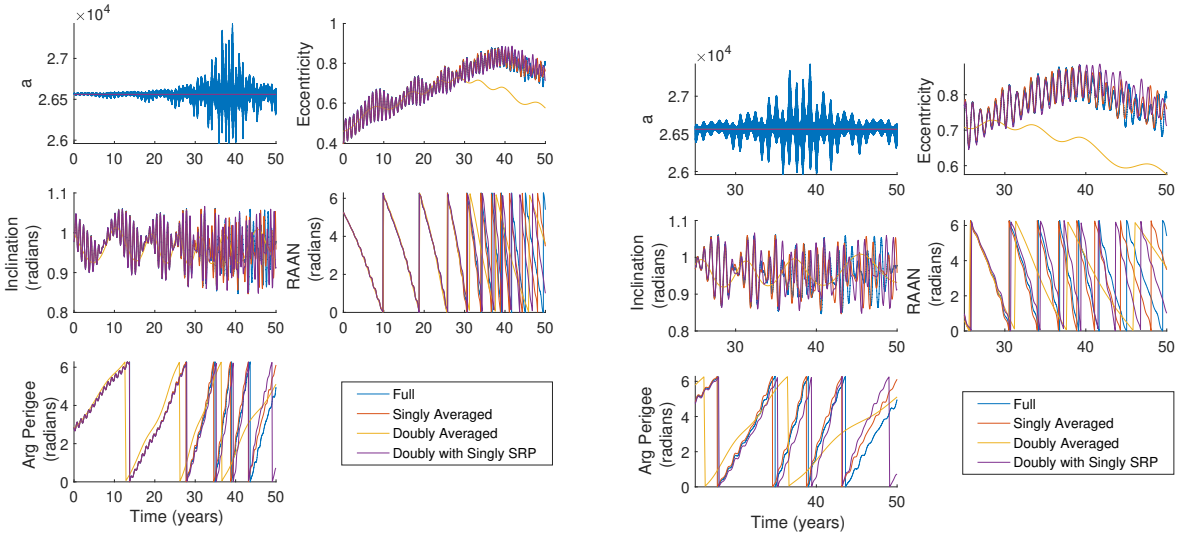

(a) Simulations over a fifty year time span

(b) Last 10 years of the simulation

Figure 3.2: Simulations of varying models for a high area-to-mass ratio

This performance is notably worse than the nominal area-to-mass ratio case in Figure 3.1, as expected given the significantly larger perturbation effects on a HAMR object. However, using the

doubly with singly-averaged SRP model gives performance that is comparable to the singly and full solution. The fully doubly-averaged and doubly-averaged with singly-averaged SRP model's performance will be further defined and investigated Section 3.3.

3.2 Nominal Satellite

This section will explore the long term propagation of a nominal area-to-mass ratio object in the medium Earth orbit regime. First, we will pick a case to study that is representative of a highly chaotic trajectory. Then, we will look at how well the doubly solution can match a single true solution and how well it will track a distribution of solutions similar to analysis presented by Pellegrino et al. [76].

3.2.1 Targeted Region

Because the aim of this research goal is to see how doubly-averaged dynamics characterize chaotic behavior, the specific region chosen is one known to be highly chaotic. It is an orbit at the GPS semi-major axis with an eccentricity and inclination shown to have a short Earth reentry time. The threshold for atmospheric reentry was chosen to be a perigee below 122 km or at the GPS semi-major axis an eccentricity of about 0.76 [68]. This region was chosen by sampling eccentricity and inclination space of a GPS semi-major axis. For each eccentricity and inclination pair, 14 different right ascension of the ascending nodes and argument of perigees were sampled to assure the target picked in eccentricity and inclination space is independent of those parameters.

Table 3.2: Targeted Orbital Parameters

a	e	i	Ω	ω	Reentry Time
26560 km	0.400	57.5°	5.5 rad	2.8 rad	30.8 years

The specific orbit, Table 3.2, was chosen for its fast reentry time and similarly chaotic neighboring trajectories (shown as the large blue area in the center of each of the plots in Figure 3.3).

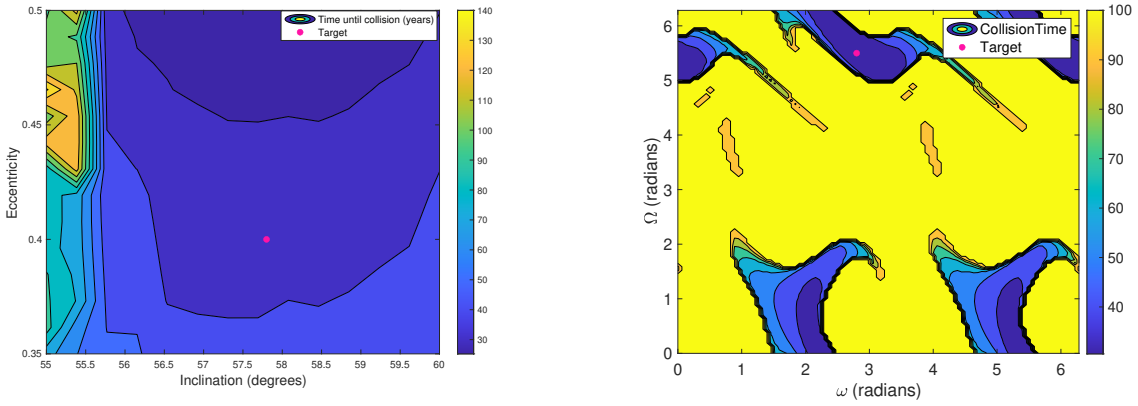

(a) (b)

Figure 3.3: Choosing a target. (a) Comparison of chaotic regions independent of Ω and ω. Each point is the smallest collision time of 14 different Ω and ω (196 cases). (b) The varying reentry time for e=0.4 and i=57.5° in ω and Ω space.

3.2.2 Capturing a Single Solution

To understand at what level the doubly-averaged dynamics captures the dynamics of the singly-averaged, we perturbed the initial conditions of the doubly-averaged and compared how the final results relate to the singly-averaged. This is done by perturbing with a white uniform distribution of a certain percentage of the initial conditions and then integrating using both a singly-averaged integrator for the non-perturbed solution and a doubly-averaged for both the perturbed set and non-perturbed solution. The only quantities perturbed are the initial conditions. This amounted to 1000 Monte Carlo runs for each scattering. The time until atmospheric reentry, also denoted as time until collision, is used as the parameter to determine how well the chaotic dynamics were captured.

By analyzing a distribution of solutions, we can create a case in which the true solution is encapsulated in the doubly-averaged set. This method quantifies to what degree of certainty the doubly-averaged solution can describe the true dynamics [69, 70].

The first results shown are for a distribution where the initial conditions are perturbed by 0.125% of their original value (with a mean deviation of 0). For each of the simulations, all six

initial conditions were perturbed at the same time.

For the 0.125% variation, the resulting trajectories had a range of orbit reentries between 30.6 and 31.1 years, graphs shown in Appendix B. This corresponds to about six months between the shortest and longest reentry times. The true solution of 30.8 years is within this threshold. To avoid any biasing due to outliers, the standard deviation is used as a descriptor for the distribution instead of the maximum and minimum. The standard deviation thus requires a tighter requirement than meeting the threshold of being within the maximum and minimum of the set. The final distributions are not necessarily going to be Gaussian but the standard deviation is still a useful parameter to remove any outliers in the set.

The standard deviation of the doubly-averaged distribution set does not encompass the final reentry time of the singly-averaged solution. Thus, we increased the perturbed range of initial conditions from 0.125% to 0.25%.

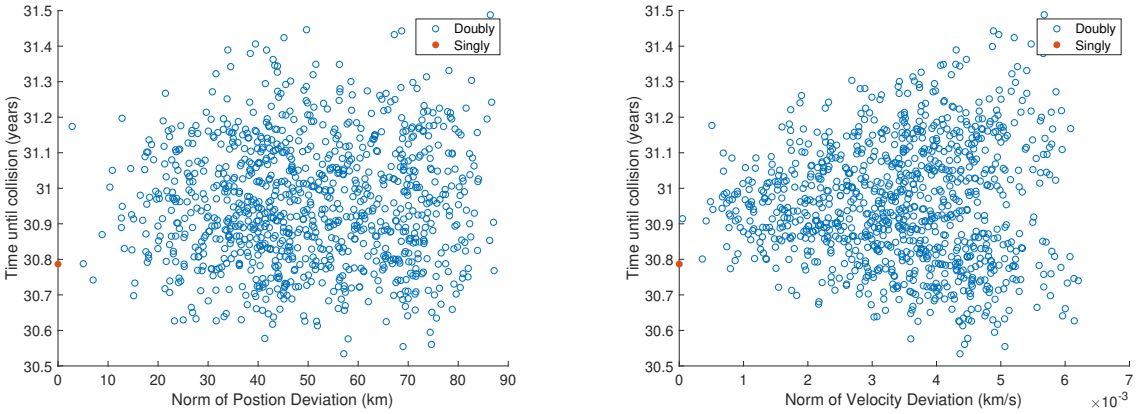

(a) Magnitude deviation of position vector

(b) Magnitude deviation of velocity vector

Figure 3.4: The deviation of the initial conditions in terms of the magnitudes of the Cartesian coordinates as compared to the final reentry times for a 0.25% initial distribution

The atmospheric reentry times for the 0.25% distribution range from about 30.6 to 31.4 years as shown in Figure 3.4. This is approximately about nine and a half months between the minimum and maximum reentry times. Figure 3.5 shows the distribution with their means and standard deviations in terms of some of the orbital elements.

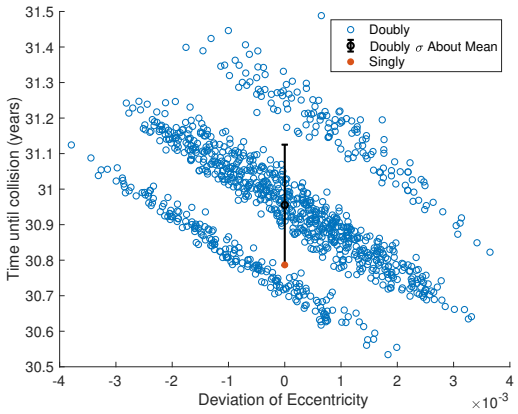

(a) eccentricity

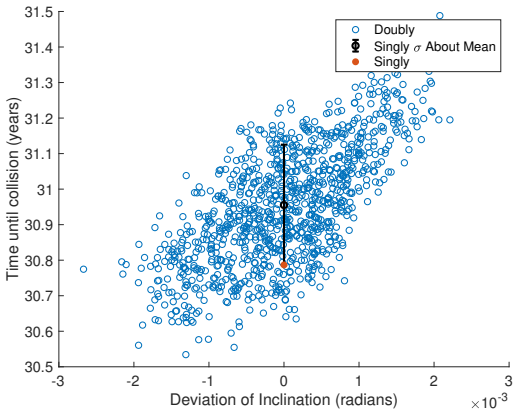

(b) inclination

(c) argument of perigee

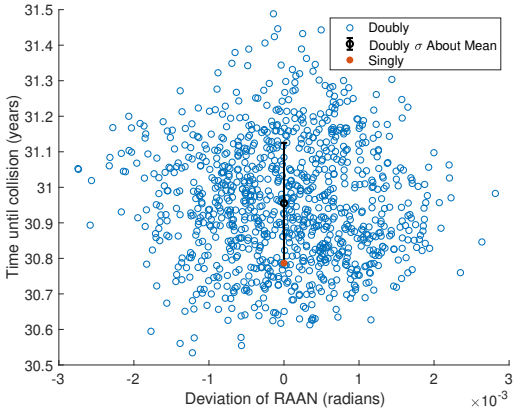

(d) right ascension of the ascending node

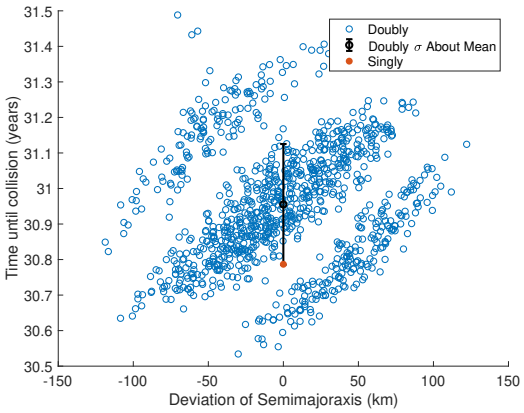

(e) semi-major axis

Figure 3.5: The deviation of the initial conditions in terms of the orbital elements as compared to the final reentry times for a 0.25% initial distribution.

In this case, the mean still comes to be about 30.95 years but the spread of results is much

higher and thus the standard deviation also encapsulates the true solution of about 30.8 years. Therefore, an initial distribution of 0.25% about the initial conditions produces a large enough distribution to describe the true solution.

3.2.3 Capturing a Distribution

In each of the previous simulations, we ran a Monte Carlo analysis of the doubly-averaged against a single solution. In order to understand the varying degrees of accuracy to study the region, we will study the description of not only one single initial condition, but also a set of initial conditions. In this analysis, we run Monte Carlo simulations of both the doubly- and singly-averaged to see how the distributions compare. Because we expect a looser requirement on comparing sets in contrast to a single point, we started our analysis at a smaller initial distribution. The distribution that was able to fit the requirement was a 0.15% initial distribution.

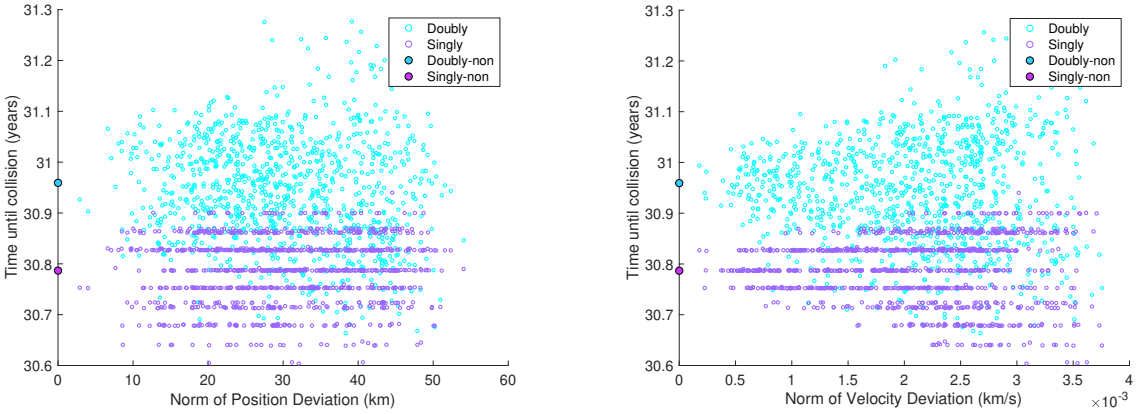

(a) Magnitude deviation of position vector

(b) Magnitude deviation of velocity vector

Figure 3.6: The deviation of solutions for a distribution of 0.15% of the initial conditions in terms of the norms from the Cartesian coordinates compared to the final reentry times of the distribution.

Figure 3.6 shows that a larger swath of initial conditions results in a larger final spread of reentry times. In this case, the final reentry times of both distributions overlap, singly from 30.6 years to 30.9 years and doubly from 30.6 years to 31.3 years.

Figure 3.7 shows how the standard deviations about the means of each distribution overlap.

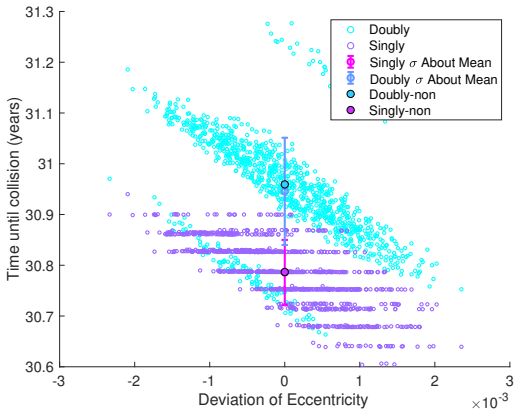

(a) eccentricity

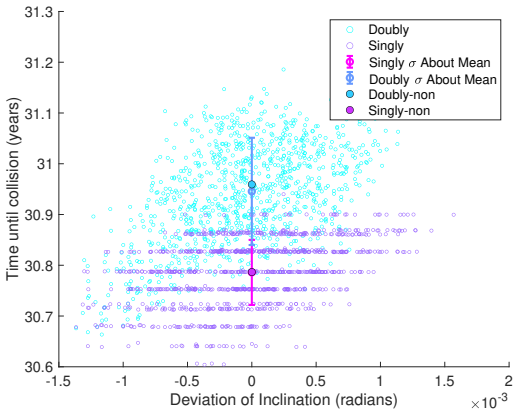

(b) inclination

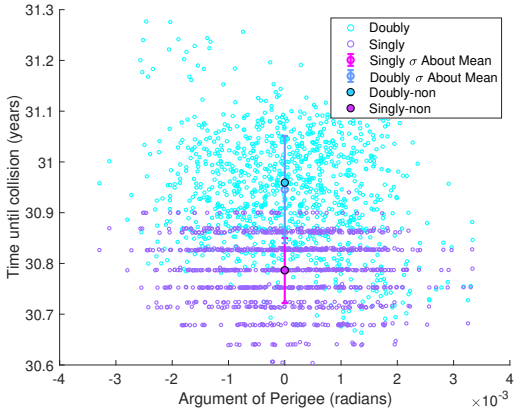

(c) argument of perigee

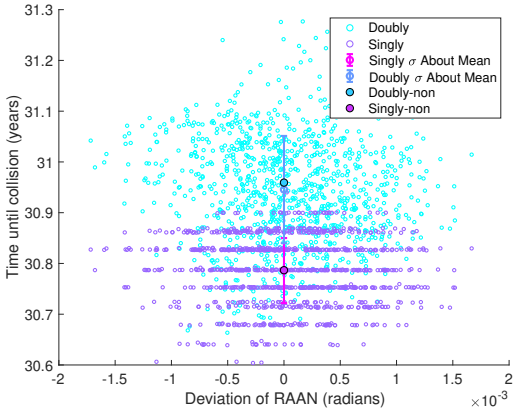

(d) right ascension of the ascending node

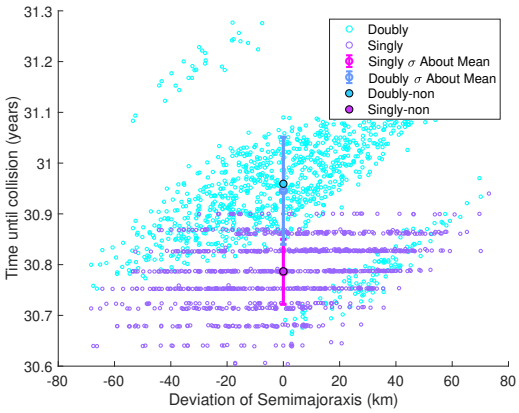

(e) semi-major axis

Figure 3.7: The deviation of solutions for a distribution of 0.15% of the initial conditions in terms of the orbital elements as compared to the final reentry times

The standard deviations crossing achieves the threshold for the distributions matching and indicates

that the dynamics could be characterized by the doubly-averaged solution for a 0.15% level of precision when describing a set of solutions.

3.3 HAMR Objects

In addition to studying nominal area-to-mass ratios representative of satellites, we also studied area-to-mass ratios representative of space debris. Our base case will be of a 6 m^2/kg object consistent with the outer layer of MLI [30], hypothesized to be a common source of debris objects.

3.3.1 Corrections to the Doubly Averaged SRP Integration

Figure 3.8 shows how an object with an area-to-mass ratio of 5 m^2/kg evolves with the singly-averaged dynamics model of SRP, Equations 2.12 and 2.13, and doubly-averaged dynamics model of SRP, Equations 2.22 and 2.23. This area-to-mass ratio was chosen because it is large enough to easily visualize the solar radiation pressure perturbation and it is similar to the representative debris case.

The doubly-averaged solution deciphers trends in the behaviors of the orbital dynamics. This is best illustrated by inclination and RAAN over the five years. However, the doubly-averaged solution is failing to capture the true average of the dynamics and is only propagating the trends from the initial conditions.

Even though the doubly-averaged solution appears to not track the dynamics well, there are some corrections we can employ to still utilize this much more rapid computation to quickly survey the phase space for HAMR objects. The first will be a numerical correction of the initial conditions to ensure the true average of the orbital elements is propagated forward in time. The second is a quick analysis of the variation of the eccentricity on a number of arcs over the integration of the solution. This will help give an understanding of the maximum around that average and therefore whether the object reenters.

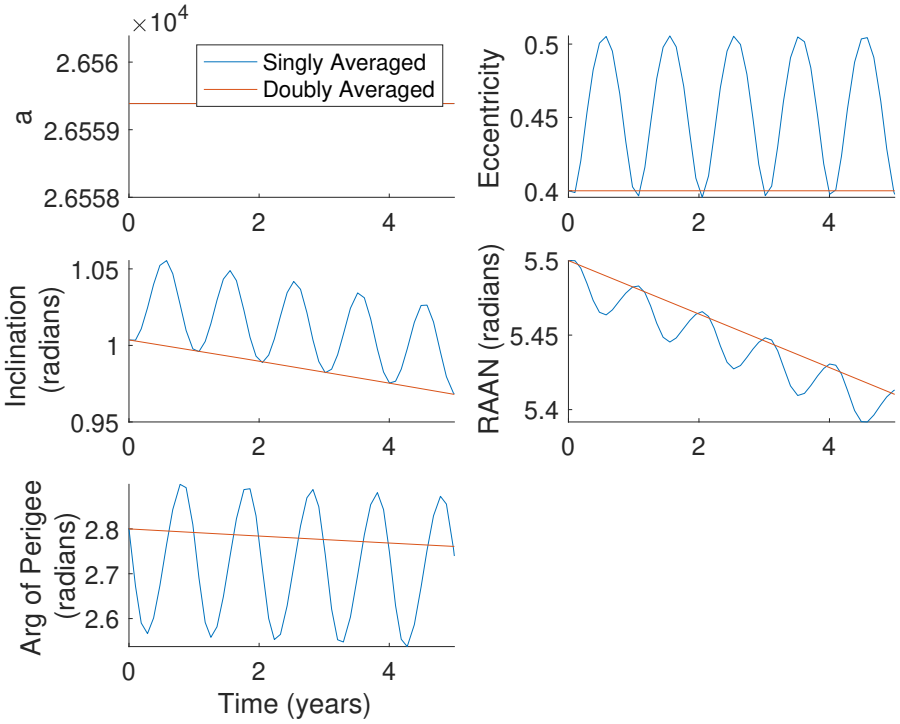

Figure 3.8: Five year simulation of dynamics due to SRP on a piece of debris in a GPS orbit

3.3.1.1 Numerical Correction

To ensure the doubly-averaged model tracks the shift in magnitude occurring over the period, we will initialize the dynamics with a process similar to the short-period correction described in Section 2.1.3. In the case of the short-period corrections, we were modifying the initial conditions over the orbits that were averaged over: modifying the satellite's initial orbital elements to the average over its period and modifying the perturbing bodies' orbital elements to the average over their periods.

The correction discussed here is coming from a failure of the doubly-averaged formulation to capture the perturbing dynamics due to SRP. The reason the formulation is failing to capture the large changes in the orbital elements (eccentricity for example) is the doubly-averaged formulation averages over the perturbing body's orbit and, in the case of SRP, these changes in orbital elements occur on a period close to that time frame, a year (the Earth's orbit about the Sun). The actual

periodicity in SRP dynamics is dependent on the strength of the SRP parameter, Equation 2.16.

In order to incorporate the behavior of the satellite that is averaged over in the doubly-averaged formulation, we run the singly-averaged formulation for a period to capture it. Then we reinitialize the initial conditions from the averages of this result. This will ensure when propagating the doubly-averaged solution for HAMR objects that the shifts in eccentricity due to SRP are incorporated. Although, in practice, adjustments can be made from simulations as short as one year, Figure 3.9 shows variations for five years to further illustrate the dynamics.

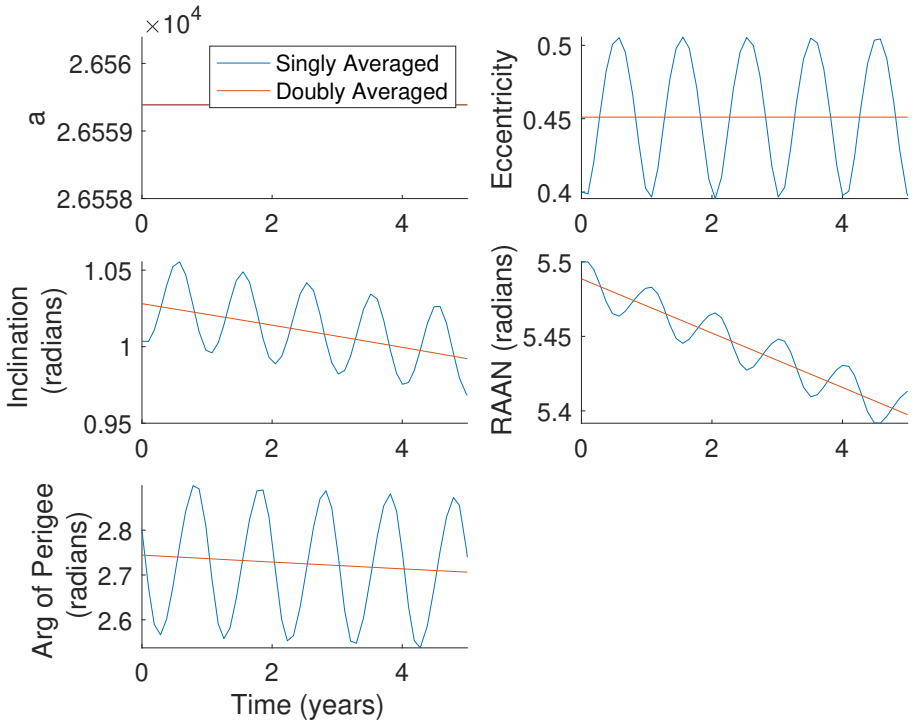

Figure 3.9: Five year simulation of dynamics due to SRP on a piece of debris in a GPS orbit with numerical corrections

With the numerical correction, the doubly-averaged formulation better describes the long term dynamics due to solar radiation pressure allowing long term dynamics to be more accurate.

3.3.1.2 Variation of the Eccentricity

Understanding the long-term behavior of eccentricity is essential for studying the lifetimes of objects. With the numerical corrections, the doubly-averaged model can incorporate the long-term secular effects due to SRP (alongside the third body perturbations that result in the luni-solar resonances). Because SRP causes large variations in eccentricity about its averaged behavior, it is important to incorporate those extrema in addition to the averaged secular behavior of the trajectories.

Realizing the full space in eccentricity the object is traversing can be done by dividing the long-term simulations into shorter arcs. At the end of each arc, the trajectory is propagated for a full SRP period with a simplified SRP model that only includes the averaged effect of SRP and thus does not include gravitational perturbations. We use the rotating averaged SRP solution to propagate the results for an SRP period shown in Equations 2.14 and 2.15 [96]. This method is rapid and does not require integration by making use of the state transition matrix, Φ_r. Because eccentricity is frame independent, the only added complexity of using this new frame is initialing $\boldsymbol{e}_{0_r}$ and $\boldsymbol{h}_{0r}$ in the correct frame, the rotating ecliptic frame.

3.3.1.3 Sensitivity of Initial Positioning

The nuances of the orientation set up in this frame will be discussed in more detail in Chapter 6. For the purposes of this chapter, they are briefly introduced to illustrate an ambiguity problem that arises from using this equation to solve for minimums and maximums of the doubly-averaged solution. Equation 3.1 transforms the vectors, $\boldsymbol{e}_0$ and $\boldsymbol{h}_0$, into the rotating ecliptic frame.

$$\boldsymbol{h}_{0r} = T_R T_E \boldsymbol{h}_0 \tag{3.1}$$

$$\boldsymbol{e}_{0r} = T_R T_E \boldsymbol{e}_0 \tag{3.2}$$

where T_E represents the transformation from the equatorial to the ecliptic and T_R represents the transformation from the inertial to the Sun-Earth line rotating frame and varies with the true anomaly of the Earth about the Sun, ν_s, Equation 3.3.

$$T_R = \begin{bmatrix} 1 & 0 & 0 \\ 0 & \cos\nu_s & \sin\nu_s \\ 0 & -\sin\nu_s & \cos\nu_s \end{bmatrix} \tag{3.3}$$

However, the doubly-averaged formulation averages out the Earth's position relative to the Sun. Therefore, there isn't a correct ν_s to solve the rotation matrix.

Although ν_s has been averaged over and there isn't a correct value to associate with it, there is information from the doubly-averaged model that can be used to correctly understand the variation of the eccentricity at any point. Since the doubly-averaged model is always propagating the average of the eccentricity, the variation of eccentricity should always have its mean equal to the initial conditions (the output from the doubly-averaged solution). For different ν_s and initial conditions, this might not necessarily be the case. However, we can apply a simple correction to force the variation about the initial conditions.

From the set of solutions from $\psi = 0$ to 2π radians of Equations 2.14 and 2.15, we find a set $e(\psi)$, the magnitude of the eccentricity vector. The magnitude of the eccentricity vector is frame independent so there is no "r" subscript on this term. Then we subtract that set by its mean and add the initial eccentricity, Equation 3.4. This forces the mean to be the initial eccentricity instead of the set's initial mean.

$$e(\psi)_{corrected} = e(\psi) - E(e) + e_0 \tag{3.4}$$

where E is the expectation operator, Equation 3.5.

$$E(e) = \frac{1}{2\pi}\int_0^{2\pi} e(\psi)d\psi \tag{3.5}$$

An example of this operation is in Figure 3.10. The black line is the variation of eccentricity over a period of 0 to 2π radians ψ from Equations 2.14 and 2.15. The initial vectors were transformed from the equatorial into the rotating ecliptic frame as shown in Equations 3.1 an 3.2. For simplicity, we use $\nu_s = 0$ making Equation 3.3 an identity matrix, I_{3x3}. The blue line shows the same set with the correction applied in Equation 3.4. The red bar indicates the initial eccentricity and is not a function of ψ.

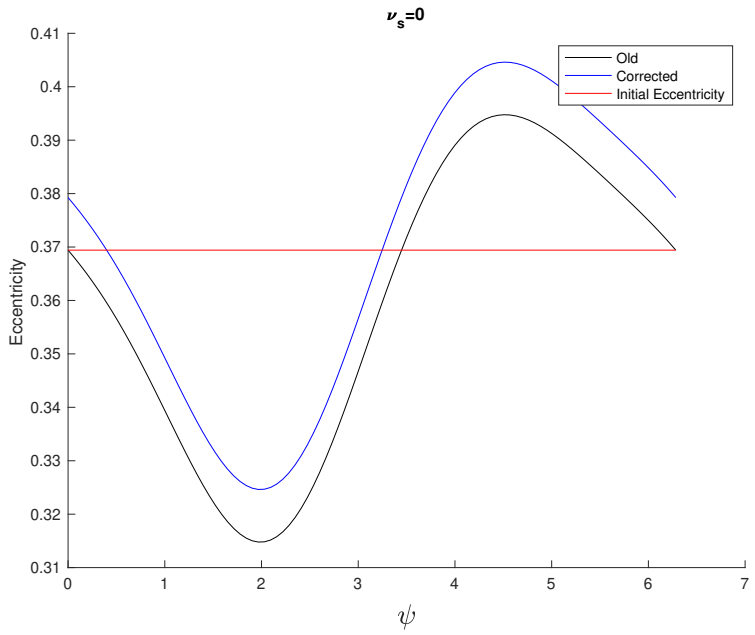

Figure 3.10: Map of eccentricity variations over an SRP period, $\psi = [0 \quad 2\pi]$ radians (close to a year) and the initial eccentricity for this case.

As Figure 3.10 shows, the initial eccentricity variation, the black line, does not have an average equaling the initial condition, the red line. With the correction applied, the black line shifts up to the blue line and now has a mean about the initial eccentricity. This makes the blue line consistent with the assumptions made in using the doubly-averaged equations, that we are propagating the mean of the eccentricity, and thus the initial conditions of the set we are checking around are the mean of that set.

This operation won't affect the amplitude or the degree of variation dependent on the orientation, but it does take out the sensitivities if the initial conditions in that orientation are closer

to the maximum or minimum rather than the true mean. Figure 3.11 shows how the maximum eccentricity can vary without this correction as compared to how it varies with the correction. This figure displays 100 different starting values of ν_s, or initial orientations, as compared to Figure 3.10 which only shows one, $\nu_s = 0$.

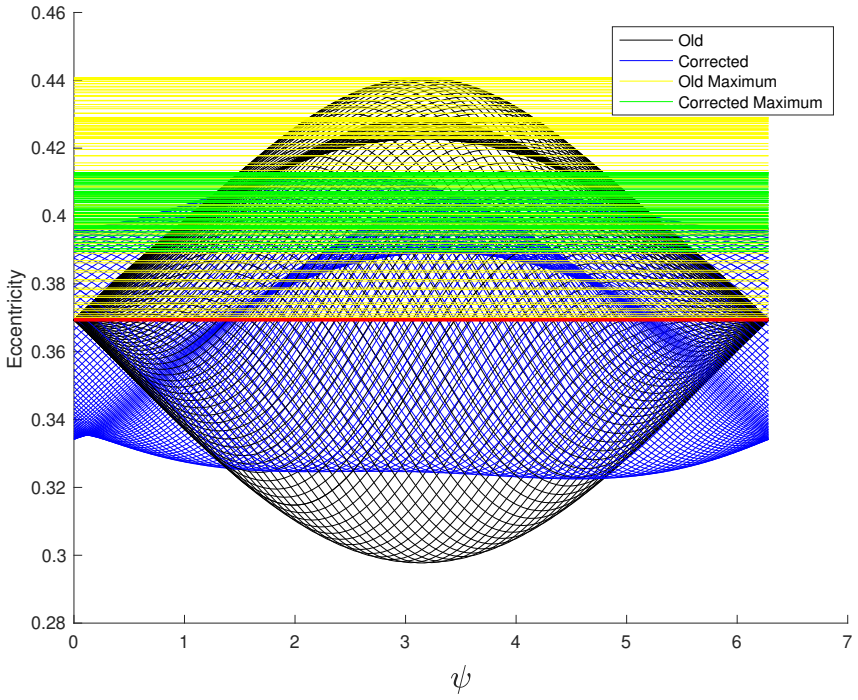

Figure 3.11: 100 different cases of ν_s. Maximum eccentricity for the non-corrected, yellow, set along with their variation, black, and maximum eccentricity for the corrected set, green, with their variation, blue.

It is apparent from Figure 3.11 that without the correction, or the "old maximum", the set can vary between the initial condition, 0.37, and 0.44 eccentricity. The correction narrows this set of possible maximum eccentricities from 0.39 to 0.41, for this particular case.

To verify that this method of checking the variation, we compared two methods, one singly-averaged integrated over a year, the other using the doubly-averaged initial conditions (applying Section 3.3.1.1) and doing a maximum-minimum analysis with the correction described where $\nu_S = 0$. Instead of studying only one initial condition, we sampled 100 different initial eccentricities and inclinations. The resulting difference between the maximums for the 10,000 set of initial

conditions is shown in Figure 3.12.

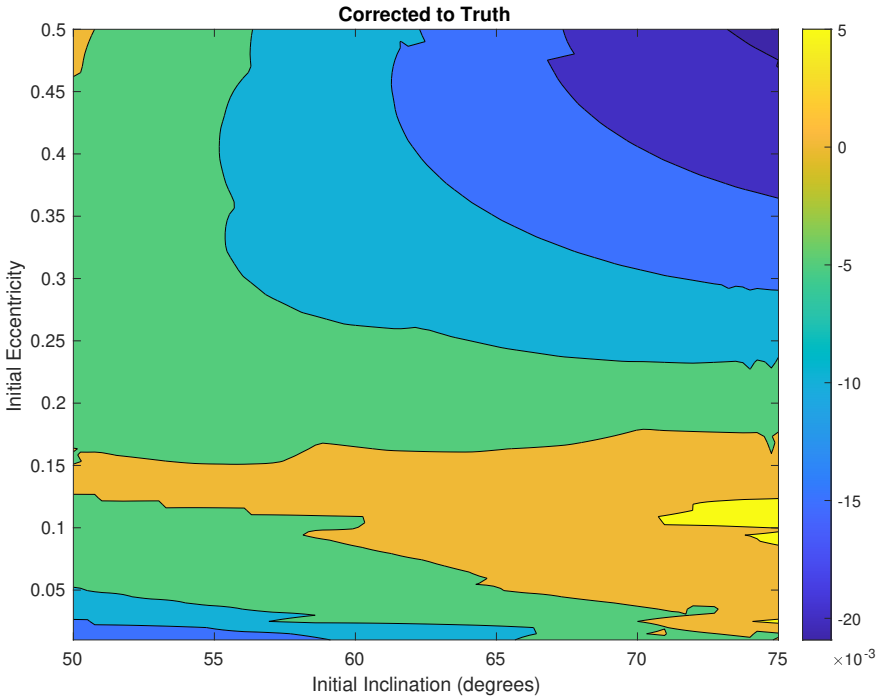

Figure 3.12: Difference between maximum from singly-averaged (truth) and maximum solved by doubly-averaged with correction method for an SRP period (about a year)

Figure 3.12 shows how for the varying eccentricities, the maximum difference from the truth using our described method does not get larger than 0.02 eccentricity. It is important to note that the method described tends to underpredict the true value, indicated by the greater area of negative difference. A consequence of this is that this method would likely predict longer reentry times than shorter ones compared to the actual reentry.

3.3.2 Performance of Doubly-Averaged SRP

Instituting these corrections, we can now utilize the doubly-averaged solution in our analysis of HAMR objects. Because we have instituted large corrections in the doubly-averaged model for SRP, we will perform some additional analysis before we compare its performance in similar methods as the nominal satellite case. This additional analysis will use Lyapunov plots to understand how

well the doubly-averaged solution with the corrections can track general trends in the regime before we hone in on a specific representative orbit.

3.3.2.1 Lyapunov Plots

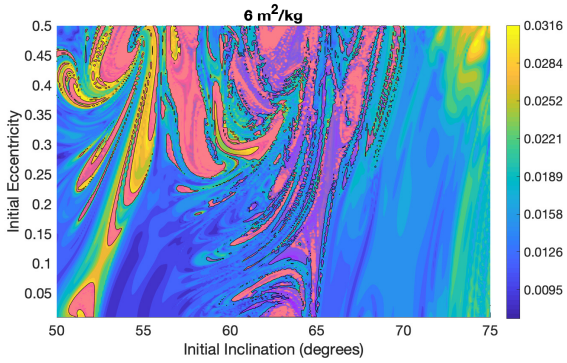

(a) Doubly with singly SRP averaged simulation

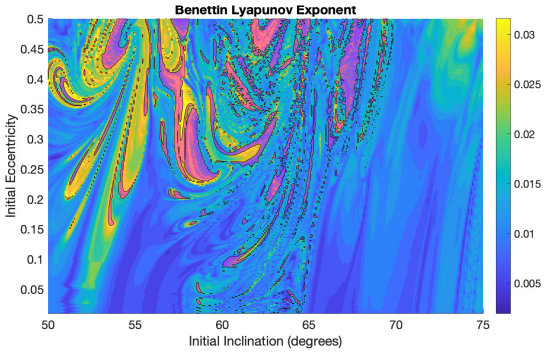

(b) Fully doubly-averaged simulation without max/min analysis

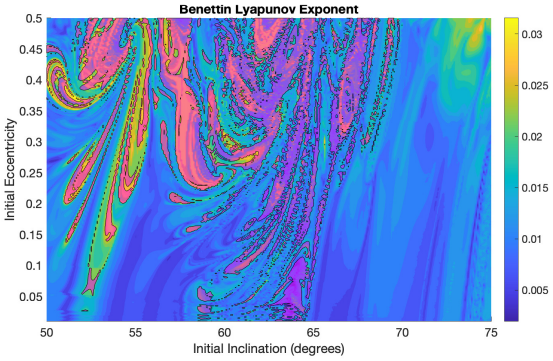

(c) Fully doubly-averaged simulation with max/min analysis

Figure 3.13: FLI maps of the same area to mass ratio with varying methods to determine the reentry condition of the object. Magenta overlay indicates where the object reentered the Earth's atmosphere before the end of the simulation.

Figure 3.13 shows a fast Lyapunov indicator, FLI, maps for a GNSS region. This plots the Lyapunov exponents (1/year) where high exponents indicate more chaotic behavior and low exponents indicate more stable behavior, discussed in Section 2.3.

In addition to the FLI map, Figure 3.13 shows the reentry cases for the same initial conditions, analyzed using varying methods in which the magenta overlay indicates where the satellite reentered

Earth's atmosphere before the end of the 200 year simulation. The first case, the doubly averaged third body with singly-averaged SRP simulation, will be the surrogate for the truth. The second case uses the doubly-averaged analysis, incorporating the numerical corrections of the initial conditions from Section 3.3.1.1. The fully doubly averaged model, b and c, appears to have consistency in the predicted chaotic behavior (blue opposed to yellow) as compared to the doubly wth singly SRP. The second case fails to fully encapsulate the reentry conditions (magenta) of the doubly with singly. The third case, c, uses the doubly-averaged analysis with the same corrections as b and also incorporates the maximum and minimum analysis. The third case more closely matches the doubly-averaged with singly-averaged SRP and illustrates the importance of adding in the maximum and minimum analysis.

With the corrections, the overall behavior of the chaotic effects are shown in the doubly-averaged case to match the ones in the singly-averaged case. With the variation analysis, the simulation can better detect when objects are reentering the Earth's atmosphere before the end of the simulation.

3.3.2.2 Targeted Region

Following Section 3.2 analysis of nominal area-to-mass ratios, we will also analyze how distributions of singly- and doubly-averaged dynamics match for HAMR objects. Because the dynamics of HAMR objects don't exactly line up to the nominal area-to-mass ratio case, we will also start by finding a highly chaotic solution for a HAMR object. Figure 3.14 shows the varying reentry times for HAMR objects integrated for 100 years.

From Figure 3.14a, an eccentricity and inclination value were chosen to be 0.4 and 56° which was a relatively low eccentricity region surrounded by fast reentering trajectories. Figure 3.14b surveys the RAAN and argument of perigee trade space for those values; two cases were chosen to understand the doubly-averaged dynamics behavior. Those two cases are $\Omega = 5.27$ rad, $\omega = 2.86$ rad and $\Omega = 5.5$ rad, $\omega = 1.84$ rad, Table 3.3. The first case was chosen for its surrounding reentering trajectories while the second case borders some non-reentering solutions. Analyzing both

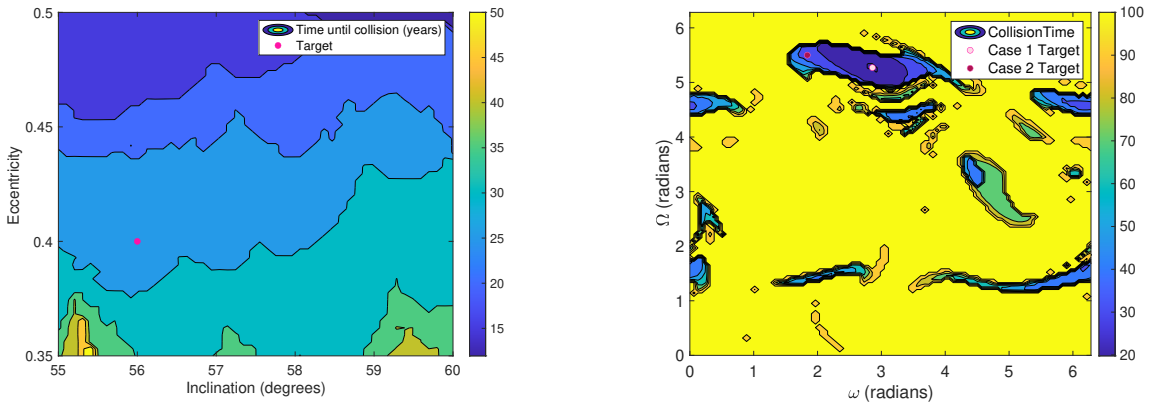

(a) (b)

Figure 3.14: Choosing a target. (a) Comparison of chaotic regions independent of Ω and ω. Each point is the smallest collision time of 14 different Ω and ω (196 cases). (b) The varying reentry time for e=0.4 and i=56°in ω and Ω space.

these types of cases will help solidify the more complex dynamics with both SRP and third body effects.

Table 3.3: Targeted Orbital Parameters for HAMR Objects

Case	a	e	i	Ω	ω	Reentry Time
Case 1	26560 km	0.400	56°	5.3 rad	2.9 rad	24.2 years
Case 2	26560 km	0.400	56°	5.5 rad	1.8 rad	38.7 years

3.3.2.3 Capturing a Distribution

The first case for studying long-term dynamics simulations of a HAMR object is initial conditions: e=0.4, i=56°, $\Omega = 302°$, and $\omega = 164°$. These initial conditions result in a nominal reentry case of ∼24 years. This case is surrounded by similar reentering solutions in Figure 3.14b.

Figure 3.15 shows how the singly-averaged solution compares to the doubly-averaged solution for this case. Figure 3.15a shows how the variation of eccentricity compares for the two sets given the case. Because the doubly-averaged solution pauses and checks the variation about the mean every few years to determine whether or not the solution reenters, the solution stops the integration when the variation is large enough that the reentry condition has been met, $e > 0.76$. Similar to

the previous method of detecting overlap in distributions (Section 3.2.3), Figure 3.15b shows a case where the two sets of solutions were varied by 0.625%, the largest initial distribution before the sets include non-reentering solutions.

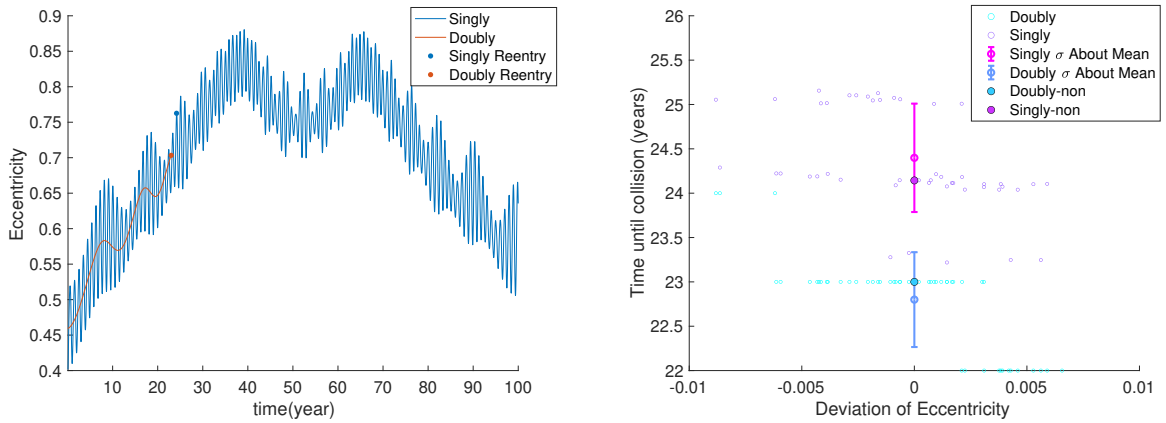

(a) (b)

Figure 3.15: First case of a HAMR object with initial conditions e=0.4, i=56°, $\Omega = 302°$, and $\omega = 164°$. (a) The variation of eccentricity of singly dynamics as compared to doubly. (b) Comparison of singly and doubly distributions' reentry times and their respective changes in eccentricity for a 0.625% initial distribution

Although some of the reentry times match between the two sets, the distributions are not large enough to have their standard deviations cross. Unfortunately, increasing the initial distribution any larger than 0.625% of the initial conditions results in some of the solutions not reentering at all and thus are unusable for our analysis.

The second case had the initial condition: e=0.4, i=56°, $\Omega = 320°$, and $\omega = 105°$. This corresponds to an area that has a reentry of 39 years but is surrounded by differing types of solutions in Figure 3.14b. Like the previous case, Figure 3.16 compares the two averaging methods.

In this case, Figure 3.16a shows how the two non-perturbed solutions' eccentricity varies with the 100 year simulation. The doubly-averaged solution begins to wander above the mean value fairly early in the simulation but then quickly drops below. Therefore, it never captures the reentry condition, which is met about 40 years into the simulation. Because the doubly-averaged solution misses the reentry condition, its reentry time is greater than 100 years and thus greater

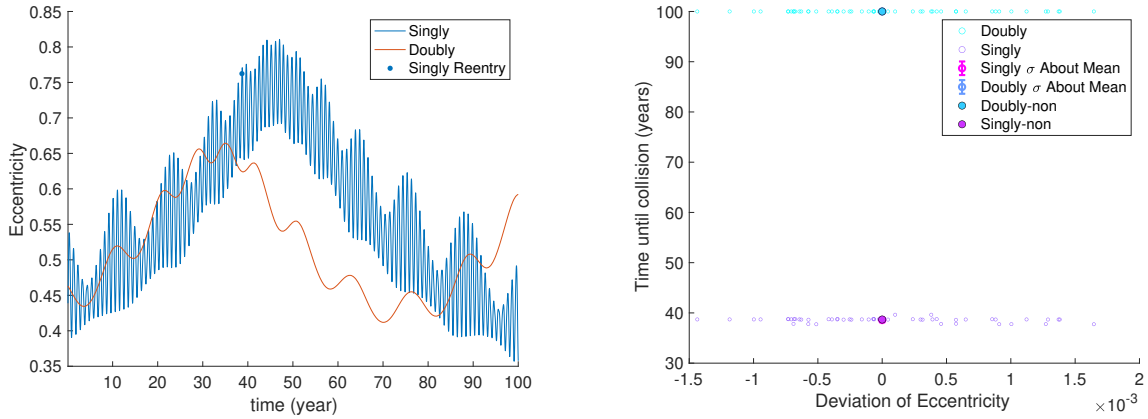

(a) (b)

Figure 3.16: Second case of a HAMR object with initial conditions e=0.4, i=56°, $\Omega = 320°$, and $\omega = 105°$. (a)The variation of eccentricity of singly dynamics as compared to doubly. (b) Comparison of singly and doubly distributions' reentry times and their respective changes in eccentricity for a 0.15% initial distribution

than 50 years off the nominal. Therefore, there is no variation about the initial conditions that could reconcile the two sets. Figure 3.16b shows a 0.15% for reference notwithstanding the nonexistence of a distribution that could describe the singly.

3.3.3 Using Singly SRP

The fully doubly-averaged solution is not robust enough to characterize the phase space to the level of accuracy needed in our analysis for HAMR objects. To help alleviate some of the shortcomings of the fully doubly-averaged analysis and maintain some of the computational efficiency, for HAMR objects, we will explore an additional scenario alluded to in Section 3.1.2. This scenario uses a doubly-averaged model for third body perturbations and a singly-averaged model for the solar radiation pressure perturbation. Therefore, we only need to track the movements of the Sun, a much slower period than the lunar period. This will allow the model to more speedily calculate the third body trajectories where the short-period effects due to the bodies is not required for a highly accurate solution. Nonetheless, it does incorporate the short-period effects due to the Sun on SRP which has a large influence on the behavior of the perturbation.

3.3.3.1 Capturing a Single Solution

We will analyze the doubly-averaged third body model with singly-averaged solar radiation pressure similar to the analysis of a nominal area-to-mass ratio. The first set of solutions studied is for the first SRP case, e=0.4, i=56°, $\Omega = 302°$, and $\omega = 164°$, with an initial condition distribution 0.3%. [1]

A 0.3% distribution was large enough to encompass the actual solution with solutions varying between 24.1 and 25.2 years, graphs in Appendix B. However, it was not large enough to encompass the standard deviation of the set. Therefore, we increased the distribution from 0.3% to 0.5% about the initial conditions which is shown in Figure 3.17. It should be noted that although the distribution is bimodal and not Gaussian, the standard deviation is still a useful metric in this data as it will remove any large outliers from the main distribution serving its purpose in this research goal.

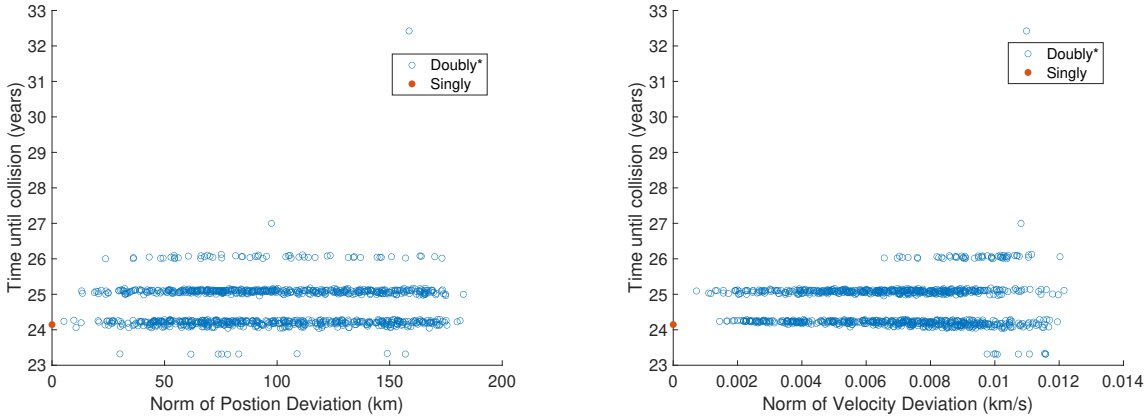

(a) Magnitude deviation of position vector

(b) Magnitude deviation of velocity vector

Figure 3.17: The deviation of the initial conditions in terms of the magnitudes of the Cartesian coordinates as compared to the final reentry times for a 0.5% initial distribution

This larger initial condition set has expanded the reentry time distribution to vary between 23 and 33 years. Figure 3.18 shows the solution set in terms of the orbital elements with the standard deviation.

[1] The asterisks in these graphs indicate that the doubly solution is using a singly SRP model

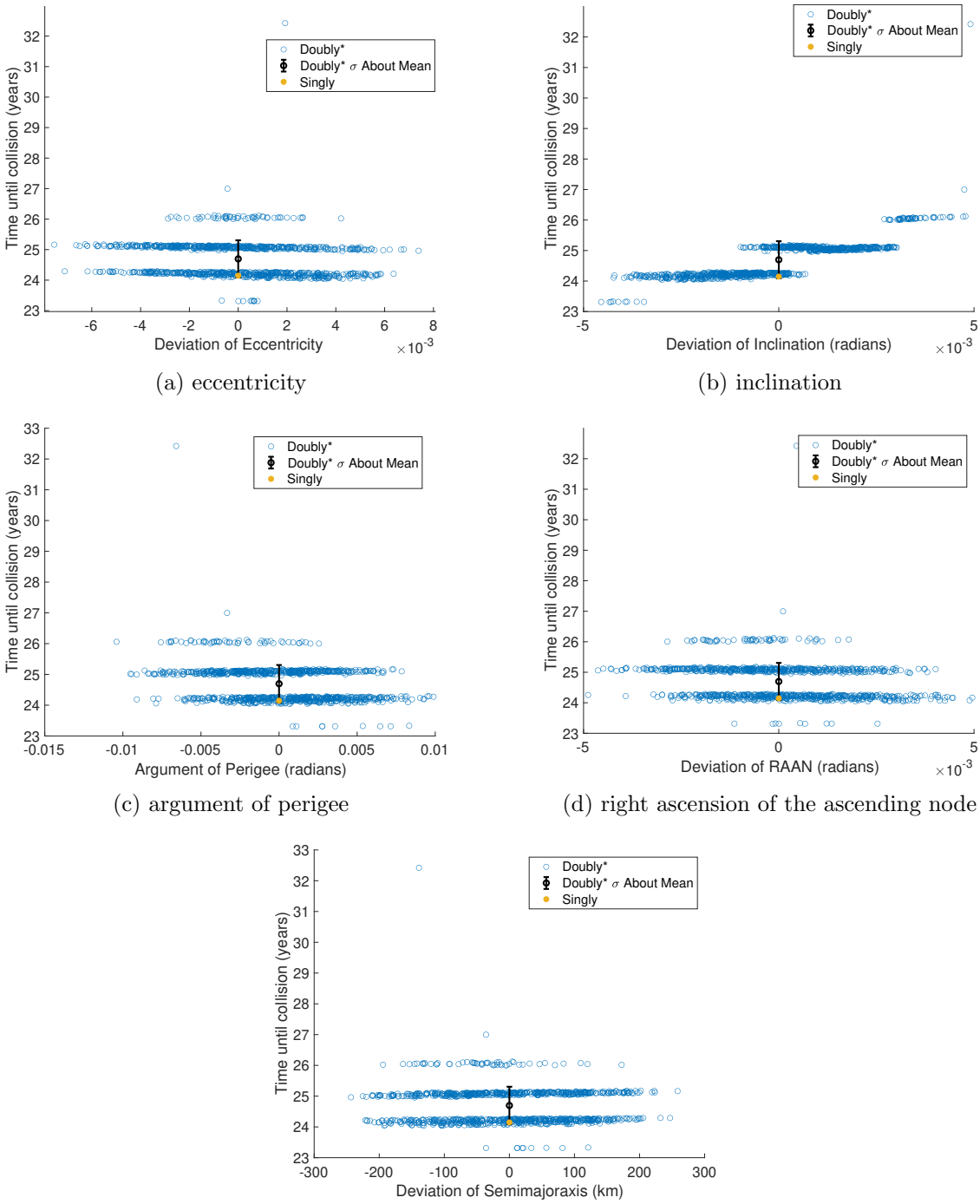

(a) eccentricity

(b) inclination

(c) argument of perigee

(d) right ascension of the ascending node

(e) semi-major axis

Figure 3.18: The deviation of the initial conditions in terms of the orbital elements as compared to the final reentry times for a 0.5% initial distribution

With the larger overall distribution, the 0.5% variation about the initial condition set's stan-

dard deviation encompasses the actual reentry time of 24.15 years.

The doubly-averaged solution with singly SRP is able to track the solution better in this case than the fully doubly-averaged result, which is expected. In this case, the singly SRP is able to compensate for the shortcomings of the previous model. However, the true test of the doubly with singly SRP model is the second case where the fully doubly-averaged result was unable to predict a reentry at all. This case was for an e=0.4, i=56°, $\Omega = 320°$, and $\omega = 105°$.

The initial distribution is 0.01% about the initial conditions to show a case with a small distribution; the small distribution encompasses the true reentry time with a final distribution of 0.02 years or about a week. Because the doubly-averaged with singly SRP is so close to the truth for this case, the two solutions are only off by 0.006 years. With the small variation in reentry times, the standard deviation of the set does not encompass the true value.

Next we increased the set to vary 0.02% about the initial distributions.

Figure 3.19 shows that the larger distribution now varying about 16 days has a standard deviation which encompasses the results.

3.3.3.2 Capturing a Distribution

To continue our analysis on the performance of the performance of the doubly-averaged with singly SRP model, we studied how the two distributions would compare in similar methodology as Section 3.2.3.

In congruence with the earlier HAMR analysis, we will examine the first case of e=0.4, i=56°, $\Omega = 302°$, and $\omega = 164°$. Figure 3.20 shows how the reentry times vary in terms of the magnitudes of the Cartesian coordinates for an initial distribution of 0.2% about the initial conditions.

The distributions overlap and the standard deviation for both sets of distributions overlap as well. Figure 3.21 shows how the initial deviation of some of the orbital elements compare.

The second case studied is for an e=0.4, i=56°, $\Omega = 320°$, and $\omega = 105°$. Because the two solutions are within weeks of each other the initial distribution is only varied by 0.0025% about the initial conditions because significant overlap is expected even with an incredibly small distribution.

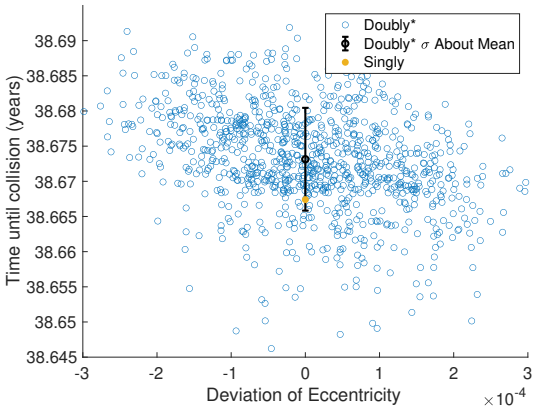

(a) eccentricity

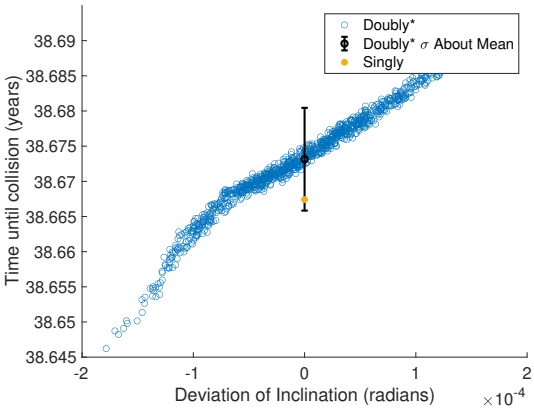

(b) inclination

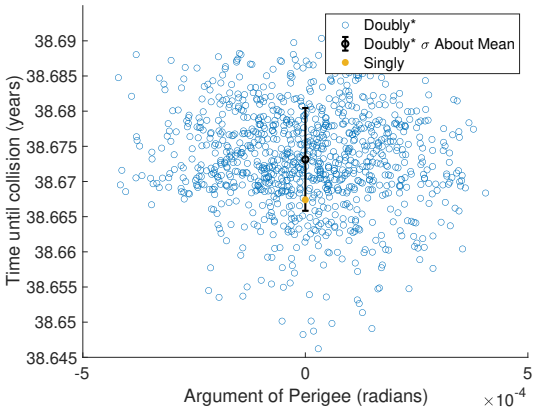

(c) argument of perigee

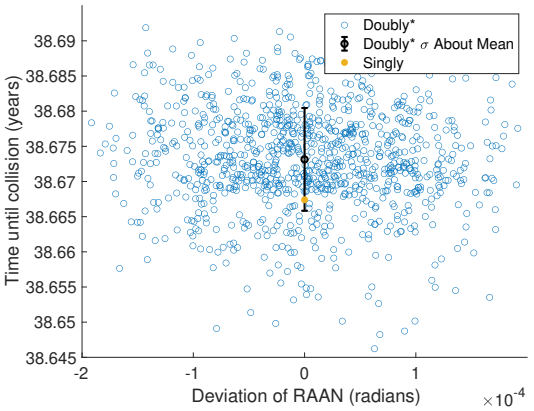

(d) right ascension of the ascending node

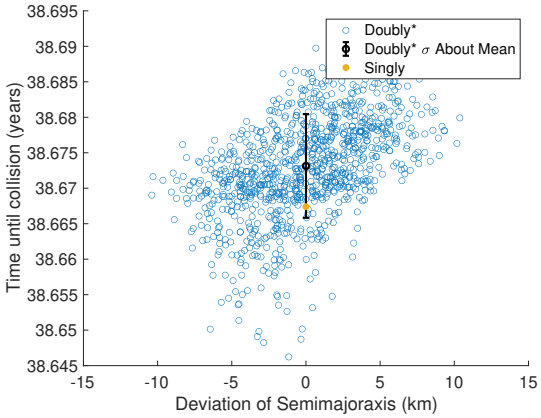

(e) semi-major axis

Figure 3.19: The deviation of the initial conditions in terms of the orbital elements as compared to the final reentry times for a 0.02% initial distribution

Figure 3.22 shows despite the initial distributions only varying by 0.0025% of the initial

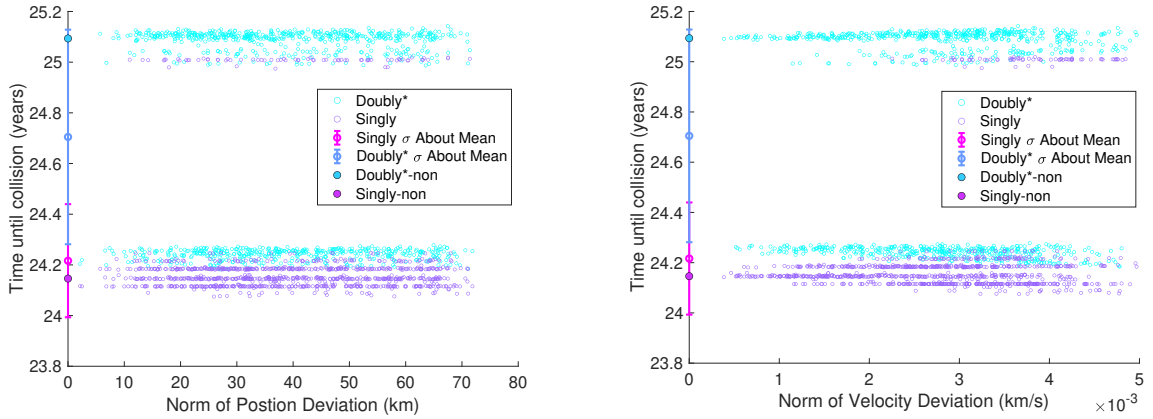

(a) Magnitude deviation of position vector

(b) Magnitude deviation of velocity vector

Figure 3.20: The deviation of the initial conditions in terms of the magnitudes of the Cartesian coordinates as compared to the final reentry times for a 0.2% initial distribution

conditions we still see significant overlap between the two sets as expected.

Figure 3.23 shows these variations in reentry times in terms of the orbital elements. It is also shown here with the standard deviations how much the two distributions overlap despite their small size. This predominately comes from the doubly model only differing by only a couple of days.

3.3.4 Varying Area-to-Mass Ratios

Area-to-mass ratios can vary up to as high as 110 m^2/kg, a value representative of inner layers of MLI [30]. The previous focus of 6 m^2/kg (representing an outer layer of MLI) was especially important because the effects due to solar radiation pressure and third body effects are on a similar order for that area-to-mass-ratio. However, to fully understand how debris would act in this region, it is important to also study higher area-to-mass ratios where solar radiation pressure would be more dominant.

Figure 3.24 shows how increasing the area-to-mass ratio will not necessarily guarantee reentry of these objects. Excluding the extremely high area-to-mass ratio case, there isn't necessarily a set threshold where all objects will enter within a year because of the other perturbations and the

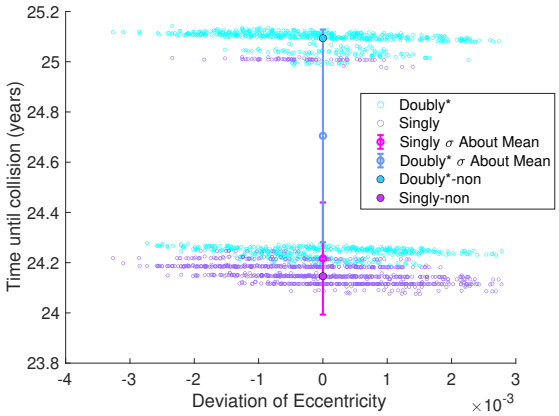

(a) eccentricity

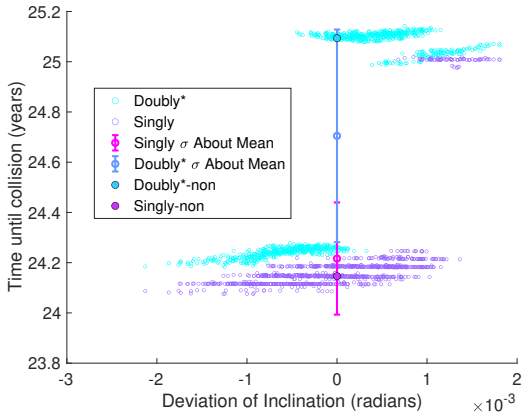

(b) inclination

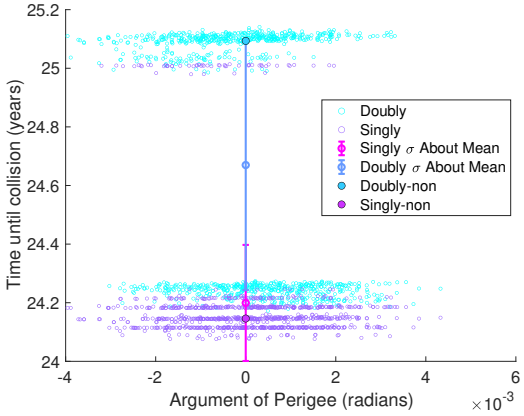

(c) argument of perigee

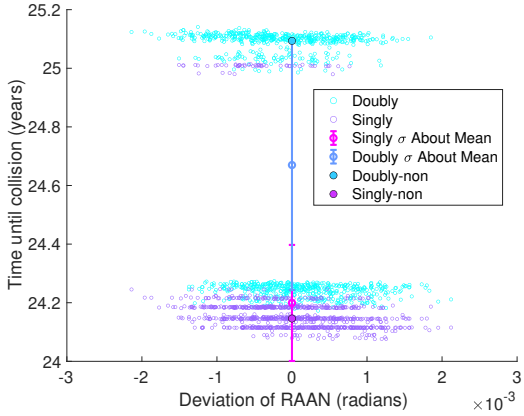

(d) right ascension of the ascending node

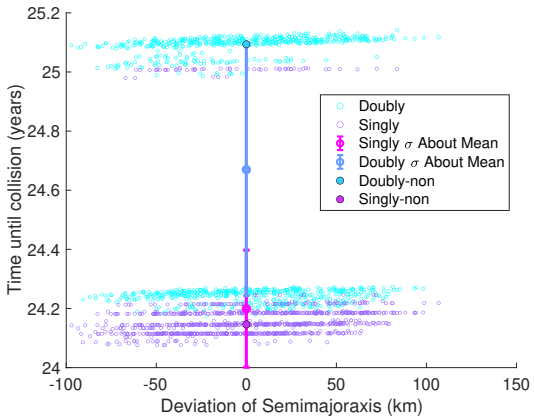

(e) semi-major axis

Figure 3.21: The deviation of solutions for a distribution of 0.2% of the initial conditions in terms of the orbital elements as compared to the final reentry times

original orientation of the orbits. The initial conditions for this set of examples were the same as

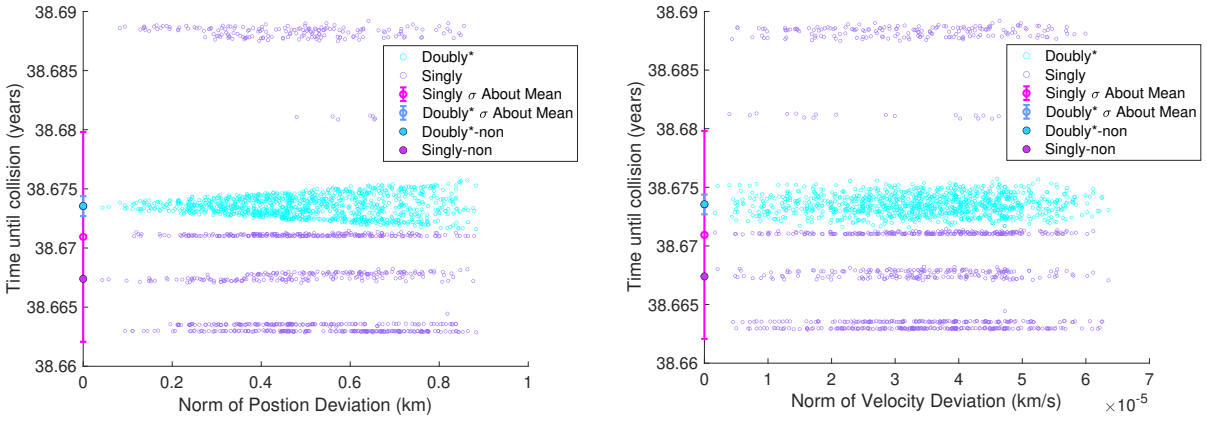

(a) Magnitude deviation of position vector

(b) Magnitude deviation of velocity vector

Figure 3.22: The deviation of the initial conditions in terms of the magnitudes of the Cartesian coordinates as compared to the final reentry times for a 0.0025% initial distribution

the nominal area-to-mass ratio targeted region. These results are consistent with nominal GPS orbits studied by Anselmo et al. [2].

3.4 Discussion

The doubly-averaged model proves to be an adequate model for analyzing highly chaotic trajectories in MEO for nominal satellite area-to-mass ratios. For these objects, the doubly-averaged solution still deviates from the singly-averaged solution but the resulting reentry times are close. Through our analysis for the particular worst case initial conditions chosen, we have found a confidence of 0.25% about the initial conditions for the model. The distribution of a set varied by 0.25% had a standard deviation that encompassed the true solution. When characterizing a distribution of solutions, the doubly-averaged model does not need the same level of accuracy. To describe a distribution, we only need the initial conditions to be varied by 0.15%.

The HAMR objects did not fare as well with the doubly-averaged model. This was primarily driven by the doubly-averaged model's failure to capture eccentricity deviations in the solution. Through several corrections, we demonstrated that we can not only track the true average but also track the variation of eccentricity about the average. This shows remarkable improvements in the

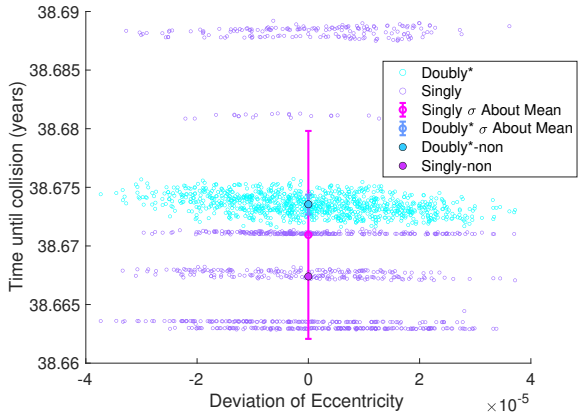

(a) eccentricity

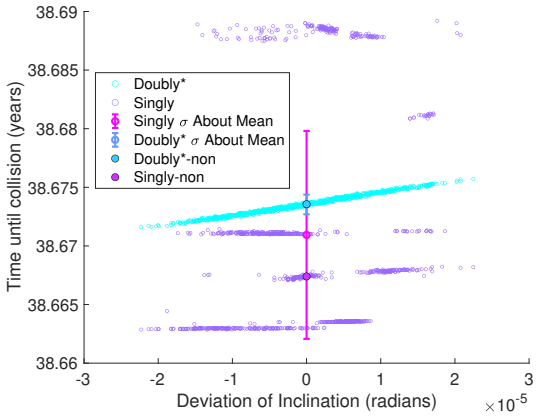

(b) inclination

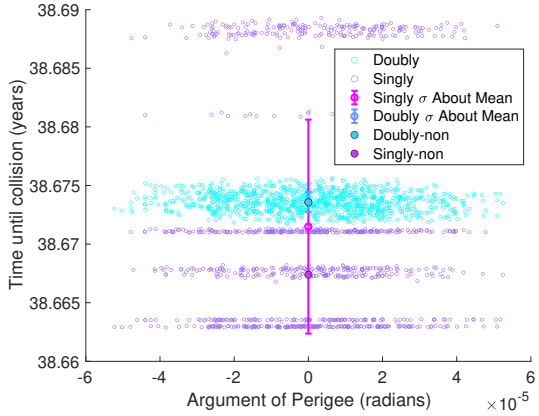

(c) argument of perigee

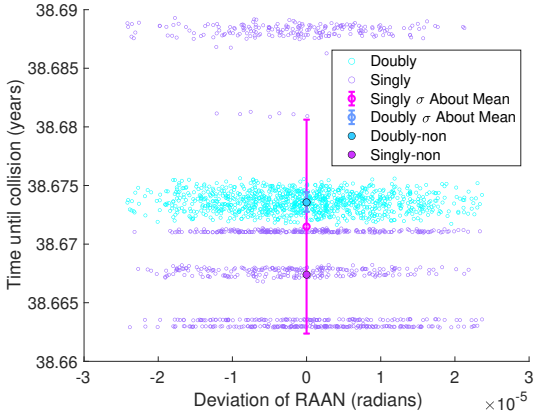

(d) right ascension of the ascending node

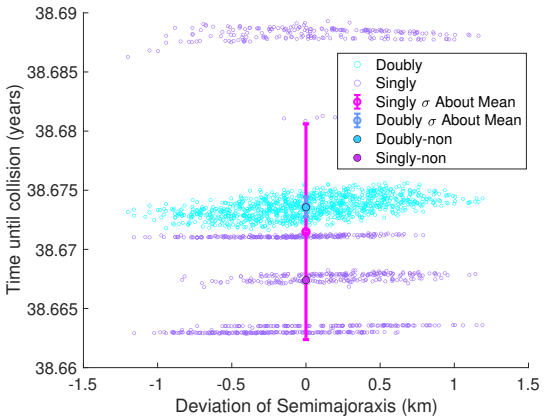

(e) semi-major axis

Figure 3.23: The deviation of the initial conditions in terms of the orbital elements as compared to the final reentry times for a 0.0025% initial distribution

doubly-averaged model for HAMR objects but does not to track the true solution close enough for

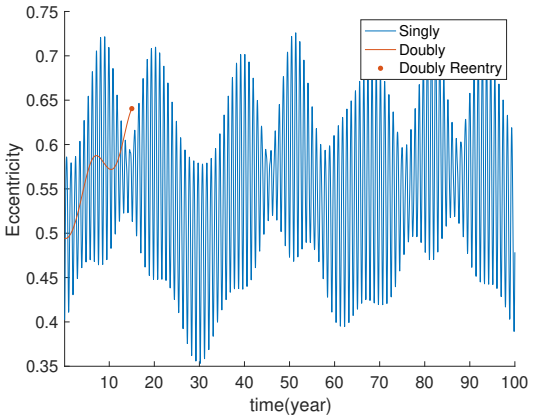

(a) 10 m^2/kg

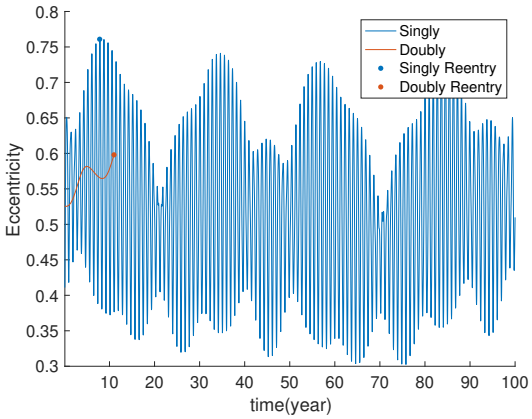

(b) 15 m^2/kg

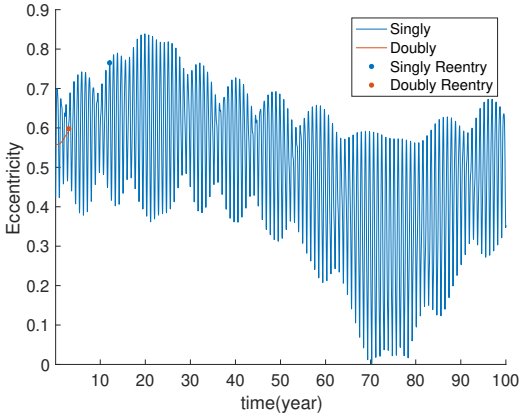

(c) 20 m^2/kg

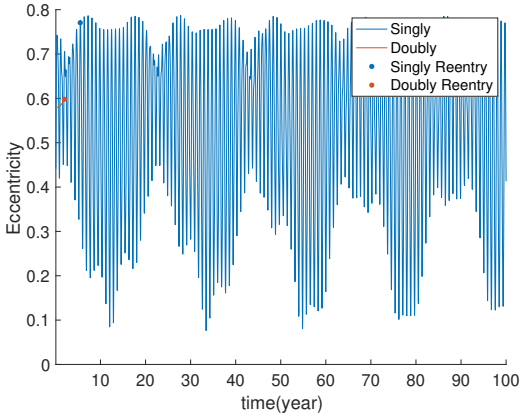

(d) 25 m^2/kg

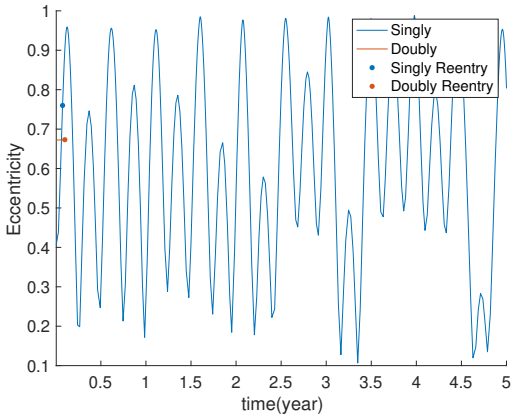

(e) 100 m^2/kg

Figure 3.24: Varying area-to-mass ratios for up to 100 years showing the complex behavior of the dynamics of the region (Except for the 100 m^2/kg case which reaches an eccentricity of 1 in the first ten years)

the precision our Monte Carlo analysis requires.

For HAMR objects, we implemented a third method to study the trajectories in this region. This method involved using the doubly-averaged model to propagate results in third body perturbations and using the singly-averaged model for solar radiation pressure. This method proves to be faster than the fully singly and more accurate than the fully doubly. The doubly-averaged with singly SRP for the less accurate chaotic case studied still only required an initial distribution about the initial conditions to be 0.5%. For capturing a distribution's results, the initial distribution only has to be varied by 0.2% of the initial conditions.

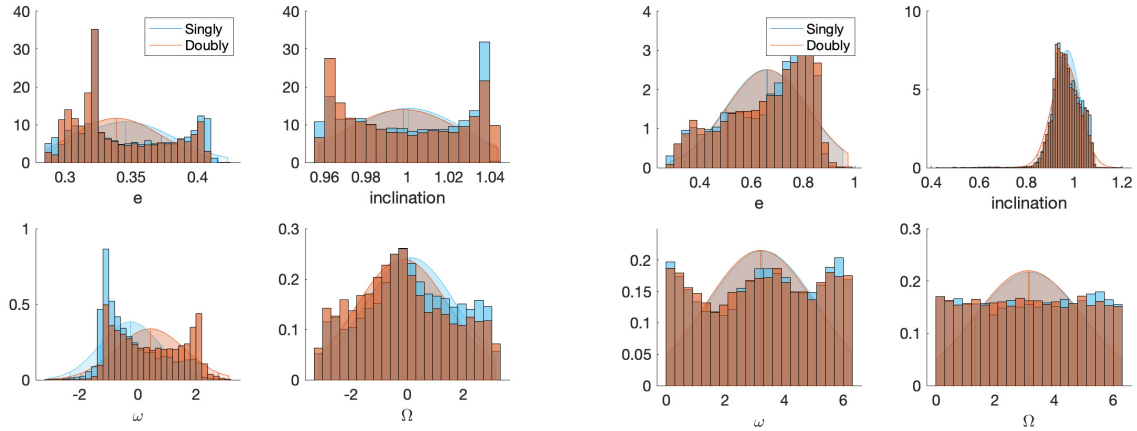

(a) (b)

Figure 3.25: 10,000 Monte Carlo distribution simulation with the respective final pdf and histograms of the orbital elements (a)Nominal satellite case (b) HAMR case where doubly is with singly SRP

To illustrate how well the doubly averaged solution would perform in practice, we applied the limitations from our findings to Gaussian distributions. For our example GPS orbit, the constraints would initialize the sigmas to be on the order of 50 km in position and 5 m/s in velocity. These deviations are large but necessary to ensure the doubly distribution captures the singly solution in this regime. This would model the typical uncertainties in terms of the initial means and sigmas for a specific satellite or known object. Figure 3.25 shows the final distributions for the orbital elements for two 200 year simulations. The first set of graphs is for a nominal area-to-mass ratio satellite case with a 0.15% distribution and the second is for a HAMR object with a 0.2% initial

distribution. These limits are consistent with the finding in this paper. In contrast, Figure 3.26 shows the same initial conditions with tighter initial uncertainty distributions on the order of 10 km and 1 m/s. The smaller initial distribution sets do not agree as well and the doubly is unable to match the behavior of the singly averaged. Figure 3.27 shows how the reentry times for the two distributions of the nominal area-to-mass ratio compare (the HAMR case is bimodal in reentry times and not as easily understood from a probability density function).

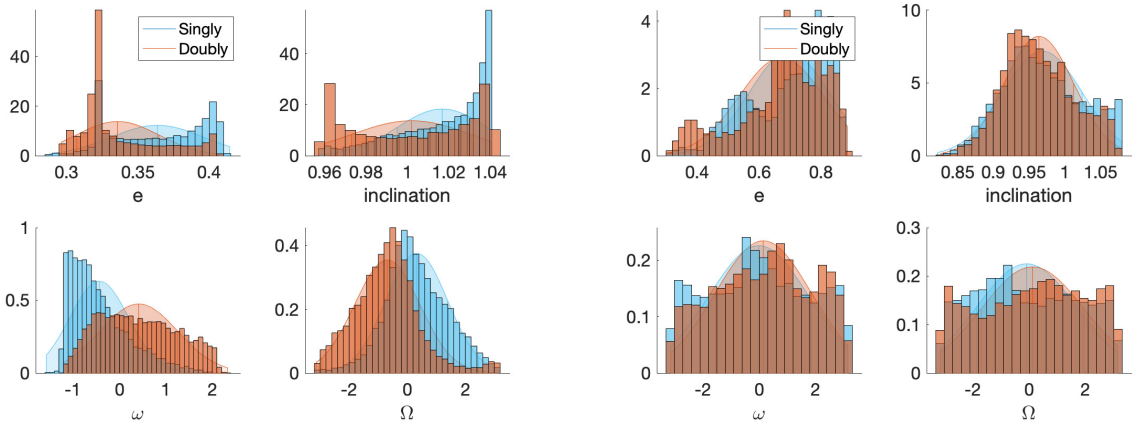

Figure 3.26: 10,000 Monte Carlo distribution simulation with the respective final pdf and histograms of the orbital elements for an order smaller distribution than Figure 3.25 (a)Nominal satellite case (b) HAMR case where doubly is with singly SRP

3.5 Conclusion

This research goal studied how well a doubly-averaged model can describe the highly chaotic trajectories in the medium Earth orbital regime. Our primary focus was on two different area-to-mass ratios, one representing a satellite in the region and the other representing a piece of debris more susceptible to SRP perturbations.

For the satellite case, the doubly-averaged solution tracks the reentry of the debris very well. Through a Monte Carlo analysis, we were able to put bounds on the confidence levels of that model characterizing a reentry and characterizing a set of solutions' reentries.

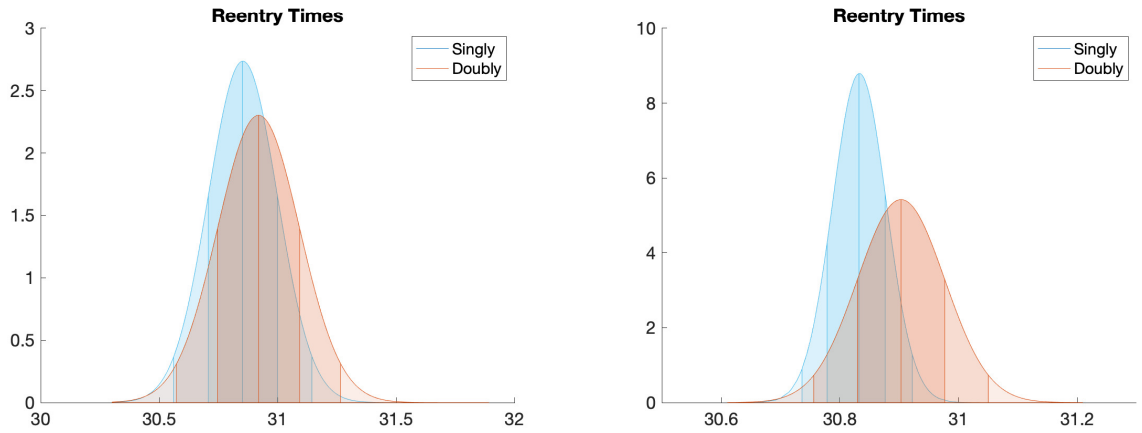

(a) (b)

Figure 3.27: 10,000 Monte Carlo distribution simulation with the respective final pdf of the reentry times for a nominal satellite (a) for a distribution at the limit of its performance 50 km and 5 m/s (b) for a distribution of 10 km and 1 m/s.

The doubly-averaged solution had shortcomings in tracking a case for a high area-to-mass ratio object. In this goal, we have demonstrated some key corrections that can be incorporated to vastly improve the performance. These corrections allow for analysis in general trends, like a Fast Lyapunov Indicator map, but still failed to characterize a specific solution or sets of solutions.

By using the singly-averaged model for solar radiation pressure in conjunction with the doubly-averaged model for third body gravitation perturbation, we were able to better characterize the solution of high area-to-mass ratio objects without sacrificing computation time the fully singly-averaged model requires. The singly-averaged SRP model also shows significant improvement in areas where the doubly-averaged SRP model fails. This could be a result of the cases where the doubly-averaged SRP model fails to even predict a reentry or cases where SRP has a more dominant effect and thus performance of the overall solution is greatly improved when that case has a more robust model for SRP.

This chapter has demonstrated through rigorous analysis that semi-analytical methods can be utilized in highly chaotic environments. The doubly-averaged formulation for third body gravitation provides an accurate, although not exact, depiction of the chaotic regime of medium Earth orbit.

Depending on the area-to-mass ratio and the level of fidelity required, we have shown two methods for analyzing how solar radiation pressure can be studied in this environment. This thesis also provides methods of using doubly-averaged dynamics for analyzing solar radiation pressure in any environment.

Chapter 4

Research Goal 2 - Stability of Debris in MEO

Graveyard orbits are already a mitigation practice for debris at high altitudes, making them an attractive potential solution to debris mitigation in medium Earth orbit. Because there are known areas of chaotic behavior of the region, stable graveyard orbits are hard to find. Previous research has looked at finding stable orbits by studying objects representative of the satellites in the region, massive satellites (area-to-mass ratios of about 0.02 m^2/kg). As noted in the previous chapter, when objects with higher area-to-mass ratios inhabit the regime, the instability maps change in structure compared to the nominal area-to-mass ratios (Figure 3.13). Therefore, when considering a breakup event, it is important to incorporate the large variance in debris types a fragment cloud contains to understand the long term stability of the orbits of the region.

This chapter will focus on understanding the long term behavior of two breakup events in MEO. The first breakup event is what Johnson et al. characterize as a low intensity explosion, representing an event like a battery exploding on a satellite in this orbital regime [47]. The second event we will characterize is a high intensity explosion, representing an event like a collision between two satellites with large relative velocities. By analyzing both types of events, we will be able to understand how debris from breakup events will interact with the luni-solar resonances in this orbital regime. This analysis will be crucial in determining whether a potential graveyard orbit could be a viable solution for MEO, or whether if, after dynamic events in the region, the debris interact with nearby unstable regions and are a potential hazard to functioning spacecraft in nearby orbits.

Before delving into the breakup events, the chapter will begin with the chaotic dynamics of the region. This will be followed by the description of the two breakup events studied. The analysis of the 200 year simulations will be broken into three parts. The first part will be dedicated to studying the reentry behavior and maximum eccentricities of the fragments in each cloud. The second part will be dedicated to understanding how much of the time fragments spend in their orbits interacting with each of the nominal orbits of the regime. The third part will be dedicated to deciphering larger trends based on right ascension of the ascending node, initial epoch, and semi-major axis.

4.1 Fragment Cloud

NASA's Orbital Debris Program Office provided the breakup fragment clouds for each of the events discussed in this paper from their breakup model [47]. The first event discussed is a low intensity event. This would be representative of an explosion or other type of breakup event. This event is low energy and results in a small cloud of fragments about the initial conditions of the original satellite. The other event modeled is a collision. Because the nominal orbits of these objects are in a circular orbit, we modeled the collision event to be where the two satellites had a difference of right ascension of the ascending node (RAAN) of π radians and collided at the equator. Because all the constellations are heavily inclined, the collision is catastrophic, a relative magnitude between the two objects close to six or seven km/s. This event results in a larger swath of fragments, some which are no longer bound to Earth orbit and some which reenter immediately.

Table 4.1 shows the initial conditions for the events in terms of the orbital elements, semi-major axis (a), eccentricity (e), inclination (i), argument of perigee (ω), RAAN (Ω), and true anomaly (ν). For simplicity, each type of event (explosion and collision) uses the same initial conditions. The impactor's initial conditions for the collision event is the same as the parent object's described in Table 4.1 but is out of phase by π radians in RAAN and true anomaly.

The masses of each of the satellites were chosen based on the following iterations. Galileo events are modeled after Galileo FOC satellites; GPS events are modeled after GPS Block IIF

Table 4.1: Initial Conditions for Breakup events.

GNSS	a (km)	e	i (deg)	ω (rad)	Ω (rad)	ν (rad)
GPS	26559	0.003	55°	5	6	$2\pi - 5$
Galileo	29600	0.003	56°	5	6	$2\pi - 5$
GLONASS	25400	0.003	64.8°	5	6	$2\pi - 5$

satellites; GLONASS events are modeled after GLONASS-K satellites [99].

4.2 Eccentricity Evolution for Fragment Clouds

4.2.1 Galileo

In this section, we will detail how fragment clouds evolve with long-term simulations in the Galileo constellation. The simulations were run for 200 years after each event. The mass of the satellite is representative of a Galileo FOC satellite [99].

4.2.1.1 Breakup

The first event represents the low-intensity breakup. This produces a fragment cloud of 378,577 fragments. The fragments themselves are binned according to size with bin numbers of 1, 10 , and 100; the smaller fragments resulting in the larger binning groups.

Figure 4.1 shows the maximum eccentricity achieved over the 200-year simulation relative to the object's area-to-mass ratio. The three scatter plots are scaled differently depending on three characteristics of the bin: number of objects, area of the object(s), and mass of the object(s) in the bin.

It is not just high-area to mass ratio objects moving toward high eccentricities. Some more massive objects start to inhabit the area. Many objects reach a maximum eccentricity to reenter the Earth's atmosphere, ~ 0.78 depending on the exact semi-major axis of the object. Figure 4.2 shows the reentry times for the objects that achieve the threshold of a radius of periapsis less than 122 km (where the atmosphere can begin to cause heating [68]).

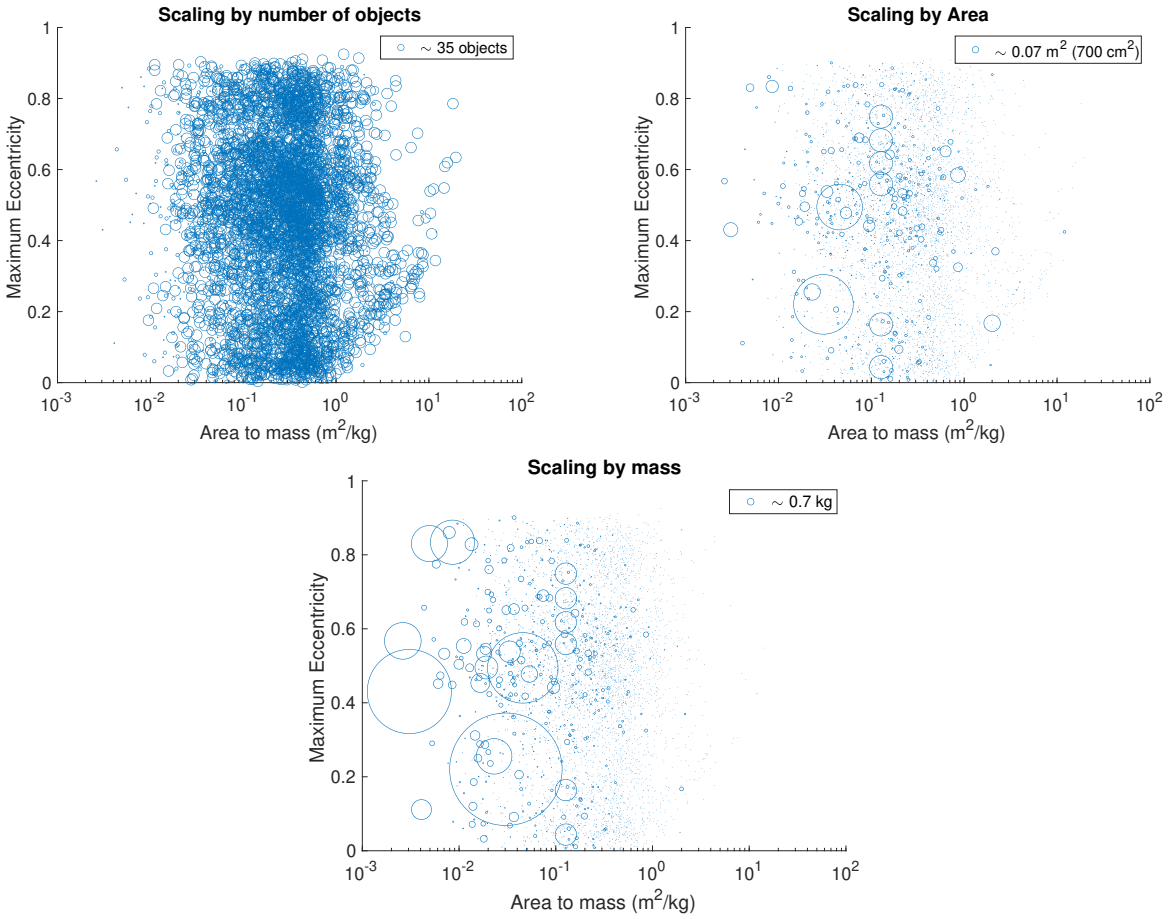

Figure 4.1: Maximum eccentricity of objects produced in a Galileo low-intensity breakup event

Before the end of the simulation (200 years), approximately 40,000 objects reentered the Earth's atmosphere. That is about 10% of the total objects produced by the breakup event. These objects did not reenter immediately following the breakup event. They instead start to reenter close to 80 years after the breakup occurred. Most of the objects reentered are on an initially circular orbit despite the distribution extending up to 0.2 eccentric-

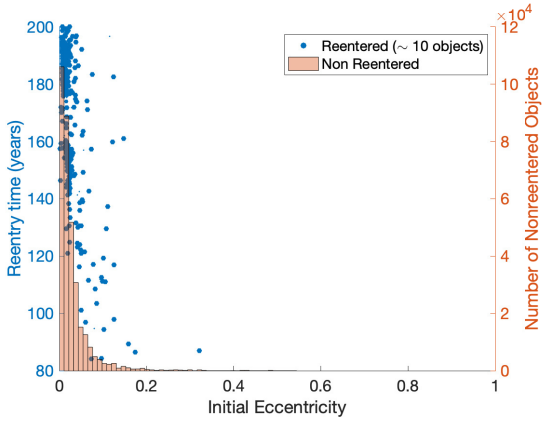

Figure 4.2: Reentry time of objects from the fragment cloud compared to a histogram of the number of non-reentered objects.

ity that can be noticeably observed in Figure 4.2.

The final set of graphs correlates to the initial conditions of the fragments and their long term behavior. Because stability of the region is described in eccentricity, inclination, and semi-major axis, the fragments were also studied in terms of how their initial conditions compared to whether or not the object reentered. The maps indicate regions of instability where resonance lines cross [85].

For simplicity, we will examine the initial conditions in terms of initial eccentricity and inclination where the resonances are drawn for the semi-major axis for Galileo. For completeness, we also binned to specific values of semi-major axis but saw no noticeable difference in the final results and did not include those graphs.

Figure 4.3 shows how close the resonance lines are to the debris cloud. A crossing resonance group is within the extrema of the cloud. With the truncated Figure 4.3b, the crossing resonance is noticeably luring above the bulk of the fragment cloud. However, we don't see a particularly large correlation to the resonance lines' crossing, the region of expected instability, and the reentered objects.

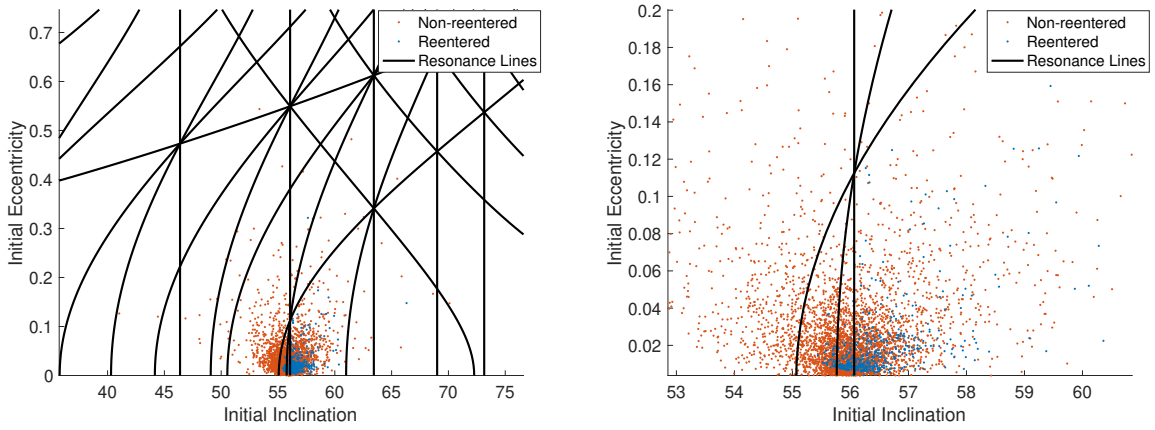

(a) (b)

Figure 4.3: Initial eccentricity by initial inclination (a) from 35° to 80° inclination (b) truncated to 53° to 61°

4.2.1.2 Collision

A higher energy event is when two satellites collide. These satellites are representative of the satellites in the regime and, as so, are massive. The impactor and parent object are modeled to be the same type of satellite. The collision is not head on; it is consistent with two satellites in near circular orbits with a RAAN separation of $\pi(180°)$ which results in $\sim 112°$ collision due to the inclination of the orbits.

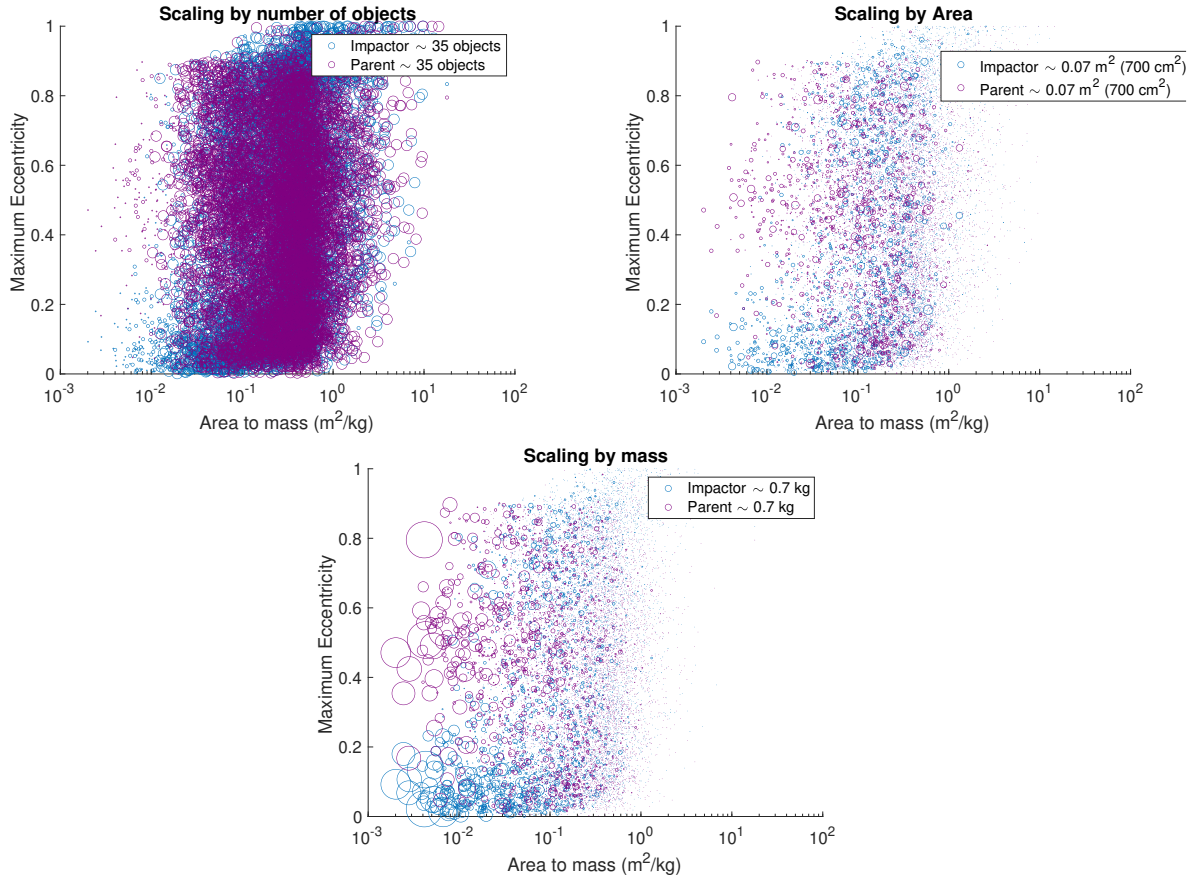

Figure 4.4: Maximum eccentricity of objects produced in a collision of Galileo FOC satellites

The data from the breakup cloud is similar to the previous session. The modeled collision produces a fragment cloud of 1,115,000 pieces of debris, the impactor producing 511,000 pieces and the parent producing 641,000 pieces. Approximately 55,000 pieces altogether reenter or are ejected immediately following the collision leaving the rest to be studied by the long-term integra-

tions. Figure 4.4 shows the maximum eccentricity each group of fragments achieve after a 200 year simulation.

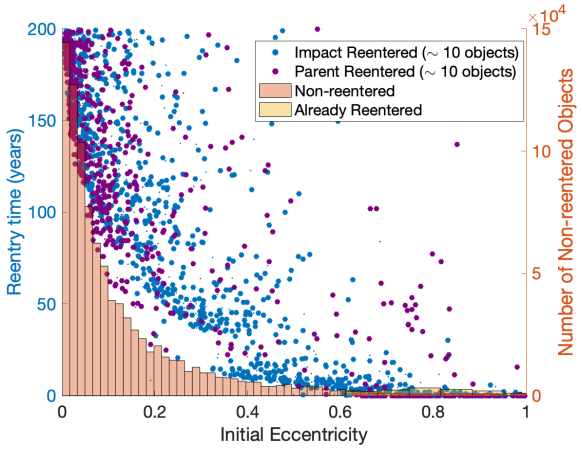

Figure 4.5: Reentry time of objects from the fragment cloud compared to a histogram of the number of non-reentered objects and already entered.

Because the collision case is more catastrophic and results in more pieces of debris, there are fewer large debris pieces as seen in the middle graphs (scaled by area) of Figures 4.1 and 4.4. There are some massive objects ($\geq$ 1 kg) that achieve high eccentricities particularly for the parent satellite.

Figure 4.5 shows the reentry times (within the 200-year simulation) for the fragment objects that do not reenter immediately following the collision, meaning that their initial conditions had a radius of periapsis above the 122 km threshold. Like the previous plot, these results are with a backdrop of the histogram of the non-reentered objects. In this case, there is also a histogram of objects that had already reentered or had been ejected.

Because the collision case produces more objects with higher initial eccentricities, the reentry times reach as low a time as within the first year of the event. The bulk of the objects with more circular orbits don't reenter until after 50 years.

For the collision event, the initial eccentricity distribution varies a lot more and so does the inclination, but the bulk of the fragments are still within a few degrees of the inclination of the par-

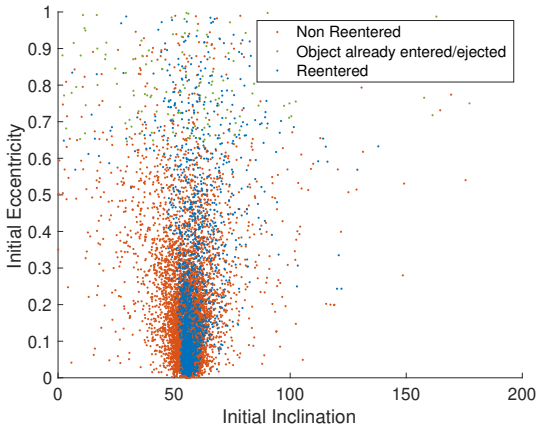

Figure 4.6: Initial eccentricity by initial inclination of objects produced in a collision of Galileo FOC

ent's (and impactor's) orbit.

Figure 4.6 shows that the bulk of the reentering objects are close to the initial inclination with slightly more reentering at higher inclinations (rather than lower inclinations) of the distribution.

Because this event results in larger changes in energy, there are some major outliers in terms of semi-major axis of the fragment cloud. Figure 4.7a shows that those major outliers are for higher eccentricities, and the bulk of the cloud has semi-major axes consistent with the nominal orbit.

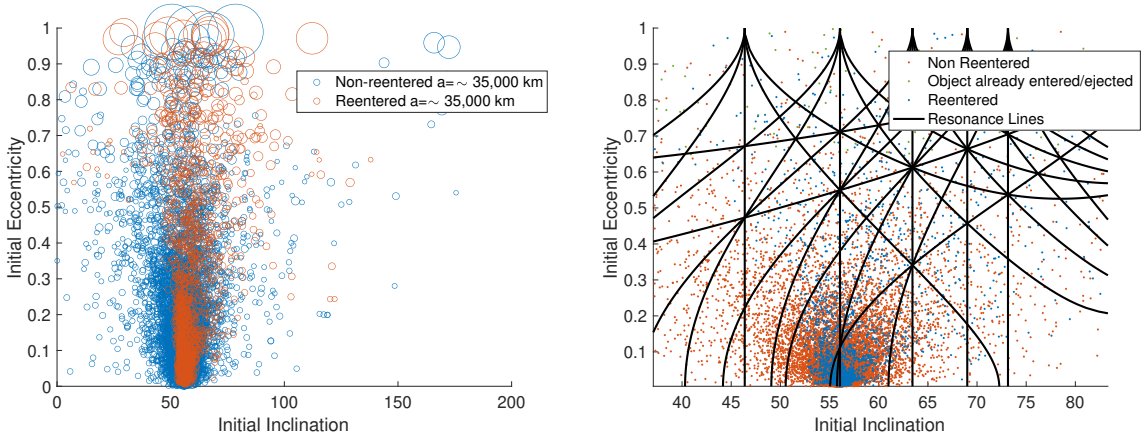

(a) (b)

Figure 4.7: Initial eccentricity by initial inclination (a) scaled by initial semi-major axis (b) with resonance lines

Figure 4.7b shows how the resonance lines do not necessarily correlate to the reentry conditions of the fragment cloud. This stresses the need for numerical studies like this one to understand the stability of the region.

Figure 4.8 shows the same distribution in terms of initial eccentricity and inclination but separates the distribution based on which object produced the fragment: impactor or parent. The interesting features of this figure is that the parent object's distribution favors reentries of higher inclinations whereas the impactor's distribution of reentries does not. The impactor's distribution of reentries follows the overall fragment distribution.

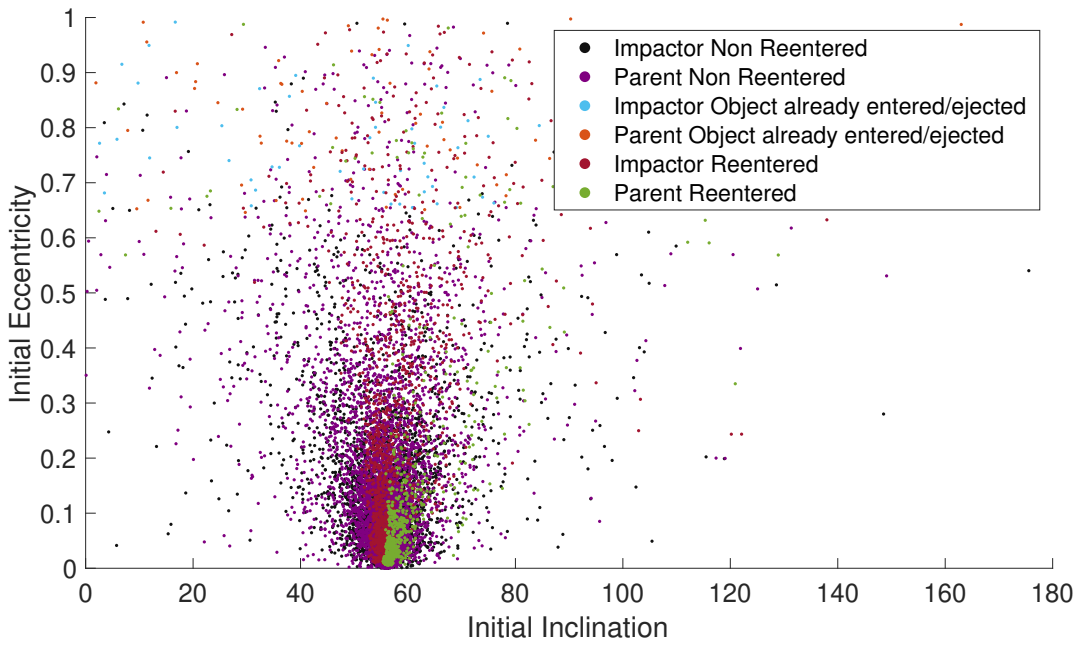

Figure 4.8: Initial eccentricity by initial inclination where distributions are separated by parent and impactor

The main distinction from the two initial distributions are from the direction of the orbits or the argument of perigee vectors. They are flipped in that a fragment in one distribution's argument of perigee will likely be the apogee in the other distribution's, Figure 4.9. The stability of the region is known to be symmetric with an argument of perigee, in that a difference in π radians should not necessarily result in large distinctions in the behavior of the satellite, [76]. This leads to the RAAN difference of π radians as possibly the candidate in the differing behavior between the fragment clouds.

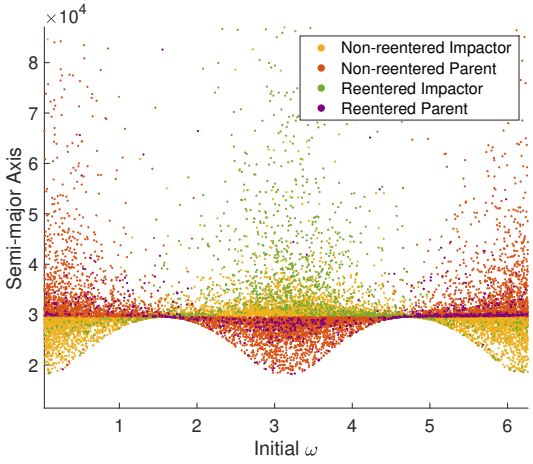

Figure 4.9: Initial argument of perigee and semi-major axis

4.2.2 GNSS Comparison

In the following section, we explore two additional constellations besides Galileo: GPS and GLONASS. We will compare the behavior of the fragment cloud distributions to each other. All the initial conditions can be found in Table 4.1.

Table 4.2 shows the properties of each of the different fragment clouds. GPS's collision case results in the largest number of fragments produced. All three of the explosions produced the same number of fragments. These figures and the number of objects already reentered were generated by the breakup model, and, though not a part of this research, help give context to the long-term behavior seen in our study. Number of objects reentered and maximum eccentricity are also included in this table but we will provide figures for more detailed analysis.

Table 4.2: Breakup Fragment Evolution

Collision Type	GPS Explosion	GPS Collision	Galileo Explosion	Galileo Collision	GLONASS Explosion	GLONASS Collision
Number of Objects in Cloud	378,577	1,202,690	378,577	1,152,871	378,577	881,082
Number of Already Reentered or Ejected Objects (% of Distribution)	-	47,214 (3.9%)	-	53,934 (4.7%)	-	31,905 (3.6%)
Number of Reentered Objects (% of Distribution)	4,387 (1.2%)	140,617 (11.7%)	40,178 (10.6%)	209,294 (18.2%)	910 (0.2%)	97,040 (11.0%)
Mean of the Maximum Eccentricity	0.093	0.296	0.457	0.455	0.421	0.378

Figure 4.10 shows the maximum eccentricity distributions for the explosion fragment clouds after the 200-year simulation. Figure 4.10a is a violin plot; violin plots are akin to histograms smoothed on their side where the largest distribution of the set is the widest part of the plot. They provide good insight on the overall distribution of the fragments but unlike histograms their widths do not necessarily correlate to an exact number of fragments. This is why Figure 4.10b is used to provide additional insight.

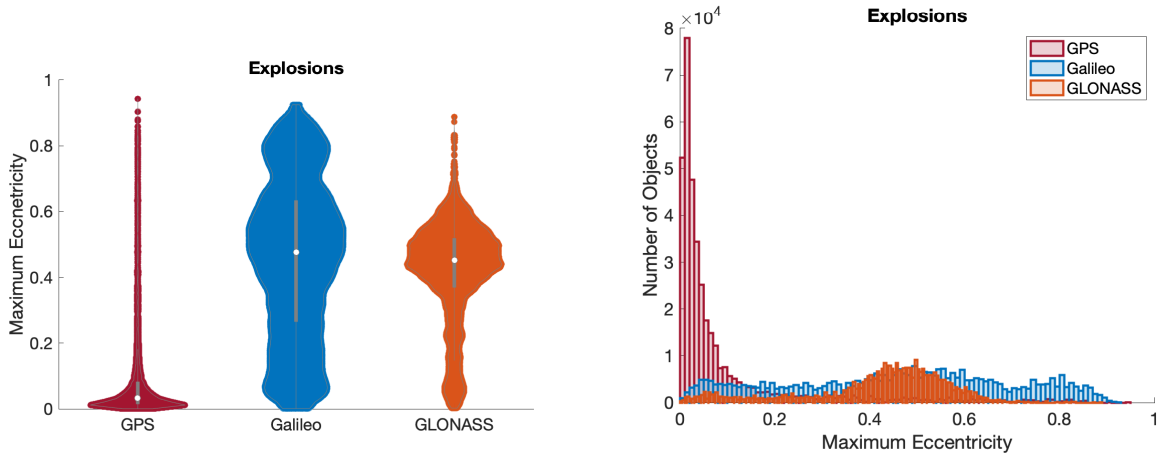

Figure 4.10: Comparisons of maximum eccentricity of fragments for explosion events (a) Violin plots (b) Histograms

The GPS fragment cloud appears to stay near the nominal circular orbit throughout the 200 years, most of the objects not achieving an eccentricity larger than 0.1. GLONASS appears to have objects growing in eccentricity to about 0.5 but not quite achieving the very high eccentricities that result in reentries. Galileo's distribution in comparison is more uniform.

All three constellations achieve maximum eccentricities that result in reentries ($e \geq\sim 0.75$ depending on the constellation). Figure 4.11 shows the distributions of reentry times with the sets. Galileo has the largest number of fragments reentering in the simulation. GLONASS only has a few parts of the fragment cloud that reenter but some reenter in less than fifty years unlike the other sets. GPS does not have a large number of reentering objects, and most reenter after 100 years.

Figure 4.12 shows the maximum eccentricities for fragments after a collision event. Again, GPS has the most objects near its nominal orbit. The collision event does provide a larger distribution of objects that reach higher eccentricities in general. For the GLONASS case we still see the bump or large number of solutions settling near the 0.5 eccentricity. The Galileo case is still the most uniformly distributed case.

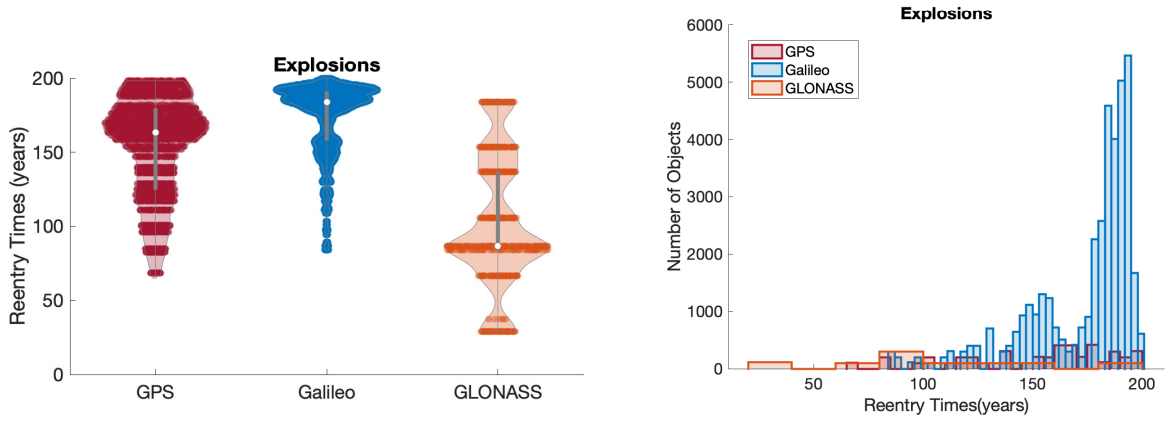

(a) (b)

Figure 4.11: Comparison of reentry times for explosion events (a)Violin plots (b) Histograms

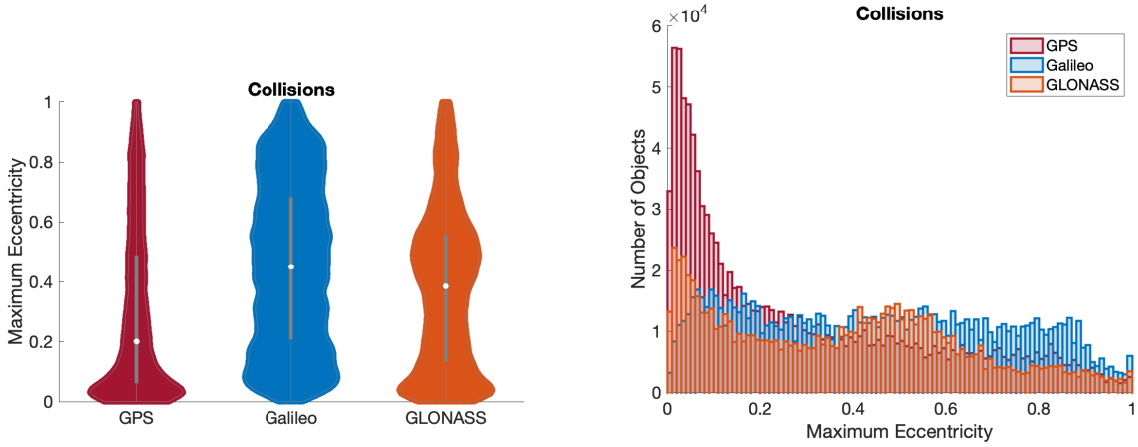

(a) (b)

Figure 4.12: Comparison of maximum eccentricity of fragments for collision events (a)Violin plots (b) Histograms

All of the constellations have maximum eccentricities that achieve reentry. Figure 4.13 shows that the majority of the reentries occur shortly after the event if they have not already entered within a few orbits of the event. The fragment cloud of Galileo has the most objects reentering after those first few years with the most entering toward the end of the 200 year simulation. Both GPS and GLONASS have objects that reenter in later years of the simulation but a much smaller fraction of those that reenter in the initial few years.

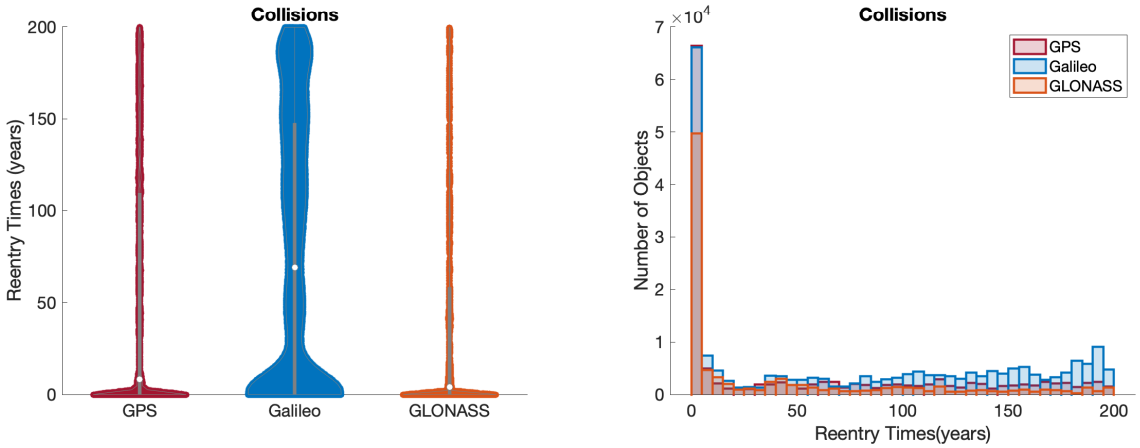

Figure 4.13: Comparison of reentry times for collision events (a)Violin plots (b) Histograms

4.3 Loitering Time for Fragment Clouds

This section will explore how each of the fragment clouds evolved within the 200 year simulation. The nearby nominal zones are plus or minus 100 km from the nominal semi-major axis of the orbit. This would amount to 26459-26659 km for GPS, 29500-29700 km for Galileo, and 25300-25500 km for GLONASS. The other constraint besides radius to determine if the satellite was in the zone of the constellation is the latitude. The latitude of the satellite on its orbit must be within the inclinations of each of the constellations, 55° for GPS, 56° for Galileo, and 63.4° for GLONASS. These conditions comprise the shell that is considered near the nominal orbit zone of each of the constellations.

Because the model integrates the Milankovitch elements, the position information of the satellite is not included over the integration. To check whether the satellite is dipping in and out of the nominal orbit shell, for each of the time steps of the integration, we propagate the orbit with respect to true anomaly from 0 to 2π radians using Equation 4.1.

$$r = \frac{a(1-e^2)}{1+e\cos\nu} \tag{4.1}$$

The other condition is latitude, λ, which is calculated by Equation 4.2.

$$\sin\lambda = \sin i \sin(\omega + \nu) \tag{4.2}$$

If these conditions are met, the fragment piece is within the shell of the constellation and considered a possible threat for the value ν. Using mean anomaly from the true anomaly values that trigger the conditions, we determine the percent of the time the fragment's orbit is interacting with the nominal orbits of each of the constellations.

4.3.1 Explosion Events

The first event represents the low-intensity breakup. The properties of these events are listed in Table 4.2.

4.3.1.1 GPS

The fragment cloud produced from a GPS satellite explosion is 378,577 fragments. No objects reenter immediately following the event. The accumulated time spent in each of the nominal satellite orbits is shown in Figure 4.14.

Because the event occurs in a GPS orbit, the fragments loiter in that region for the longest amount of time. Some fragments remain in the area for the full 200 years of the simulation. Most fragments only loiter for a total of twenty years in the region with the largest bin between two and four years. The total number of fragments that loiter for any amount of time in the GPS regime is 378,577 or all of the fragments. We also investigated how long the GPS fragments impacted the nearby constellations of MEO. GLONASS has the second highest number of fragments that reach its regime: 166,152 fragments. The longest accumulated time for the fragments of this region is just over 40 years. Some fragments reach Galileo accounting for 79,702 fragments. The total accumulated time in this region is not longer than 15 years.

Figure 4.15 shows when a few example pieces of debris interact with the GPS nominal orbit. This figure shows how the percent of time near the GPS orbit changes throughout the 200 year

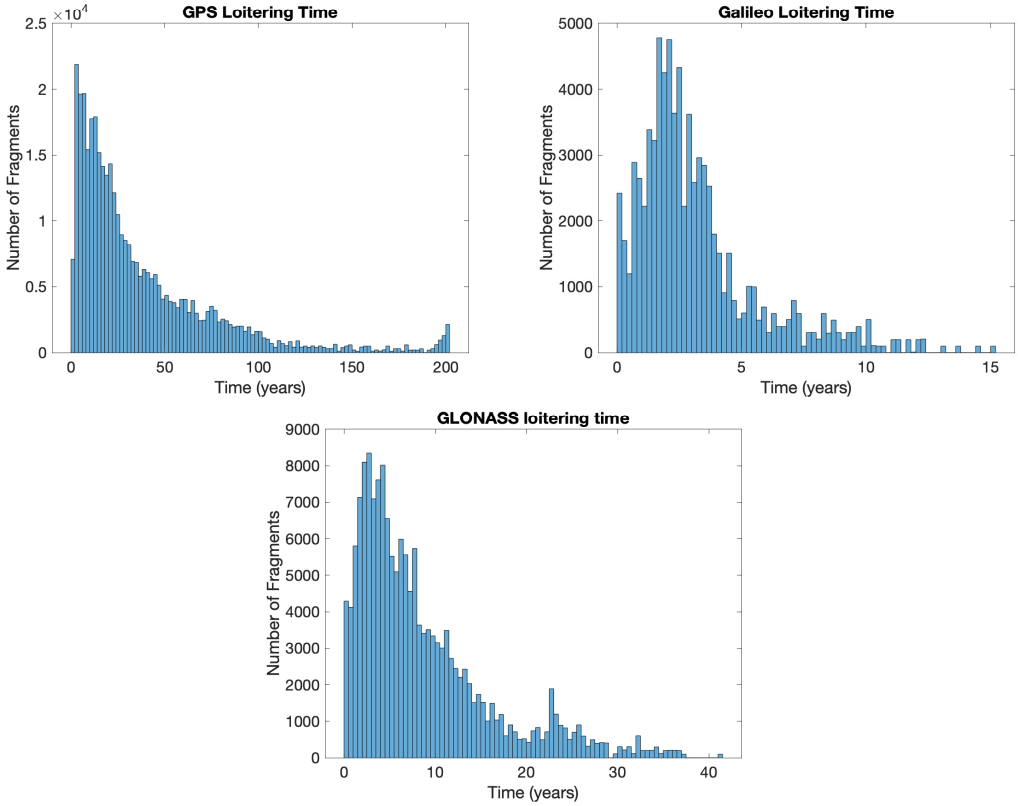

Figure 4.14: Histograms of total accumulated loitering time per fragment for a GPS explosion event

simulation.

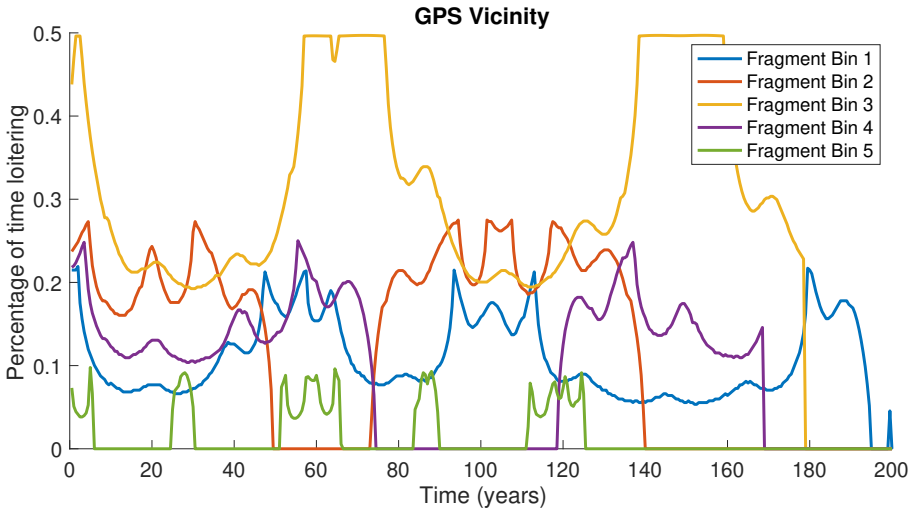

Figure 4.15: Percent of the orbit that interacts with the GPS nominal orbit over the 200 year simulation for five example fragments (taken from five different bins of fragment initial conditions).

Through these five example cases, it can be seen how the amount of time the objects dip in and out of the shell varies but tends to drop off towards the end of the simulation. A few objects appear to recircularize periodically early in the simulation. For a full picture of how the fragments interact with each of the shells over the 200 years, we formulated a similar plot but took the average of each fragment's percent time loitering for each time step in Figure 4.16. The average, $\bar{P}$, was taken by summing each of the fragment bins percent of time in each of the shells and dividing by the total number of bins, n, as shown in Equation 4.3.

$$\bar{P} = \frac{1}{n} \sum_{k=1}^{n} P(k) \tag{4.3}$$

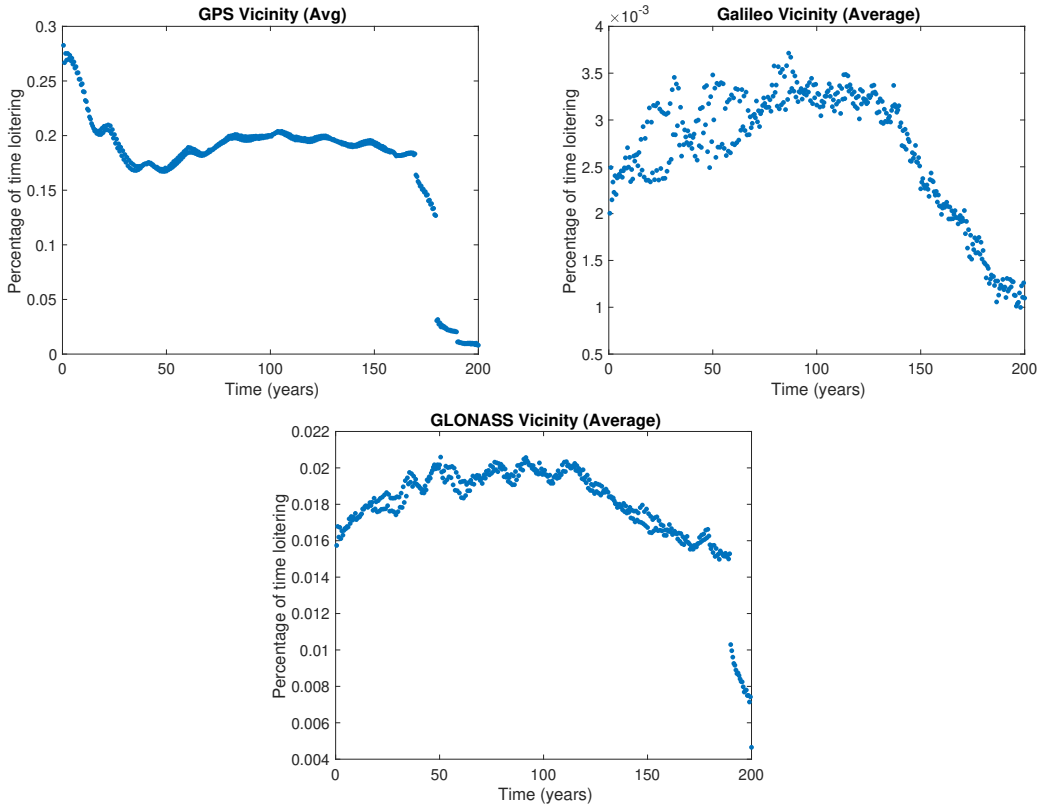

Figure 4.16: Average percentage of time loitering of the GPS explosion fragment cloud for the 200 year simulation in each of the nominal constellation shells

From the general representations in Figure 4.16, the same trends are seen in the previous figure; as the simulation progresses, fewer objects are interacting with either of the three shells.

This is most likely due to the increase in eccentricity of the orbits toward the latter parts of the simulation. Like Figure 4.14, this graph shows that most of the fragments interact with the GPS orbit they originated from. However, many fragments are still interacting with the other two constellations even toward the end of the simulation.

4.3.1.2 Galileo

The fragment cloud produced from a Galileo satellite explosion is also 378,577 fragments. No objects reenter immediately following the event. The accumulated time spent in each of the nominal satellite orbits is shown in Figure 4.17.

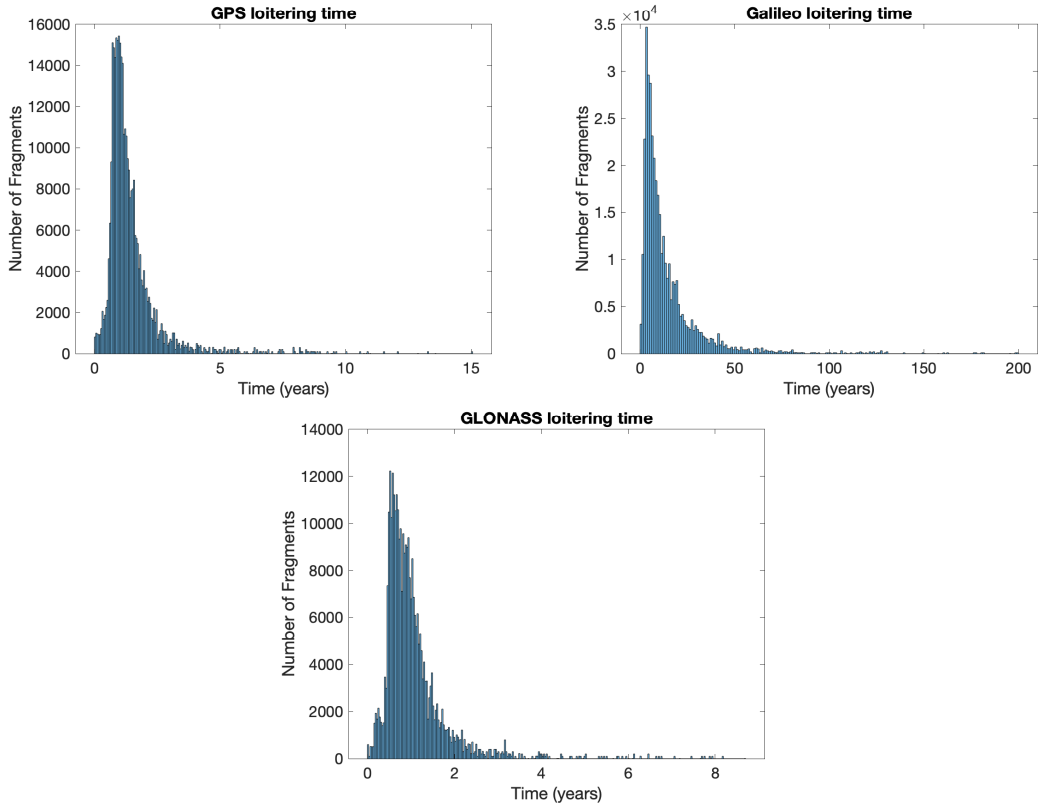

Figure 4.17: Histograms of total accumulated loitering time per fragment for a Galileo explosion event

Compared to the GPS case, much fewer objects spend an accumulated time in the nominal orbit past 50 years. The fragments from a Galileo explosion only spend up to fifteen years total

interacting with the GPS shell and nine years total interacting with the GLONASS shell. All 378,577 objects interact with the Galileo nominal orbit for some period of time. Of those objects, 341,926 interact with the nominal GPS orbit and 326,735 objects interact with the GLONASS nominal orbit at some point. Because Galileo is in the most chaotic of the semi-major axes, this fragment cloud seems to be showing more eccentricity growth and thus interacting with more orbits but for less time.

Figure 4.18 shows when a few example pieces of debris interact with the Galileo nominal orbit. It shows how the percent near Galileo orbit changes throughout the 200 year simulation.

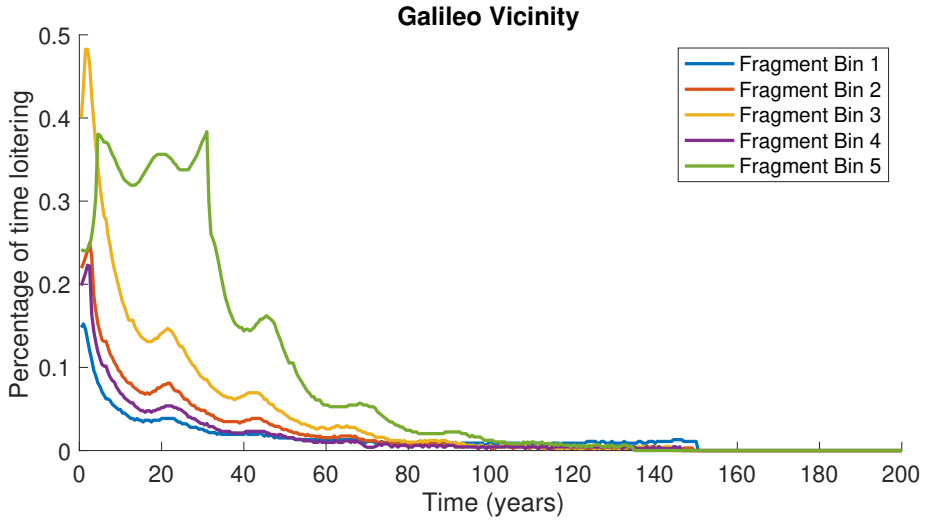

Figure 4.18: Percent of the orbit that interacts with the Galileo nominal orbit over the 200 year simulation for five example fragments (taken from five different bins of fragment initial conditions).

The fragments in this example spend much less time in the vicinity of Galileo's nominal orbit toward the end of the simulation, many reaching zero percent of time loitering close to 200 years indicating they may have depopulated the orbit. To see the larger trends, we will explore how the average of each of the fragments percent near orbit varies throughout the 200 year simulation in Figure 4.19.

Most of the objects interact with the other two orbits around the 50 to 100 year mark. This corresponds to a large enough eccentricity growth for fragments to reach the other orbits but not too large that they spend so little time in them. The trends seen in Figure 4.18 are consistent with

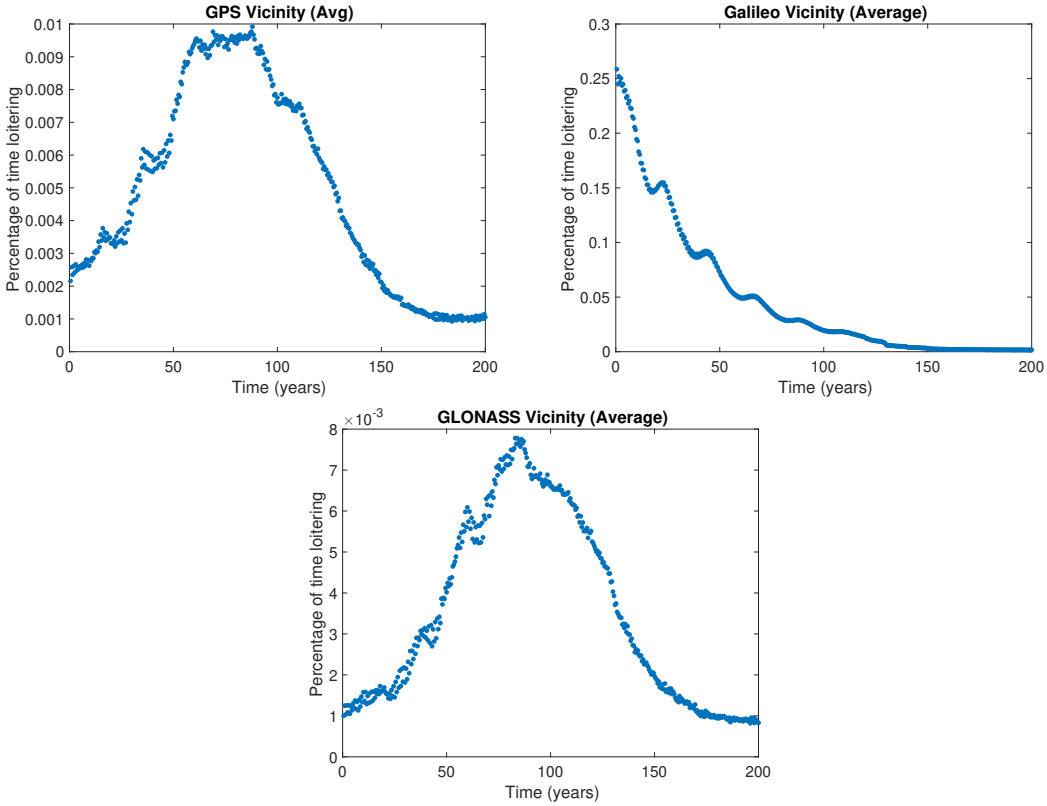

Figure 4.19: Average percentage of time loitering of the Galileo explosion fragment cloud for the 200 year simulation in each of the nominal constellation shells

the ones seen in the averaged results. The bulk of the time in the vicinity of the Galileo orbit is at the beginning of the simulation and exponentially decays.

4.3.1.3 GLONASS

The final fragment cloud for the explosion case is also 378,577 fragments. None of the objects reaches a reentry condition immediately following the breakup event and thus all are included in our analysis. The accumulated time spent in each of the nominal satellite orbits is shown in Figure 4.20.

Like the Galileo case, most objects do not loiter in the nominal orbit of GLONASS for a total of over 50 years. The objects then interact with GPS orbits the most since that constellation's semi-major axis is closest ot GLONASS's. This amounts to 363,720 fragments. The Galileo orbit

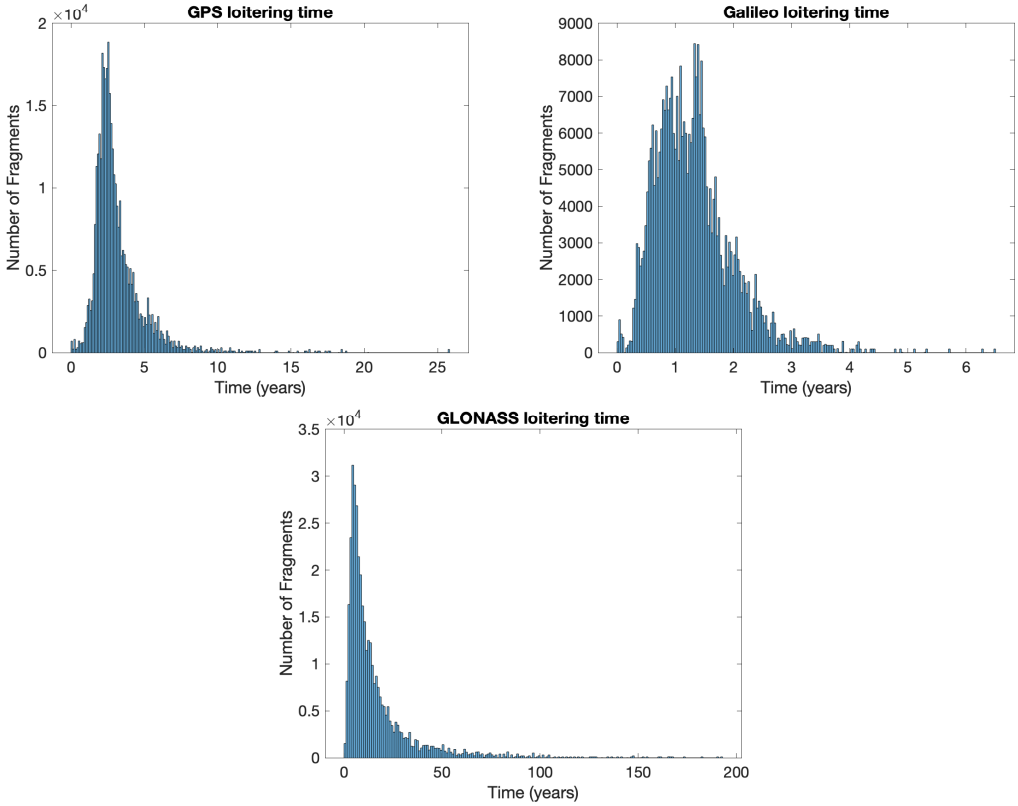

Figure 4.20: Histograms of total accumulated loitering time per fragment for a GLONASS explosion event

interacts with 337,343 of the objects in the fragment cloud for up to six years total spent in the vicinity.

Like the previous cases, Figure 4.21 shows the percent of time spent in the nominal GLONASS orbit for a few fragments and when those interactions occur in the timescale of the simulation.

Most of the fragments dwindle in time spent near GLONASS after the first 100 years with some dipping in and out of the constellation briefly close to the 200 year mark or the end of the simulation. One object despite spending a large portion of its orbit in the GLONASS nominal region for the early years of the simulation pretty rapidly decreases time spent as the simulation progresses. To understand the general trends, we look at the average behavior of a fragment bin over the 200 year simulation in Figure 4.22.

Figure 4.22 shows how most of the objects interact with the GLONASS nominal orbit at the

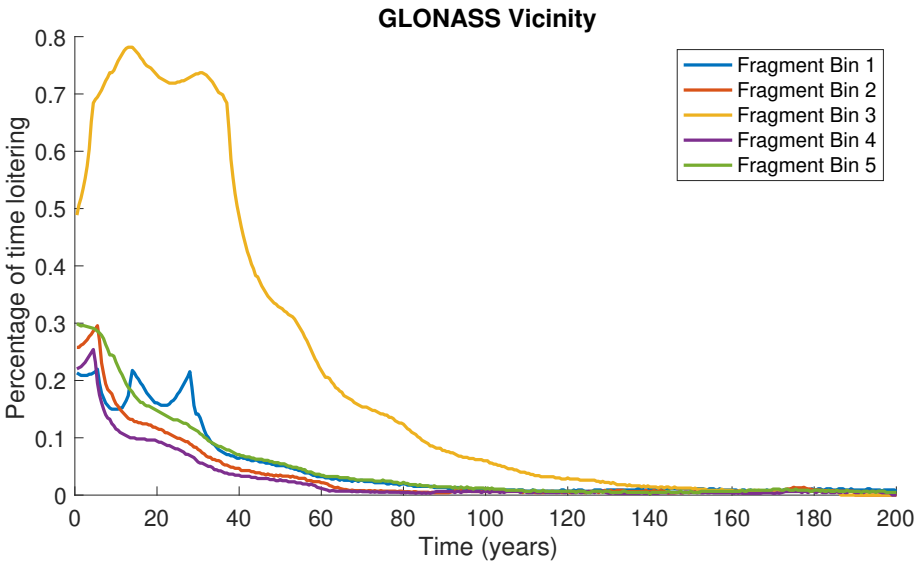

Figure 4.21: Percent of the orbit that interacts with the GLONASS nominal orbit over the 200 year simulation for five example fragments (taken from five different bins of fragment initial conditions).

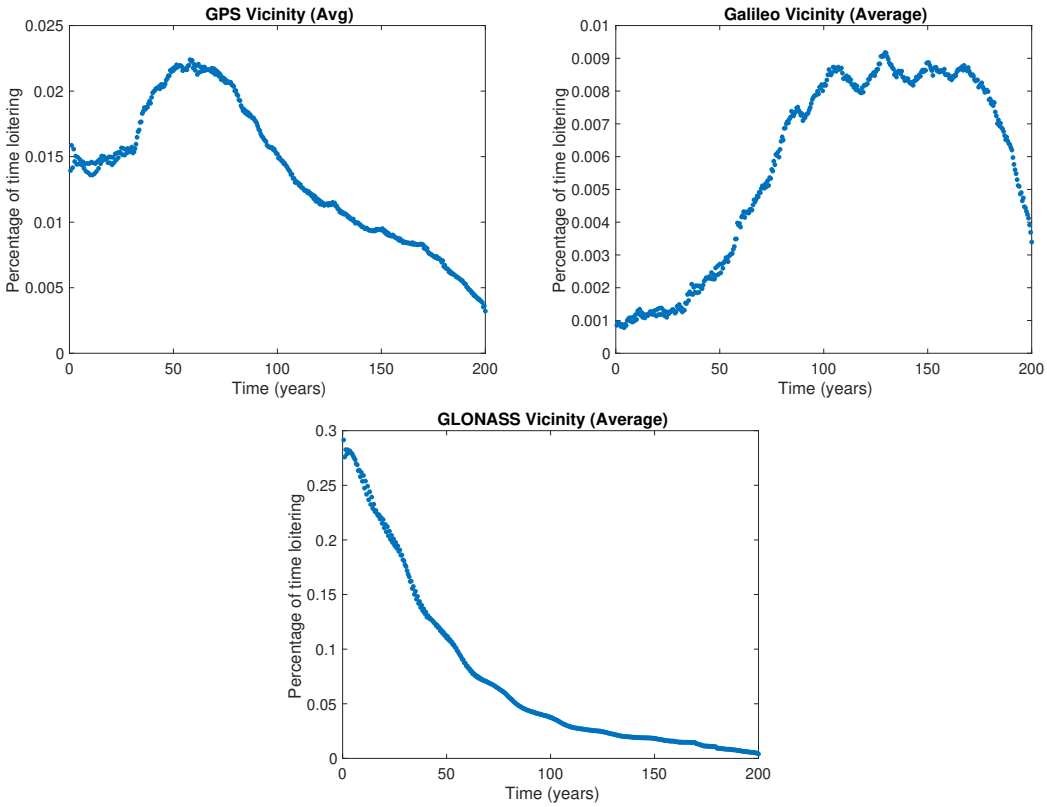

Figure 4.22: Average percentage of time loitering of the GLONASS explosion fragment cloud for the 200 year simulation in each of the nominal constellation shells

beginning, but, unlike the Galileo case, many objects are still interacting with the nominal orbit towards the end of the simulation. Because GPS is close to GLONASS, the increase in objects in its vicinity is early in the simulation. Because GLONASS has more eccentricity growth than the GPS case, the fragment cloud eventually reduces time loitering in the GPS orbits as well and toward the end of the simulation increases time spent near the Galileo nominal orbit.

4.3.2 Collision Events

4.3.2.1 GPS

The first collision is one that occurs between two nominal satellites in GPS orbit. The accumulated time spent in each of the nominal satellite orbit shells is shown in Figure 4.23.

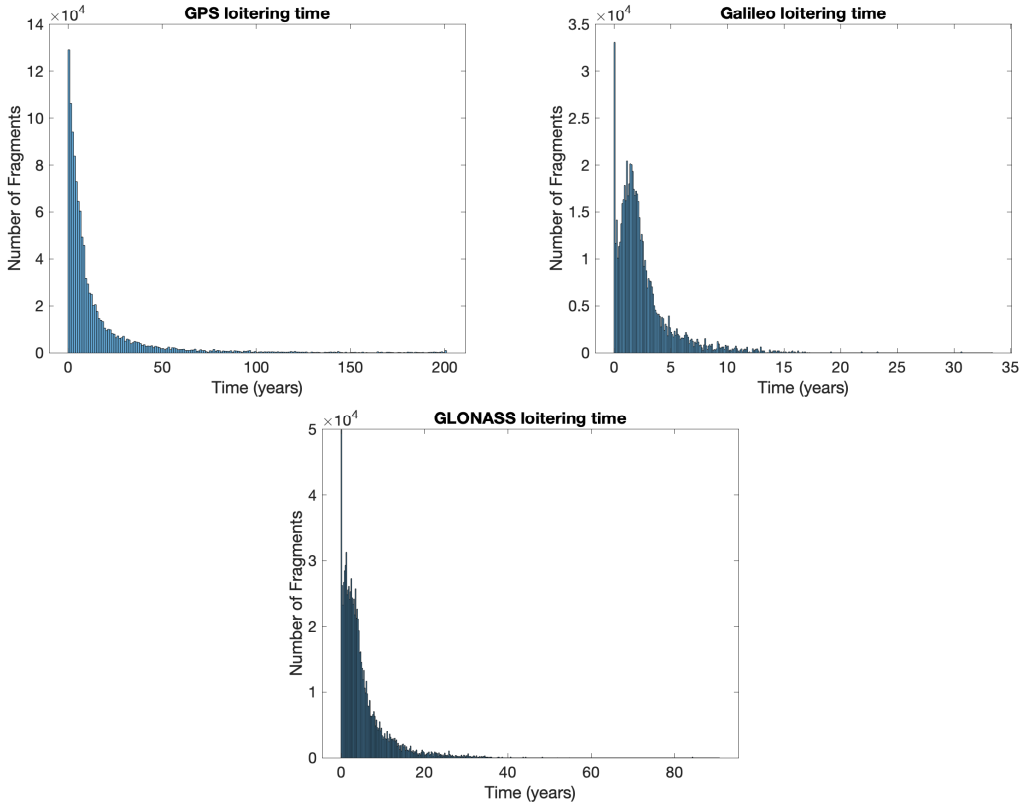

Figure 4.23: Histograms of total accumulated loitering time per fragment for a GPS collision event

Most of the objects do not spend much more than a year of accumulated time in each of the shells. The GPS shell has a few fragments that spend the entire simulation in the region. Most

of the 1,146,521 pieces of debris that inhabit GPS do not spend more than a total of ten years interacting with the shell. There are 922,819 fragments that reach the GLONASS shell, but the total time spent in that regime does not amount to more than half the simulation. The Galileo region interacts with 615,940 pieces of debris which results in a maximum of 35 years accumulated for some fragments.

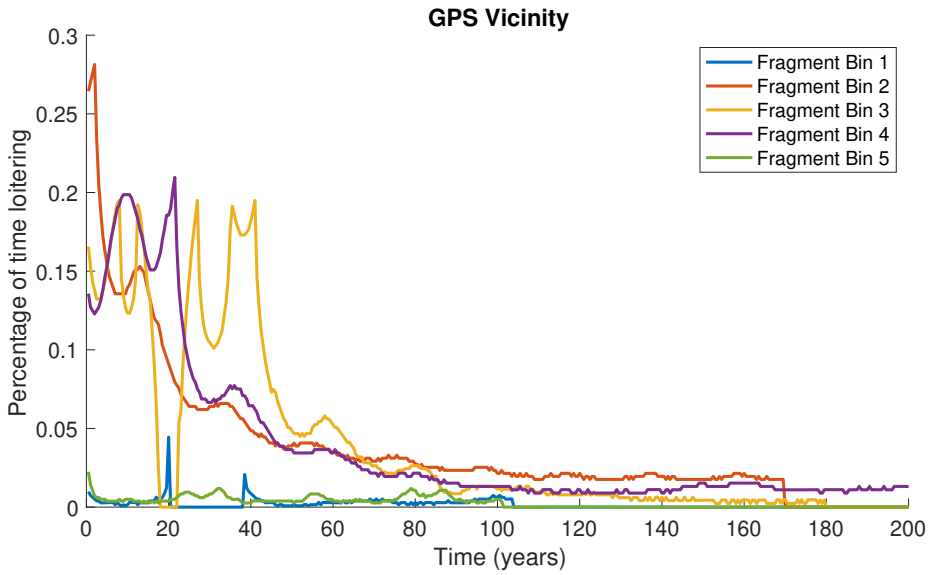

Figure 4.24: Percent of the orbit that interacts with the GPS nominal orbit over the 200 year simulation for five example fragments (taken from five different bins of fragment initial conditions).

Figure 4.24 explores five example cases to see how the time interacting with the GPS orbit shell evolves with the simulation. Most of the objects in the example pass in and out of the GPS vicinity for the first 60 years and then tend to only briefly pass through, indicative of some eccentricity growth. A few objects spend little time to begin with in the orbit representing some of those initially highly eccentric orbits created by the event. The overall trends of the fragment cloud are depicted by Figure 4.25.

The trends of when the fragments interact with the nominal GNSS orbits are similar to those in Figure 4.16 except the percent of time loitering is smaller in these sets. This could be due to the fact that more of the initial eccentricities of the fragments in this cloud are high and thus spending a smaller fraction of their orbit lifetimes interacting with each of the regions.

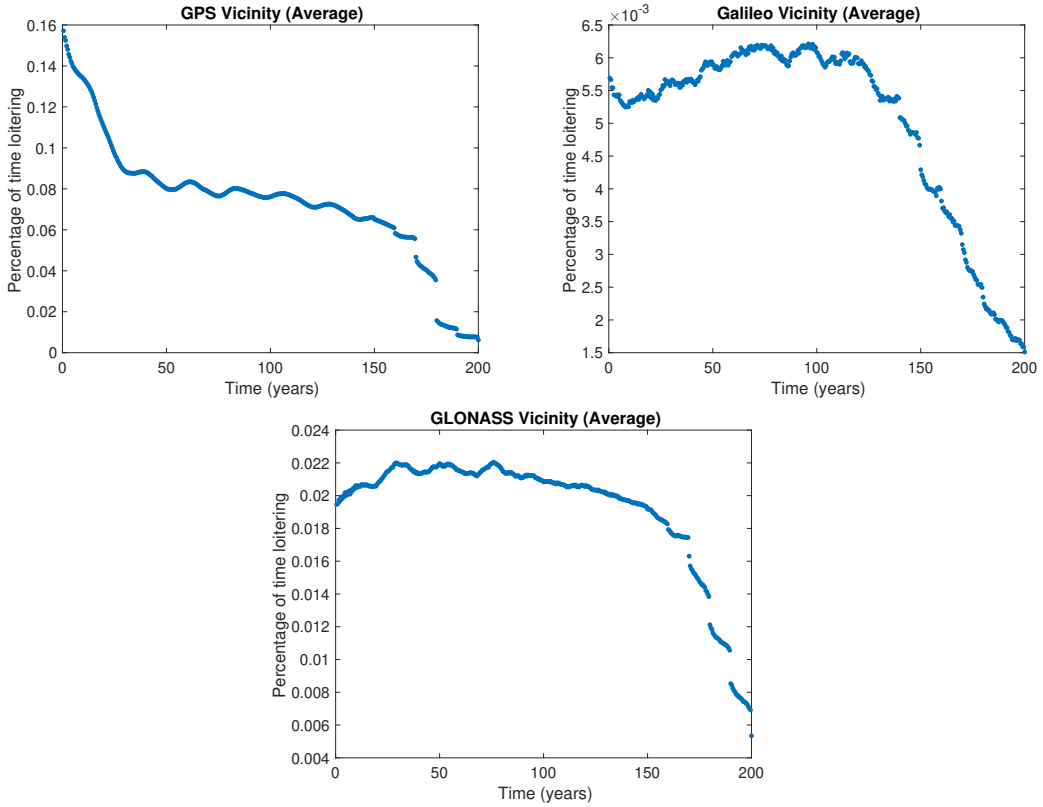

Figure 4.25: Average percentage of time loitering of the GPS collision fragment cloud for the 200 year simulation in each of the nominal constellation shells

4.3.2.2 Galileo

The accumulated time spent in each of the nominal satellite orbit shells is shown in Figure 4.26.

Like the GPS case, most of the fragments from the cloud only interact with the nominal satellite shells for a very short fraction of time since the initial eccentricities of many of these debris objects are high to begin with. The collision event interacts with its nominal satellite regime the most (some objects remaining for the full 200 years). The other two are not far behind with 910,769 and 963,427 objects interacting with them for a total time of about fifteen years.

The behavior of a few fragments over the 200 year simulation is depicted by Figure 4.27. Some objects only spend a small percentage of their time in the Galileo shell for the duration of the simulation. Most objects seem to predominantly spend their time near the Galileo orbit in the

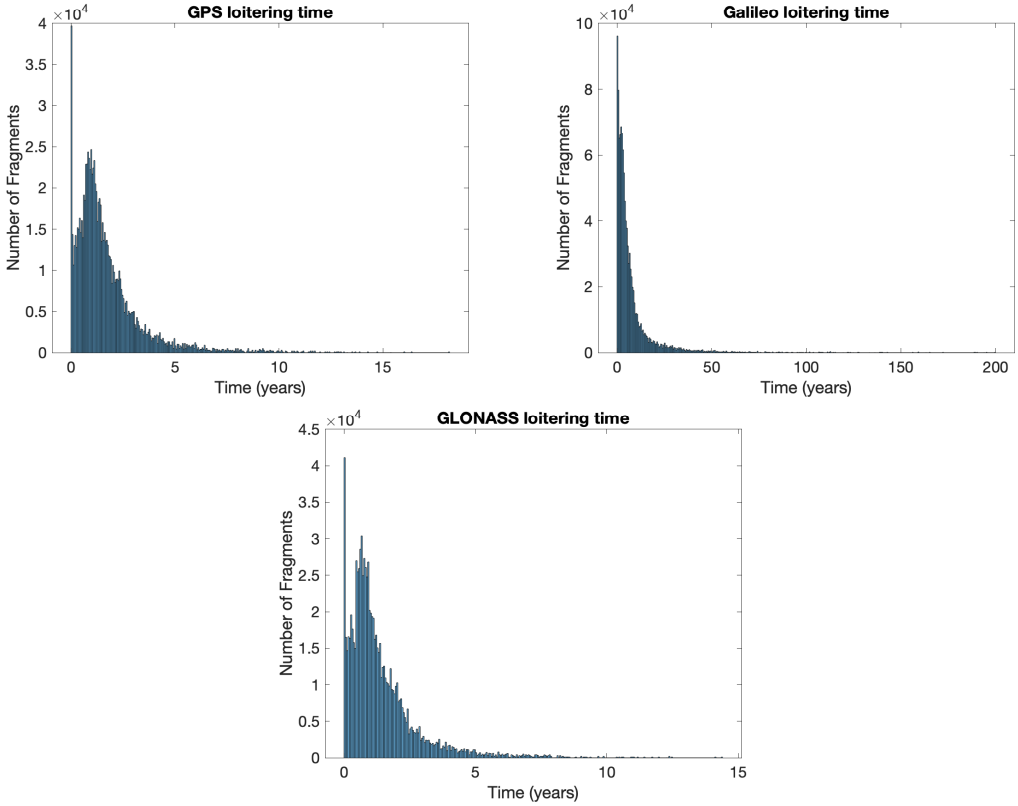

Figure 4.26: Histograms of Total Accumulated Loitering Time per Fragment for a Galileo Collision Event

first twenty years. There is an interesting case here with Fragment Bin 5 where the fragment most likely recircularized around the 80 year mark and thus started increasing its interaction with the nominal orbit before it eventually reentered at the 120 year mark. The average trends are shown in Figure 4.28.

The fragment cloud interacts with the GPS and GLONASS shells much earlier in the simulation than the cloud does in the explosion case. It also sustains these interactions up to 100 years where it then reduces the overall interactions toward the end of the simulation. The cloud interacts with the nominal Galileo orbit less than the explosion case's cloud but shows similar trends of exponentially reducing its interactions over the 200 years. This is likely due to the greater amount of initially eccentric orbits but it is interesting to note that these orbits still require about a 100 years to become less of a threat to all three regimes.

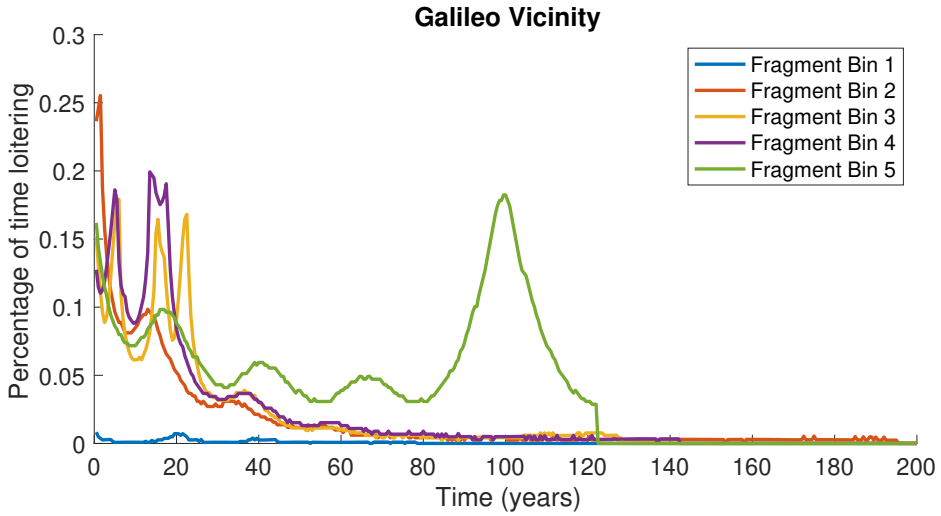

Figure 4.27: Percent of the orbit that interacts with the Galileo nominal orbit over the 200 year simulation for five example fragments (taken from five different bins of fragment initial conditions).

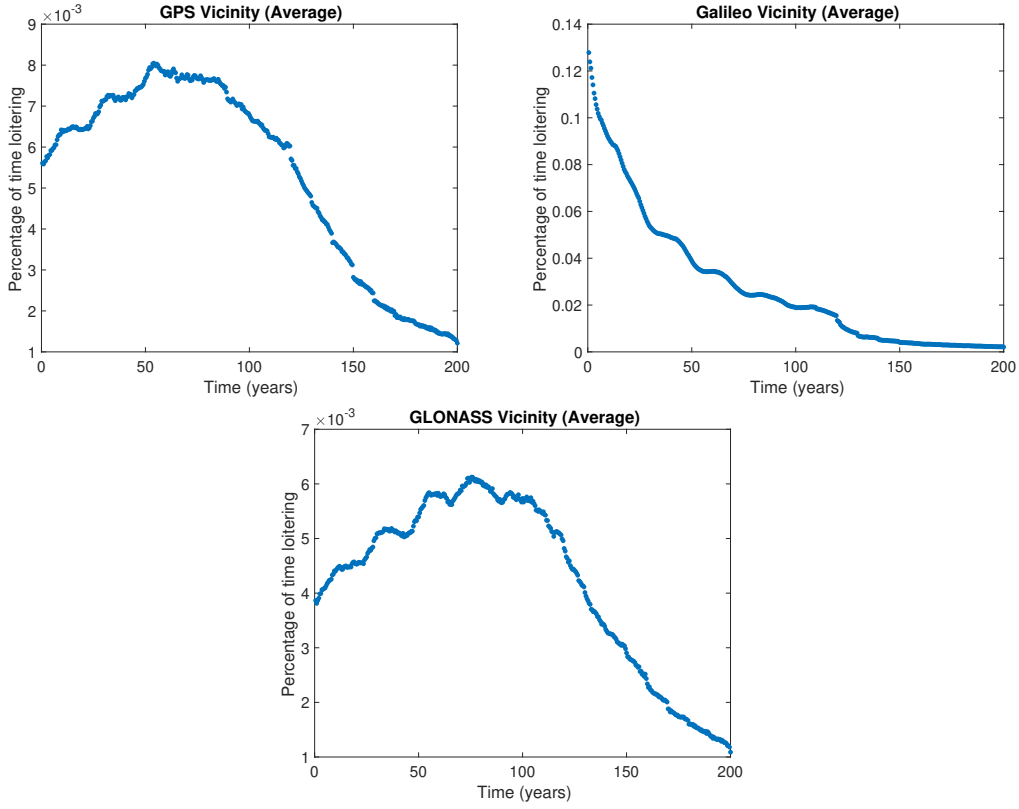

Figure 4.28: Average percentage of time loitering of the Galileo collision fragment cloud for the 200 year simulation in each of the nominal constellation shells

4.3.2.3 GLONASS

The final breakup event is a collision in GLONASS's orbit. The accumulated times in each of the nominal satellite shells are shown in Figure 4.29.

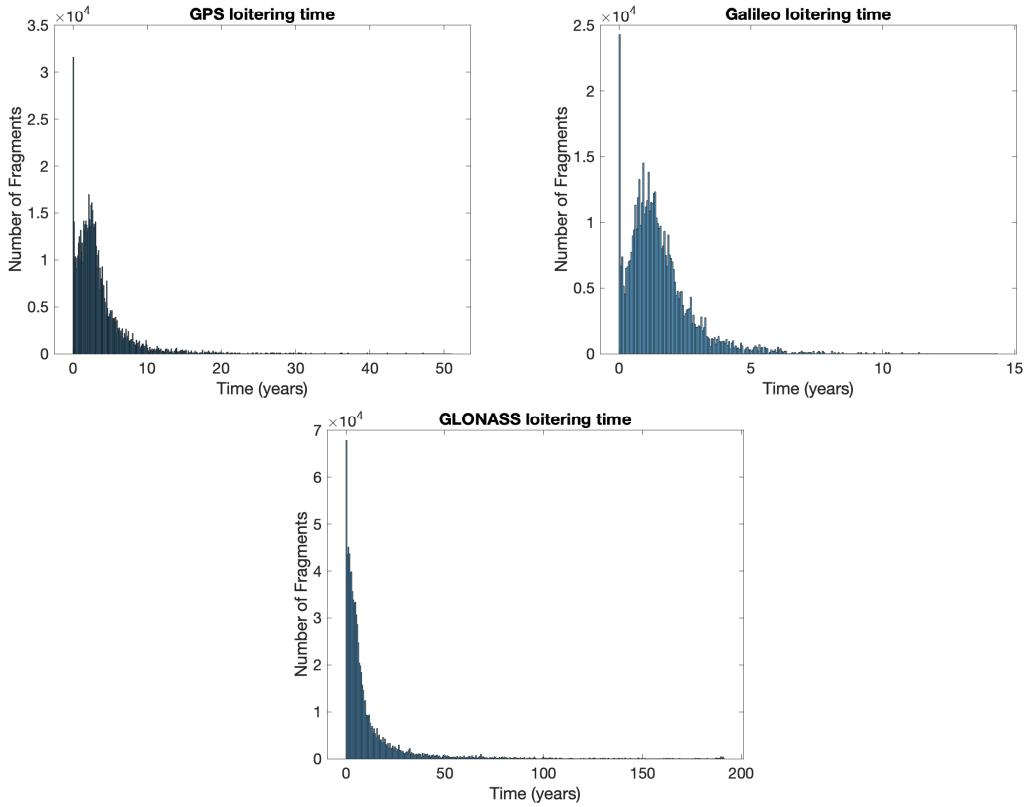

Figure 4.29: Histograms of total accumulated loitering time per fragment for a GLONASS collision event

Most objects spend less than a year in all three shells. There are a few objects that linger near GLONASS for the entirety of the simulation. There are 684,262 fragments that inhabit the GPS orbits for some duration and the total time accumulated in that region for each of the fragments is fifty years or less. The 520,767 fragments that reach Galileo spend an accumulated time of fifteen years or less.

Figure 4.30 shows how a few fragments interact with the nominal orbit of GLONASS in terms of percent of time interacting with the region and when those interactions take place in the simulation. This group of fragments gives a wide variety of orbits evolving in the simulation.

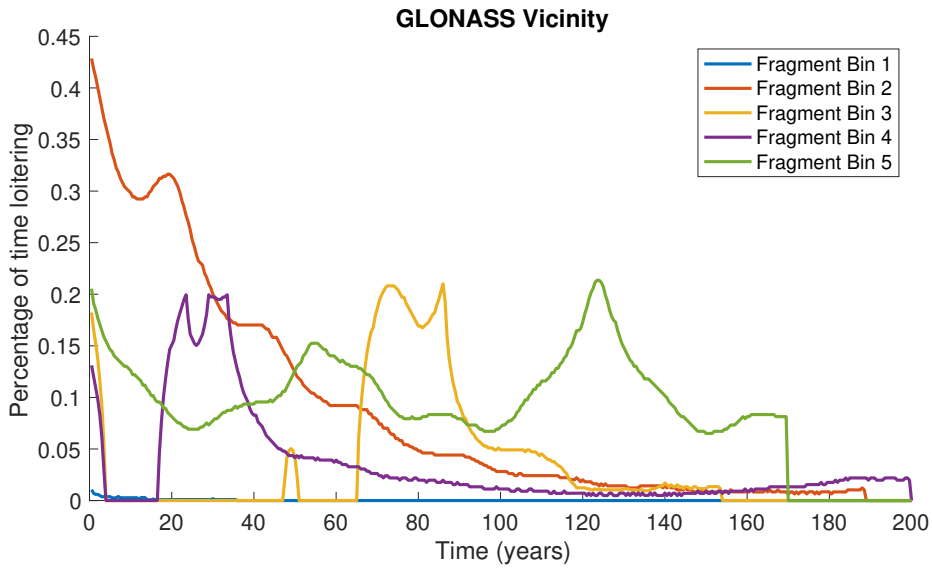

Figure 4.30: Percent of the orbit that interacts with the GLONASS nominal orbit over the 200 year simulation for five example fragments (taken from five different bins of fragment initial conditions).

Fragment one represents an initially highly eccentric orbit that reenters the Earth's atmosphere relatively quickly. Fragments two and four represent more circular orbits that grow in eccentricity over time. Fragments three and five represent orbits that recircularize late in the simulation and eventually reenter. These examples are a select few fragments but the overall trends are depicted by the average behavior of each of the fragments in Figure 4.31.

The general trends seem to reduce the percentage of loitering time to about half that of the explosion case in the GLONASS region. The cloud also doesn't exponentially decay like it does in the explosion case; it goes through an evolution more closely mimicking the GPS cases where there is a sustained time impacting the orbit (from 50 to 150 years) and then that drops off toward the last fifty years of the simulation. The fragment cloud tends to impact GPS in a decreasing fashion throughout the simulation. It impacts the Galileo shell increasingly until about 100 years and then the amount of time spent in the region decreases for the last 50 years.

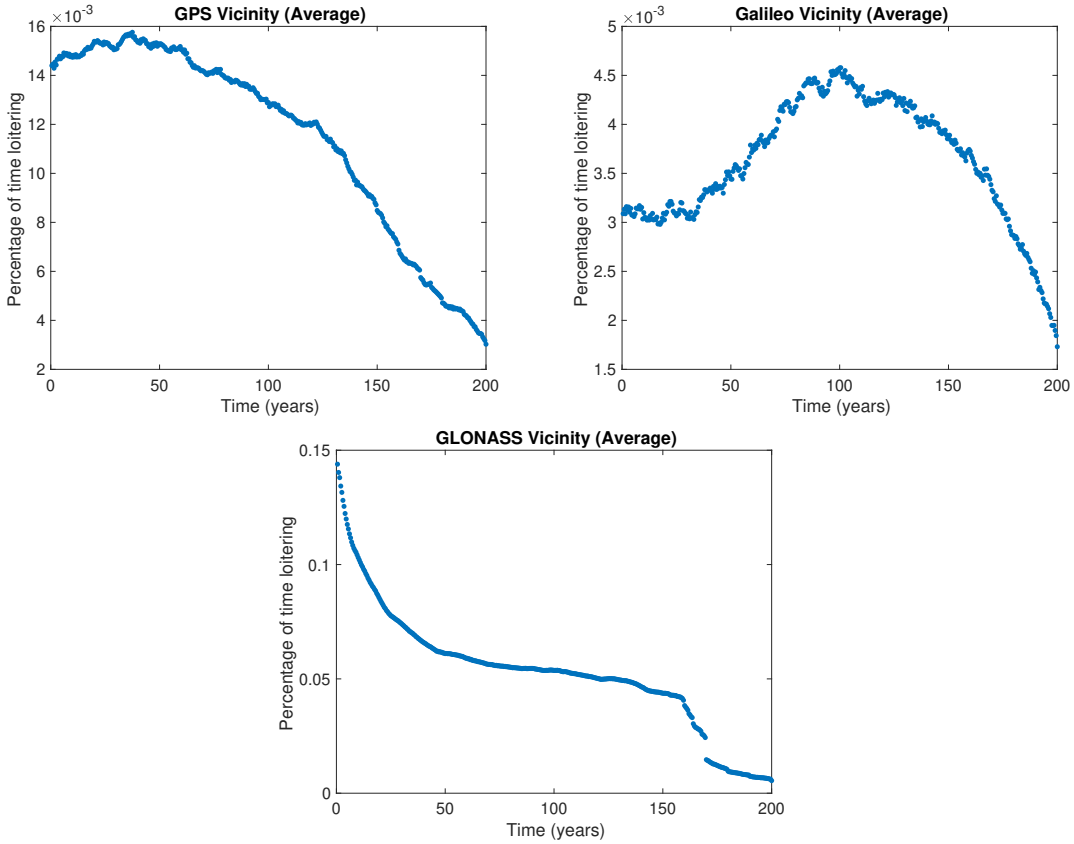

Figure 4.31: Average percentage of time loitering of the GLONASS collision fragment cloud for the 200 year simulation in each of the nominal constellation shells in the case of a GLONASS collision event

4.4 Varying Parameters of the Fragment Cloud

This section explores how varying initial conditions of the breakup cloud will affect the long-term evolution of the cloud. Parameters such as RAAN and epoch have studied structure with respect to argument of perigee. In varying these parameters, we can compare the fragment clouds to the known architecture in the region. Semi-major axis is also included in the discussion as a current debris mitigation practice at high altitudes, placing an object at a higher semi-major axis or a graveyard orbit. Understanding how these clouds would propagate with respect to this characteristic will help extrapolate this work to possible nearby graveyard orbits.

4.4.1 Varying RAAN

4.4.1.1 Known Structure in the Region

The areas of instability in MEO are known to have a structure with respect to RAAN. In particular, Alessi et al. have demonstrated how these structures exist with respect to argument of perigee [8]. We have replicated these results in Figure 4.32 for two cases. The first case, Figure 4.32a, shows the variations in RAAN and argument of perigee for a stable base case of low eccentricity. The second case, Figure 4.32b, is for an unstable base case of high eccentricity. This case was examined in Figure 2.5. Islands of instability migrate from $\Omega = \pi$ radians to $\Omega = 0/2\pi$ radians for the higher eccentricities. Both maps show a general trend of long skinny islands of stability from from 2 to 2π radians along the inverse direction of argument of perigee.

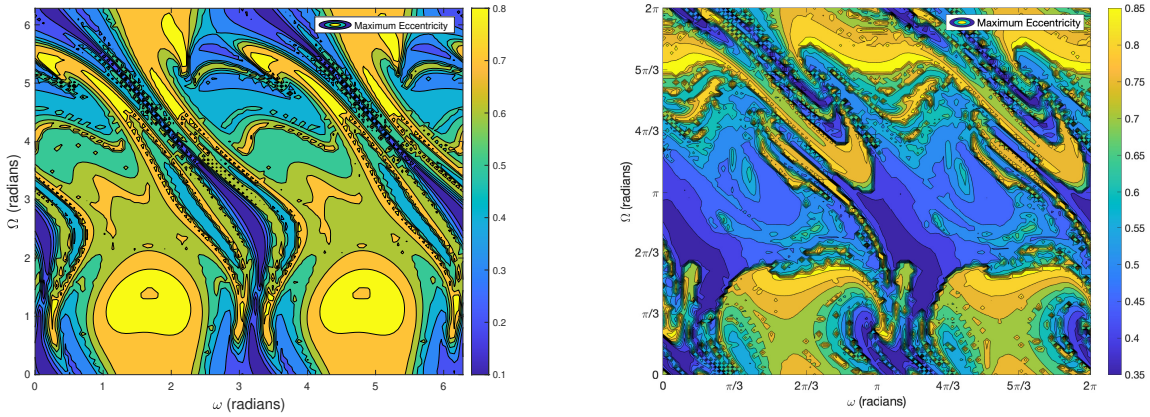

(a) Stable Base Case (low eccentricity e=.1)

(b) Unstable Base Case (high eccentricity e=.4)

Figure 4.32: Argument of perigee structure vs RAAN

4.4.1.2 Explosions

Given the known structure of the region, we study how the variation of RAAN in the breakup cloud matches the existing structure. We vary the breakup clouds in RAAN from 0 to 2π radians. This will compare events occurring along different points of the equator. The base case is $\Omega = 5$ radians. Each of these variations will be along the y-axis. The argument of perigee spread is

determined after the event and is in the debris cloud structure varying from 0 to 2π radians along the x-axis. Because there are many other variables including eccentricity and other orbital parameters along with area-to-mass ratio that goes with the identity of each debris piece associated with a particular argument of perigee, the structure should not exactly match. It should look more like streaks associated with each debris piece with unstable behavior triggering higher eccentricities along the variation of RAAN. Figure 4.33 shows these maps for the three explosion cases.

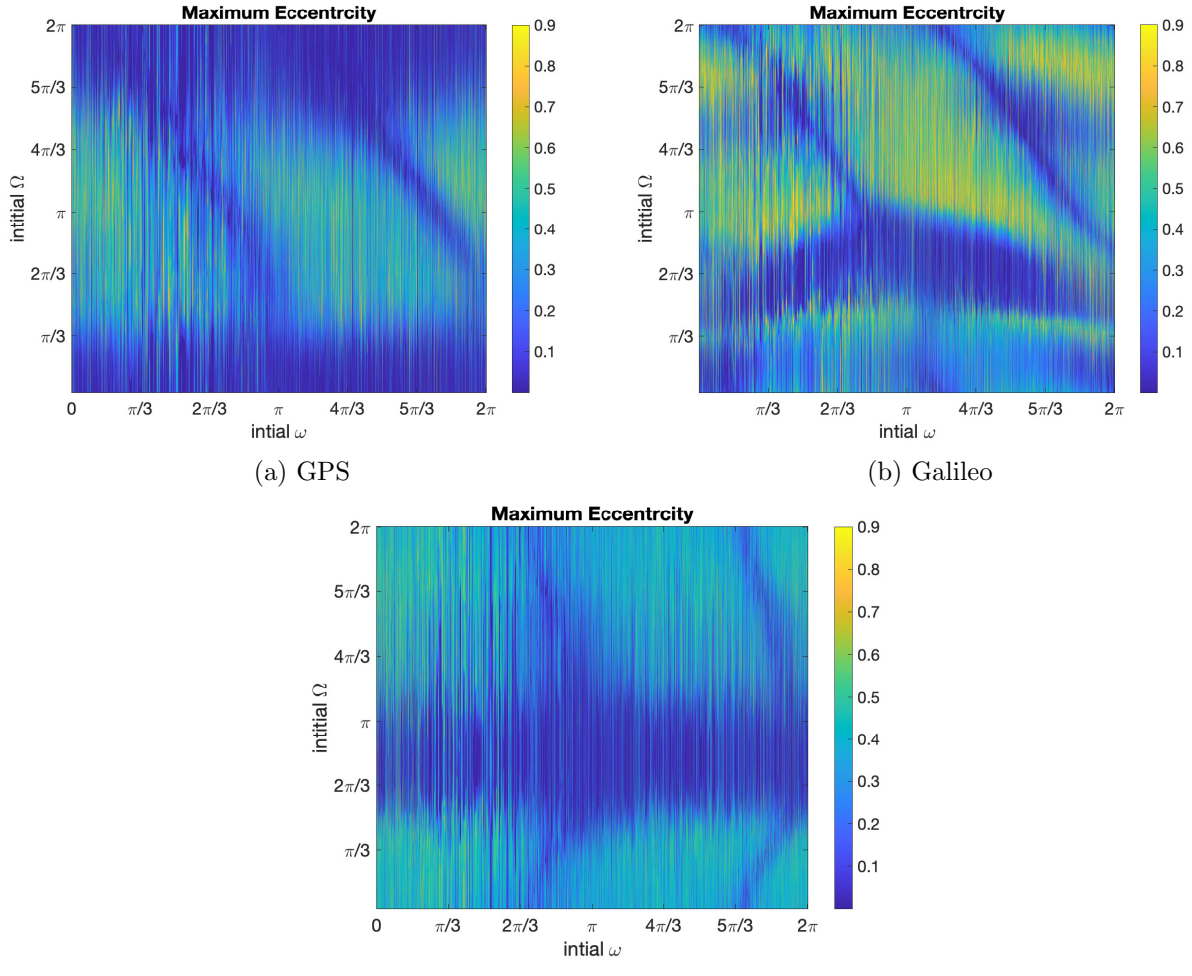

(a) GPS

(b) Galileo

(c) GLONASS

Figure 4.33: Argument of perigee vs RAAN structure of objects produced in explosion events

The GPS structure seems to mimic the stable case in 4.32a while the other two, Galileo and GLONASS, more closely match the unstable base case in Figure 4.32b. This is consistent with the overall trends of the base cases of the two clouds where GLONASS and Galileo both have their

explosion cases reaching high eccentricities in the simulations as compared to GPS [78]. The graphs don't exactly match but the larger trends do, indicating the breakup clouds are heavily influenced by the resonance structure of the region. The thin islands referenced in the known structure section also exist in each of the maps in Figure 4.33.

The differing behavior between the clouds can also be seen in the overall trends of the clouds with varying RAAN. Figure 4.34 shows the violin plots for the distributions of maximum eccentricities of the debris in the breakup cloud. Because there are many violin on this graph, the denser populations can be seen by the darker regions of the graph rather than their specific widths. The white circles indicate the mean for each distribution set.

The base GPS case (which was a RAAN of 5 radians) had the most stable behavior in our original analysis. However, the trends show that can change with varying RAAN. Galileo and GLONASS show valleys around a little less than π radians consistent with the unstable base case behavior. Even the GPS case has a small dip around a little less than π radians in its peak behavior. Galileo fragment clouds appear to have the least consistency with varying RAAN.

To keep this chapter concise, instead of showing the distributions of the reentry times of all the objects, we will just show the means on one plot since the number of solutions varies so much between the constellations. The full distributions can be found in Appendix C. Figure 4.35 shows the number of solutions reentered for each breakup cloud and the means of those reentry times.

Similar to the other figures, GPS and Galileo have a smaller number of reentering solutions just under π radians and around $0/2\pi$ radians. Although GLONASS consistently has objects reaching high maximum eccentricities, not many of these objects reach a high enough value to reenter. Therefore, there are less objects that reenter in that constellation but they do reenter in a shorter amount of time than the other two which hover about 20 years apart, GPS fragments having on average longer reentry times.

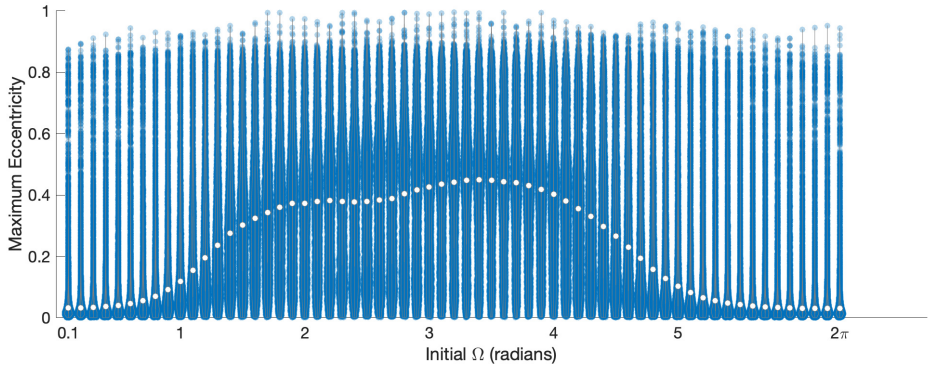

(a) GPS

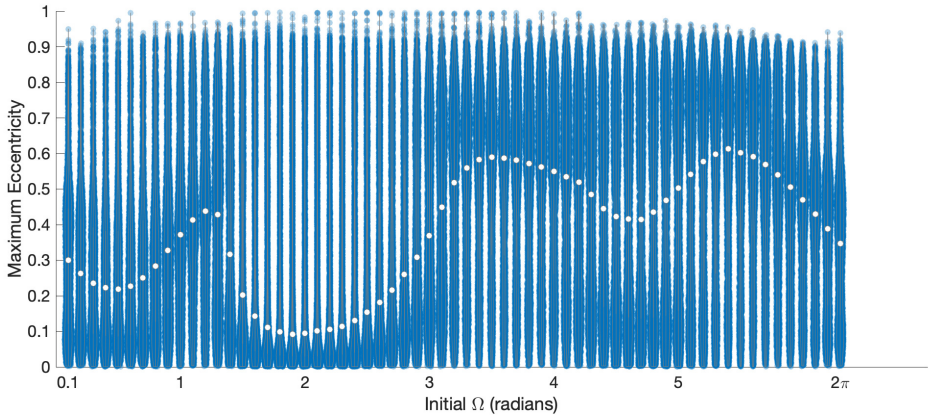

(b) Galileo

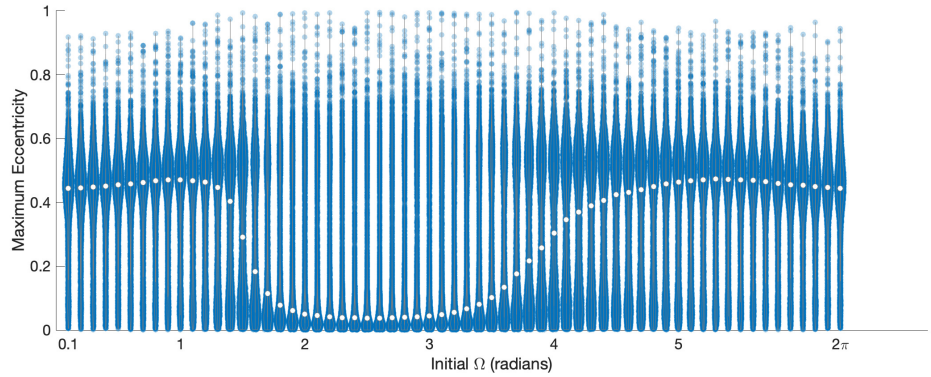

(c) GLONASS

Figure 4.34: Maximum eccentricity of objects produced in explosion events

4.4.1.3 Collisions

In the case of collisions, there are two fragment clouds: one originating from the parent satellite and one originating from the impactor satellite. These satellites collide along the equator.

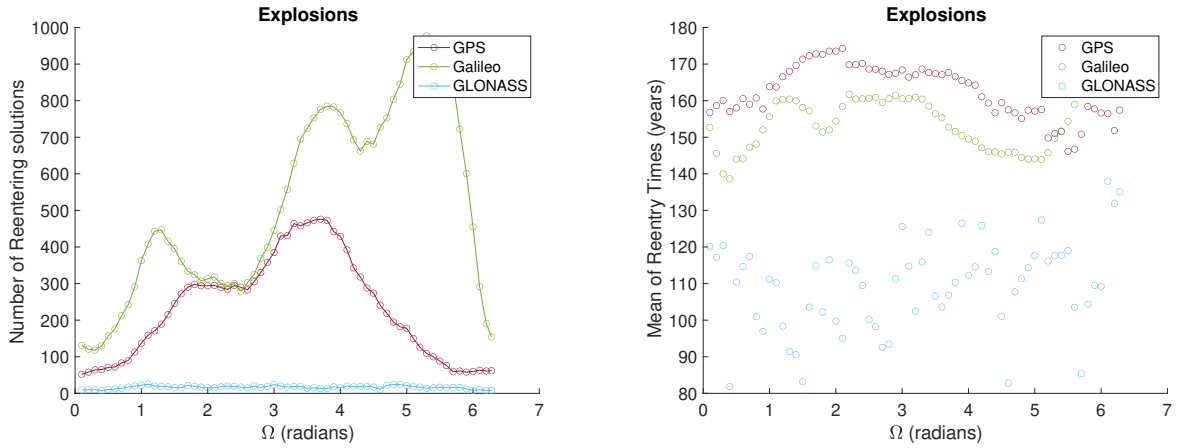

(a) Number of reentering objects for the breakup cloud

(b) Mean of reentry times of the objects that reentered

Figure 4.35: Reentry of objects in debris clouds compared to RAAN for explosions

Their resulting debris field profiles are opposite one another (Figure 4.9); this is important when thinking about the characteristics of the higher energy particles in the debris field. In this section, we will show the structure of the RAAN and argument of perigee graphs for each satellite separately but then will show them together which will represent the total debris field of the event. This is because the parent and impactor are separated by a RAAN of π radians so the combined forms will be graphed in terms of the impactor RAAN (with the parent RAAN out of phase by π radians).

Figure 4.36 shows that the impactor satellites in each of the constellations follow the trends in the unstable base case. Galileo has an interesting pocket of stability around an argument of perigee of π radians possibly due to this part of the argument of perigee profile having the highest energy. These maps were binned to remove any extremely high semi-major axes (objects about to be ejected) to better understand the bulk of the cloud, but not every debris fragments' behavior is uniform along the argument of perigee profile.

The parent satellites show the opposite behavior for Galileo in Figure 4.37 because the higher energy argument of perigees are around $0/2\pi$ radians. Interestingly, the GPS parent object's breakup cloud more closely matches the stable structure in line with the explosion breakup cloud's profile for GPS.

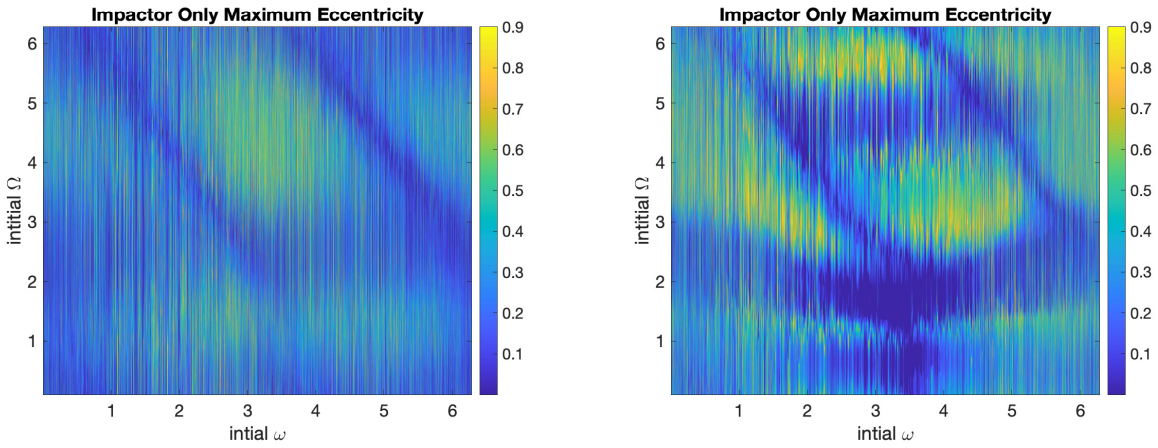

(a) GPS

(b) Galileo

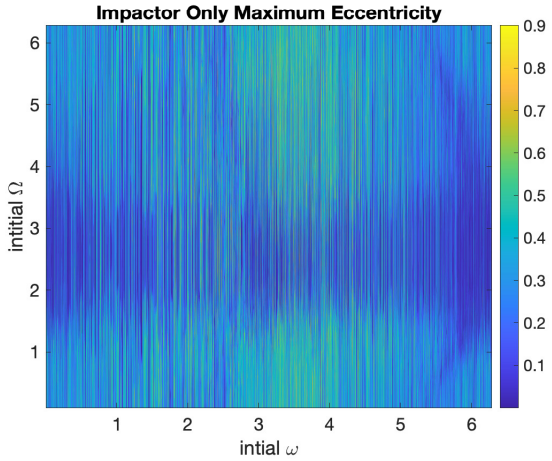

(c) GLONASS

Figure 4.36: Argument of perigee vs RAAN structure of objects produced in a collision event for the impactor set

Figure 4.38 shows how the full event's structure appears in argument of perigee vs RAAN space. In this case, the debris fragments are listed by impactor initial RAAN and corresponding parent initial RAAN (impactor + π radians). The base case is an impactor around 2π radians.

Figure 4.39 shows how the maximum eccentricity distributions of the breakup clouds vary with respect to RAAN. They are plotted on the graph with respect ot the impactor RAAN where each distribution has the parent cloud out of a phase by π radians.

All three constellations show variations in their distributions due to the RAANs of the satellites colliding. All three constellations also show peaks around similar areas. GPS fragment clouds

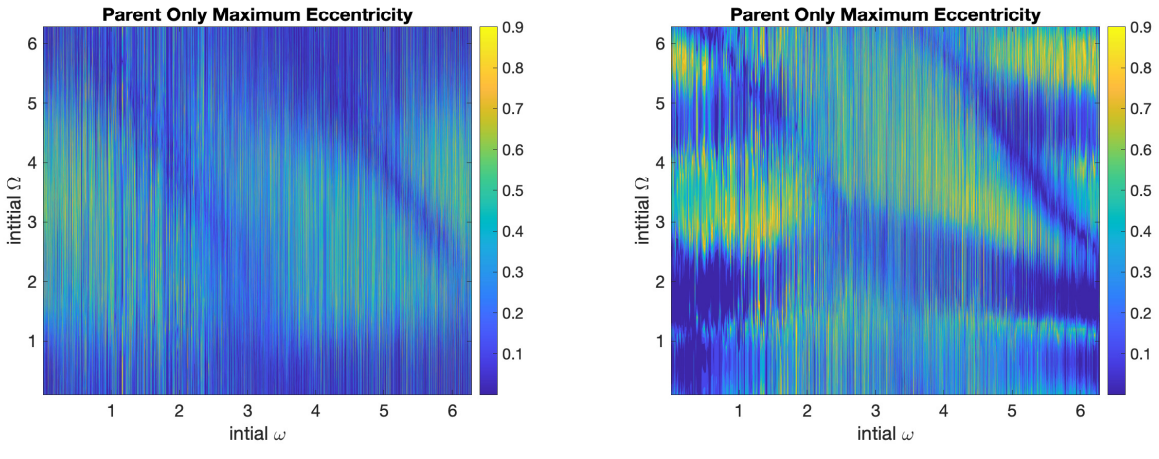

(a) GPS

(b) Galileo

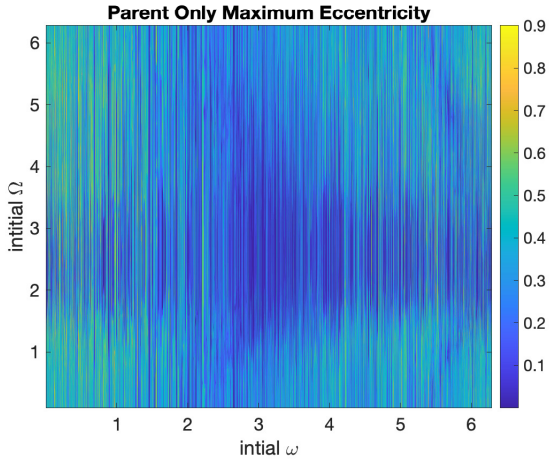

(c) GLONASS

Figure 4.37: Argument of perigee vs RAAN structure of objects produced in a collision event for the parent set

peak at 1 and 5 radians RAAN while the other two are slightly shifted. GLONASS fragment clouds have the least pronounced differences in the maximum eccentricity achieved by the fragments.

Figure 4.40 shows the characteristics of the reentry times of the distributions. Like the explosion case, the collision cases show a similar trend in the number of reentering solutions. All three constellations have the least reentries around π radians and the most around $\pi/2$ and $3\pi/2$ radians.

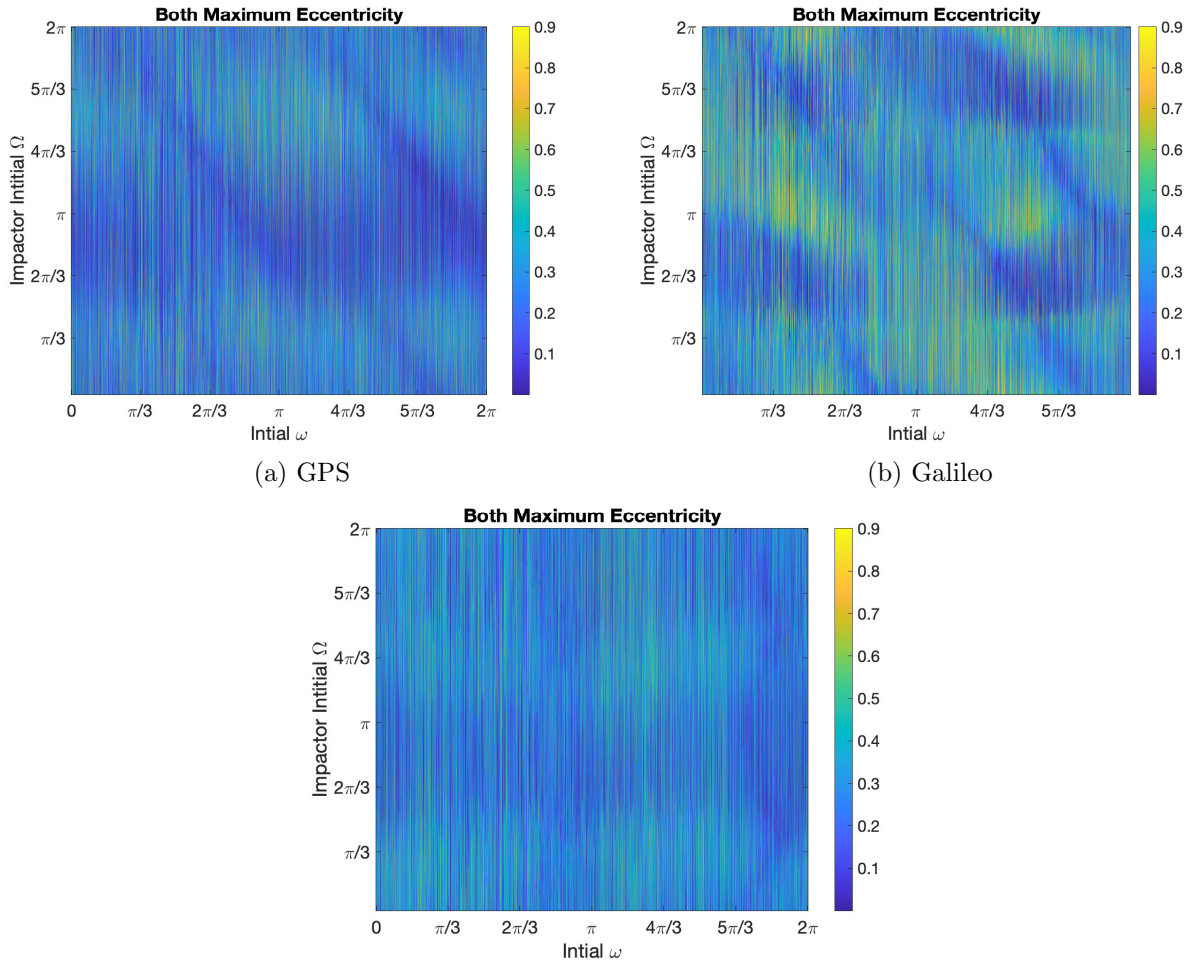

(a) GPS

(b) Galileo

(c) GLONASS

Figure 4.38: Argument of perigee vs RAAN structure of objects produced in a collision event for both the impactor and the parent set

4.4.2 Varying Epoch

4.4.2.1 Known Structure of the Region

The epoch or initial positions of the Sun and Moon can affect the stability of objects due to luni-solar resonances in MEO. Previous research has shown that this behavior is cyclic with respect to the period of the lunar node which is about 19 years. Figure 4.41 shows the patterns for a stable base case and unstable case over this period. These results are consistent with previous findings in Alessi et al. [8]. The regions of instability sprout from $\omega = \pi$ and 2π radians depending on the

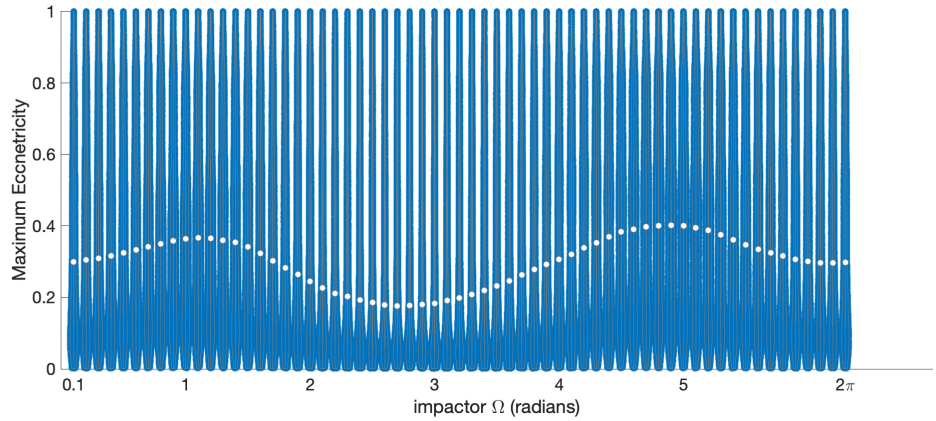

(a) GPS

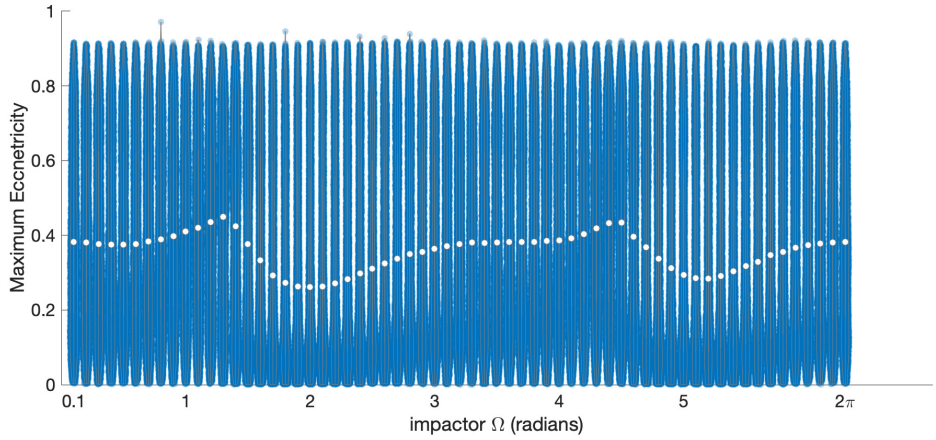

(b) Galileo

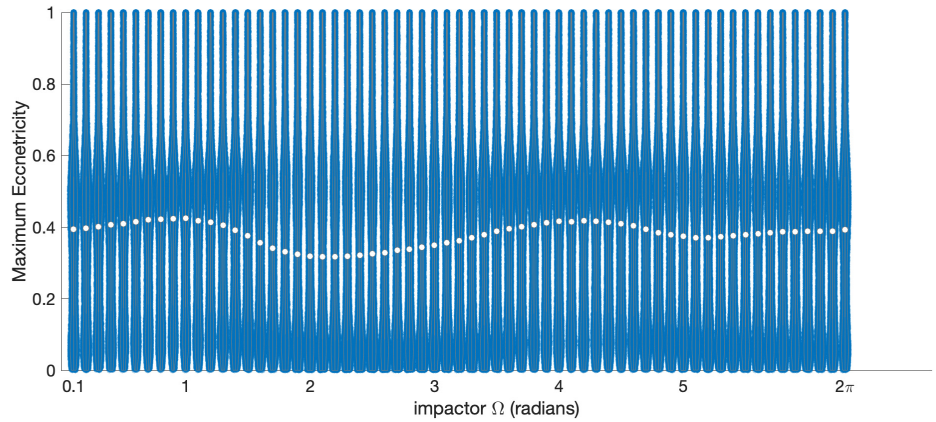

(c) GLONASS

Figure 4.39: Maximum eccentricity of objects produced in a collision event

epoch for each of the graphs. For the stable base case, events toward the end of the simulation tend

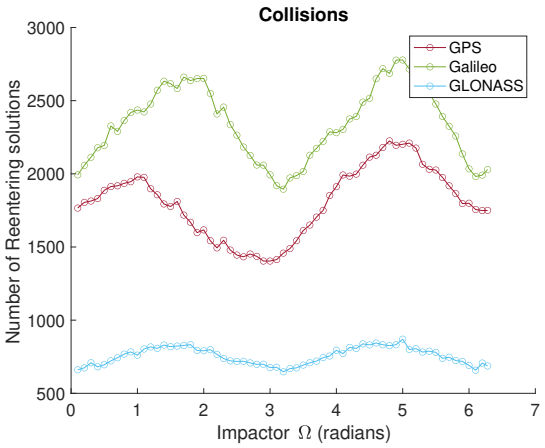

(a) Number of reentering objects for the breakup cloud

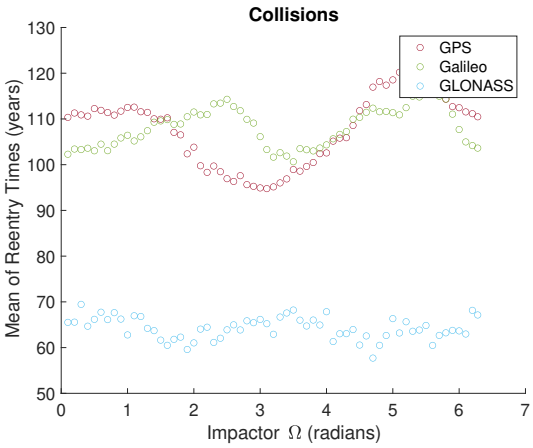

(b) Mean of reentry times of the objects that reentered

Figure 4.40: Reentry of objects in debris clouds compared to RAAN

to produce more stable trajectories while it is somewhat uniform throughout the unstable case just varying in regions of instability.

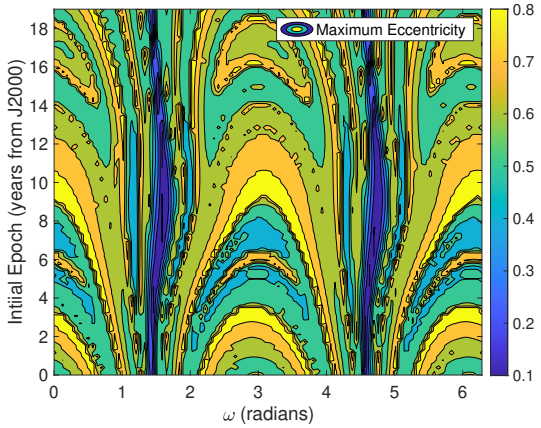

(a) Stable Base Case (low eccentricity e=.1)

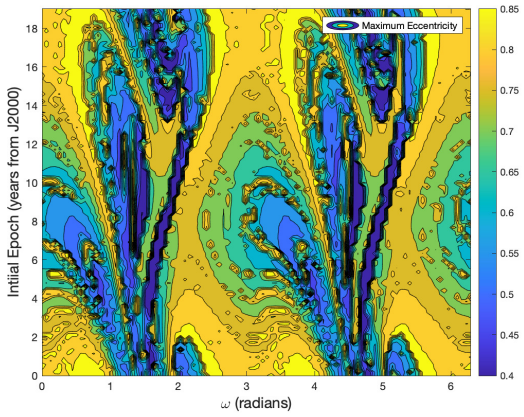

(b) Unstable Base Case (high eccentricity e=.4)

Figure 4.41: Argument of perigee vs initial epoch structure

4.4.2.2 Explosions

In this section, we replicate these graphs for the fragment clouds made from explosion events in each of the constellations. Like the previous section, the debris objects have more varying

characteristics than their argument of perigee. Thus, the graphs will not appear one to one to one with Figure 4.41 and will instead appear streaking with some zones of highly eccentric orbits compared to hot spots of that figure.

Figure 4.42 shows how the three constellations compare to the variations due to epoch. The GPS cloud hardly reaches any regions of high eccentricity making it difficult to decipher any clear patterns. The GLONASS cloud shows little variation due to epoch and the Galileo cloud appears to be the most sensitive to epoch with some of the structure seen in Figure 4.41.

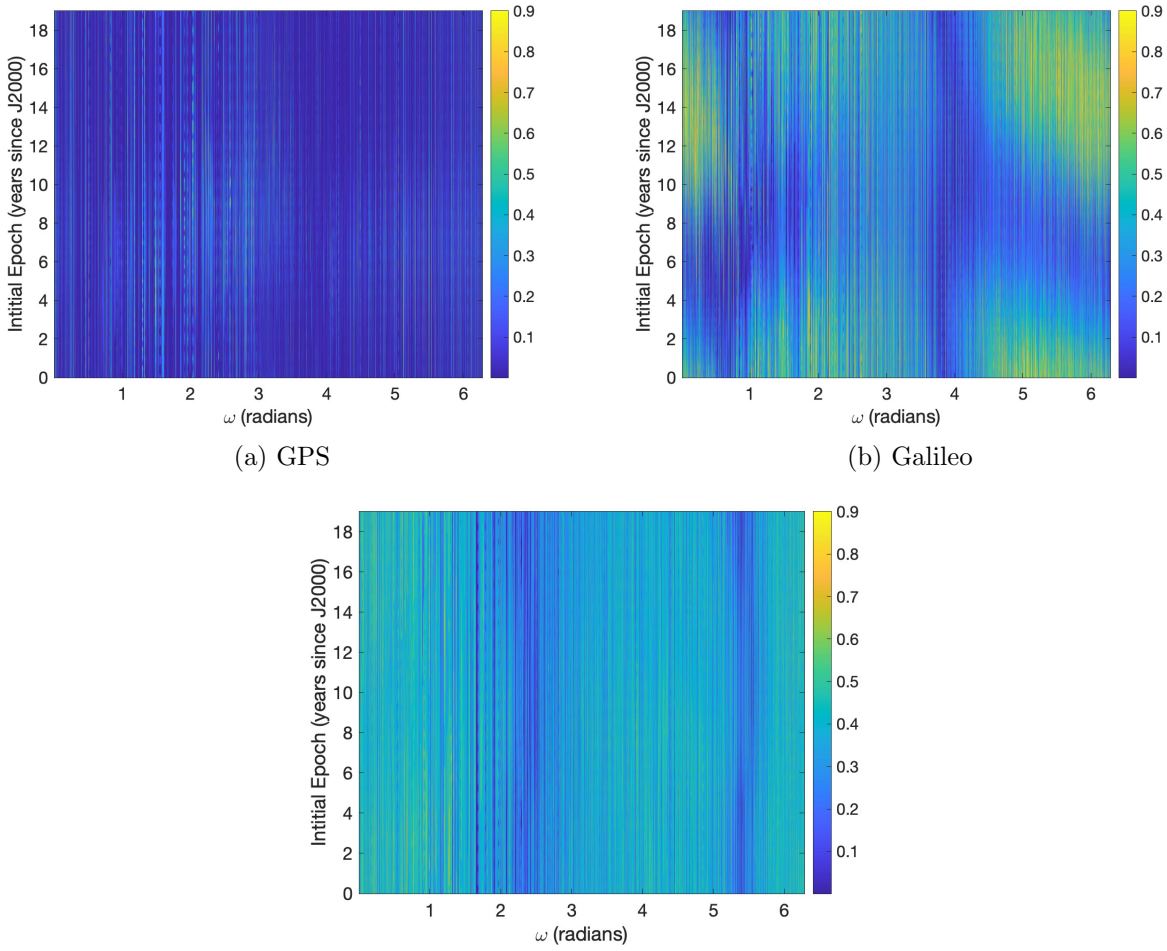

(a) GPS

(b) Galileo

(c) GLONASS

Figure 4.42: Argument of perigee vs initial epoch structure of objects produced in an explosion event

Looking at the distributions independent of argument of perigee tells a similar story. Figure

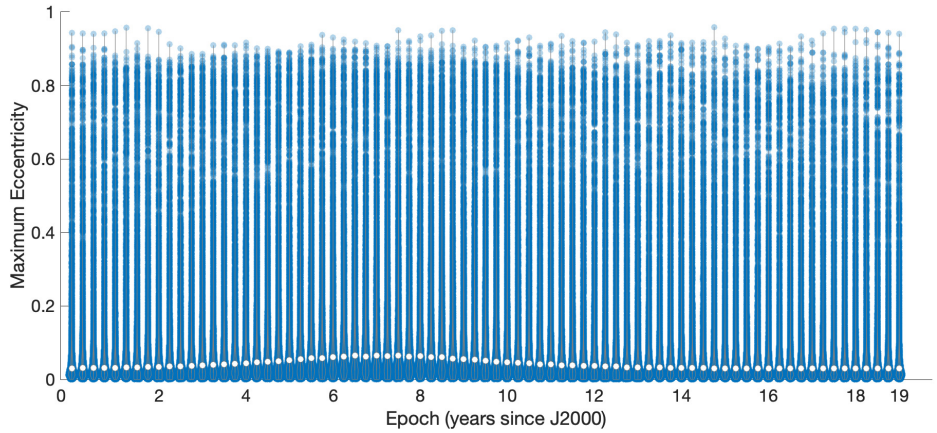

(a) GPS

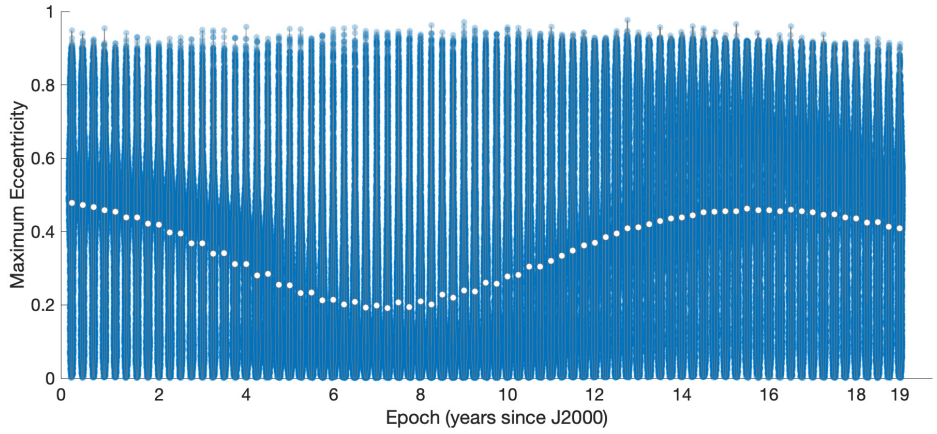

(b) Galileo

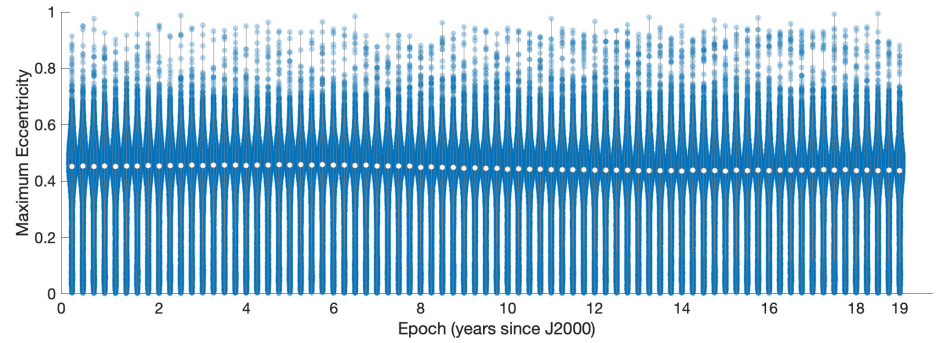

(c) GLONASS

Figure 4.43: Maximum eccentricity of objects produced in explosion event

4.43 shows how Galileo is the most sensitive to variations in epoch. This is followed by GPS which has most of its objects near circular throughout the 200 year simulation for all of the variations in epoch. GLONASS has many objects reaching high eccentricities but this behavior does not seem

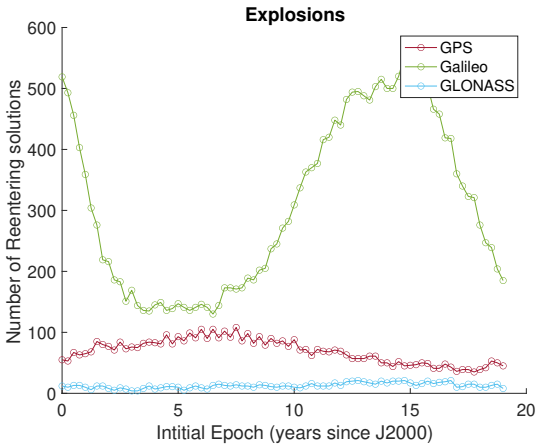

(a) Number of reentering objects for the breakup cloud

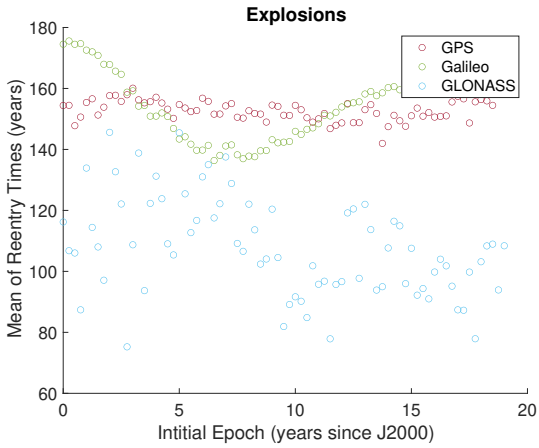

(b) Mean of reentry times of the objects that reentered

Figure 4.44: Reentry of objects in debris clouds compared to epoch

dependent on the changes in the timing of the event.

The reentry times of the clouds tell a similar story to the maximum eccentricity distributions. Figure 4.44 shows how Galileo is the most sensitive to changes in the timing of the event. Interestingly, the number of reentries follows a cycle slightly different than the regression of the node cycle, but this might be due to the sensitivity of the variable (or condition) in comparison to the eccentricity's behavior.

4.4.2.3 Collisions

The breakup clouds due to collisions can also be compared to the known structure of the regions. Figure 4.45 shows how the impactor's fragment clouds structure compares. In each of the clouds, there are hot spots of increased eccentricity with regard to the timing of the event and the argument of perigee.

The parent satellite's fragment cloud follows the known structure of the region more closely. Figure 4.46 shows how closely the Galileo fragment cloud matches the known structure followed by the GPS fragment cloud while the GLONASS fragment cloud does not appear to have much structure to it.

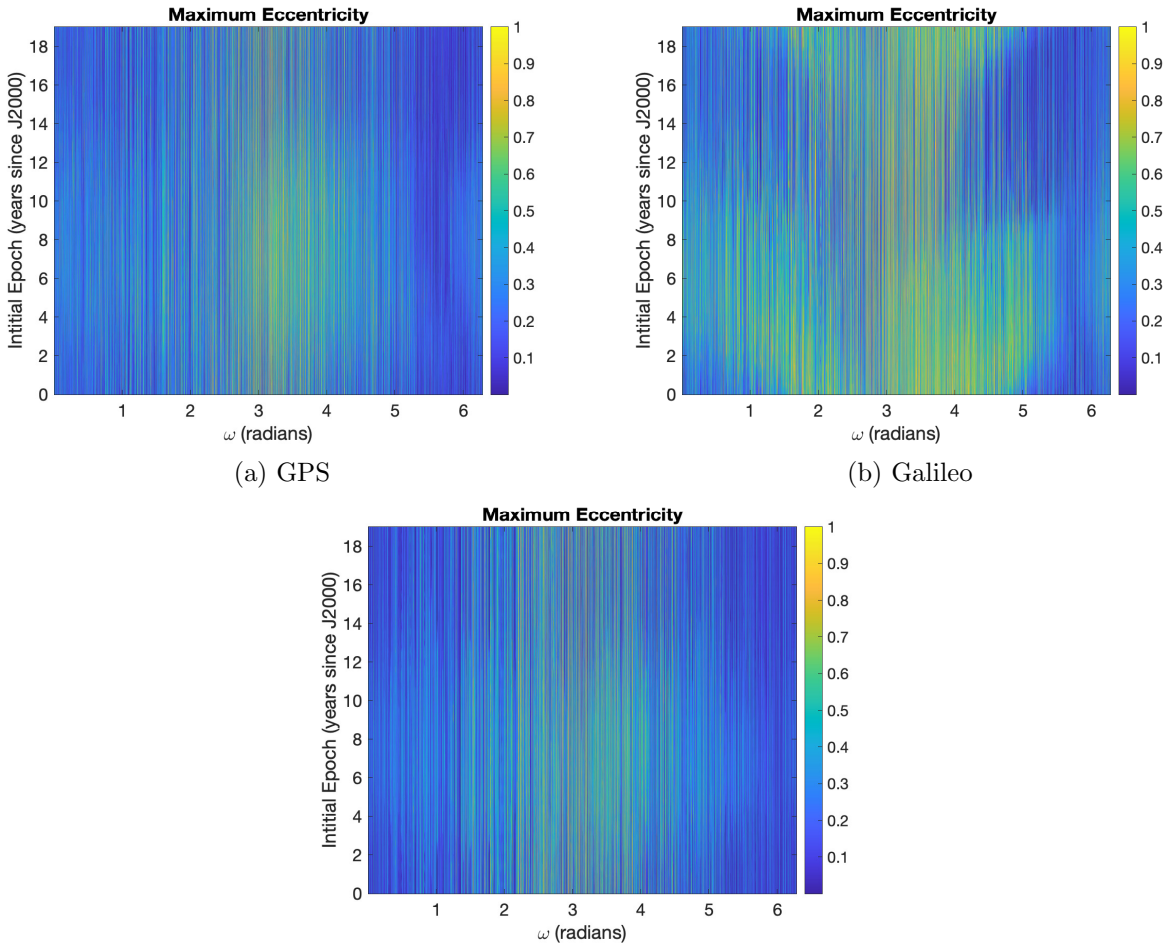

(a) GPS

(b) Galileo

(c) GLONASS

Figure 4.45: Argument of perigee vs initial epoch structure of objects produced in a collision event for the impactor set

The entire event is depicted in Figure 4.47. The entire event follows the similar structure as the argument of perigee and epoch maps earlier.

Although the epoch dependent structure is easy to decipher in the contour maps, the distributions of the maximum eccentricities look relatively uniform among varying epochs in the violin plots (Figure 4.48). Galileo shows the most structure in the contour maps but when the whole distribution is mapped out into the violin plots, it loses this structure. This could be a result of what was alluded to in the known structure maps about how without separating the objects by argument of perigee in an unstable case, the patterns due to epoch are not as obvious. The effects

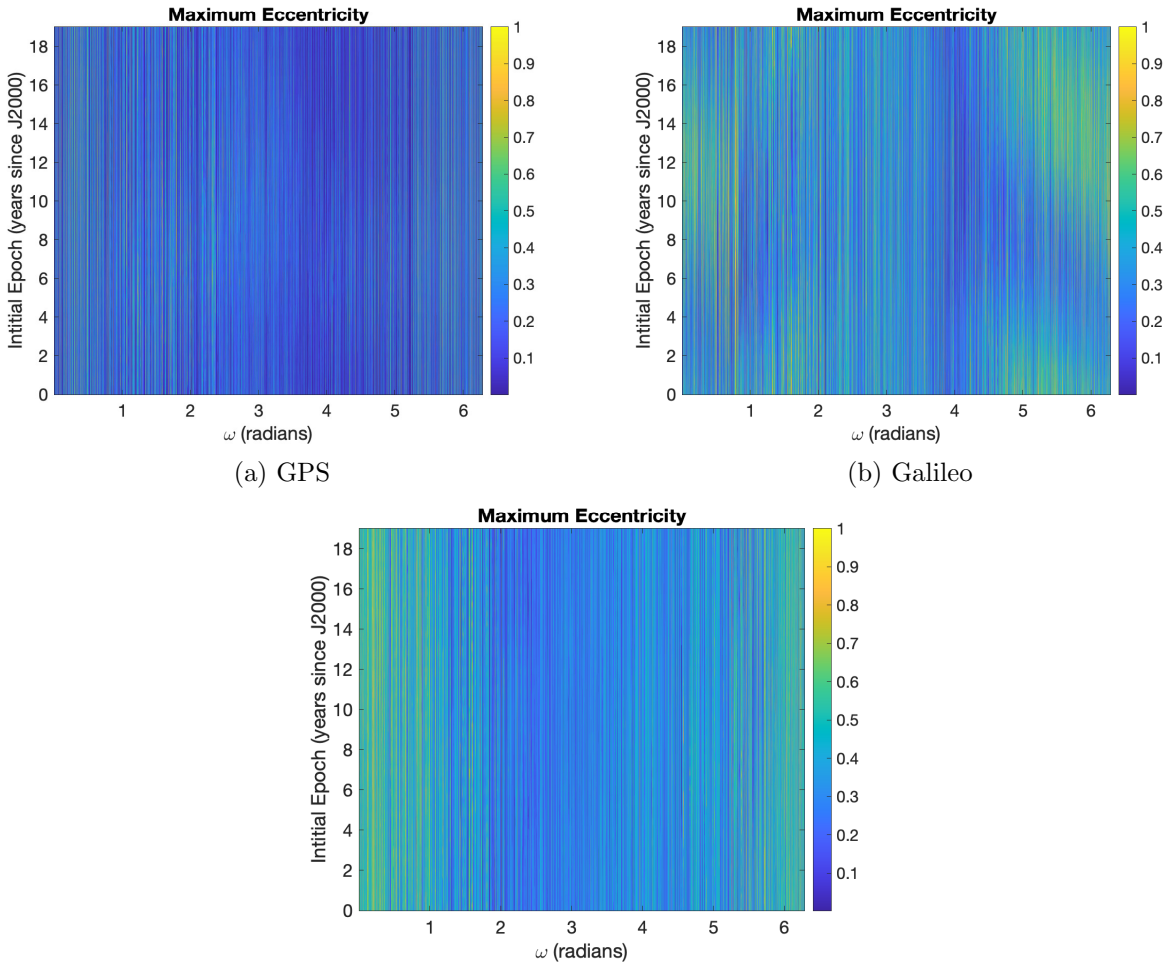

(a) GPS

(b) Galileo

(c) GLONASS

Figure 4.46: Argument of perigee vs initial epoch structure of objects produced in a collision event for the parent set

average out over the entire distribution. The GPS cloud has the largest dependency on epoch for the mean of its maximum eccentricity distribution, peaking at about seven years past J2000. GLONASS also has some variation on the average behavior of its distribution dependent on epoch where between four and five years favor a more bimodal behavior than the others.

The characteristics of the reentry times of the collision events have some dependency on epoch. Figure 4.49 shows how the number of solutions changes with the timing of the event and the mean of those reentry times. In terms of reentry times, the Galileo cloud and the GPS cloud have some dependency on epoch with GPS having larger number of reentries around seven years

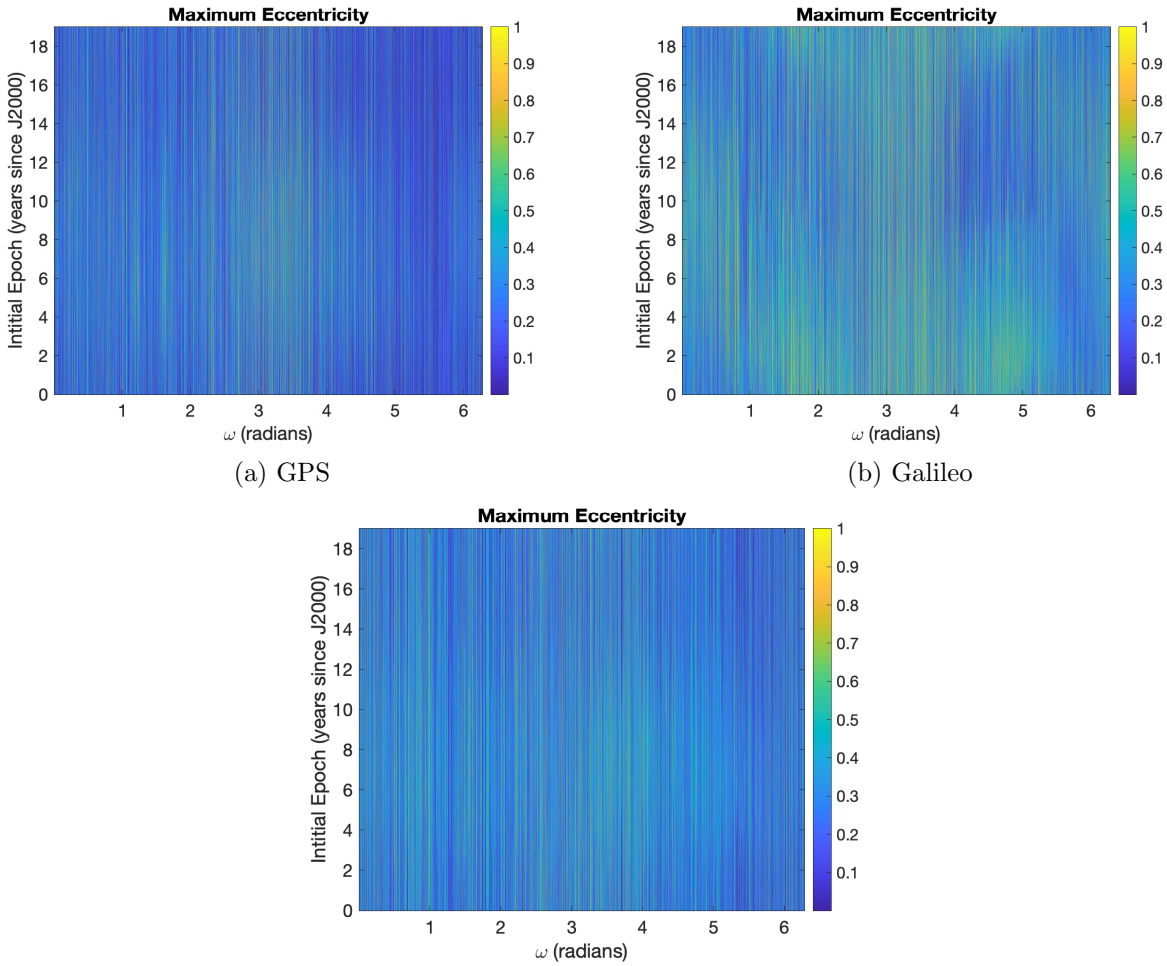

(a) GPS

(b) Galileo

(c) GLONASS

Figure 4.47: Argument of perigee vs initial epoch structure of objects produced in a collision event

but a longer mean reentry time.

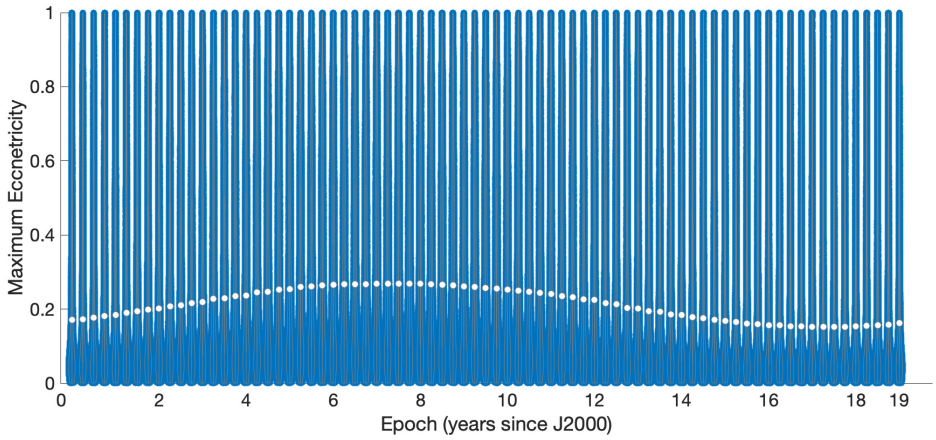

(a) GPS

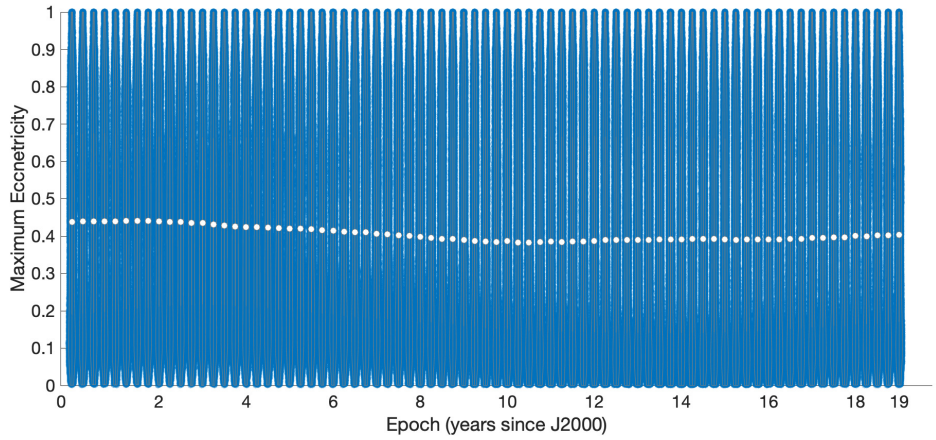

(b) Galileo

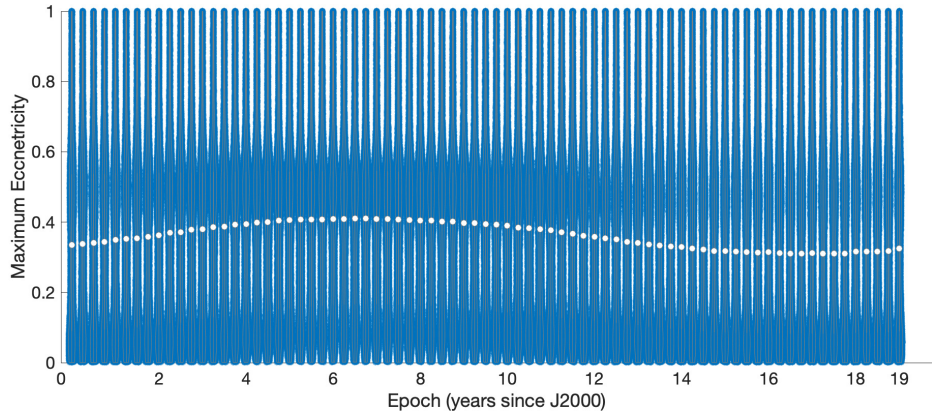

(c) GLONASS

Figure 4.48: Maximum eccentricity of objects produced in collision event

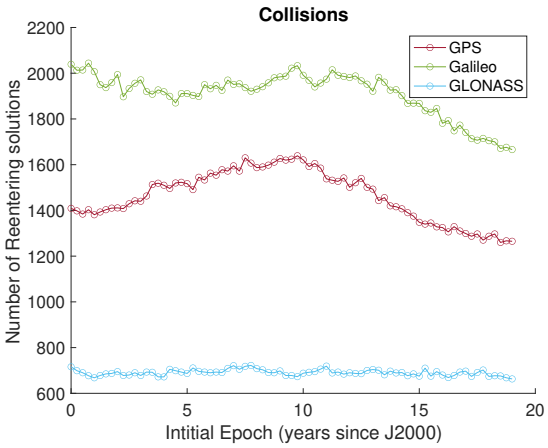

(a) Number of reentering objects for the breakup cloud

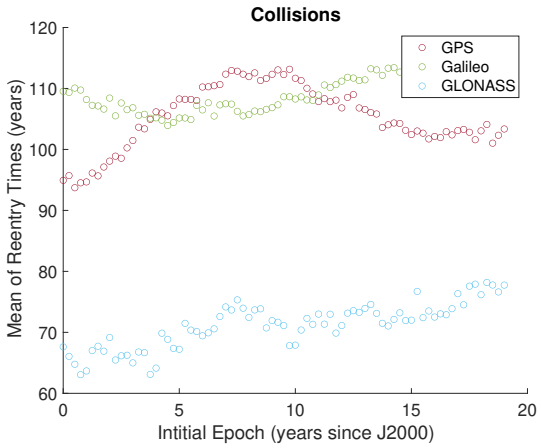

(b) Mean of reentry times of the objects that reentered

Figure 4.49: Reentry of objects in debris clouds compared to epoch

4.4.3 Vary Semi-major Axis

The final variable we explore is semi-major axis. This study was motivated by the possibility of graveyard orbits surrounding the GNSS regions. The current practice in Geosynchronous orbit is to raise the perigee by 300 km above the nominal orbit (or by increasing the circular orbit's semi-major axis to 300 km more than its previous value) [46, 13]. This study aims to explore if the event took place in a nearby orbit to the nominal as what might happen if a graveyard orbit was a practiced mitigation technique in this regime.

Semi-major axis contributes to the resonance structure; resonances are mapped out analytically in eccentricity, inclination, and semi-major axis space [83]. However, as will be discussed in Chapter 5, 10-100 km variations in semi-major axis do not result in largely different trajectories [77]. Therefore, we expect to see slight fluctuations based on varying semi-major axis.

Because these fragment clouds were generated independently of the research by NASA's orbital debris program office, the creation of differing fragment clouds from varying semi-major axes was not feasible. Each of the previous variables were easily varied because RAAN remains the same after the event and could be easily replaced and because we chose the initial timing of the simulation. Instead, this variable was varied after the event by adding a change to the semi-major

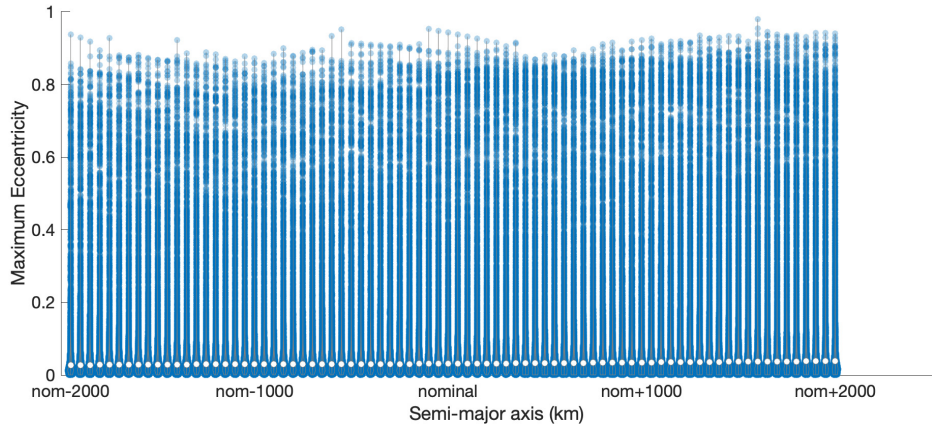

(a) GPS

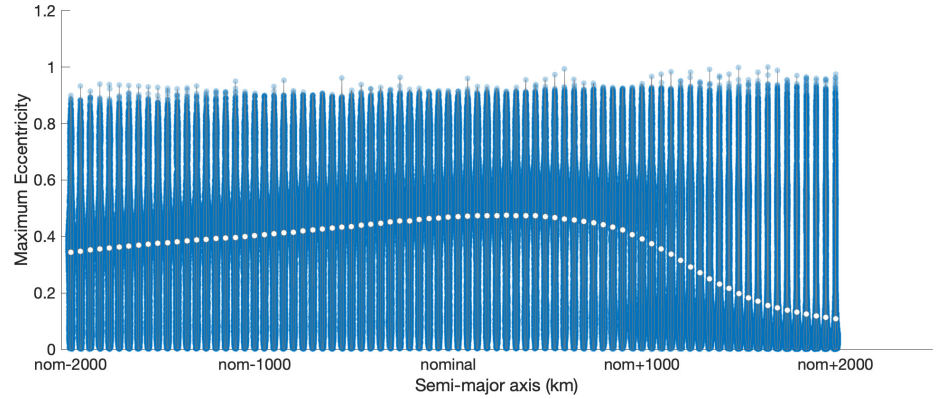

(b) Galileo

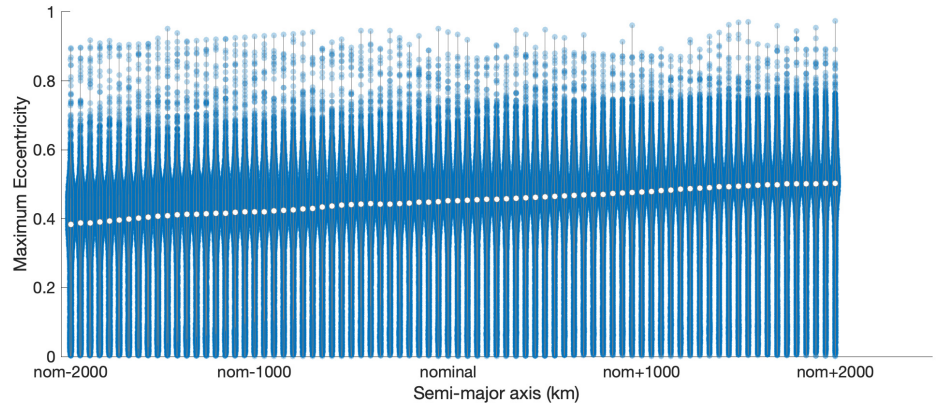

(c) GLONASS

Figure 4.50: Maximum eccentricity of objects produced in explosion event

axis to each of the fragments in the fragment cloud. Collisions provide too large an array of semi-major axes due to the highly energetic nature of the event for this process of editing the fragment

cloud post event to be meaningful. Therefore, we only investigate how explosions might vary due to occurrences at differing semi-major axes.

Figure 4.50 shows the maximum eccentricity distributions for the explosion events for differing semi-major axes. In both the GPS fragment clouds and GLONASS fragment clouds, there is a trend of increasing eccentricity distributions with increasing semi-major axis. This might be due to the lowering of some of the resonance webs closer to circular orbits as semi-major axis increases or the unstable regions' occurring closer to the objects with near circular orbits generated by the explosion event thus exciting more of them. Galileo is known to have a region of instability close to its nominal orbit for its semi-major axis. This could explain why the fragment cloud's maximum eccentricity peaks close to its nominal orbit. However, it is interesting to note that it similarly has an increasing eccentricity behavior up until about 1000 km above its nominal orbit. This seems to be the cutoff where the region of instability is no longer near circular orbits.

The reentry conditions of the fragment clouds shown in Figure 4.51 tell a similar story. The GPS and GLONASS fragment clouds increase in number of reentering solutions as the semi-major axis increases. Galileo's fragment cloud has a peak number of reentering solutions close to its nominal orbit.

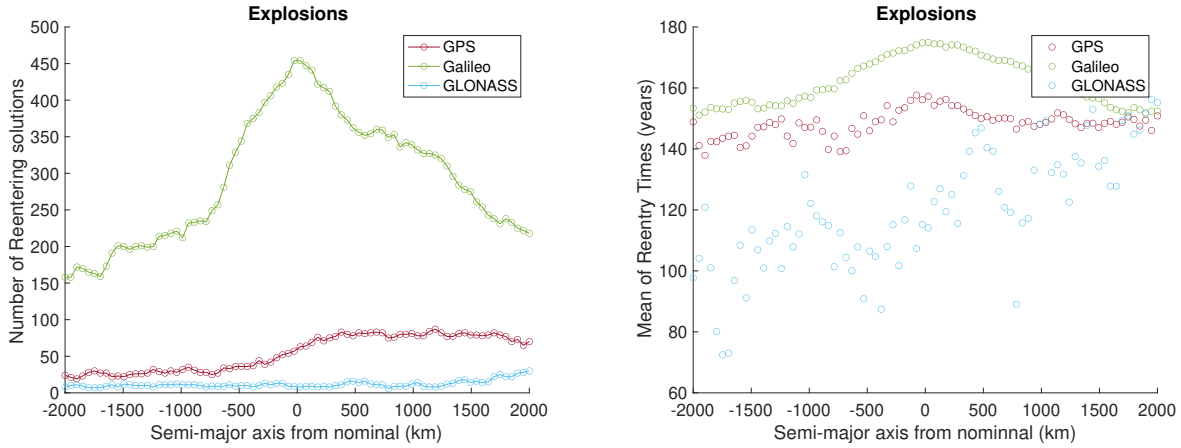

(a) Number of reentering objects for the breakup cloud

(b) Mean of reentry times of the objects that reentered

Figure 4.51: Reentry of objects in debris clouds compared to semi-major axis

4.5 Conclusion

The evolution of collision and explosion fragment clouds in medium Earth orbit shows some interesting dynamics. Massive objects with relatively low area-to-mass ratios result in reentries in the fragment cloud. A large number of those reentries occur toward the end of the 200-year simulation for the explosion case and with the collision case most of the objects reenter within a few years of the event.

All six breakup events show varying behavior in terms of loitering near the nominal orbits of the GNSS regime. The types of events show a large impact on how long the objects inhabit the nominal orbital regime. Explosions tend to have less dynamic debris objects and thus a larger percentage loiter close to the event further into the simulation. Collisions have a larger variation in debris objects, and many of them, due to their higher eccentricities, don't loiter near the nominal orbits. However, these objects are still interacting with the nominal orbits late into the simulation.

Events in the GPS regime tend to produce breakup clouds that loiter for the longest time in hazardous areas or close to the nominal satellite orbits of the varying constellations. In contrast, Galileo events lead to fragments which inhabit all of the orbits relatively quickly but those objects decrease in time spent in nearby nominal orbits in the latter half of the simulation. GLONASS events show interesting behavior in that more debris objects tend to inhabit the nearby nominal orbits in the latter portion of the simulation as compared to the prior two.

Beyond the base cases, this work has shown that right ascension of the ascending node, epoch, and semi-major axis can largely influence a fragment event's long-term behavior. Some of these patterns have followed the known resonance structure of the region. The Galileo fragment events seemed to be the most sensitive to the changes in these initial conditions. However, variations in right ascension of the ascending node caused large shifts in the behavior in all three constellations.

The explosions and collisions showed varying behavior due to sensitivities in the initial conditions. For right ascension of the ascending node, the explosion events provided the most intelligible variations in the cloud behavior as compared to the collision cases, as the collisions had two initial

satellites out of phase by π radians. The variations in epoch showed that the Galileo region was sensitive to the initial positions for the explosion event, but when the initial distributions between the parent and impactor satellite were larger in the collision event, the sensitivities due to epoch seemed to diminish.

The chaotic nature of medium Earth orbit proves to cause wide variation in the behavior of fragment clouds in the regime. The known eccentricity growth of the region impacts each of the semi-major axes of the nominal constellation orbits studied differently. Some general trends can be pulled from the type of event and the nominal orbit studied. This work proves that breakup events in medium Earth orbit will remain a hazardous risk for many objects in neighboring regimes and not all the objects will immediately depopulate due to the known eccentricity growth of the region; many will begin to interact with neighboring functioning orbits due to an increase in eccentricity but not a large enough increase to depopulate the region.

Additionally, this research has shown when considering the debris mitigation practices in medium Earth orbit, it is important to consider the wide range of possible outcomes of dynamic events in these orbits. Simple variations in the timing of such an event can cause a fragment cloud to drift towards nominal orbits of surrounding satellites rapidly due to the instabilities of the region. Current mitigation practices of increasing the semi-major axis of high altitude orbits will help in the short term of preventing collision hazards, but the unstable nature of the region is not avoided by this practice.

Chapter 5

Research Goal 3 - Targeting Regions of Chaos

This chapter is motivated by the potential use of targeting regions of chaos for direct reentry and considers the question of how precisely these impacting orbits need to be targeted. If we are to target specific orbital parameters for reentry, it is important to understand the likelihood of that satellite reentering. As the chaoticity of orbits in these regions has been established, and because one of the hallmarks of chaos is sensitivity to initial conditions, the sensitivity of these reentry orbits and whether nearby orbits will also reenter needs to be characterized. We study the targeting behavior independent of the method used to target the initial states; possible examples include solar sailing and multiple chemical burns. We recognize that the targeted orbit might change depending on the propulsion method used. In this chapter, we will study the sensitivity of such orbits that impact within a few decades to changes in their initial conditions, thus determining how accurately a satellite must hit a targeted orbit to achieve the expected reentry.

The chapter is structured as follows. First, we explore in detail the singly-averaged dynamics performance. It was used as a reference in Chapter 3 but now that we are requiring a higher level of precision in this chapter, we will discuss its behavior too. Then, we detail the structure of these resonances and the degrees of freedom of the system. Subsequently, we analyze each of the targeted regions using a Monte Carlo method varying the initial conditions of the target. We will be discussing three navigation constellations with a focus on the GPS which has an inclination of 55° and semi-major axis of 26560 km. Also included are the European navigation system Galileo which has an inclination of 56° and semi-major axis 29600 km, and the Russian GLONASS, GLObal

NAvigation Satellite System, which has an inclination of 64.8° and semi-major axis of 25440 km.

5.1 Model Comparison

Many different initial conditions were tested to compare the long-term behavior of each of the equations of motion. In particular, we will focus on two representative cases. As this chapter is using singly-averaged integration to study the sensitivity of orbits in the GNSS region, we will explore two typical candidate trajectories: one that experiences an impact after 35 years and one which does not over a fifty-year time span. Both of these orbits are subjected to luni-solar resonances. For the highly excited region, the satellite impacts the Earth in about 35 years and has a Lyapunov exponent of 0.0163/year (Lyapunov time of 61.4 years). For the slightly excited case, the satellite does not impact within the fifty-year simulation and has a Lyapunov exponent of 0.0110/year (Lyapunov time of 91.1 years).

The comparisons show that the averaged dynamics closely follow the full numerical integrations. This provides confidence in their use to define the sensitivity of these trajectories. For all the integrations, we used the seventh-eighth order Runge-Kutta Fehlburg method [28].

5.1.1 Slightly Excited

In the slightly excited case, the singly-averaged equations track the real solution well over the entire time span. While we clearly see the short period fluctuations of the full dynamics as compared to the secular, singly-averaged dynamics, we note that the overall secular trends are well captured (Figure 5.1).

The semi-major axis shows the largest short period oscillations with variations as large as 9 km from the original value. These variations do not amount to larger trends, and thus the averaged integrator performs as expected. The other elements track overall trends well. Figure 5.2 shows the difference between the two solutions.

The averaged solutions overall deviate with time from the full numerical model. The largest deviations are from argument of perigee and right ascension of the ascending node (RAAN) which

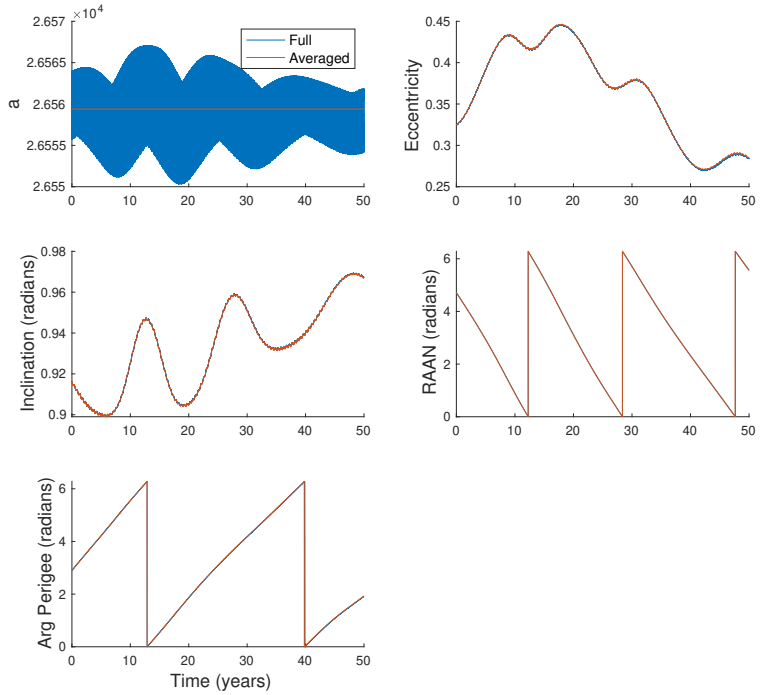

Figure 5.1: Slightly excited comparison. Semi-major axis variation is on the order of 10 km. Lines are coincident where not distinguishable.

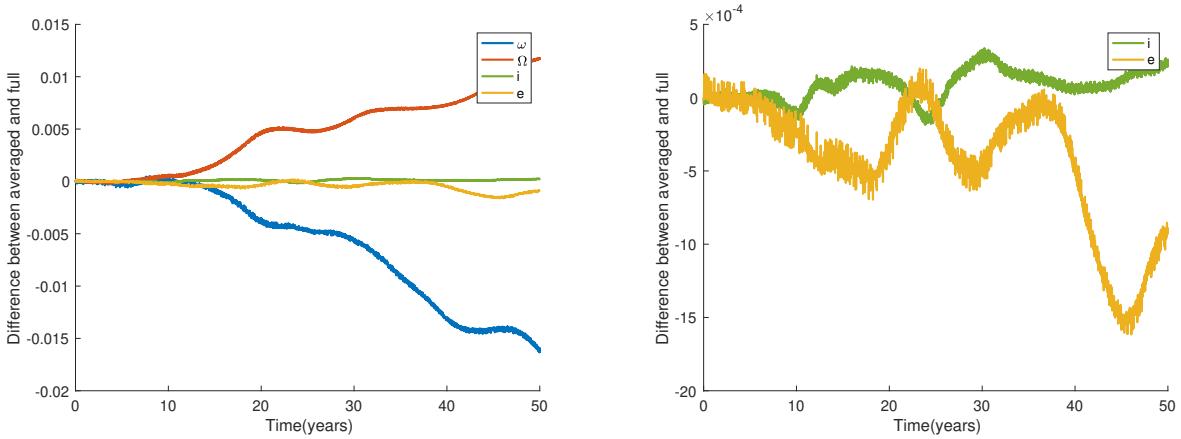

Figure 5.2: Difference of comparison in Figure 5.1 for the orbital elements except for semi-major axis. All angles are represented in radians.

at the end of the simulation have offsets of about 0.94° and 0.68° respectively. Eccentricity and inclination have much smaller offsets with respect to the full numerical solution. Eccentricity ends

with a peak offset of 1.6×10^{-3} while inclination's largest deviation is 0.019°.

5.1.2 Highly Excited

When the simulations were conducted with initial conditions that show large increases in eccentricity, the results were similar. The singly averaged solution was able to track the behavior of the real solution throughout the simulated fifty years. In this particular case, an eccentricity of 0.76 would be required for reentry and is not achieved until closer to thirty years. The two simulations are in agreement to that point (Figure 5.3). We note that we ran the solution out beyond this epoch to test the robustness of the solution.

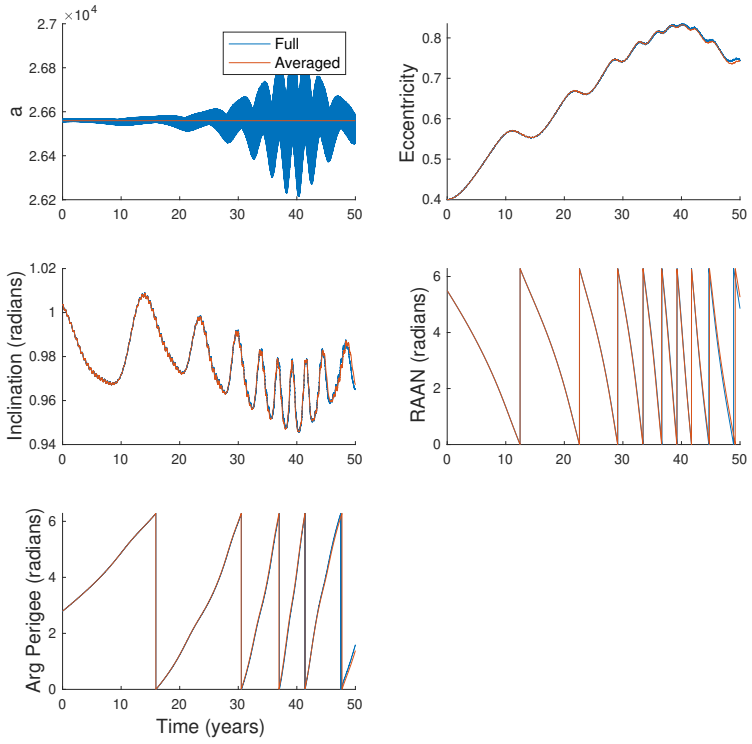

Figure 5.3: Highly excited comparison. Semi-major axis variation is on the order of 100 km. Lines are coincident where not distinguishable.

Semi-major axis shows the largest short period oscillations with variations up to 300 km from the original value. These variations do not lead to larger secular trends and thus the averaged

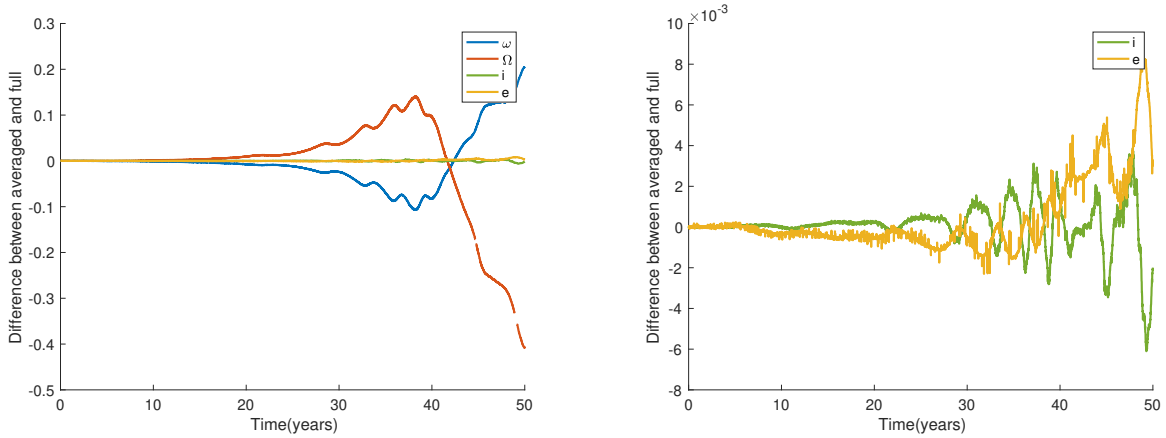

Figure 5.4: Difference of highly excited comparison in Figure 5.3 for the orbital elements except for semi-major axis. All angles are represented in radians.

integrator performs as expected. The short period oscillations are an order larger than the slightly excited case. The other elements track overall trends well. Figure 5.4 shows the difference between the two solutions.

Like the slightly excited case, the largest deviations are from argument of perigee and RAAN which at the end of the simulation have offsets of about 11° and 23°, respectively. These offsets are quite large at the end of the simulation; however, they occur after the orbit has come within the radius of the Earth. At the point of impact for this solution, the offsets for argument of perigee and RAAN are about 5.9° and 7.8°. Eccentricity and inclination still have much smaller offsets with respect to the full numerical solution. Eccentricity ends with a peak offset of 8.2×10^{-3} while inclinations' largest deviation is 0.35°. At the point of impact the offsets were 9.1×10−4 and 0.080°.

5.2 Choosing Targets

For each of the GNSS constellations, we will explore two targeted disposal cases. Target 1 will be a target that is surrounded by fast impacting neighbors. Target 2 has an eccentricity and inclination closer to the nominal orbit but is neighbored by locations that do not reenter. Therefore, target 1 is hypothesized to be more robust, while target 2 is less expensive to reach.

This study is independent of the method of propulsion used as we are focused on the perfor-

mance of the targets not the method to reach them. It is important to note that we keep constant the semi-major axis of the nominal orbits we study commensurate with using a spherical solar sail for propulsion [72, 9]. A set of two chemical burns can also reach an eccentricity change while holding semi-major axis constant if chemical propulsion is used. However, it might be more optimal to target a different semi-major axis (a GPS orbit targeting a Galileo target instead) to potentially reduce fuel cost. For the purposes of this paper, we will not study the differences in optimization of the targets except for how target 1 compares to target 2. In case of either propulsion method, target 2, having a closer eccentricity and inclination to the nominal orbit, would be easier to reach than target 1.

For GLONASS, although the inclination is on a secular resonance, numerical simulations show that the chaotic areas for its semi-major axis are in lower inclinations. Figure 5.5 shows that the closest region of chaotic activity for its semi-major axis is in the 55° to 60° inclination range. Thus, for all three navigation systems we will be exploring this range of inclinations, even though only Galileo and GPS have nominal orbits in this range.

To pick the targets, we used numerical integration to survey the nearby region for chaotic trajectories or decadal reentry times, similar to those in Figures 2.4, 2.5, and 5.5. In this case, we surveyed varying eccentricity and inclination for each semi-major axis. Unlike Figures 2.4 and 5.5, we do not use one RAAN and argument of perigee for each eccentricity and inclination combination but 14 different ones. Meaning, for every eccentricity and inclination pair, 14 different RAANs and 14 different argument of perigees are tested, totaling 196 cases. Because there is a trend of non reentering solutions in RAAN around π radians, the 14 RAAN cases were taken from 0 to $\pi/2$ radians and $3\pi/2$ to 2π radians while the 14 cases in argument of perigee were selected from a uniform distribution from 0 to 2π. The shortest reentry time from this set is plotted in Figure 5.6. This helps prevent any biases in choosing the eccentricity and inclination of a target based on an initial RAAN or argument of perigee of the surveyed space. This method averages out the fractal structure in Figures 2.4 and 5.5 and produces a uniform reentry time map.

After choosing an eccentricity and inclination to target, we determine the RAAN and argu-

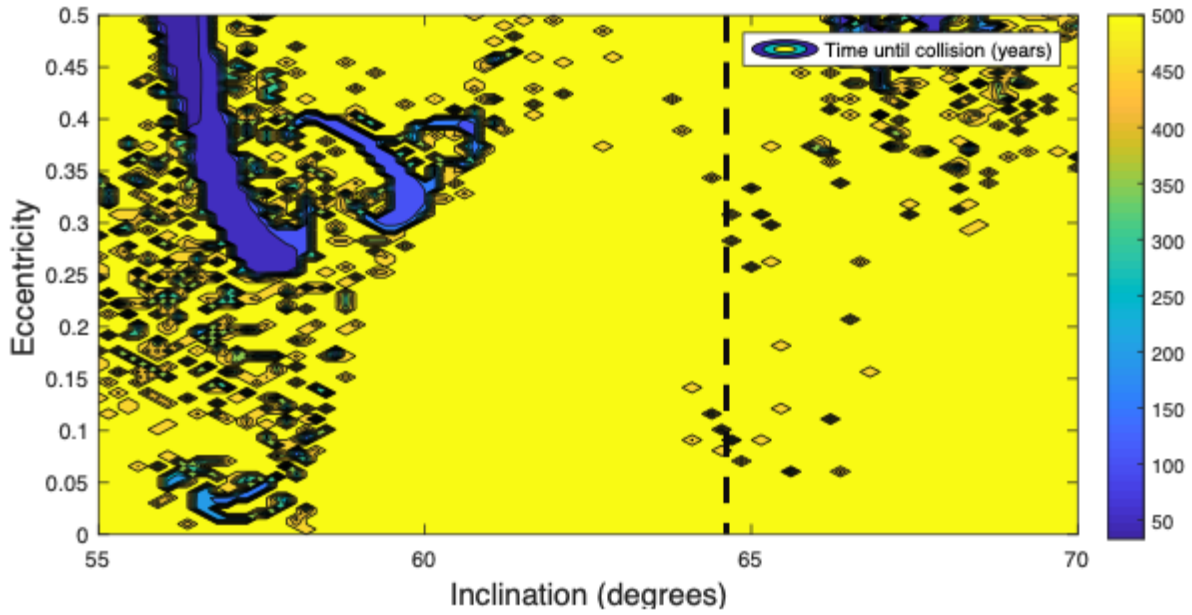

Figure 5.5: Map of years until Earth reentry for varying eccentricities and inclination for the GLONASS semi-major axis. The inclination for the nominal orbit is the dashed line. The colorbar represents the time of reentry. 500 year entries may not have reentered.

ment of perigee through a similar method. This time surveying over 100 RAANs and arguments of perigee, 10,000 cases, we pick a pair that is surrounded by the most neighboring reentering solutions. Figure 5.7 shows for the eccentricity and inclination of Galileo's target 2, the choices of RAAN and argument of perigee we select to target. Table 5.1 shows the chosen targets for each of the navigation constellations. Semi-major axis is defined by the navigation constellation [83].

Table 5.1: Targeted Orbital Parameters

	GPS T1	GPS T2	GLONASS T1	GLONASS T2	Galileo T1	Galileo T2
a	26560km	26560km	25440km	25440km	29600km	29600km
e	0.400	0.359	0.374	0.243	0.362	0.270
i	57.5°	57.6°	57.9°	59.3°	58.7°	58.1°
Ω	315°	40.0°	331°	36.4°	305°	287°
ω	160°	280°	171°	178°	171°	178°
Reentry Time	31 yrs	49 yrs	38 yrs	69 yrs	30 yrs	38 yrs

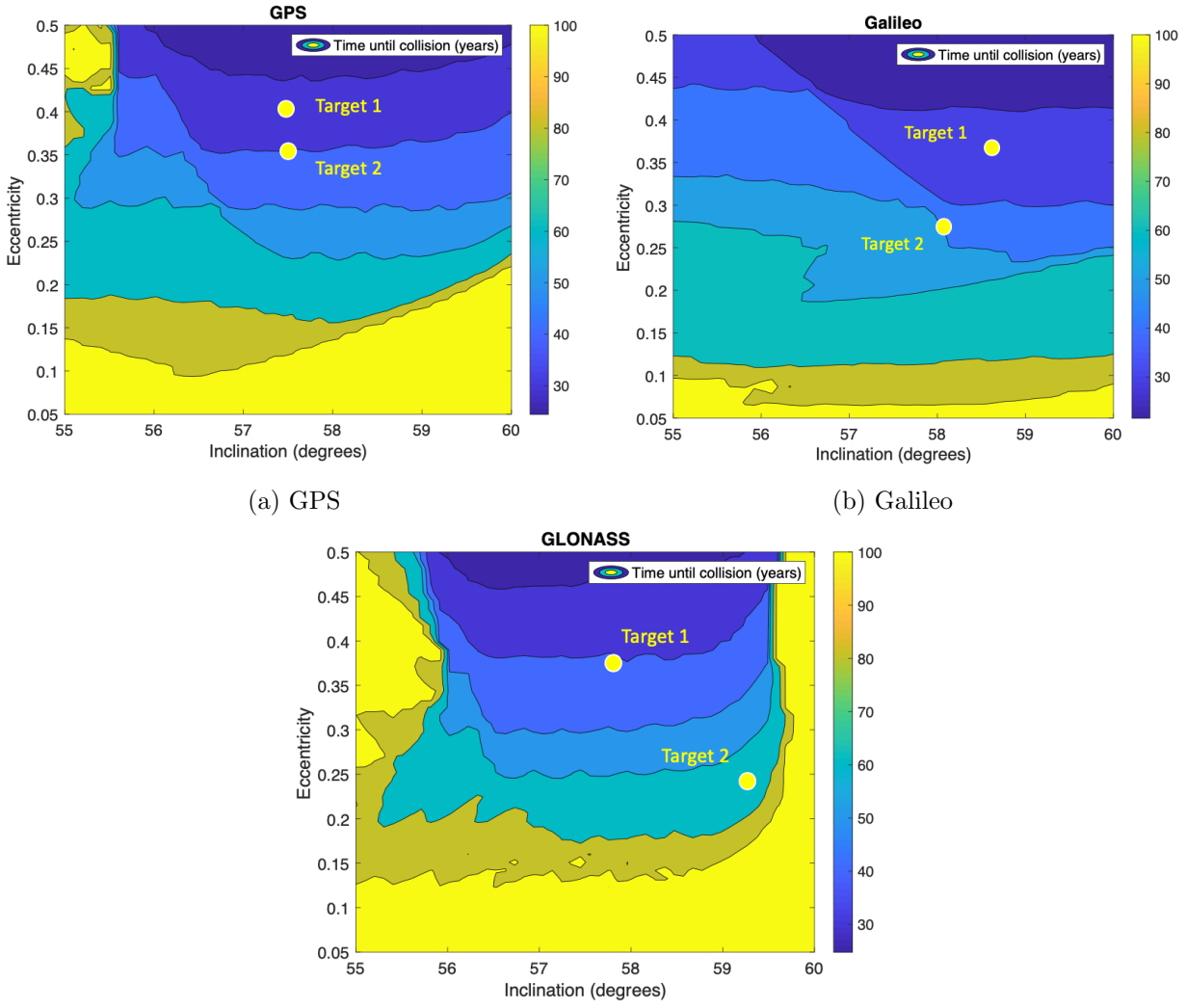

(a) GPS

(b) Galileo

(c) GLONASS

Figure 5.6: Comparison of chaotic regions independent of Ω and ω. Each point is the shortest collision time of 14 different Ω and ω (196 cases). The colorbar represents time until reentry. Entries of 100 years may not have reentered.

5.3 Robustness Analysis

In comparison to previous works which studied the stability of the overall region and varying trajectories [7], this work focuses on analyzing the neighborhood of the unstable trajectories. To determine the robustness of each of these targets, we used a Monte Carlo method of analysis using the averaged dynamic equations. As described in more detail in the subsections, for each of the targets, the initial conditions were varied by the position, velocity, orbital elements, and other

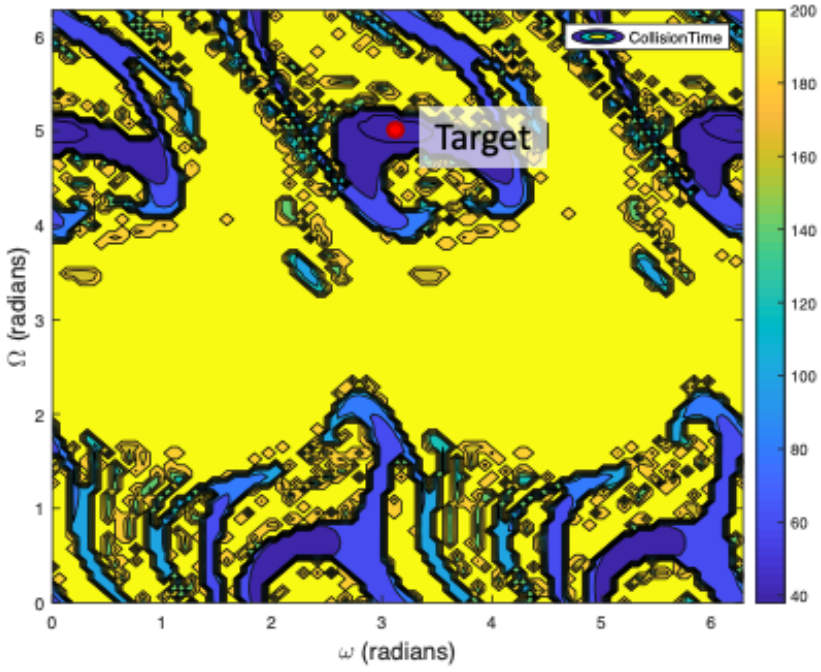

Figure 5.7: Varying Ω and ω for the eccentricity and inclination for Galileo's target 2. The colorbar shows time until reentry. Entries of 200 years may not have reentered.

parameters around the nominal target. These initial distributions were drawn from a uniform distribution within a set of values. The initial epoch is J2000.

We show a detailed analysis of the GPS Monte Carlo results for each of the varying initial conditions. In an effort to consolidate the information, the GLONASS and Galileo results are not discussed in the same detail but the overall inferences are compared alongside the GPS targets. These comparisons are pulled from the exact same methods and similar data as the GPS targets but will allow the reader to understand the greater implications of the robustness of these regimes.

5.3.1 GPS

5.3.1.1 GPS Target 1

Target 1 was chosen to be in an area that we hypothesize should show robust behavior. This is due to the fact that the area is dominated by unstable behavior and thus nearby trajectories

will also have decadal Earth reentry times. The orbital parameters targeted are listed in Table 5.1. The reentry time of the target is approximately 31 years.

The target position was varied for 1,000 runs as shown in Figure 5.8. Each of the directions was varied in a uniform distribution from the nominal orbit by -10 to 10 km and -100 to 100 km respectively. The norm of the deviation from the reference is used in order to compare each run. The results show that for variations of up to 10 km, the range of reentry times are within a matter of months. For the 100 km variations, the range is approximately a year.

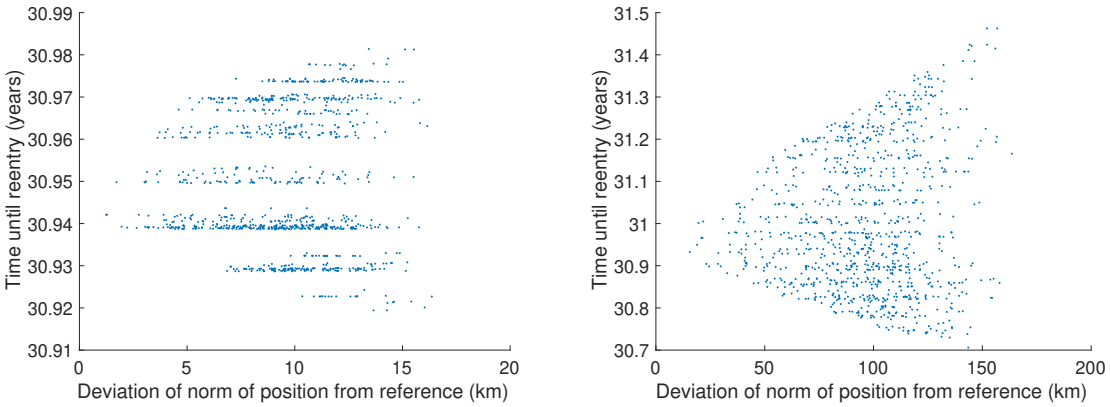

(a) Target position varied by 10 km.

(b) Target position varied by 100 km.

Figure 5.8: 1,000 Monte Carlo runs for target 1

The target velocity was varied for 1,000 runs as shown Figure 5.9. Each of the directions was varied from the nominal orbit by -1 to 1 m/s and -10 to 10 m/s respectively. The range of reentry times for the 1 m/s case is about 3 years. The 10 m/s deviation case shows that the simulations result in a high variation of reentry times. Most of the deviated cases do not reenter over the full 200 years of the simulation. Therefore, a targeting accuracy of 10 m/s would not ensure an orbit reentry. Instead, an apparent requirement of targeting with 1 m/s is needed to ensure the satellite reenters using the naturally chaotic dynamics of the region.

In addition to analyzing the Cartesian Coordinates, we also studied variations in the orbital elements. By isolating the orbital elements, the analysis will provide a better understanding of the sensitivities to the geometry of the targets. Figure 5.10 shows the results from varying the

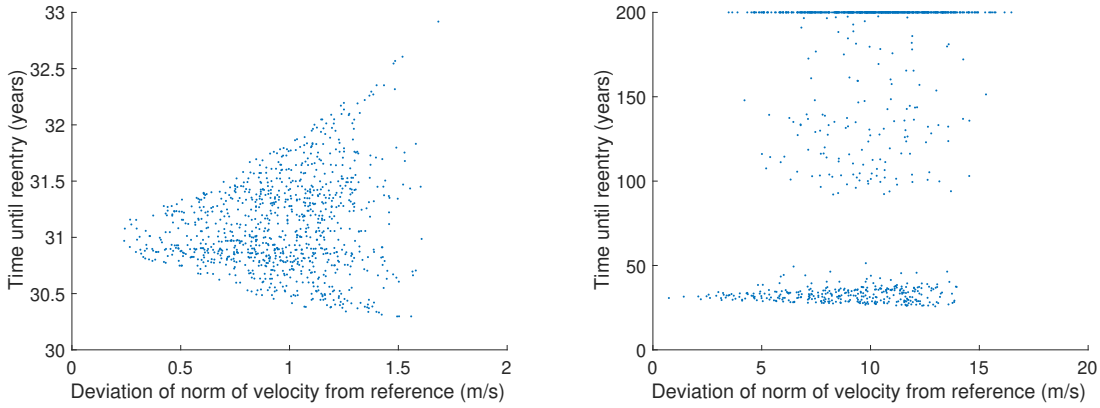

(a) Target velocity varied by 1 m/s. (b) Target velocity varied by 10 m/s

Figure 5.9: 1,000 Monte Carlo runs for target 1

orbital elements. Clear trends can be seen in variation of the orientation of the orbit. Decreasing RAAN and argument of perigee result in longer reentry times. Smaller eccentricities also result in longer reentry times, which fits the larger trends shown in Figure 5.6. Inclination proves to be the most sensitive to variations, requiring a targeting accuracy of less than one degree in inclination. Changes in semi-major axis do not appear to have a large effect on the reentry time.

Other cases taken into consideration were timing and solar radiation pressure. Solar radiation pressure was varied by manipulating the area-to-mass ratio to be plus or minus 100% of the nominal value. This shows whether the solution was robust to deviations from attitude, overall understanding of the effect on the satellite, and any debris shedding events that occur once the satellite reaches the target. Figure 5.11a displays that changes in solar radiation pressure does not have a large effect on time to impact.

Another condition we accounted for was how robust the solution was to the targeting epoch, detailed effects of epoch on chaoticity are in Chapter 4. As Figure 5.11b shows deviations on time scales as large as a year show no meaningful effect on the time until reentry. Thus, the initial positions of the Moon and Sun are not a concern for implementation.

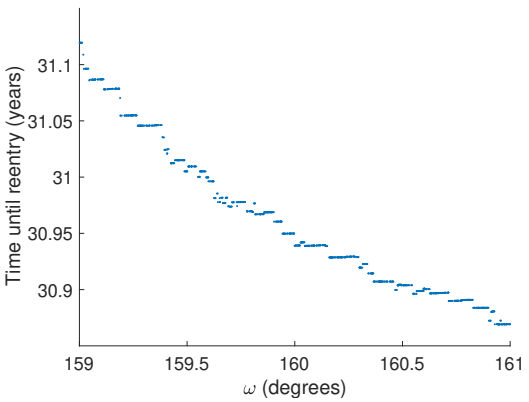

(a) Argument of perigee varied by 1 degree

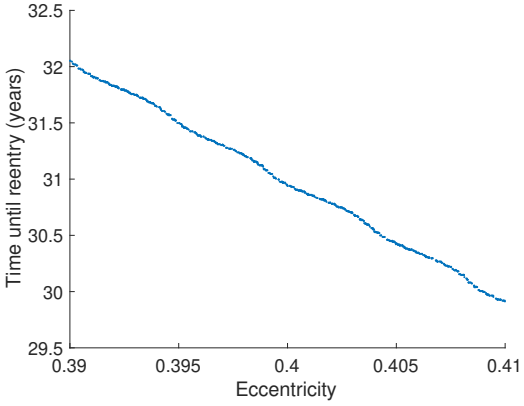

(b) Eccentricity varied by 0.01

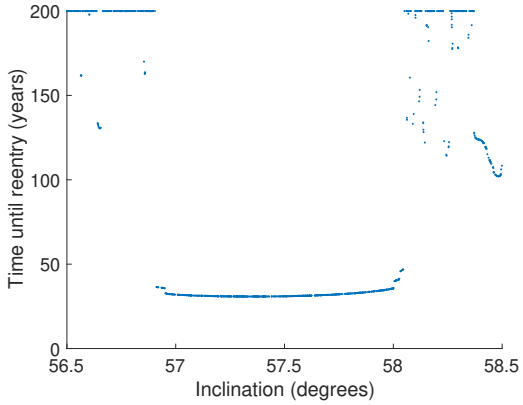

(c) Inclination varied by 1 degree

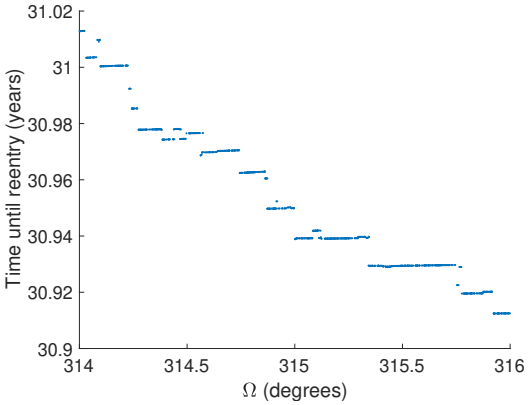

(d) RAAN varied by 1 degree

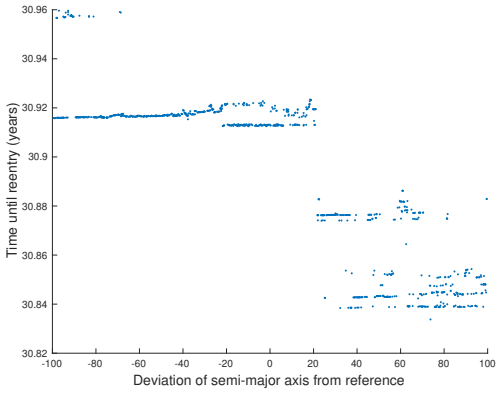

(e) Semi-major axis varied by 100 km

Figure 5.10: 1,000 Monte Carlo runs for target 1

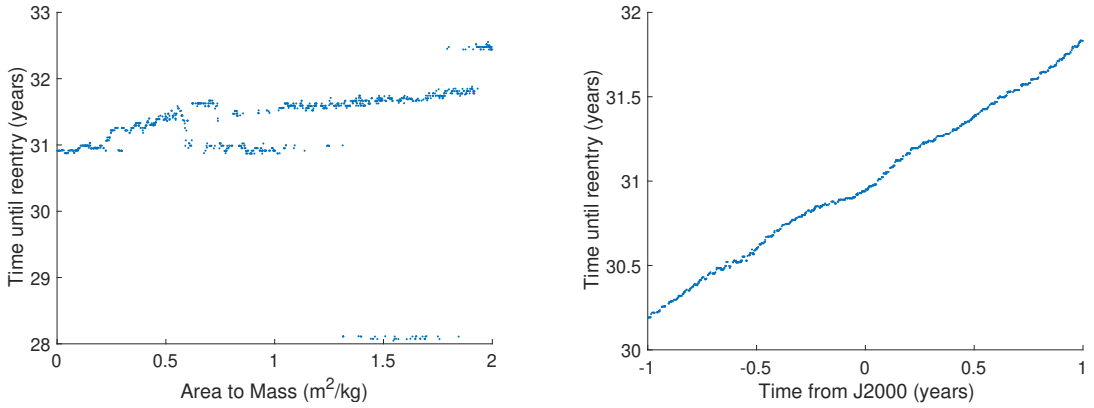

(a) Area-to-mass ratio was varied .001 to 2 m^2/kg for target 1

(b) Target time varied by 1 year for target 1

Figure 5.11: Variations in area-to-mass ratio and epoch

5.3.1.2 GPS Target 2

Target 2 was chosen to be more easily reached. With a lower eccentricity of 0.359, it would not require as much propulsion to change from the original GPS orbital eccentricity, about 0, as target 1's 0.4. The other orbital parameters are in Table 5.1. The eventual impact time of target 2 is approximately 49 years.

Target 2 was shown to be more sensitive than target 1 in Cartesian coordinates. Deviations in position of more than 10 km will result in missing the impacting trajectory as shown in Figure 5.12. Velocity also requires a higher level of precision in target 2 than target 1. Figure 5.13 shows that to guarantee reaching an impacting trajectory the velocity needs to be within 0.1 m/s in each direction of the targeted value.

Target 2 showed different sensitivities than target 1 in the orbital elements. Figure 5.14 shows the variations due to changes in the orbital elements. This region is much closer to non-impacting neighboring regions which can be shown in the inability to drop the inclination or eccentricity much below the target. The argument of perigee and RAAN show similar trends to target 1 over the variations with no significant deviations from the nominal reentry time. Semi-major axis, like in target 1, does not show a trend in the behavior and has a small range of reentry times of months

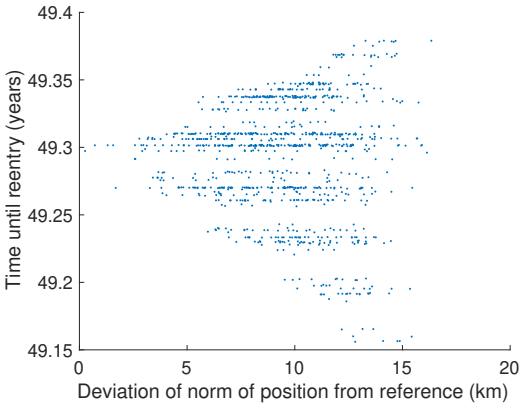

(a) Target position varied by 10 km.

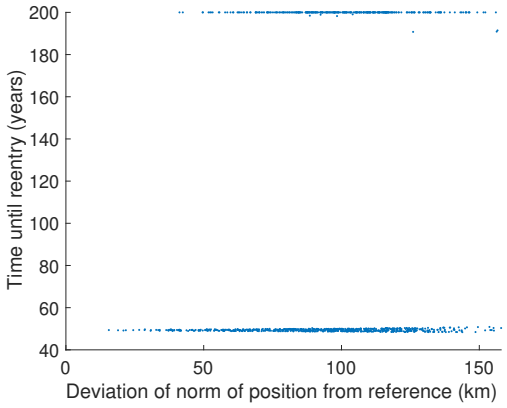

(b) Target position varied by 100 km.

Figure 5.12: 1,000 Monte Carlo runs for target 2

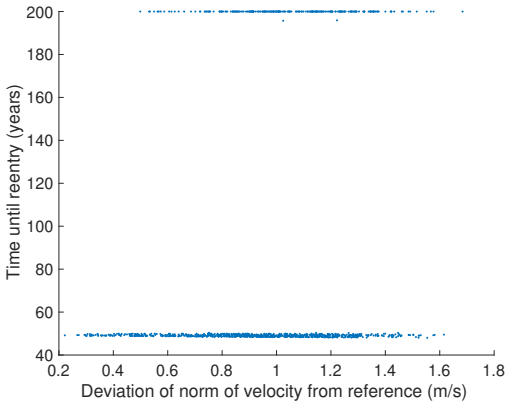

(a) Target velocity varied by 1 m/s.

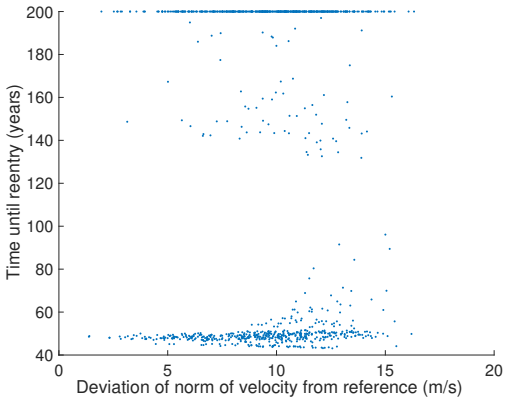

(b) Target velocity varied by 10 m/s

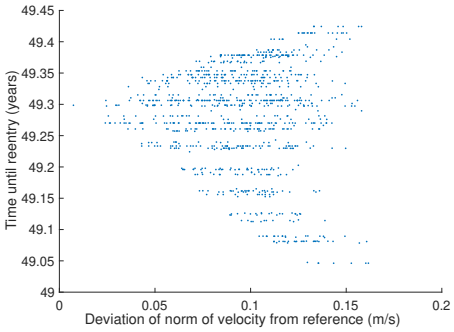

(c) Target velocity varied by 0.1 m/s

Figure 5.13: 1,000 Monte Carlo runs for target 2

for 100 km deviation.

We also analyzed variations in solar radiation pressure and target time for target 2. Solar

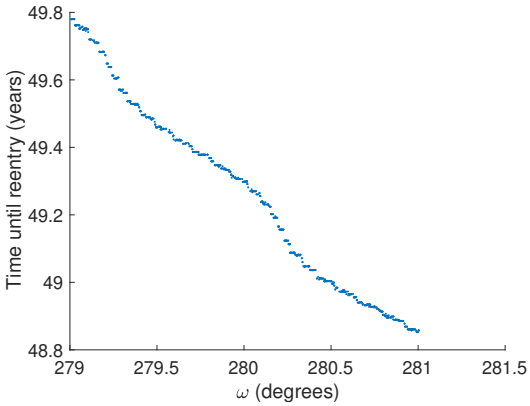

(a) Argument of perigee varied by 1 degree

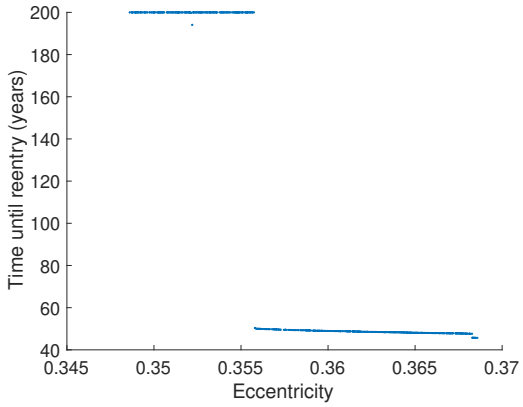

(b) Eccentricity varied by 0.01

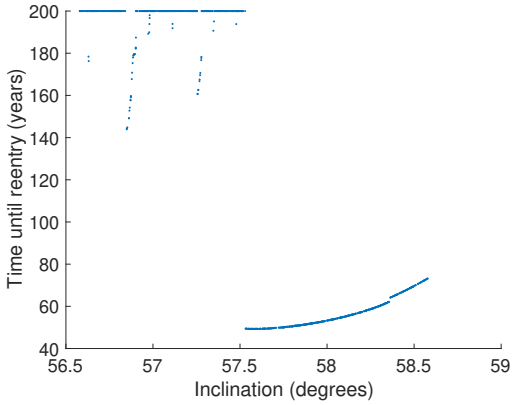

(c) Inclination varied by 1 degree

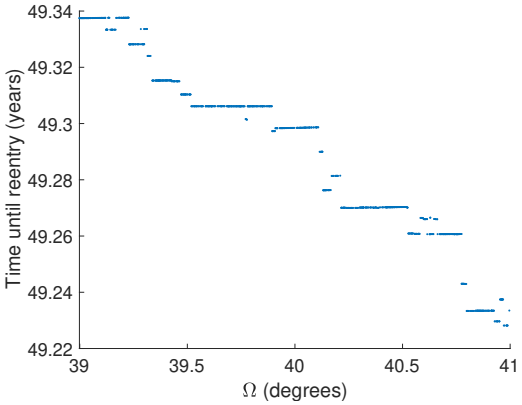

(d) RAAN varied by 1 degree

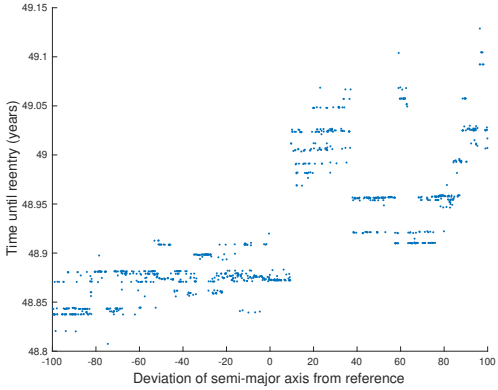

(e) Semi-major axis varied by 10 km

Figure 5.14: 1,000 Monte Carlo runs for target 2

radiation pressure variations show reentry times to be approximately the same as the nominal target (Figure 5.15a). GPS target 2 was the only case where there was a sudden shift between reentering

solutions and non-reentering solutions dependent on area-to-mass ratio. The sudden shift for high area-to-mass ratio objects (>1m^2/kg) could be the result of an interaction between solar radiation pressure and the luni-solar resonance structure discussed in the previous chapter.

Over deviations of a year, there are cases of missing the chaotic region (Figure 5.15b). However, this requirement on time to target is on the order of two months. Thus, time is a factor in achieving chaos in target 2 but can easily be addressed by a robust mission schedule.

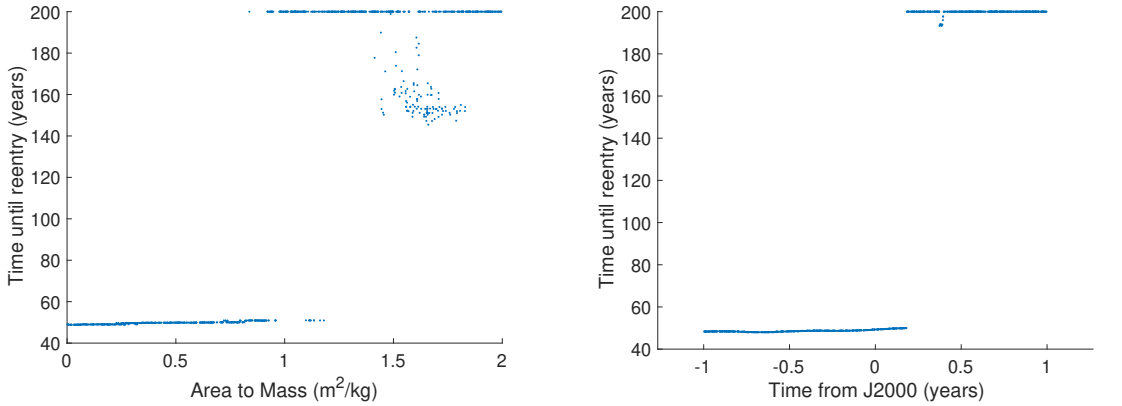

(a) Area-to-mass ratio was varied .001 to 2 m^2/kg for target 2

(b) Target time varied by 1 year for target 2

Figure 5.15: Variations in area-to-mass ratio and epoch

5.3.2 GNSS Comparison

The same process of running 1,000 Monte Carlo runs of varying initial distributions was conducted for the Galileo and GLONASS targets. To be more concise, we do not examine the GLONASS and Galileo results in the same detail so that more target cases can be compared. In this section, instead of showing how every initial condition translated into a final reentry time, we will use two graphs to compare the overall trends of the distribution sets.

The first graph shows how much variation in reentry time results from the same initial condition distribution for each target. For example, in the case of eccentricity, each set of distributions being compared is initialized by a uniform distribution around the target of plus or minus 0.01.

From the same initial sets of distribution, we compare how much the final reentry time varies using a violin plot. The violin plots also plot the mean result which is zero for each of the graphs because each of the plots is normalized about the nominal reentry time in order to compare the different targets; although, the target's nominal reentry times vary from 30 years to 69 years. The thick gray bar represents the interquartile of the distribution and the thin gray bar represents the upper and lower adjacent values.

The second graph shows how much the initial conditions can vary and still result in reentering solutions. As some of the previous figures show, many of the distributions do not reenter for large variations of initial conditions. This graph will use bar plots to show how much variation in initial conditions still results in solutions that reenter. This graph also distinguishes between solutions that reenter within the 200 year simulation and those that reenter within 10% of their nominal reentry time. For GPS, the nominal reentry time for target 1 is about 31 years and target 2 is about 49 years. For GLONASS, targets 1 and 2 are approximately 38 and 69 years, respectively. For Galileo, targets 1 and 2 are about 30 and 38 years, respectively. As with the violin plot, everything is normalized about the nominal reentry time and nominal initial condition.

Cartesian position and velocity variations are discussed first to provide context on overall maneuver execution accuracy requirements. These are followed by individual orbital variations to provide insight into how error geometry affects the resulting reentry time.

5.3.2.1 Position

Large errors in the targeted position still reenter. Figure 5.16 shows the variation of reentry times for a uniform distributions of plus or minus 10 km in each direction.

GLONASS target 2 has the largest variation and is the only one to vary close to 10% of the nominal reentry. There is a bimodal behavior in GLONASS target 2 and a stratification of the reentry times of all of the targets. This settling of specific reentry times is because the trajectory's eccentricity oscillates. Larger oscillations occur on the year timescale as can be seen in the settling of two sets of solutions for the GLONASS target, and smaller oscillations occur closer to a week

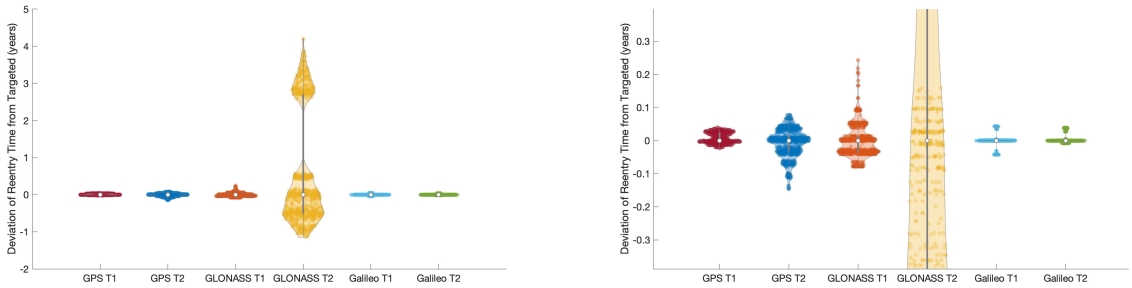

(a) Full range of reentry times

(b) Truncated to $\pm \sim 0.4$ years

Figure 5.16: Violin plots of reentering times of varying targets with the same initial position distribution of $\pm$ 10 km in each direction.

scale as can be seen in the bands of the violin plots. Depending on how close the trajectory is able to follow the target's trajectory, it will settle on or near the target's reenntry time. In contrast, in the case of GLONASS target 2, the trajectory will not be able to achieve the reentry in the vicinity of the target's reentry time and will have to wait for the eccentricity to oscillate back to that higher eccentricity a few years later.

Because all the solutions enter within 10% of the reentry time, the additional analysis of how precise knowledge of position would be required to target these regions is not necessary (they all can be off by ten kilometers in each direction).

5.3.2.2 Velocity

Velocity was also varied in each direction of the vector. Figure 5.17 shows the violin plots for the velocity vector's variation of plus or minus 0.1 m/s in each direction. Due to the large outlier in GLONASS target 2, the results are also truncated in the figure.

GLONASS target 2 has the largest variation due to errors in velocity. GPS target 2 and GLONASS target 1 are the next biggest distributions with GPS target 1 and the Galileo targets all reentering within 0.1 years of the nominal reentry time.

Figure 5.18 shows how many solutions can reenter for large changes in the velocity vector.

Galileo targets 1 and 2 are by far the most robust to errors in velocity knowledge, allowing

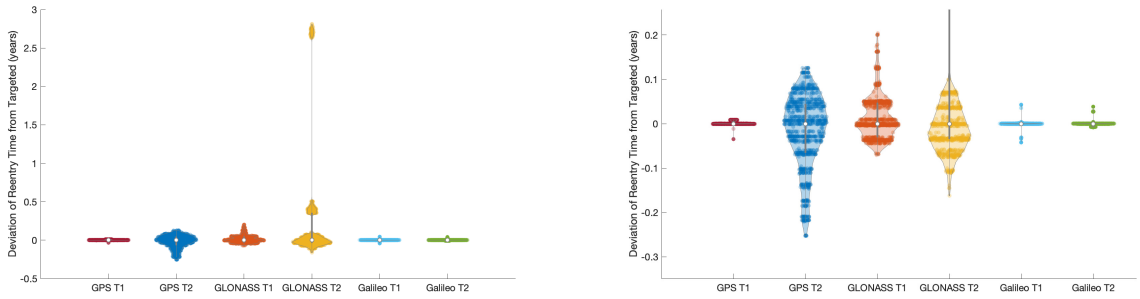

(a) Full range of reentry times

(b) Truncated to $\pm \sim 0.3$ year

Figure 5.17: Violin plots of reentering times of varying targets with the same initial velocity distribution of $\pm$ 0.1 m/s in each direction.

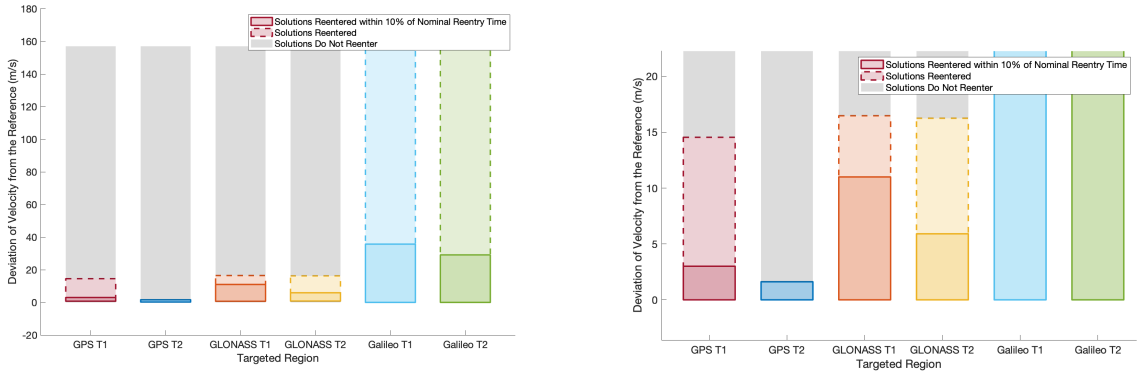

(a) Full range of deviated velocities

(b) Truncated to 25 m/s or less

Figure 5.18: Variation of the magnitude of the velocity vector that result in reentering solutions.

solutions to be off by over 100 m/s and still reenter. These solutions require the deviations to be smaller than 30 m/s to ensure a speedy reentry time. The GLONASS targets are the second most robust to errors in velocity targeting. GPS target 2 has the tightest requirement of all three constellations; it has the largest deviation in the magnitude of the velocity vector, 1.6 m/s.

5.3.2.3 Eccentricity

The first orbital element set compared is the eccentricity variation for each of the targets. Figure 5.19 shows the final reentry distributions for a uniform eccentricity variation of plus or minus 0.01 around the nominal target.

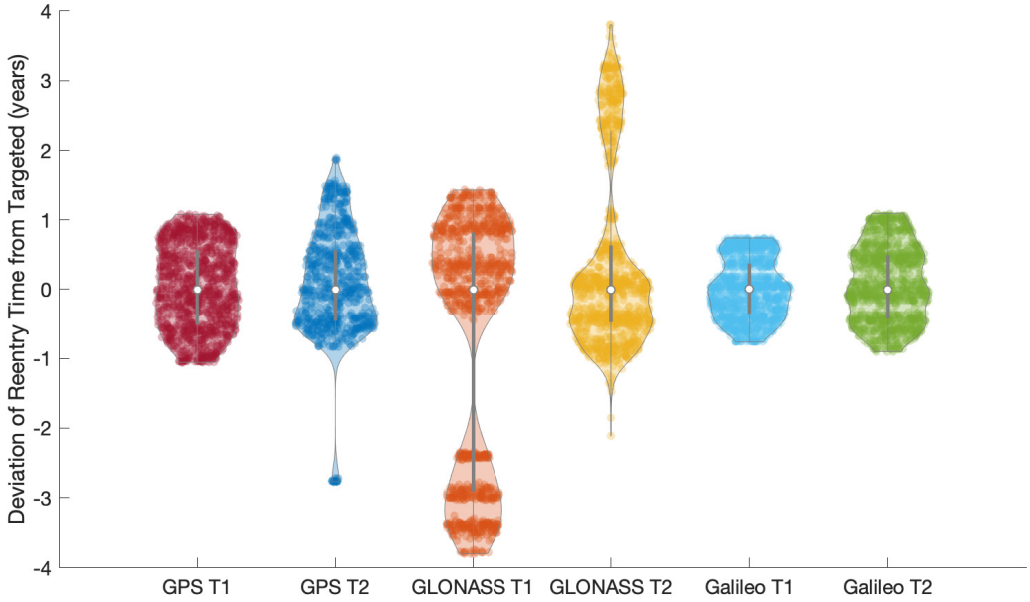

Figure 5.19: Violin plots of reentering times of varying targets with the same initial eccentricity distribution of ±0.01.

GLONASS targets 1 and 2 both have the largest distribution of final reentry times with about 5 and 6 years of variation respectively. They both show bimodal behavior in the reentry time variation. For GPS target 2, there is a small group of outliers from the main set causing the overall distribution to be about 5 years.

Figure 5.20 shows for a maximum change of plus or minus 0.1 in eccentricity which solutions will still reenter and which solutions will reenter within 10% of the nominal reentry time.

GPS target 2 has the tightest requirement of the targets. Solutions with an eccentricity decrease of greater than 0.0073 or an increase greater than .0915 will no longer reenter. GLONASS target 2 will also result in non-reentering solutions when the eccentricity is increased by more than 0.0798. GPS target 1, GLONASS target 1, and Galileo targets 1 and 2 solutions all reenter for eccentricity deviations as large as ±0.1.

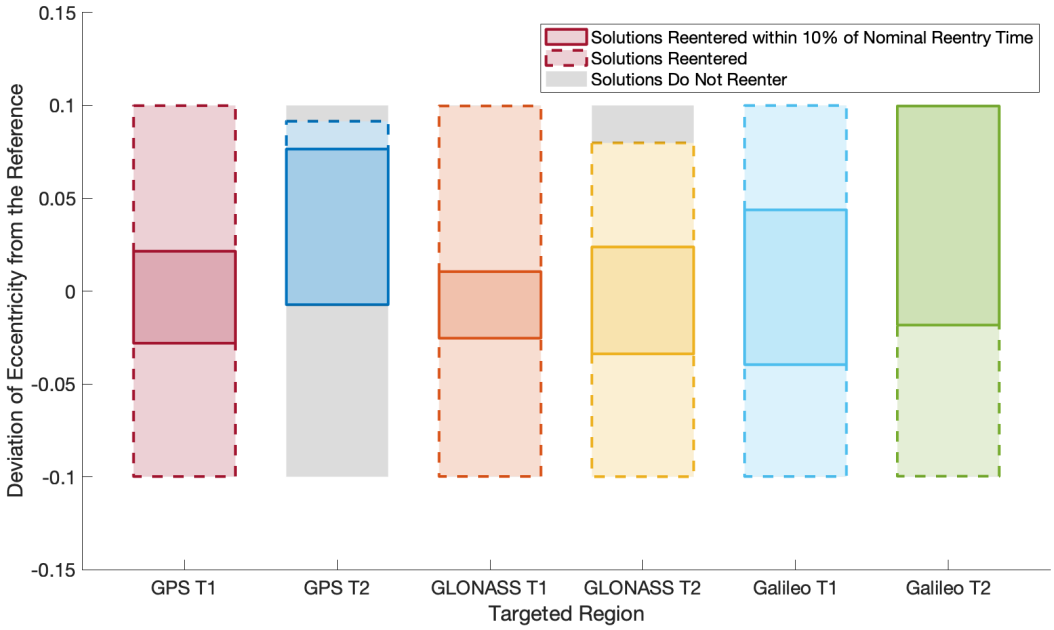

Figure 5.20: Variation of eccentricity with reentering solutions

5.3.2.4 Inclination

The inclination was varied by plus or minus 0.1 degrees from the nominal reentry to achieve the final distributions captured in Figure 5.21. Because the two targets of GLONASS have almost an order of magnitude larger distribution than the others, Figure 5.21 was also truncated to compare the smaller distributions.

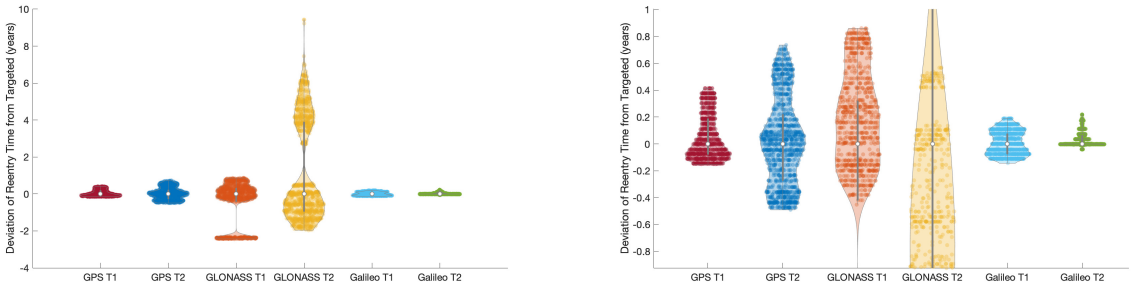

(a) Full range of reentry times

(b) Truncated to ± 1 year

Figure 5.21: Violin plots of reentering times of varying targets with the same initial inclination distribution of ± 0.1 degrees.

The targets for GLONASS have the largest final reentry distribution for the same set of initial inclinations and a bimodal distribution of the reentry times. GLONASS target 1 has a range of 4 years, and target 2 has a range of 12 years. The GPS targets in general have a greater difference in reentry times than the Galileo targets.

Figure 5.22 shows how much the initial inclination can be varied for a maximum of plus or minus 1 degree.

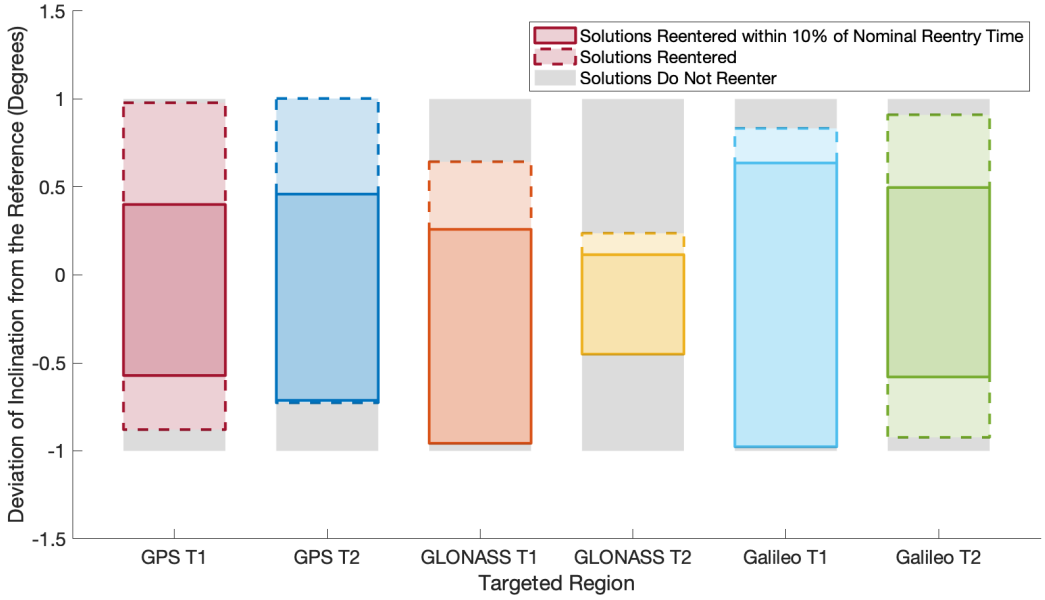

Figure 5.22: Variation of inclination with reentering solutions

None of the targets results entirely in reentering solutions for plus or minus 1 degree. For the GPS targets, decreasing the inclination by too much (more that 0.88 degrees for target 1 and 0.73 degrees for target 2) can result in non-reentering solutions. GLONASS target 1 has to be within +0.64 and −0.96 degrees of the targeted inclination. GLONASS target 2 has the tightest requirement on inclination: for the solution to reenter the inclination has to be within +0.23 and -0.45 degrees. Galileo targets have some flexibility, similar to the GPS targets. Galileo target 1 cannot have an inclination increase more than 0.83 degrees from the target. Galileo target 2 has less strict of a restriction of +0.91 and -0.92 degrees from the nominal target, but target 2 has more

solutions that reenter at later times.

5.3.2.5 Semi-major Axis

Because large variations in semi-major axis still result in reentering solutions close to the nominal reentry time, the only plots discussed are the violin plots which compare the variation of reentry times for a semi-major axis deviation of plus or minus 100 km, Figure 5.23.

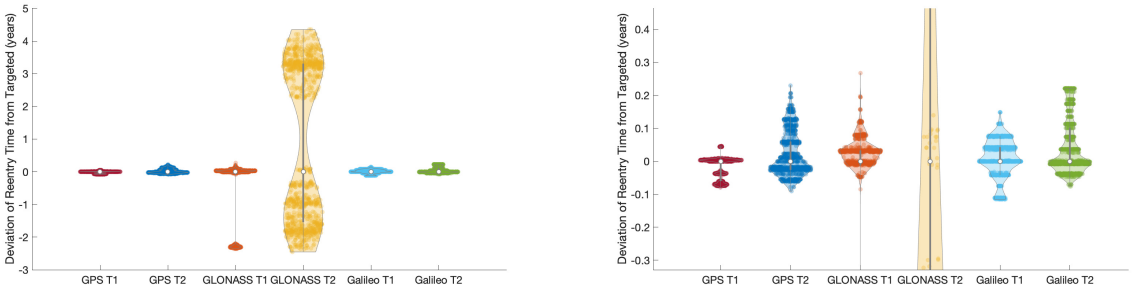

(a) Full range of reentry times

(b) Truncated to $\pm \sim 0.4$ years

Figure 5.23: Violin plots of reentering times of varying targets with the same initial semi-major axis distribution of $\pm$ 100km.

The GLONASS targets have substantially longer reentry times than the other targets. However, these reentry variations are within 10% of their nominal reentry times, 38 and 70 years. The rest of the targets reenter within a year of their nominal reentry time.

5.3.2.6 Right Ascension of the Ascending Node

For RAAN, the initial conditions were all varied by plus or minus 1 degree of the nominal value. GLONASS target 2 has an order of magnitude larger distribution than the rest of the targets, so there is a truncated version of the violin plot in addition to the full one in Figure 5.24.

All of the reentry times are close to their nominal reentry time with the large change in RAAN. The GPS targets are closest to their nominal reentry times out of all the targets. GLONASS target 2 has the largest deviation with reentry time as long as 4 years after the nominal targeted reentry time.

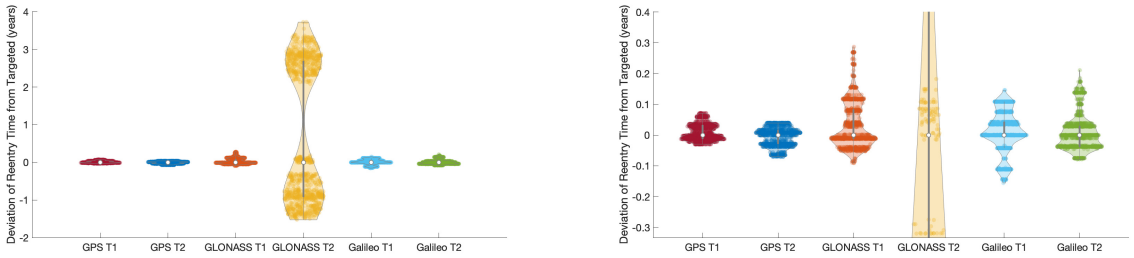

(a) Full range of reentry times

(b) Truncated to ± 0.4 year

Figure 5.24: Violin plots of reentering times of varying targets with the same initial RAAN distribution of ± 1 degree.

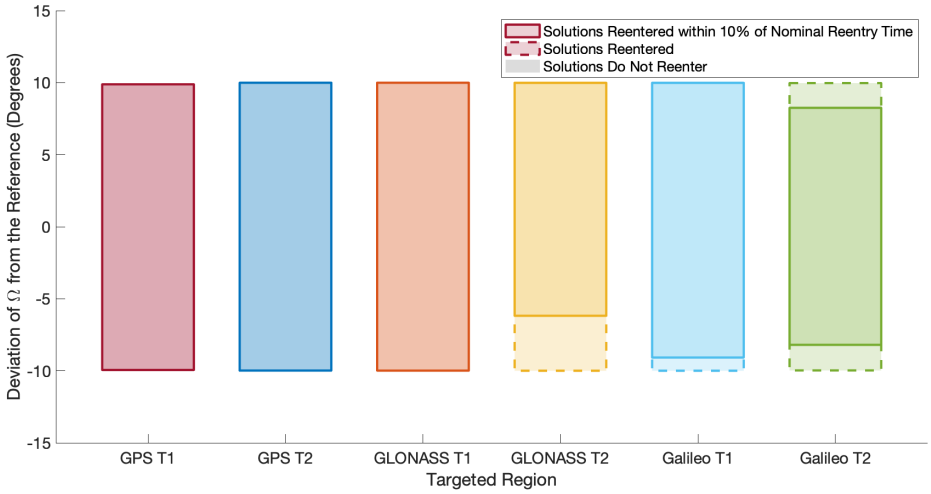

Figure 5.25: Variation of RAAN with reentering solutions

Figure 5.25 shows for a maximum deviation of 10 degrees in RAAN how many of the solutions reenter. For every target, all of the solutions reenter with deviations up to plus or minus 10 degrees. For GLONASS target 2, the reentry time is longer than 10% of the nominal for a RAAN decrease of more than 6.18 degrees. For Galileo target 1, a decrease of 9.1 degrees or more will cause a change greater than 10% of the nominal reentry time. For Galileo target 2, a RAAN deviation of plus or minus 8.5 degrees will cause solutions to reenter more than 10% of the nominal reentry time.

5.3.2.7 Argument of Perigee

The argument of perigee initial conditions were varied in Figure 5.26 by a distribution between plus or minus 1 degree. Some of the distributions were on an order of magnitude larger than the others so the graph is also truncated.

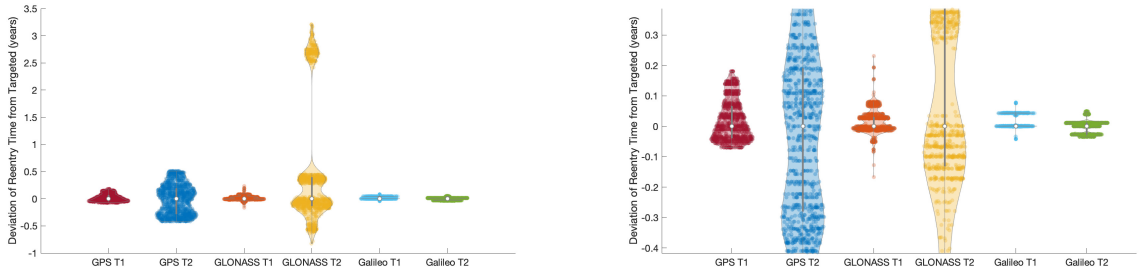

(a) Full range of reentry times

(b) Truncated to $\pm \sim 0.4$ year

Figure 5.26: Violin plots of reentering times of varying targets with the same initial argument of perigee distribution of $\pm$ 1 degree.

GLONASS target 2 shows the highest range in reentry times for the fluctuation in argument of perigee followed by the GPS targets. The targets for Galileo show the smallest range in reentry times of all the sets.

Figure 5.27 shows how solutions reenter up to a maximum of plus or minus 10 degrees in argument of perigee. GPS Target 2 is the only target which has solutions that do not reenter; this occurs with a decrease of more than 8.5 degrees. GLONASS target 2 also shows some sensitivity with some results entering beyond the 10% of the nominal reentry time.

5.3.2.8 Epoch

To see how initial epoch affected the solution and how important timing is to targeting, we varied the starting time of the simulations.

Figure 5.28 shows that GLONASS target 2 results in the greatest distribution in final reentry times for a change of up to one month in the targeted disposal time. The remaining targets have reentry times within a year of their nominal with the exception of the outlier group in GLONASS

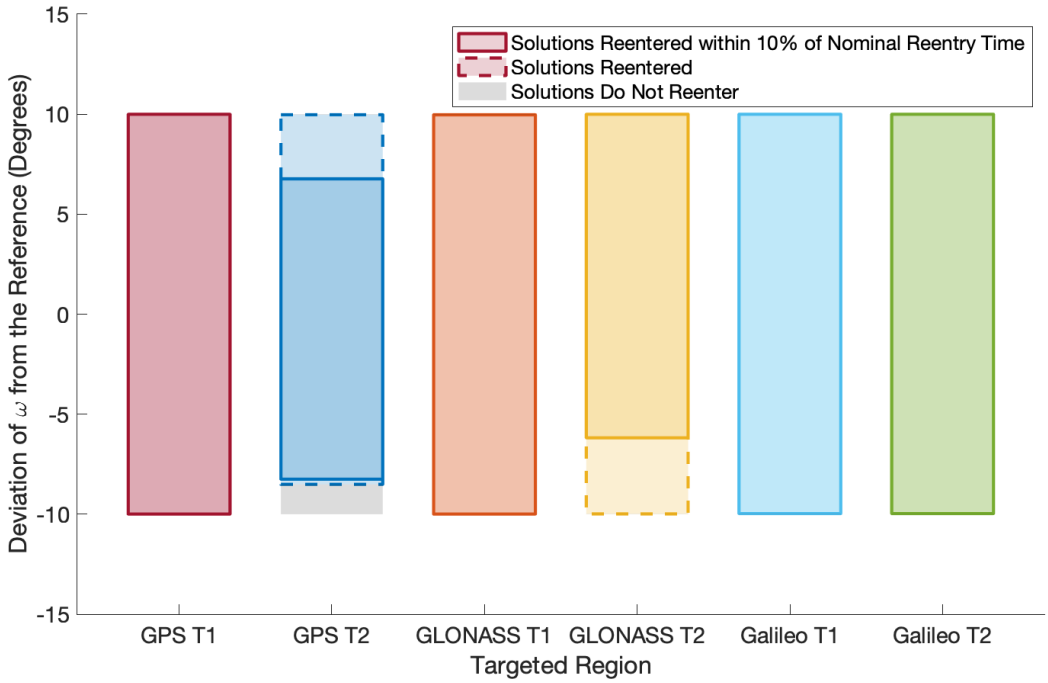

Figure 5.27: Variation of ω with reentering solutions

target 1.

Figure 5.29 shows which solutions will still reenter based on failing to target the reentry at the appropriate time with a maximum change of plus or minus one year.

GPS target 2 has the tightest cut off which was discussed in the previous section. GLONASS target 2 is the only other target to have solutions that do not reenter if the epoch is less than a year off. However, GLONASS target 2 will only not reenter if the mission targets the region too early. It does have flexibility in delaying targeting.

5.4 Discussion

In all three GNSSs discussed, the closer target to the nominal orbit (target 2) required tighter uncertainty knowledge to achieve the planned reentry trajectory than the farther but more robust target (target 1) required. Therefore, there is a trade between moving farther in eccentricity and inclination space and accuracy needed to achieve Earth reentry. For example, between the two GPS

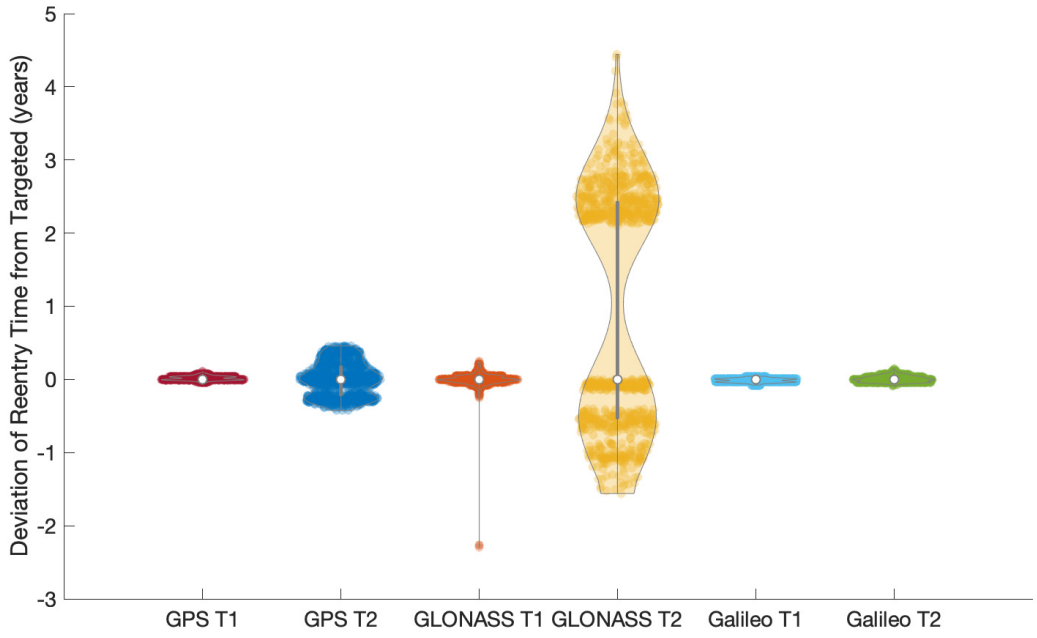

Figure 5.28: Violin plots of reentering times of varying targets with the same initial epoch distribution of ± one month.

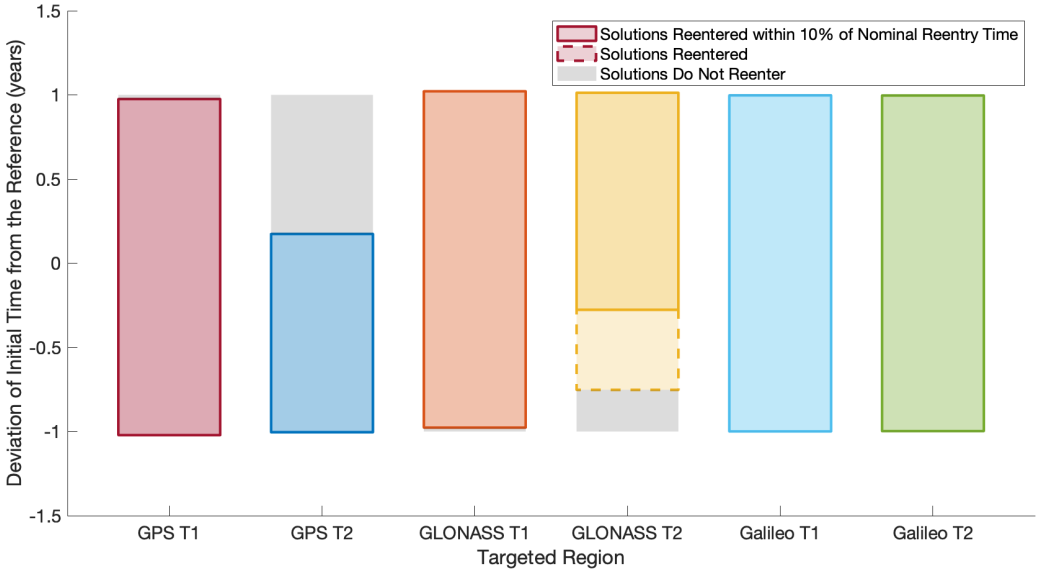

Figure 5.29: Variation of initial epoch with reentering solutions

cases, target 1 could be missed by 1 m/s in each direction whereas target 2 requires an accuracy

of 0.1 m/s in each direction. At the same time, maneuvering to the farther eccentricity, 0.400 for target 1 versus 0.359 for target 2, requires about 79.5 m/s greater change in velocity. Similarly, to reach target 1 would require a sail size 12% larger than that of target 2 [72, 71]. These trends are also true for GLONASS's and Galileo's targets as both target 1s are at higher eccentricities but have more robust behavior to changes in initial conditions.

In addition to understanding the trade off due to farther eccentricities between targets 1 and 2, we also analyze the differences in targeting inclination in GLONASS's targets. This is because for GLONASS, the re-impacting trajectories are far in inclination space from the nominal orbit. Figure 5.5 illustrates how far the inclination range is from the nominal orbit. GLONASS target 2, the closer target to its nominal orbit, had the largest variation of reentry trajectory times of all the targets and tighter constraints than those of GLONASS target 1, the farther target. Figure 5.6 shows that the target closer in inclination space to the nominal orbit is neighbored by more non reentering trajectories than the other five targets. Maneuvering to the farther inclination, 6.9° away from the nominal orbit for target 1 versus 5.5° away for target 2, requires 96.6 m/s larger change in velocity than maneuvering to the closer target. Because eccentricity change is the main driver in needing to increase solar sail area size, the inclination deltas only cause a 0.4% increase in sail size.

5.5 Conclusion

Through our analysis, we have found that it can be feasible to target regions of unstable dynamics for debris mitigation through Earth reentry over decadal time spans. All of the solutions are robust enough to achieve reentry through a chemical burn to the target. For solar sailing, where it might not be feasible to achieve the required level of accuracy to reenter on a closer trajectory, it would be more beneficial to reach a slightly farther target in eccentricity and inclination space where the trajectory is surrounded by impacting neighbors. For the case of Galileo, satellites do not need large changes in eccentricity and inclination for a fast atmospheric reentry trajectory. Most of the constellation targets reenter within a year for small variations in the target variables. The

exception is GLONASS target 2 which had the widest swaths of reentry times but still achieved reentries for small fluctuations. This demonstrates that small uncertainties will not magnify despite these trajectories being in a chaotic regime. This insight is especially important when determining whether unstable reimpacting trajectories can be a feasible debris mitigation method for satellites in this region.

Chapter 6

Research Goal 4 - Utilizing Solar Radiation Pressure

In this chapter, we explore how to use solar radiation pressure for debris mitigation. Satellite orbiters subject to solar radiation pressure (SRP) will have periodic variations in eccentricity and inclination that could be utilized for mission design purposes. These periodic variations have been described before, but have not been applied to mission design purposes for solar sails in Earth orbit [89]. Current development of sail technology makes it feasible to deploy a sail from a satellite in an initially circular orbit and then jettison it later [81][33]. Applications of this can be developed for orbit design and transfer to higher eccentric orbits, satellite deorbit, or plane changes. This chapter seeks to utilize sailing to conduct an orbit change by deploying a sail, reaching the desired eccentricity and inclination change, and finally releasing the sail after the desired orbit is achieved.

We will particularly focus on leveraging averaged solutions to satellites subject to strong SRP forces to take advantage of the secular effects in Earth's orbit. Our focus, however, will be on the more simplistically described cannonball model. Concepts for spherical solar sails have been described as early as 1958 by Ehrike [25] and as recently as 2013 by Lücking et al. [56], and would be particularly attractive to use for the deorbit of defunct satellites or debris, one of the applications discussed later in this chapter. Alessi et al. discussed using the design of the spherical sail as possible disposal methods for GNSS satellites [9].

This research goal is built off the orthonormal matrix defined in Equation 2.15 which we use to demonstrate how the control of the maximum plane change or eccentricity change can be realized just by the choice of sun-relative node when the sail is furled. First, we maximize the

eccentricity change due to the node choice. This exemplifies the direct reentry case. We then describe a targeting algorithm to target a specific eccentricity and a change in inclination. This algorithm can leverage the sun node line again to achieve the maximum change in both for a given SRP parameter. This case depicts targeting a specified orbit.

6.1 Maximizing Eccentricity in an Initially Circular Orbit

In this study the satellite is assumed to initially lie on a circular orbit. This simplifies the analysis and fits with the orbits of the vast majority of Earth-orbiting satellites.

6.1.1 Initially Circular Orbits

Because we assume the initial satellite orbits are circular and study sail dynamics once deployed in a circular orbit, $\boldsymbol{e_0}$ is zero and $\hat{\boldsymbol{h}}_{\boldsymbol{0}}$ is a unit vector initially, simplifying the dynamics. Substituting these initial conditions into Equation 2.14 yields Equations 6.1 and 6.2.

$$\boldsymbol{e} = \Phi_{eh}\hat{\boldsymbol{h}_{\boldsymbol{0}}} \tag{6.1}$$

$$\boldsymbol{h} = \Phi_{hh}\hat{\boldsymbol{h}_{\boldsymbol{0}}} \tag{6.2}$$

where

$$\begin{aligned}\Phi_{eh} = \quad = \quad & \big(1-\cos(\psi)\big) \times \Big[\; -\sin\Lambda\cos\Lambda\left(\hat{\boldsymbol{z}}\hat{\boldsymbol{d}} + \hat{\boldsymbol{d}}\hat{\boldsymbol{z}}\right) \; \Big] \\ & + \sin(\psi) \Big[\; \sin\Lambda\tilde{\hat{\boldsymbol{d}}} \; \Big]\end{aligned} \tag{6.3}$$

$$\Phi_{hh} = \cos(\psi)I_{3x3} + (1-\cos(\psi)[\cos^2\Lambda\hat{\boldsymbol{z}}\hat{\boldsymbol{z}} + \sin^2\Lambda\hat{\boldsymbol{d}}\hat{\boldsymbol{d}}] - \sin\psi\cos\Lambda\tilde{\hat{\boldsymbol{z}}} \tag{6.4}$$

To study the dynamics, we focus on eccentricity and inclination. As a reminder, these vectors are not in the Earth Centered Inertial (ECI) frame but instead are given relative to the

frame rotating with the Sun line, so a subscript of *rot* will be used to distinguish orbital parameters typically defined by the Earth centered frame.

Eccentricity is defined by Equation 6.5.

$$e^2 = \hat{\boldsymbol{h_0}} \cdot A \cdot \hat{\boldsymbol{h_0}} \tag{6.5}$$

where we define matrix A as Equation 6.6.

$$A = \Phi_{eh}\Phi_{eh} = \sin^2\Lambda\,(1-\cos\psi)^2 \begin{bmatrix} \cos^2\Lambda & -\cos\Lambda\cot(\psi/2) & 0 \\ -\cos\Lambda\cot(\psi/2) & \cot^2(\psi/2) & 0 \\ 0 & 0 & \cot^2(\psi/2)+\cos^2\Lambda \end{bmatrix} \tag{6.6}$$

Inclination is defined by Equation 6.7.

$$\cos i_{rot} = \frac{\boldsymbol{h}\cdot\hat{\boldsymbol{k}}}{|\boldsymbol{h}|} = \frac{\hat{\boldsymbol{k}}\cdot\Phi_{hh}\cdot\hat{\boldsymbol{h}}_{\boldsymbol{0}}}{\sqrt{1-e^2}} \tag{6.7}$$

which yields Equation 6.8.

$$\cos i_{rot} = \frac{1}{\sqrt{1-e^2}}[\cos^2\Lambda + \cos\psi\sin^2\Lambda]\cos i_{rot0} \tag{6.8}$$

Given the form of the orbit eccentricity, we can now study it in detail, in particular finding its maximum value and defining the initial conditions that will achieve it.

6.1.2 Eigenvalues and Eigenvectors of A

In order to determine the maximum eccentricity we solve for the eigenvalues and eigenvectors of the matrix in Equation 6.6. This matrix's eigenvalues and eigenvectors will describe its fundamental properties which we will later tie to the maximum eccentricity that can be achieved for a certain size sail.

6.1.2.1 Eigenvalues of A

The eigenvalues are solved from the relationship in Equation 6.9.

$$|\lambda \mathrm{I}_{3x3} - A| = 0 \tag{6.9}$$

Because of the structure of A when solving for the determinant, the condition decouples as Equation 6.10.

$$|\lambda \mathrm{I}_{3x3} - A| = \begin{vmatrix} \lambda \mathrm{I}_{2x2} - A' & 0_{1x2} \\ 0_{2x1} & \lambda - \sin^2\Lambda(1-\cos\psi)^2(\cot^2(\psi/2)+\cos^2\Lambda) \end{vmatrix} = 0 \tag{6.10}$$

leading to Equation 6.11

$$|\lambda \mathrm{I}_{2x2} - A'| \cdot |\lambda - \sin^2\Lambda(1-\cos\psi)^2(\cot^2(\psi/2)+\cos^2\Lambda)| = 0 \tag{6.11}$$

This simplification allows us to break up the 3x3 matrix and easily find the first eigenvalue, equal to $\sin^2\Lambda(1-\cos\psi)^2(\cot^2(\psi/2)+\cos^2\Lambda)$. To find the other two eigenvalues, the first part of Equation 6.11 is expanded where A' is expressed as Equation 6.12.

$$A' = \sin^2\Lambda\,(1-\cos\psi)^2 \begin{bmatrix} \cos^2\Lambda & -\cos\Lambda\cot(\psi/2) \\ -\cos\Lambda\cot(\psi/2) & \cot^2(\psi/2) \end{bmatrix} \tag{6.12}$$

leading to Equation 6.13.

$$\lambda^2 - \lambda\big[\sin^2\Lambda(1-\cos\psi)^2\big]\big[\cos^2\Lambda + \cot^2(\psi/2)\big] = 0 \tag{6.13}$$

We see that $\lambda = 0$ is an eigenvalue and the other eigenvalue is equal to the initial one found, meaning that there is a double eigenvalue equal to

$$\lambda = 4\sin^2(\psi/2)\sin^2\Lambda(1-\sin^2(\psi/2)\sin^2\Lambda) \tag{6.14}$$

We note that the double eigenvalue is always positive, and thus the matrix A is a positive semi-definite matrix.

6.1.2.2 Eigenvectors of A

To solve for the eigenvectors, we use the relationship in Equation 6.15.

$$A \cdot \boldsymbol{v} = \lambda \boldsymbol{v} \tag{6.15}$$

For $\lambda = 0$, Equation 6.16

$$A \cdot \boldsymbol{v} = 0 \tag{6.16}$$

This gives Equation 6.17.

$$\begin{aligned} 0 = &\quad \cos^2\Lambda v_i - \cos\Lambda\cot(\psi/2)v_j \\ 0 = &\quad \cos\Lambda\cot(\psi/2)v_i + \cot^2(\psi/2)v_j \\ 0 = &\quad (\cot^2(\psi/2) + \cos^2\Lambda)v_k \end{aligned} \tag{6.17}$$

We see that $v_k = 0$, the eigenvector will follow the form $[v_i \quad v_j \quad 0]^T$ thus v_i is defined by Equation 6.18

$$v_i = \frac{\cot(\psi/2)}{\cos\Lambda}\frac{\cot(\psi/2) + \cos\Lambda}{\cos\Lambda}v_j \tag{6.18}$$

In a more simplified readable form, the unit magnitude eigenvector for $\lambda = 0$ is defined by Equation 6.19.

$$\frac{1}{\sqrt{1 - \sin^2(\psi/2)\sin^2\Lambda}}\begin{bmatrix} \cos(\psi/2) \\ \sin(\psi/2)\cos\Lambda \\ 0 \end{bmatrix} \tag{6.19}$$

Using a similar analysis for the double eigenvalues, $\lambda = 4\sin^2(\psi/2)\sin^2\Lambda(1 - \sin^2(\psi/2)\sin^2\Lambda)$, we find the eigenvectors, Equations 6.20.

$$\begin{bmatrix} 0 \\ 0 \\ 1 \end{bmatrix} \quad , \quad \frac{1}{\sqrt{1 - \sin^2(\psi/2)\sin^2\Lambda}}\begin{bmatrix} -\sin(\psi/2)\cos\Lambda \\ \cos(\psi/2) \\ 0 \end{bmatrix} \tag{6.20}$$

and note that all of the eigenvectors are mutually orthogonal, as expected for a symmetric matrix. The matrix of eigenvectors is defined by Equation 6.21.

$$T = \frac{1}{\sqrt{1-\sin^2(\psi/2)\sin^2\Lambda}} \begin{bmatrix} 0 & -\sin(\psi/2)\cos\Lambda & \cos(\psi/2) \\ 0 & \cos(\psi/2) & \sin(\psi/2)\cos\Lambda \\ \sqrt{1-\sin^2(\psi/2)\sin^2\Lambda} & 0 & 0 \end{bmatrix} \tag{6.21}$$

Then from the property of positive semi-definite matrices we have Equation 6.22.

$$A = T \begin{bmatrix} \lambda(\psi,\Lambda) & 0 & 0 \\ 0 & \lambda(\psi,\Lambda) & 0 \\ 0 & 0 & 0 \end{bmatrix} T^T \tag{6.22}$$

where $\lambda(\psi,\Lambda) = 4\sin^2(\psi/2)\sin^2\Lambda - 4\sin^4(\psi/2)\sin^4\Lambda$.

6.1.2.3 Relationship between e and λ

The evolution of eccentricity in Equation 6.5 is nicely decoupled with the initial conditions captured with the angular momentum unit vector and the time evolution for a given angle Λ defined by the matrix A. As such, we can study the totality of the time variation results by analyzing A, and, in particular, by breaking this matrix down into its component eigenvalues and eigenvectors.

When first defining A in Equation 6.5, we note that it maps to eccentricity using the initial angular momentum. To separate that relationship, we develop a new angular momentum, $\hat{\boldsymbol{h}}' = T^T\hat{\boldsymbol{h}}_{\mathbf{0}}$, which exists in the eigen space, where T is defined in Equation 6.21 and leading to Equation 6.23

$$e^2 = \hat{\boldsymbol{h}}' \begin{bmatrix} \lambda & 0 & 0 \\ 0 & \lambda & 0 \\ 0 & 0 & 0 \end{bmatrix} \hat{\boldsymbol{h}}' \tag{6.23}$$

or Equation 6.24.

$$e^2 = \lambda(\hat{h}_i'^2 + \hat{h}_j'^2) = \lambda(1 - \hat{h}_k'^2) \tag{6.24}$$

We note that at any time the maximum value that the eccentricity can take on is equal to $\sqrt{\lambda}$. Thus, the maximum eccentricity attainable is proportional to the maximum value of the eigenvector over one period of motion when it occurs simultaneously with $h_k' = 0$. We note that λ will have a maximum value over each SRP cycle, and that if we want e to take on that maximum value, we must choose the initial conditions such that $h_k' = 0$ when $\lambda = \lambda_{max}$. First, we will delve into what λ_{max} is. Then we will utilize the eigenvector's relationship to determine where to deploy the satellite.

6.1.3 Finding λ_{max}

Due to the fact that ψ is the variable that changes along Earth's orbit, ψ determines the evolution of the eccentricity while Λ is fixed. To solve for the relative extrema, the partial derivative is taken with respect to ψ and set to zero, Equation 6.25.

$$\frac{\partial \lambda}{\partial \psi} = 0 = \sin(\psi/2)\cos(\psi/2)\sin^2\Lambda[1 - 2\sin^2(\psi/2)\sin^2\Lambda] \tag{6.25}$$

This leads to the points of interest at Equation 6.26.

$$\psi = 0, \pi, \text{ and } \sin(\psi^*/2) = \pm\frac{1}{\sqrt{2}\sin\Lambda} \tag{6.26}$$

where we note that $\sin(\psi/2) = \pm\frac{1}{\sqrt{2}\sin\Lambda}$ is only defined for $\Lambda > \pi/4$.

Evaluating the second derivative at $\psi = 0$ gives $\frac{1}{2}$ which is positive and thus indicates a minimum. The second derivative at $\psi = \pi$ is $\sin^2\Lambda - 1/2$ and thus is dependent on Λ whether it is a minimum or maximum. For $\Lambda < \pi/4$, $\psi = \pi$ is a local maximum and for $\Lambda > \pi/4$, $\psi = \pi$ is a local minimum. Likewise, at $\sin(\psi/2) = \pm\frac{1}{\sqrt{2}\sin\Lambda}$ the second derivative is also a function of Λ, $-\frac{\sin\Lambda}{\sqrt{2}}\left(1 - \frac{1}{2\sin^2\Lambda}\right)^{3/2}$. In this case, it is negative for $\Lambda > \pi/4$ indicating that $\sin(\psi/2) = \pm\frac{1}{\sqrt{2}\sin\Lambda}$ is a maximum for $\Lambda > \pi/4$. Therefore, we have two local maximums depending on the value of Λ.

For $\Lambda < \pi/4$, these values correspond to Equations, 6.27, 6.28, and 6.29.

$$\psi^* = \pi \tag{6.27}$$

$$\lambda_{max} = \sin^2(2\Lambda) \tag{6.28}$$

$$e_{max} = \sin(2\Lambda) \tag{6.29}$$

For $\Lambda \geq \pi/4$, these values correspond to Equations, 6.30, 6.31, and 6.32.

$$\sin(\psi^*/2) = \frac{1}{\sqrt{2}\sin\Lambda} \tag{6.30}$$

$$\lambda_{max} = 1 \tag{6.31}$$

$$e_{max} = 1 \tag{6.32}$$

In Figure 6.1 we show a contour plot of the value of λ as a function of ψ and Λ. We note that for all $\Lambda > \pi/4$ the maximum value of eccentricity is unity, but that the maximum value appears at different values of ψ. Figure 6.2 plots the eigenvalue, $\lambda = 4\sin^2(\psi/2)\sin^2\Lambda(1 - \sin^2(\psi/2)\sin^2\Lambda)$, showing its behavior as a function of ψ for a few different values of Λ.

We note that at $\psi = 0$, $\lambda = 0$ and thus is at a minimum. For $\psi = \pi$, $\lambda = 4\sin^2\Lambda\cos^2\Lambda$ there are two cases; $\Lambda \geq \pi/4$, it is a local minimum, but for $\Lambda < \pi/4$, it is at a local maximum. This maximum is consistent with results presented in Scheeres's work [94].

6.1.4 Utilizing Eigenvectors to Denote the Location for Maximal Eccentricity Change.

Figures 6.1 and 6.2 show how the eccentricity's evolution is dependent on two parameters: Λ, how strong of an effect SRP has on the object; and ψ, which measures the change in Earth true anomaly from the location where the sail is unfurled. We have developed an expression of what the eccentricity maximizes to, but now we will show when to deploy the sail to achieve that

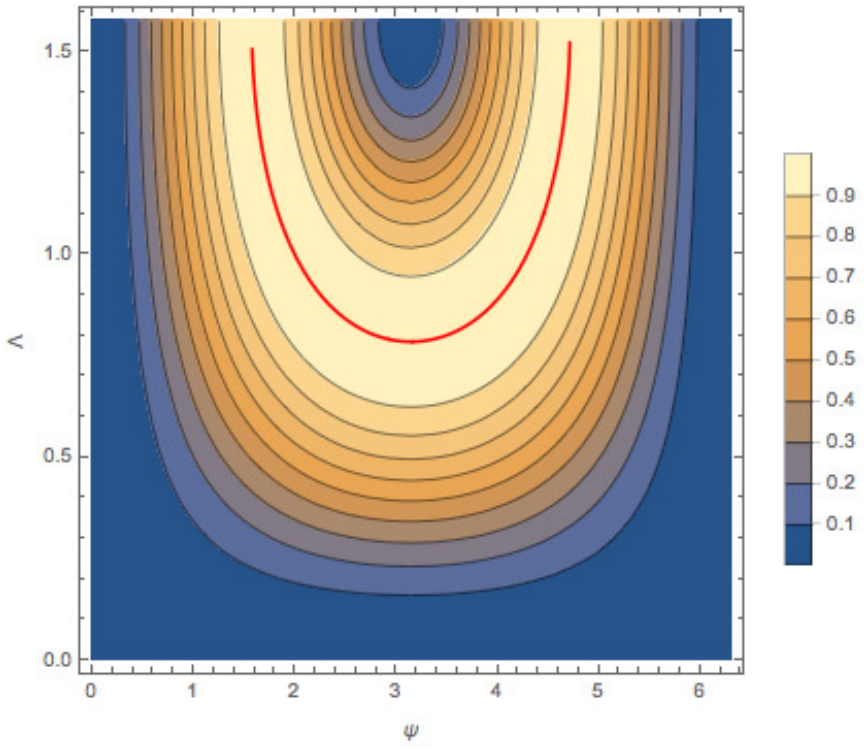

Figure 6.1: Contour Plot of eigenvalues with respective ψ and Λ. The red line indicates where λ maximizes to 1.

maximum. In particular taking ψ^* and relating it to the angular momentum of the satellite utilizing the eigenvectors.

As stated earlier e_{max} reaches λ_{max} when $\hat{h}'_k$ is 0 in the eigenspace frame. The initial angular momentum that will achieve this maximum is defined as the angular momentum that lies in the 2-D plane defined by the two non-zero eigenvectors at the time when the maximum eccentricity appears. We note that any initial angular momentum vector that leads to components off of this 2-D plane at ψ^* will yield a smaller eccentricity by mixing the components with the zero eigenvalue eigenvector.

The k direction of the eigenspace angular momentum, $\hat{h}'_k$, can be described in the Sun line rotating frame by Equation 6.33.

$$\hat{h}'_k = \begin{bmatrix} 0 & 0 & 1 \end{bmatrix} T^T \cdot \hat{\boldsymbol{h}}_0 \tag{6.33}$$

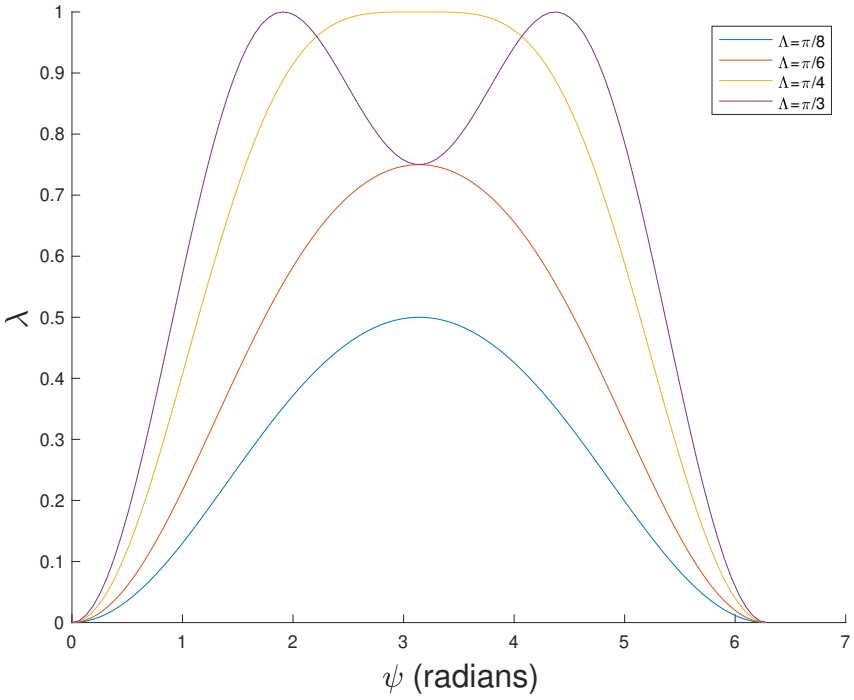

Figure 6.2: How eigenvalues vary with respect to ψ for 3 different cases: 2 of $\Lambda < \pi/4$, $\Lambda > \pi/4$, and $\Lambda = \pi/4$

Because we are particularly interested in when the maximum occurs, when $\psi = \psi^*$, the T matrix is solved separately for the two cases of ψ^*, Equations 6.34 and 6.39.

For $\Lambda \geq \pi/4$

$$T(\psi^*, \Lambda)^T = \frac{1}{\sqrt{1 - \left(\frac{1}{\sqrt{2}\sin\Lambda}\right)^2 \sin^2\Lambda}} \begin{bmatrix} 0 & 0 & \sqrt{1 - \left(\frac{1}{\sqrt{2}\sin\Lambda}\right)^2 \sin^2\Lambda} \\ -\frac{1}{\sqrt{2}\sin\Lambda}\cos\Lambda & \sqrt{1 - \left(\frac{1}{\sqrt{2}\sin\Lambda}\right)^2} & 0 \\ \sqrt{1 - \left(\frac{1}{\sqrt{2}\sin\Lambda}\right)^2} & \frac{1}{\sqrt{2}\sin\Lambda}\cos\Lambda & 0 \end{bmatrix} \tag{6.34}$$

Inserting into Equation 6.33 yields the following relationship of the initial angular momentum, Equation 6.35.

$$\hat{h_k'} = \sqrt{1 - \left(\frac{1}{\sqrt{2}\sin\Lambda}\right)^2}\,\hat{h_{0i}} + \frac{1}{\sqrt{2}\sin\Lambda}\cos\Lambda\hat{h_{0j}} \tag{6.35}$$

Now using the condition $\hat{h_k'} = 0$, Equations 6.36, 6.37, and 6.38.

$$-\frac{1}{\sqrt{2}\sin\Lambda}\cos\Lambda\hat{h_{0j}} = \sqrt{1-\frac{1}{2\sin^2\Lambda}}\hat{h_{0i}} \tag{6.36}$$

$$\hat{h_{0j}} = -\sqrt{2-\frac{1}{\sin^2\Lambda}}\tan\Lambda\hat{h_{0i}} \tag{6.37}$$

$$\hat{h_{0j}} = -\sqrt{\tan^2\Lambda - 1}\hat{h_{0i}} \tag{6.38}$$

Thus, to maximize eccentricity, the orbit orientation must meet the condition $\hat{h_{0j}} = -\sqrt{\tan^2\Lambda - 1}\hat{h_{0i}}$, making it dependent on the SRP parameter for the $\Lambda > \pi/4$ case.

Using the same process for $\Lambda < \pi/4$ we solve for the initial angular momentum by Equations 6.39, 6.40, and 6.41.

$$T(\psi^*, \Lambda)^T = \frac{1}{\cos\Lambda}\begin{bmatrix} 0 & 0 & \cos\Lambda \\ -\cos\Lambda & 0 & 0 \\ 0 & \cos\Lambda & 0 \end{bmatrix} \tag{6.39}$$

$$\hat{h_k'} = \frac{1}{\cos\Lambda}\begin{bmatrix} 0 & \cos\Lambda & 0 \end{bmatrix} \cdot \hat{h_0} \tag{6.40}$$

$$\hat{h_k'} = \hat{h_{0j}} \tag{6.41}$$

Then specifically using that $\hat{h_k'} = 0$ we find Equation 6.42.

$$0 = \hat{h_{0j}} \tag{6.42}$$

Therefore, the orbit plane for when eccentricity maximizes for $\Lambda > \pi/4$ is dependent on Λ while for $\Lambda < \pi/4$ it is not. For this case, the angular momentum of the circular orbit must initially be in the $\hat{\boldsymbol{d}}\hat{\boldsymbol{z}}$ plane when the sail is deployed to achieve the maximum eccentricity.

Given the initial angular momentum that maximizes eccentricity, we find what angle the orbit needs to initially be with respect to the Sun by solving for the right ascension of the ascending node in the rotating ecliptic frame using Equation 6.43.

$$\hat{h_0} = \begin{bmatrix} \sin i_{rot} \sin \Omega_{rot} \\ -\sin i_{rot} \cos \Omega_{rot} \\ \cos i_{rot} \end{bmatrix} \tag{6.43}$$

It is important to note that in both cases the initial angular momentum for maximum eccentricity does not depend on the h_{0k} term, and thus is independent of inclination. Therefore, inclination does not influence the maximum eccentricity, and we can strictly look at the right ascension of the ascending node, relative to the Sun-line.

Using Equation 6.43, the relationship between angular momentum and Ω_{rot} can be described as Equation 6.44

$$\frac{\hat{h_{0j}}}{\hat{h_{0i}}} = \frac{-\sin i_{rot} \cos \Omega_{rot}}{\sin i_{rot} \sin \Omega_{rot}} = -\cot \Omega_{rot} \tag{6.44}$$

For $\Lambda >= \pi/4$ the condition depends on the angle Λ, Equations 6.45 and 6.46, but the maximum eccentricity is 1.

$$\frac{\hat{h_{0j}}}{\hat{h_{0i}}} = -\sqrt{\tan^2 \Lambda - 1} = -\cot \Omega_{rot} \tag{6.45}$$

$$\Omega_{rot} = \operatorname{arccot}\left(\sqrt{\tan^2 \Lambda - 1}\right) \tag{6.46}$$

For $\Lambda < \pi/4$ the condition is independent of Λ, Equations 6.47 and 6.48, although the maximum eccentricity equals $\sin(2\Lambda)$.

$$\hat{h_{0j}} = 0 = -\sin i_{rot} \cos \Omega_{rot} \tag{6.47}$$

$$\Omega_{rot} = \pm \frac{\pi}{2} \tag{6.48}$$

For $\Lambda < \pi/4$, the orbit plane of the satellite must face the Sun, the angular momentum vector in the $\hat{\boldsymbol{d}}\hat{\boldsymbol{z}}$ plane, to achieve the maximum change in eccentricity, while for $\Lambda > \pi/4$ the orbit plane's positioning is dependent on the specific value of Λ.

This is illustrated in Figure 6.3 which varies rotating RAAN and the SRP parameter. At $\Lambda = \pi/4$ or 45°, the maximum switches from $\Omega_{rot} = \pi/2$ or 90° to higher RAAN values depending on Λ. This figure is shown with the most sensitive case, when the orbit is inclined 90° to the ecliptic.

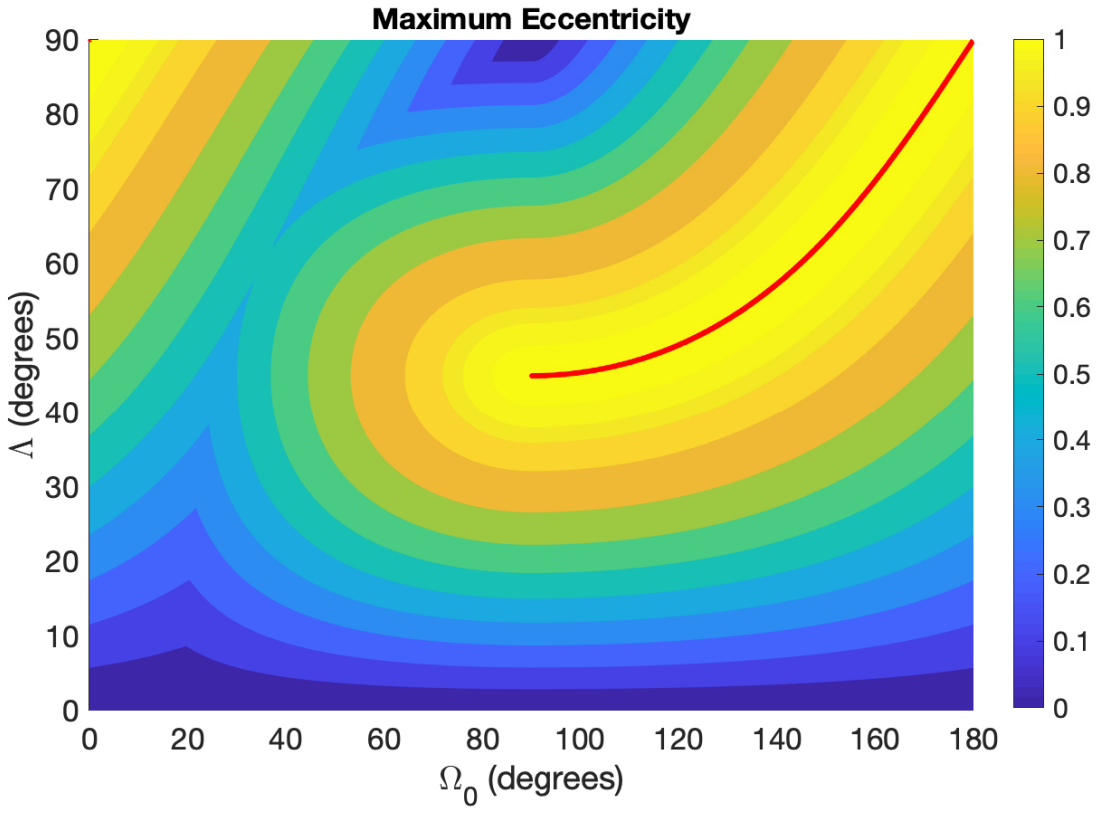

Figure 6.3: Maximum eccentricity for varying SRP strength and initial node orientation in the rotating ecliptic frame. The red line indicates a maximum eccentricity of 1. The solution repeats itself at 180°.

6.2 Dynamics in Earth Equatorial Frame

Everything up until this point has been expressed in the Sun-line Ecliptic rotating frame. This has allowed us to define important characteristics in the effects due to solar radiation pressure. To

utilize these characteristics, the orbital elements will need to be transferred into the Earth centered equatorial frame which was briefly discussed when using this frame in Chapter 3.

6.2.1 Orientation of the Optimal Direction in the Earth Inertial Frame

To describe the averaged solution in an ECI frame involves two frame changes, one from a frame rotating with the Sun-line to an inertial frame, technically just the ecliptic frame, and the other going from the ecliptic to an Earth centered equatorial frame.

The Sun line rotating frame as compared to the inertial ecliptic frame differs based on Earth's position around the Sun or its argument of latitude, u. A rotation about the z axis of the ecliptic by u degrees converts ecliptic and the sun line rotation frame. Figure 6.4 shows the physical rotation happening while Figure 6.5a shows how the rotation looks on the three axis system. The rotating axes as are $[\boldsymbol{d}, \boldsymbol{t}, \boldsymbol{z}]$ and the ecliptic inertial axes are $[\boldsymbol{x'}, \boldsymbol{y'}, \boldsymbol{z'}]$. The rotation matrix for this transformation is Equation 6.49.

$$T_R = \begin{bmatrix} 1 & 0 & 0 \\ 0 & \cos u & \sin u \\ 0 & -\sin u & \cos u \end{bmatrix} \tag{6.49}$$

Transforming between the ecliptic and the equatorial frames involves rotating the equatorial frame by the tilt of the Earth. Because of the J_2 perturbation, $\hat{\boldsymbol{h}}$ precesses about the Earth's rotation pole, $\hat{\boldsymbol{z}}$. Thus as time progresses, the angular momentum precesses about $\hat{\boldsymbol{z}}$, giving different inclinations with respect to the ecliptic pole, $\hat{\boldsymbol{z'}}$. The $\boldsymbol{x}$ axis is defined by the vernal equinox, as does the equatorial frame we use (ECI). Figure 6.5b shows how the frame rotates and thus how the angular momentum vector should be represented in the ecliptic frame. The equatorial frame is denoted by axes $[\boldsymbol{x}, \boldsymbol{y}, \boldsymbol{z}]$ and the ecliptic frame is denoted by axes $[\boldsymbol{x'}, \boldsymbol{y'}, \boldsymbol{z'}]$. The rotation matrix

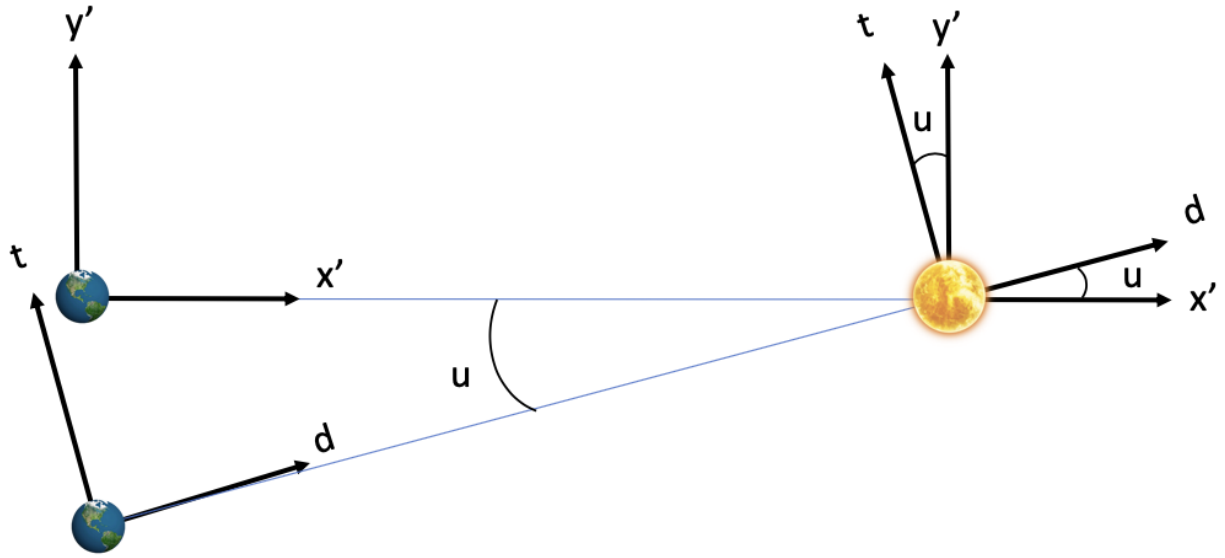

Figure 6.4: Visualization of how the rotation frame changes with respect to the inertial frame

for this transformation is Equation 6.50.

$$T_E = \begin{bmatrix} \cos\epsilon & \sin\epsilon & 0 \\ -\sin\epsilon & \cos\epsilon & 0 \\ 0 & 0 & 1 \end{bmatrix} \tag{6.50}$$

All together, to switch from the equatorial frame to the rotating ecliptic frame, two rotations are needed. Then, the angular momentum vector can be mapped between the two frames so that it can be described in terms of the Earth equatorial frame using the transport theorem [92] in Equation 6.51.

$$\boldsymbol{h}_{equatorial} = T_E T_R \boldsymbol{h}_{rotating} \tag{6.51}$$

The final piece of the puzzle is using the information of the right ascension of the ascending node to describe the optimal point in Earth's orbit to deploy a solar sail. The angle of the orbit with respect to the Sun is described by the argument of latitude of the Earth and the right ascension of the ascending node of the orbit. Because the RAAN will be defined by the satellite's orbit

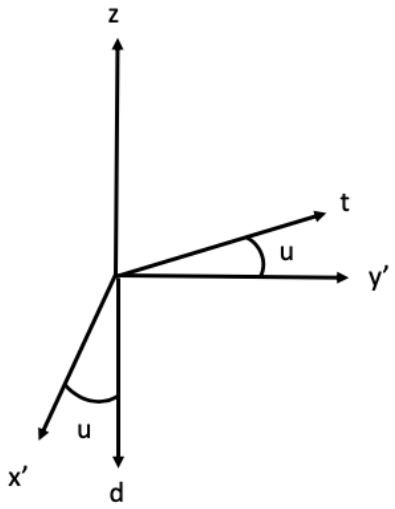

(a) Rotation between Earth Ecliptic Frame [x',y',z'] and the Sun-line Rotating Frame [d,t,z]

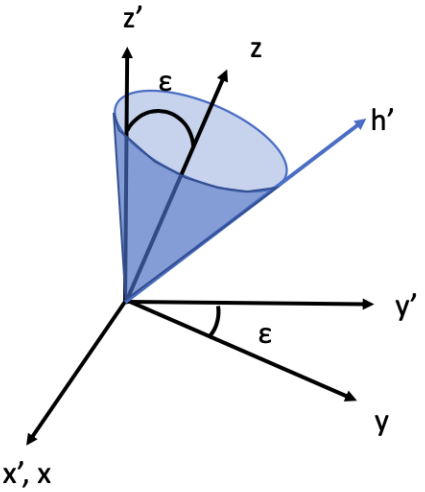

(b) Rotation between Earth Equatorial Frame [x,y,z] and Earth Ecliptic Frame[x',y',z']. ϵ denotes inclination of Earth's orbit with respect to the ecliptic.

Figure 6.5: Coordinate frame rotations

and therefore cannot be changed, the focus will be on the initial argument of latitude or where in Earth's orbit the solar sail is deployed. Thus, we will define the deployment argument of latitude of the Earth about the Sun as a function of the rotating RAAN, Ω_{rot}, and the satellite's RAAN in the Earth Centered Inertial frame, Equation 6.52.

$$u = \Omega - \Omega_{rot} \tag{6.52}$$

6.2.2 Regression of the Node Due to J_2

As noted in Figure 6.5b, the perturbing effects due to zonal harmonics cause a node regression around the pole. The expression for nodal regression due to J_2 is given by Vallado as Equation 6.53 [101],

$$\dot{\Omega}_{sec} = -\frac{3nR_E^2 J_2}{2p^2}\cos i \tag{6.53}$$

where n is the mean motion of the satellite, R_E is the radius of the Earth, J_2 is the first zonal coefficient = 0.0010826269, and p is the orbit's parameter. The inclination and right ascension variation is expressed in the equatorial frame. The lower the altitude the larger an effect the perturbation has on the object. Thus, the oblateness of the Earth can greatly influence the reentry conditions for low Earth orbit.

Despite having a ten order of magnitude less of an influence on dynamics than SRP, J_2 can shift the solution to not reenter for LEO as high as 5000 km altitude. Figure 6.6 demonstrates how the model is mismatched when the perturbation is accounted for with LEO satellite reentries. The assumptions made in this work thus cannot be applied to studying low Earth orbit. Alessi et al. have studied the analytical representation of solar radiation pressure and oblateness phase space for these LEO solutions [8]. This work will instead focus on higher altitudes where J_2 has a much smaller effect on the overall dynamics.

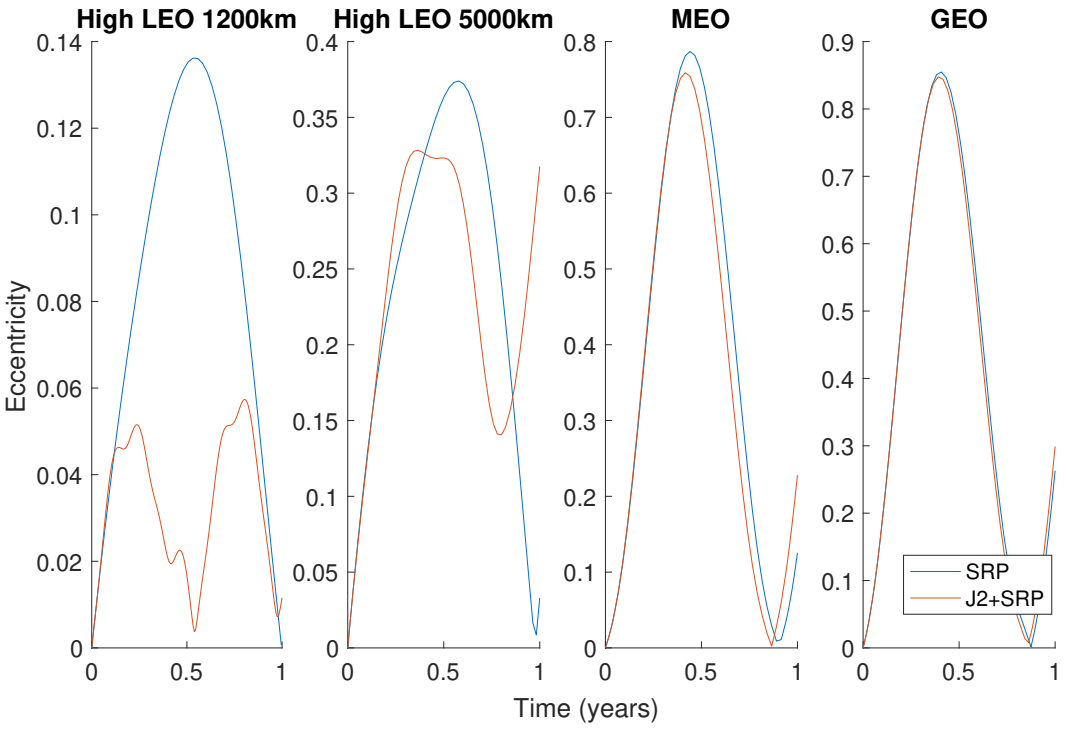

Figure 6.6: Eccentricity evolution with J_2 perturbations compared to just solar radiation pressure for a satellite with a sail attached equaling an area-to-mass ratio of 7.5 m^2/kg.

6.2.3 Targeting an Orbit

With the proper rotation sequence to transform the angular momentum in and out of the rotating frame, we can use equatorial elements and characterize their behavior in the equatorial frame using the averaged solution. Although RAAN can be solved simplistically by Equation 6.52, inclination requires rotation matrices to describe it in the rotating frame as compared to the equatorial frame, Equation 6.51.

Two tuning parameters are used to target the eccentricity and inclination: the right ascension of the ascending node in the rotating frame and the SRP Parameter. The SRP parameter, which is defined by Equation 2.16, can be varied by changing the area-to-mass ratio, such as by varying the size of the solar sail. The RAAN can be varied based on where in the Earth's revolution about the Sun the sail is deployed. The algorithm minimizes the distance between the guessed set of points and the targeted point in eccentricity and inclination space. It continues iterating until a given acceptable error distance is met.

The magnitude of the eccentricity vector will be used to describe the evolution of eccentricity. In the algorithm, we will be using the cosine of the inclination instead of inclination as it is easier to target. The cosine of the inclination is the third element in the angular momentum vector (after it has been transformed from the ecliptic to the equatorial frame).

For the purpose of this example, we will be targeting a GPS resonance location which has an eccentricity of 0.4 and a cosine of inclination of 0.56 ($\sim i = 56°$). The initial orbit is consistent with a nominal GPS orbit of an eccentricity 0 and inclination of 55°. Targeting is done by initializing at a set Λ and solving over an arc of right ascension of the ascending nodes to ensure the optimal solution is based on both parameters.

This arc can be seen by the outer most points on each of the loops in Figure 6.7. Instead of sweeping through the entire year, as the loops shown in that graph do, we only calculate each loop's farthest reach which occurs at approximately halfway through the year. This efficiently surveys the various RAANs because we are only calculating the portions of the solar sail's journey when the

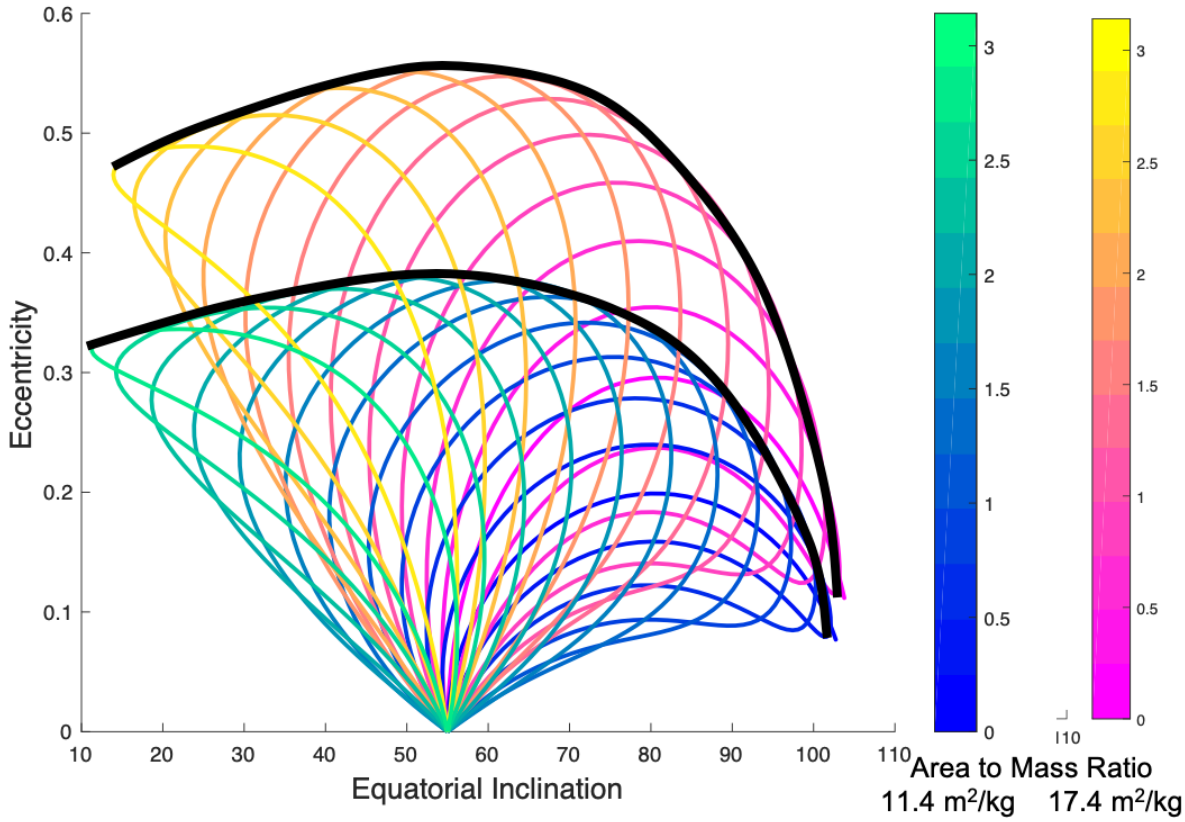

Figure 6.7: How eccentricity and inclination evolve over the course of a year. The colorbars indicate what the initial RAAN was in the simulation in radians. The black bars indicate the farthest reach for each of the area-to-mass ratios.

satellite is deposited or the targeting phase of the orbit.

Once the evolved cosine and eccentricity is solved, the solution is then iterated until the distance between the solved and target values are within a specified threshold (10^{-13} for these calculations). This distance is characterized by Equation 6.54

$$J = (e - e^*)^2 + (\cos i - \cos i^*)^2 \tag{6.54}$$

To account for the varying right ascension of the ascending node, the algorithm takes the minimum of the solved distances at each iteration. For each iteration where J_{min} is the minimum distance, we update the SRP parameter at each time step over the values of right ascension of the

ascending node, Equation 6.55.

$$\Lambda_{i+1} = \Lambda_i - \frac{\Delta\Lambda}{\Delta J_{min}} J_{min} \tag{6.55}$$

6.3 Application to Space Debris Mitigation

Lücking et al. looked into using spherical solar sails for space debris mitigation purposes [56]. The spherical sail is especially useful for the space debris application as it does not require attitude control which might not be available on a defunct satellite.

This section will explore using solar sailing for end of life operations of satellites at high altitude orbits. This is done by two methods. One is deorbiting straight from the satellites functioning orbit to an atmospheric reentry, achieved by targeting the maximum possible eccentricity. The other case involves an alternative to directly coming back to Earth: targeting the satellite into an orbit where it can utilize chaotic dynamics to grow in eccentricity and reenter Earth's atmosphere.

6.3.1 Deorbiting Using Only SRP

The first situation explored is using solely solar radiation pressure to deorbit a satellite. In this approach, a mission would use a solar sail to increase the eccentricity to bring its periapsis to the upper atmosphere, letting drag deorbit it the rest of the way. To be most efficient, the sail is deployed where the eccentricity is maximized due to solar radiation effects in order to get the most out of a solar sail.

6.3.1.1 Area-to-Mass Ratio Required for Atmospheric Reentry

As stated in Section 6.2.3, besides choosing the time of year to deploy the sail, the other factor that can be changed is Λ, more specifically the area-to-mass ratio of the object in Λ. To find what area-to-mass ratio is needed for a given orbit, we look at the area-to-mass ratio as a function of semi-major axis as that is the only satellite orbit element defined parameter in Λ, Equation 2.16. The amount of area-to-mass ratio needed is based on reentry at an altitude of 122km where NASA

defines reentry interface begins (full breakup at 78km) [68]. This condition for radius of periapsis will be denoted as $r_p^* = R_E + 122$ in Equation 6.56. In order to minimize solar sail size, $\Lambda < \pi/4$ is studied. The maximum eccentricity from Equation 6.29 is achieved to result in Equation 6.57.

$$e_{max} = 1 - \frac{r_p^*}{a} \tag{6.56}$$

$$\Lambda_{max} = \frac{1}{2} \arcsin e_{max} \tag{6.57}$$

To determine the area-to-mass ratio needed to achieve the maximum eccentricity, Equation 2.16 is solved for the area-to-mass ratio using the SRP parameter solved in Equation 6.57 to result in Equation 6.58.

$$\eta = \frac{2 \tan \Lambda_{max}}{3(1+\rho)P_0} \sqrt{\frac{\mu_E \mu_S a_S (1 - e_S^2)}{a}} \tag{6.58}$$

Figure 6.8 illustrates this relationship between the semi-major axis of the initial orbit and the area-to-mass ratio needed for a solar sail for atmospheric reentry. This figure is showing the general trends while later examples will explore the feasibility of implementing this method.

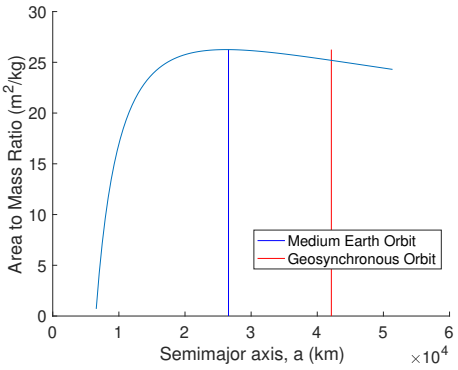

(a) For Earth orbits from LEO to GEO

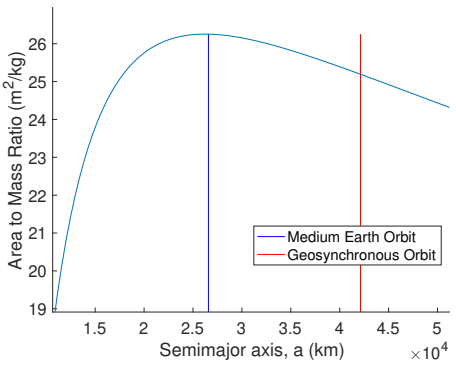

(b) Truncated for Earth orbits from MEO to GEO

Figure 6.8: Needed area-to-mass ratio of a solar sail to reach atmospheric reentry based on initial semi-major axis

6.3.1.2 Solar Sail Sizing for Current Satellites

To see how satellites would use this technology for end of life operations, we compared active satellites with their current orbit parameters and masses to see how large of a solar sail they would require to deorbit. Table 6.1 shows what the required solar sail size would be for different satellites at varying positions: GEO and MEO. As solar sail sizes are often described by their length/width both the area needed and the square root of the area are listed. The final satellite in the list explores the option if, in the future, CubeSats inhabit the geosynchronous orbit regime.

Table 6.1: Current satellites and what solar sail area would be needed to deorbit

Spacecraft Name	Semi-major Axis	Mass of S/C	Area of Sail (ηm)	Length/Width of Sail
GOES-8	42128 km [67]	2165 kg[67]	54542 m^2	233 m
Viasat-2	42165 km [5]	1464 kg [5]	36877 m^2	192 m
Intelsat VA	42166 km [40]	902 kg [64]	22720 m^2	151 m
Galileo FOC	29600 km [83]	710 kg [99]	18581 m^2	136 m
GPS-IIf	26754 km [83]	1633 kg [99]	42867 m^2	207 m
GPS-IIR	26574 km [83]	1080 kg [99]	28351 m^2	168 m
CubeSat at GPS	26574 km[83]	1 kg [52]	26.3 m^2	5.12 m
CubeSat at GEO	42128 km	1 kg [52]	25.2 m^2	5.02 m

Missions for solar sails have been proposed for sizes as large as 40m, NASA's Sunjammer [39] and JAXA's OKEANOS [66]. The majority of these proposed sail sizes are larger due to the massive size of the types of satellites currently inhabiting these regimes. This work can be used to ensure safe orbiting of CubeSat missions in these areas like the proposed GCPM [50] and GRIFEX, a launched satellite used to demonstrate radar capabilities to be used in geostationary orbit [65].

6.3.2 Deorbiting Using Luni-Solar Resonances

The mass of the satellite has a direct relationship to the size of the solar sail needed because solar radiation pressure is a function of area-to-mass ratio. Therefore, the fact that satellites currently in medium Earth orbit are navigation satellites and are relatively massive makes solar

sailing for Earth reentry and burn up difficult, even when deploying the sail in a smart location to reach the maximum eccentricity that sized sail can achieve. This helps motivate the decision to utilize other perturbations to help deorbit satellites in this region.

Because SRP provides a large and predictable change in inclination and eccentricity for satellites and can be described using a simple averaged formulation, SRP is a prime candidate for placing satellites directly into orbits that will be in resonance and that decay more rapidly. Proper design and deployment can move a satellite from a given zero eccentricity and inclination value into a region of strong resonances, effectively cutting off "centuries" of random motion where the satellite will drift along the resonance to a region of crossing resonances and injecting it right into the destabilizing region thus speeding up its removal. Movement into resonances occurs in less than one year, so the solar sail would dominate the dynamics of the satellite. Resonance structure can be defined in higher dimensions, incorporating factors including the epoch and other orbital parameters, but, for the purposes of this study, we will focus on the analytical definition of the region which is defined by semi-major axis, eccentricity, and inclination.

Studies have looked at deorbiting strategies utilizing solar radiation pressure in conjunction with tesseral resonances. Krivov studied the perturbations using high-altitude balloon satellites [53]. Lücking described a deorbiting strategy using solar radiation pressure and J_2 at medium Earth orbit [57]. This chapter, on the other hand, does not look at resonances due to oblateness but instead due to gravitation perturbations. In this case, we split the two effects into two phases of the deorbiting strategy. The first, happening on a timescale of less than a year is the unfurling of the sail to target the region of chaos where SRP is the dominant force. The second is when the sail is jettisoned, the sail's dynamics follows the SRP cycle and the satellite follows the resonance dynamics due to the Sun and Moon's gravity happening on the timescale of decades.

6.3.2.1 Targeting Resonance Locations

To implement these targeting algorithms, we note that the description of the dynamics is in the ecliptic frame whereas the orbit is defined in the equatorial frame. With the proper rotation

sequence to transform the angular momentum in and out of the rotating frame, equatorial elements can characterize their behavior using the averaged solution, as done in Section 6.2.1.

As shown in Figure 6.7, changing inclination is mainly dependent on when the sail is deployed rather than its area-to-mass ratio. Therefore, it is cheaper in terms of size of sail needed to target regions that are farther away than the nominal orbit in inclination, but these regions require smaller jumps in eccentricity. Therefore the optimal region to target the numerical solution for GLONASS is about 0.15 eccentricity and about 55 degrees inclination.

6.3.2.2 Solar Sail Sizing for Current Satellites

Utilizing this method, the SRP parameter can often be much smaller because the regions of chaos require less of a change in eccentricity and inclination. This results in a smaller area-to-mass ratio needed and a smaller sail overall. By roughly estimating target locations from the literature [83], the target eccentricities reduce from 0.76, 0.74, 0.78, and 0.77 to 0.40, 0.29, 0.09, and 0.24. These are different from the targets chosen in Chapter 5 as those were picked after extensive numerical analysis where these targets were chosen solely based on the analytical maps. Table 6.2 shows approximate Λ values and solar sail sizes for GNSS satellites. Notice how the GPS block sails reduce by about 30 meters using this method; Galileo, which has a fairly easy resonance to get to, reduces by over 50 meters.

6.3.2.3 Sail Dynamics After Release

In the case where a mission wants to leave the satellite in the targeted region, after the satellite reaches the target the sail will be jettisoned. Then the sail's mass significantly decreases, thus increasing the area-to-mass ratio and causing Λ to become close to the largest strength of $\pi/2$ radians. For the purposes of this study, we will assume that after the satellite is released, it follows the dynamics of $\Lambda = \pi/2$ radians. The limiting case was solved to equal Equation 2.19.

The $\Lambda = \pi/2$ case can theoretically reach a maximum eccentricity of 1. However, the orbit's orientation at the time of deployment (or, in this case, time of releasing the satellite) is critical to

Table 6.2: Current satellites and what solar sail area would be needed to deorbit either into a resonant region or direct reentry

Spacecraft Name	Mass of Spacecraft	Sail Size for Earth Reentry	Sail Size for Resonance Disposal
Galileo FOC	710kg[99]	136 m	44 m
GPS IIf	1633 kg [99]	207m	140m
GPS-IIR	1080 kg [4]	168 m	114 m
GLONASS-K	750 kg [79]	120 m	78 m
BeiDou	1100 kg[3]	170 m	121 m
CubeSat at GPS	1 kg	5.1 m	3.5 m

achieve this maximum eccentricity. As Figure 6.1 shows for an initially circular orbit the values vary from 0.1 to 1 depending on Ω_{rot0}.

In the targeting example, the sail will only achieve a maximum eccentricity of approximately 0.6 after being jettisoned. The path of the sail over the course of a year for this example is shown in Figure 6.9, where green is the path after deployment of the sail with the satellite attached and blue is the path after the satellite has been released into its targeting orbit. This could be an issue leaving the sail as a potential debris hazard.

To guarantee reentry of the sail into the atmosphere after the satellite is released, the orbital orientation at the point of satellite release would have to change. Instead of determining the location where the satellite is released solely by what was found to achieve the ideal inclination and eccentricity change, another factor of achieving the sail reentry of an eccentricity of about 0.76 must be included. An illustration of what that sail's path would look like with the post release eccentricity taken into consideration is shown in Figure 6.10.

In this case, the satellite is not released at the maximum inclination and eccentricity but instead is released after. This will ensure the sail will reenter Earth's atmosphere because the orientation of the sail's orbit with respect to the Sun has changed due to waiting later in the year to release the satellite. In order to still achieve the correct inclination and eccentricity, despite not

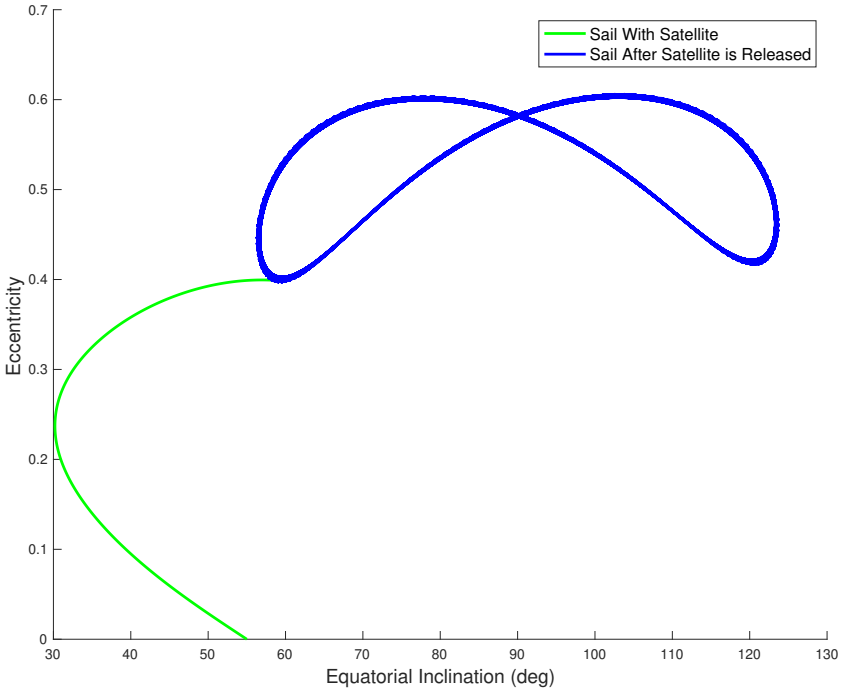

Figure 6.9: The solar sail's journey after deployment if sail disposal is not considered.

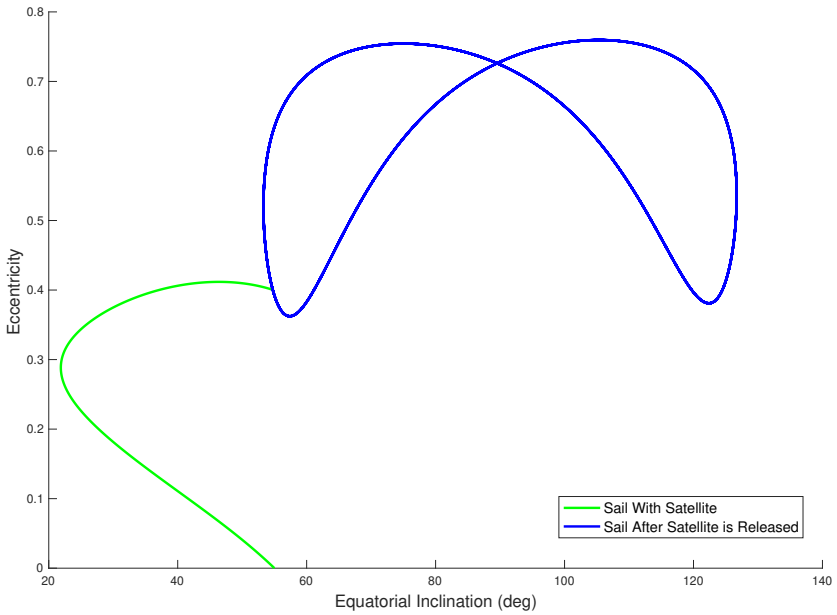

Figure 6.10: The solar sail's journey after deployment with positioning to dispose of the sail.

releasing it at its maximal change, the initial Λ and RAAN at deployment will need to change. In the case shown in Figure 6.9, the Λ parameter was increased by 0.1 radians and the initial RAAN was shifted by 0.4 radians to achieve the desired path as shown in Figure 6.10. This additional factor would be needed to be taken into consideration in future targeting algorithms.

6.4 Conclusion

This research leverages the simplistic descriptions of averaged dynamics to maximize plane changes and changes in eccentricity. By choosing a point on Earth's orbit to unfurl a sail, we can leverage the orbit geometry to maximize the effect due to the solar radiation pressure perturbation for a particular area-to-mass ratio, thereby allowing mission designers to pick the smallest sail to fulfill their objectives.

For lower area-to-mass ratio values, we demonstrated that an angular momentum vector in the plane $\hat{\boldsymbol{d}}\hat{\boldsymbol{z}}$ would provide the highest eccentricity change. If a program is interested in targeting a specific inclination as well, a simple targeting algorithm is applied to minimize the area-to-mass ratio needed.

If the satellite is to be placed in a targeted region and the sail be jettisoned, the sail orientation at time of placement becomes more critical. The sail on its own represents a very high area-to-mass ratio case. In this case, the sail can maximize to eccentricity of 1 at two points around Earth's orbit dependent on the strength of the perturbation due to Solar Radiation Pressure (SRP). Therefore, a mission designer in this scenario would have to consider time of deployment and time of placement to ensure both changes in solar radiation pressure occur at times that maximize its effects and bring the sail back after it completes the transfer.

Solar sailing has wide applications around Earth orbit. In particular, utilizing sailing as an end of life operation for atmospheric reentry can open the market to smaller satellites in high altitude orbits and ensure orbit safety for the future. This chapter has explored ways in which mission designers can utilize solar sailing by maximizing the solar radiation pressure effect based on orbit orientation. Through a detailed derivation of the averaged dynamics, we have noted key

points about Earth's orbit that a sail can be unfurled maximizing the effects due to solar radiation pressure without requiring the sail to be Sun pointing throughout the mission.

Chapter 7

Conclusions

This research has outlined several ways to approach debris mitigation at high altitudes using naturally occurring perturbations. At higher altitudes, where the Earth's atmosphere won't naturally decay orbits, dynamics due to third body perturbations and solar radiation pressure can be exploited to deobrit satellites. This can be done by placing a satellite in a known region of chaotic activity due to third body effects as explored in research goal three. This region can be reached by using a solar sail or a solar sail can be used to directly deorbit as explored in research goal four. To study the regions of chaos, the accuracy of averaged models was described in research goal one along with improvements on the doubly averaged model for solar radiation pressure when dealing with high area-to-mass ratio objects. Potential graveyard orbits as a method of debris mitigation specific to the medium Earth orbit regime was explored in research goal two where it was shown to be difficult to find regions of stability for the wide variation of objects that make up space debris. The summation of each of the results from the research goals are as follows.

7.1 Research Goals

7.1.1 Research Goal 1 - Validation and Formulation of Doubly Averaged Method

For nominal area-to-mass ratio objects the doubly-averaged model was able to follow trends found in the full dynamical solution. The statistical uncertainties the doubly-averaged model provides would be large for navigation purposes but were close enough to understand the trends decades in the future. The doubly-averaged model for solar radiation pressure was not able to

characterize the magnitude shifts in eccentricity for high area-to-mass ratio objects. By applying a numerical correction at the beginning of the simulation, the doubly-averaged model was able to track the dynamics more consistently. However, for a statistically significant level of overlap between the models, the singly averaged model for solar radiation pressure needs to be used. This results from this analysis will provide researchers with a quantifiable degree of confidence when using these tools in the chaotic regime.

7.1.2 Research Goal 2 - Stability of MEO

Finding stable graveyard orbits in medium Earth orbit is extremely challenging when considering debris type objects. High area-to-mass ratio objects interact with the resonance structure in MEO differently than the nominal satellites of the region. Therefore, it is difficult to find a stable region across all debris types. For more chaotic regions, like Galileo, dynamic events like collisions and explosions relatively quickly depopulate the region due to its unstable nature. GPS fragment clouds are in a more stable environment, and therefore the eccentricity distributions stay relatively circular years in the future but thus interact with the nominal orbit for longer time-spans. GLONASS fragmentation events do not necessarily reach a high enough eccentricity to totally depopulate but many objects are excited to high eccentricities where they can pose a risk to various orbits. We have shown through this research goal how the complex dynamics of fragment events propagate in this chaotic regime which will be fundamental to informing the eventual mitigation mandate for these orbits.

7.1.3 Research Goal 3 - Targeting Regions of Chaos

Targeting regions of chaos can be a feasible debris mitigation tactic in medium Earth orbit. Depending on the location of the target, satellites can reach reentry trajectories with relatively large uncertainties in their placement. Targets that are easier to reach (require less fuel to hit) require tighter requirements on their placement. Therefore, it will be a balancing act for satellite providers to consider their technological capabilities (or their ability to target the region with certainty) and

the cost of reaching the region. This mitigation tactic would guarantee depopulation of the orbit and therefore reduce collision risks from breakup events that the graveyard scenario would create. This analysis adds to the validity of targeting chaotic trajectories as a debris mitigation solution and helps strengthen the argument to employ this technique in medium Earth orbit.

7.1.4 Research Goal 4 - Utilizing Solar Radiation Pressure

Solar sailing is a debris mitigation tactic that could be used in a multitude of high altitude orbits. The potential issue is that the expensive enormous satellites that currently occupy this region are too heavy to attach a reasonably sized solar sail to achieve reentry. One potential mitigation strategy for the region of medium Earth orbit is to target a closer region of chaos instead of returning the satellite all the way to Earth using solar radiation pressure. Another consideration for future use is requiring any small satellites that would propose to use one of these orbits to employ this method of debris mitigation where the sail size requirements are much smaller. This would potentially help space commerce grow by allowing smaller budget private companies to use the same orbits that are currently occupied by satellites crucial to our national security without concern of overpopulation of the orbit. By leveraging the geometry of the orbit, we derived an optimal location to deploy a sail for either reentry or targeting a specified orbit. This ensures satellite providers can incorporate this debris mitigation method with the maximum output of their sail.

7.2 Published Papers

The Feasibility of Targeting Chaotic Regions in the GNSS Regime Jun 2021

Journal of Astronautical Sciences

M. Pellegrino, D. Scheeres, B. Streetman

Modeling of Breakup Events in Medium Earth Orbit Apr 2021

8th European Conference on Space Debris

M. Pellegrino, D. Scheeres, B. Streetman

Reachability of a Passive Solar Sail in Earth Orbit Nov 2020

AIAA Journal of Guidance, Control, and Dynamics

M. Pellegrino, D. Scheeres

Development and Analysis of the Doubly Averaged Model for Solar Radiation Pressure Aug 2020

1st International Orbital Debris Conference

M. Pellegrino, D. Scheeres, B. Streetman

Long Term Dynamics of Debris Objects in MEO Dec 2019

AAS/AIAA Astrodynamics Specialist Conference

M. Pellegrino, D. Scheeres, B. Streetman

Rapid Computation of MEO Satellite Deorbit Times Using Doubly Averaged Dynamics Oct 2019

70th International Astronautical Congress (IAC)

M. Pellegrino, D. Scheeres, B. Streetman

Robustness of Targeting Regions of Chaos in the GNSS Regime Jan 2019

29th Space Flight Mechanics Meeting

M. Pellegrino, D. Scheeres

Targeting Regions of Chaos in the GNSS Regime Aug 2018

AAS/AIAA Astrodynamics Specialist Conference

M. Pellegrino, D. Scheeres

Optimal Deployment of Solar Radiation Pressure Enhancement Devices for Space Debris Mitigation Jan 2018

AIAA SciTech 2018

M. Pellegrino, D. Scheeres

The Near Earth Asteroid Characterization and Observation (NEACO) Mission to Asteroid (469219) 2916 HO3 Feb 2019

AIAA Journal of Spacecraft and Rockets

C. Venigalla, N. Baresi, J. Aziz, B. Bercovici, D. Brack, A. Dahir, S. De Smet, J. Fulton, N. Parrish, **M. Pellegrino**, S. Van wal

"GTOC 9: Results from the University of Colorado Boulder" Feb 2017

Acta Futura

N.Parrish, D. Scheeres, S. Tardivel, C. Venigalla, J. Aziz, **M. Pellegrino**, O. Fuentes, S. De Smet

Bibliography

[1] Geo spacecraft disposals in 1997-1998. The Orbital Debris Quarterly News, page 6–6, Oct 1999.

[2] Dynamical evolution of high area-to-mass ratio debris released into gps orbits. Advances in Space Research, 43(10):1491 – 1508, 2009.

[3] Beidou 3 (compass navigation satellite system), 2017. Available at`http://spaceflight101.com/spacecraft/beidou-3/`.

[4] GPS IIR/IIR-M, November 2017. Available at `http://www.losangeles.af.mil/About-Us/Fact-Sheets/Article/343727/gps-iiriir-m/`.

[5] Viasat-2 at a glance, 2017. Available at `https://www.viasat.com/sites/default/files/media/documents/vs-2_launch_infographic_007-web.pdf`.

[6] A. A. Albuja, D. J. Scheeres, and J. W. McMahon. Evolution of angular velocity for defunct satellites as a result of YORP: An initial study. Advances in Space Research, 56:237–251, July 2015.

[7] E. M. Alessi, F. Deleflie, A. J. Rosengren, A. Rossi, G. B. Valsecchi, J. Daquin, and K. Merz. A numerical investigation on the eccentricity growth of GNSS disposal orbits. Celestial Mechanics and Dynamical Astronomy, 125:71–90, May 2016.

[8] Elisa Maria Alessi, Camilla Colombo, and Alessandro Rossi. Phase space description of the dynamics due to the coupled effect of the planetary oblateness and the solar radiation pressure perturbations. Celestial Mechanics and Dynamical Astronomy, 131(9):43, 2019.

[9] Elisa Maria Alessi, A Rossi, GB Valsecchi, L Anselmo, C Pardini, Camilla Colombo, HG Lewis, J Daquin, F Deleflie, Massimiliano Vasile, et al. Effectiveness of gnss disposal strategies. Acta Astronautica, 99:292–302, 2014.

[10] Dean Alhorn, Joseph Casas, Elwood Agasid, Charles Adams, Greg Laue, Christopher Kitts, and Sue O'Brien. Nanosail-d: The small satellite that could! 2011.

[11] RR Allan and GE Cook. The long-period motion of the plane of a distant circular orbit. Proceedings of the Royal Society of London. Series A. Mathematical and Physical Sciences, 280(1380):97–109, 1964.

[12] RR Allan and GN Ward. Planetary equations in terms of vectorial elements. In Mathematical Proceedings of the Cambridge Philosophical Society, volume 59, pages 669–677. Cambridge University Press, 1963.

[13] L Anselmo and C Pardini. Space debris mitigation in geosynchronous orbit. Advances in Space Research, 41(7):1091–1099, 2008.

[14] Roberto Armellin and Juan F San-Juan. Optimal earth's reentry disposal of the galileo constellation. Advances in Space Research, 61(4):1097–1120, 2018.

[15] Sergey A Astakhov, Andrew D Burbanks, Stephen Wiggins, and David Farrelly. Chaos-assisted capture of irregular moons. Nature, 423(6937):264–267, 2003.

[16] Daniel Casanova, Alexis Petit, and Anne Lemaître. Long-term evolution of space debris under the j_2 effect, the solar radiation pressure and the solar and lunar perturbations. Celestial Mechanics and Dynamical Astronomy, 123(2):223–238, 2015.

[17] Alessandra Celletti, Cătălin Galeş, Giuseppe Pucacco, and Aaron J Rosengren. Analytical development of the lunisolar disturbing function and the critical inclination secular resonance. Celestial Mechanics and Dynamical Astronomy, 127(3):259–283, 2017.

[18] C Chao. Geosynchronous disposal orbit stability. In AIAA/AAS Astrodynamics Specialist Conference and Exhibit, page 4186, 1998.

[19] CC Chao and RA Gick. Long-term evolution of navigation satellite orbits: Gps/glonass/galileo. Advances in Space Research, 34(5):1221–1226, 2004.

[20] Camilla Colombo. Long-term evolution of highly-elliptical orbits: luni-solar perturbation effects for stability and re-entry. Frontiers in Astronomy and Space Sciences, 6:34, 2019.

[21] GE Cook. Luni-solar perturbations of the orbit of an earth satellite. Geophysical Journal International, 6(3):271–291, 1962.

[22] Bernd Dachwald. Optimal solar sail trajectories for missions to the outer solar system. Journal of Guidance, Control, and Dynamics, 28(6):1187–1193, 2005.

[23] Jérôme Daquin, Aaron J Rosengren, Elisa Maria Alessi, Florent Deleflie, Giovanni B Valsecchi, and Alessandro Rossi. The dynamical structure of the meo region: long-term stability, chaos, and transport. Celestial Mechanics and Dynamical Astronomy, 124(4):335–366, 2016.

[24] S. Dodge. Orbital Debris Management and Risk Mitigation. NASA.

[25] Krafft A Ehricke. Instrumented comets—astronautics of solar and planetary probes. In VIIIth International Astronautical Congress Barcelona 1957/VIII. Internationaler Astronautischer Kongress/VIIIe Congrès International D'Astronautique, pages 74–126. Springer, 1958.

[26] Todd A Ely. Eccentricity impact on east-west stationkeeping for global positioning system class orbits. Journal of Guidance, Control, and Dynamics, 25(2):352–357, 2002.

[27] Todd A Ely and Kathleen C Howell. Dynamics of artificial satellite orbits with tesseral resonances including the effects of luni-solar perturbations. Dynamics and Stability of Systems, 12(4):243–269, 1997.

[28] Erwin Fehlberg. Classical fifth-, sixth-, seventh-, and eighth-order Runge-Kutta formulas with stepsize control. National Aeronautics and Space Administration, 1968.

[29] Larry Jay Friesen, Albert A Jackson IV, Herbert A Zook, and Donald J Kessler. Analysis of orbital perturbations acting on objects in orbits near geosynchronous earth orbit. Journal of Geophysical Research: Planets, 97(E3):3845–3863, 1992.

[30] Carolin Früh, Thomas M Kelecy, and Moriba K Jah. Coupled orbit-attitude dynamics of high area-to-mass ratio (hamr) objects: influence of solar radiation pressure, earth's shadow and the visibility in light curves. Celestial Mechanics and Dynamical Astronomy, 117(4):385–404, 2013.

[31] Carolin Früh and Thomas Schildknecht. Variation of the area-to-mass ratio of high area-to-mass ratio space debris objects. Monthly Notices of the Royal Astronomical Society, 419(4):3521–3528, 2012.

[32] M. Garcia. Space debris and human spacecraft, July 2016.

[33] Charles Garner, Benjamin Diedrich, and Manfred Leipold. A summary for solar sail technology developments and proposed demonstration missions. 1999.

[34] Richard L Garwin. Solar sailing-a practical method of propulsion within the solar system, 1958.

[35] R Gick. Gps disposal orbit stability and sensitivity study. In Proceeding of the 11 th Annual AAS/AIAA Space Flight Mechanics Meeting, Santa Barbara, CA, pages 2005–2017, 2001.

[36] Ioannis Gkolias, Jérôme Daquin, Fabien Gachet, and Aaron J Rosengren. From order to chaos in earth satellite orbits. The Astronomical Journal, 152(5):119, 2016.

[37] Ioannis Gkolias, Jérôme Daquin, Despoina K Skoulidou, Kleomenis Tsiganis, and Christos Efthymiopoulos. Chaotic transport of navigation satellites. Chaos: An Interdisciplinary Journal of Nonlinear Science, 29(10):101106, 2019.

[38] David J Gondelach, Roberto Armellin, and Alexander Wittig. On the predictability and robustness of galileo disposal orbits. Celestial Mechanics and Dynamical Astronomy, 131(12):60, 2019.

[39] Jeannette Heiligers, Ben Diedrich, William Derbes, and Colin McInnes. Sunjammer: preliminary end-to-end mission design. In AIAA/AAS Astrodynamics Specialist Conference, page 4127, 2014.

[40] A Heilmann, LDD Ferreira, CA Dartora, and KZ Nobrega. Antenna radiation effects on the orbits of gps and intelsat satellites. Acta Astronautica, 88:1–7, 2013.

[41] Ch Hubaux and A Lemaître. The impact of earth's shadow on the long-term evolution of space debris. Celestial Mechanics and Dynamical Astronomy, 116(1):79–95, 2013.

[42] S Hughes. Earth satellite orbits with resonant lunisolar perturbations i. resonances dependent only on inclination. Proceedings of the Royal Society of London. A. Mathematical and Physical Sciences, 372(1749):243–264, 1980.

[43] Alan B Jenkin and R Anne Gick. Collision risk posed to the global positioning system by disposal orbit instability. Journal of spacecraft and rockets, 39(4):532–539, 2002.

[44] Alan B Jenkin and R Anne Gick. Collision risk posed to the global positioning system by disposed upper stages. Journal of Spacecraft and Rockets, 43(6):1412–1418, 2006.

[45] Les Johnson, Mark Whorton, Andy Heaton, Robin Pinson, Greg Laue, and Charles Adams. Nanosail-d: A solar sail demonstration mission. Acta Astronautica, 68(5-6):571–575, 2011.

[46] Nicholas L Johnson. Protecting the geo environment: policies and practices. Space Policy, 15(3):127–135, 1999.

[47] Nicholas L Johnson, PH Krisko, J-C Liou, and PD Anz-Meador. Nasa's new breakup model of evolve 4.0. Advances in Space Research, 28(9):1377–1384, 2001.

[48] Ahmed Kamel, Donald Ekman, and Richard Tibbitts. East-west stationkeeping requirements of nearly synchronous satellites due to earth's triaxiality and luni-solar effects. Celestial Mechanics, 8(1):129–148, 1973.

[49] Donald J Kessler and Burton G Cour-Palais. Collision frequency of artificial satellites: The creation of a debris belt. Journal of Geophysical Research: Space Physics, 83(A6):2637–2646, 1978.

[50] Richard Key, Stanley Sander, Annmarie Eldering, Charles Miller, Christian Frankenberg, Vijay Natraj, David Rider, Jean-Francois Blavier, Dmitriy Bekker, and Yen-Hung Wu. The geostationary carbon process mapper. In 2012 IEEE Aerospace Conference, pages 1–16. IEEE, 2012.

[51] Holger Krag, Stijn Lemmens, Tim Flohrer, and H Klinkrad. Global trends in achieving successful end-of-life disposal in leo and geo. In SpaceOps 2014 Conference, page 1933, 2014.

[52] H. J. Kramer. Canx-7, 2019. Available `https://earth.esa.int/web/eoportal/satellite-missions/c-missions/canx-7`.

[53] Alexander V Krivov and Juan Getino. Orbital evolution of high-altitude balloon satellites. Astronomy and Astrophysics, 318:308–314, 1997.

[54] Sergey P Kuznetsov. Hyperbolic chaos. Hyperbolic Chaos: A Physicist's View, ISBN 978-3-642-23665-5. Higher Education Press, Beijing and Springer-Verlag GmbH Berlin Heidelberg, 2012, 2012.

[55] Edward N Lorenz. The Essence of Chaos. University of Washington press, 1995.

[56] C. Lücking, C. Colombo, and C. R. McInnes. Solar radiation pressure-augmented deorbiting: Passive end-of life disposal from high-altitude orbits. Journal of Spacecraft and Rockets, 50:pp.1256–1267, 2013.

[57] Charlotte Lücking, Camilla Colombo, and Colin R McInnes. A passive satellite deorbiting strategy for medium earth orbit using solar radiation pressure and the j2 effect. Acta Astronautica, 77:197–206, 2012.

[58] Colin R McInnes. Solar sailing: technology, dynamics and mission applications. Springer Science & Business Media, 2013.

[59] Colin R McInnes, Malcolm MacDonald, Vassilis Angelopolous, and David Alexander. Geosail: Exploring the geomagnetic tail using a small solar sail. Journal of Spacecraft and Rockets, 38(4):622–629, 2001.

[60] Jay W McMahon and Daniel J Scheeres. New solar radiation pressure force model for navigation. Journal of Guidance, Control, and Dynamics, 33(5):1418–1428, 2010.

[61] F Mignard and M Henon. About an unsuspected integrable problem. Celestial mechanics, 33(3):239–250, 1984.

[62] Esther Morrow, Daniel J Scheeres, and Dan Lubin. Solar sail orbit operations at asteroids. Journal of Spacecraft and Rockets, 38(2):279–286, 2001.

[63] David Nesvornỳ, David Vokrouhlickỳ, and Alessandro Morbidelli. Capture of irregular satellites during planetary encounters. The Astronomical Journal, 133(5):1962, 2007.

[64] P Neyret, K Betaharon, L Dest, L Templeton, and F Dietrich. The intelsat vii-a spacecraft. In 14th International Communication Satellite Systems Conference and Exhibit, page 1946, 1990.

[65] Charles Norton, Steve Chien, Paula Pingree, David Rider, John Bellardo, James Cutler, and Michael Pasciuto. Nasa's earth science technology office cubesats for technology maturation. 2013.

[66] Tatsuaki Okada, Yoko Kebukawa, Jun Aoki, Jun Matsumoto, Hajime Yano, Takahiro Iwata, Osamu Mori, Jean-Pierre Bibring, Stephan Ulamec, Ralf Jaumann, et al. Science exploration and instrumentation of the okeanos mission to a jupiter trojan asteroid using the solar power sail. Planetary and Space Science, 161:99–106, 2018.

[67] World Meteorological Organization. Satellite: Goes-8, 2017.

[68] Chris L Ostrom and Kira Abercromby. Open source toolkit for reentry object modeling. In AIAA Atmospheric Flight Mechanics Conference, page 4208, 2017.

[69] Inkwan Park, Kohei Fujimoto, and Daniel J Scheeres. Effect of dynamical accuracy for uncertainty propagation of perturbed keplerian motion. Journal of Guidance, Control, and Dynamics, 38(12):2287–2300, 2015.

[70] Inkwan Park and Daniel J Scheeres. Hybrid method for uncertainty propagation of orbital motion. Journal of Guidance, Control, and Dynamics, 41(1):240–254, 2018.

[71] Marielle Pellegrino and Daniel J Scheeres. Reachability of a passive solar sail in earth orbit. Journal of Guidance, Control, and Dynamics, 44(2):360–369, 2021.

[72] Marielle M Pellegrino and Daniel Scheeres. Optimal deployment of solar radiation pressure enhancement devices for space debris mitigation. In 2018 Space Flight Mechanics Meeting, page 2229, 2018.

[73] Marielle M Pellegrino and Daniel Scheeres. Targeting regions of chaos in the gnss regime. In 2018 Space Flight Mechanics Meeting, 2018.

[74] Marielle M Pellegrino and Daniel Scheeres. Robustness of targeting regions of chaos in the gnss regime. In 2019 Space Flight Mechanics Meeting, 2019.

[75] Marielle M Pellegrino, Daniel J Scheeres, and Brett J Streetman. Long term dynamics of debris objects in meo. In First International Orbital Debris Conference, 2019.

[76] Marielle M Pellegrino, Daniel J Scheeres, and Brett J Streetman. Rapid computation of meo satellite deorbit times using doubly averaged dynamics. In 70th International Astronautical Congress (IAC), 2019.

[77] Marielle M Pellegrino, Daniel J Scheeres, and Brett J Streetman. The feasibility of targeting chaotic regions in the gnss regime. The Journal of the Astronautical Sciences, pages 1–32, 2021.

[78] Marielle M Pellegrino, Daniel J Scheeres, and Brett J Streetman. Modeling of breakup events in medium earth orbit. In 8th European Confernce on Space Debris, 2021.

[79] GM Polischuk, VI Kozlov, VV Ilitchov, AG Kozlov, VA Bartenev, VE Kossenko, NA Anphimov, SG Revnivykh, SB Pisarev, and AE Tyulyakov. The global navigation satellite system glonass: Development and usage in the 21st century. Technical report, RUSSIAN AEROSPACE AGENCY MOSCOW (RUSSIA), 2002.

[80] K Richter and HU Keller. On the stability of dust particle orbits around cometary nuclei. Icarus, 114(2):355–371, 1995.

[81] Rex W Ridenoure, Riki Munakata, Stephanie D Wong, Alex Diaz, David A Spencer, Douglas A Stetson, Bruce Betts, Barbara A Plante, Justin D Foley, and John M Bellardo. Testing the lightsail program: Advancing solar sailing technology using a cubesat platform. Journal of Small Satellites, 5(2):531–550, 2016.

[82] Samantha M Rieger and Daniel J Scheeres. Laplace plane dynamics with solar radiation pressure in the vicinity of an asteroid. In AIAA/AAS Astrodynamics Specialist Conference, page 4459, 2014.

[83] A. J. Rosengren, E. M. Alessi, A. Rossi, and G. B. Valsecchi. Chaos in navigation satellite orbits caused by the perturbed motion of the Moon. Monthly Notices of the Royal Astronomical Society, 449:3522–3526, June 2015.

[84] Aaron J Rosengren, Elisa Maria Alessi, Giovanni B Valsecchi, Alessandro Rossi, Florent Deleflie, and Jér ˆome Daquin. Dynamical instabilities in medium earth orbits: chaos induced by overlapping lunar resonances. In Proceedings of the 25th AAS/IAAA Space Flight Mechanics Meeting, Williamsburg, VA, USA, paper AAS, pages 15–435, 2014.

[85] Aaron J Rosengren, Jérôme Daquin, Kleomenis Tsiganis, Elisa Maria Alessi, Florent Deleflie, Alessandro Rossi, and Giovanni B Valsecchi. Galileo disposal strategy: stability, chaos and predictability. Monthly Notices of the Royal Astronomical Society, 464(4):4063–4076, 2016.

[86] Aaron J Rosengren, Jérôme Daquin, Kleomenis Tsiganis, Elisa Maria Alessi, Florent Deleflie, Alessandro Rossi, and Giovanni B Valsecchi. Galileo disposal strategy: stability, chaos and predictability. Monthly Notices of the Royal Astronomical Society, 464(4):4063–4076, 2016.

[87] Aaron J Rosengren and Daniel J Scheeres. Long-term dynamics of high area-to-mass ratio objects in high-earth orbit. Advances in Space Research, 52(8):1545–1560, 2013.

[88] Aaron J Rosengren and Daniel J Scheeres. Laplace plane modifications arising from solar radiation pressure. The Astrophysical Journal, 786(1):45, 2014.

[89] Aaron J Rosengren and Daniel J Scheeres. On the milankovitch orbital elements for perturbed keplerian motion. Celestial Mechanics and Dynamical Astronomy, 118(3):197–220, 2014.

[90] A Rossi, EM Alessi, GB Valsecchi, HG Lewis, C Colombo, L Anselmo, et al. Disposal strategies analysis for meo orbits. Contract No. 4000107201/12/F/MOS, 2015.

[91] Alessandro Rossi, Camilla Colombo, Kleomenis Tsiganis, James Beck, Jonathan Becedas Rodriguez, Scott Walker, Federico Letterio, Florio Dalla Vedova, Volker Schaus, Rada Popova, et al. Redshift: A global approach to space debris mitigation. Aerospace, 5(2):64, 2018.

[92] Hanspeter Schaub and John L Junkins. Analytical mechanics of space systems. American Institute of Aeronautics and Astronautics, 2009.

[93] Volker Schaus, Elisa Maria Alessi, Giulia Schettino, Alessandro Rossi, and Enrico Stoll. On the practical exploitation of perturbative effects in low earth orbit for space debris mitigation. Advances in Space Research, 63(7):1979–1991, 2019.

[94] D J Scheeres. Orbital mechanics about small bodies. Acta Astronautica, 72:1–14, 2012.

[95] Daniel J Scheeres. Satellite dynamics about small bodies: averaged solar radiation pressure effects. Journal of the Astronautical Sciences, 47(1):25–46, 1999.

[96] Daniel J. Scheeres. Orbital Motion In Strongly Peturbed Enviornments. Springer, 2012.

[97] Daniel J Scheeres. Close proximity dynamics and control about asteroids. In 2014 American Control Conference, pages 1584–1598. IEEE, 2014.

[98] Scott S Sheppard and David C Jewitt. An abundant population of small irregular satellites around jupiter. Nature, 423(6937):261–263, 2003.

[99] Peter Steigenberger, Steffen Thoelert, and Oliver Montenbruck. Gnss satellite transmit power and its impact on orbit determination. Journal of Geodesy, 92(6):609–624, 2018.

[100] TC Tsu. Interplanetary travel by solar sail. ARS Journal, 29(6):422–427, 1959.

[101] David A Vallado. Fundamentals of astrodynamics and applications, volume 12. Springer Science & Business Media, 2001.

Appendix A

Averaging Background

A.1 Derivation of Averaged Form of SRP

The following derivation of the rotating averaged solution is adapted from Scheeres [96]. To derive the averaged description of the dynamics, we will begin with the disturbing function, Equations A.1 and A.2.

$$\boldsymbol{a}_{SRP} = \frac{\partial \boldsymbol{\mathcal{R}_{srp}}}{\partial \boldsymbol{r}} \tag{A.1}$$

$$\boldsymbol{\mathcal{R}_{srp}} = \boldsymbol{a_{SRP}} \cdot \boldsymbol{r} \tag{A.2}$$

We then average the disturbing function over an orbit, Equation A.3.

$$\bar{\boldsymbol{\mathcal{R}}}_{\boldsymbol{srp}} = \frac{1}{2\pi} \int_0^{2\pi} \boldsymbol{\mathcal{R}_{srp}} dM \tag{A.3}$$

where M is the mean anomaly, to find Equation A.4.

$$\bar{\boldsymbol{\mathcal{R}}}_{\boldsymbol{srp}} = \frac{P_0 \Sigma (1+\rho)}{d^2} \hat{\boldsymbol{d}} \cdot \bar{\boldsymbol{r}} \tag{A.4}$$

Here $\hat{\boldsymbol{d}}$ is the unit vector pointing from the Sun to the Earth and $\bar{\boldsymbol{r}}$ is the average position vector defined as Equation A.5 [96].

$$\bar{\boldsymbol{r}} = -\frac{3}{2} a \boldsymbol{e} \tag{A.5}$$

Substituting this expression into the Lagrange Planetary Equations, Appendix A.2, yields the dynamics for the averaged problem, Equations A.6 and A.7.

$$\dot{\boldsymbol{h}}_{srp} = -\frac{3}{2}\sqrt{\frac{a}{\mu}}\frac{P_0\Sigma(1+\rho)}{d^2}\tilde{\hat{\boldsymbol{d}}}\cdot\boldsymbol{e} \tag{A.6}$$

$$\dot{\boldsymbol{e}}_{srp} = -\frac{3}{2}\sqrt{\frac{a}{\mu}}\frac{P_0\Sigma(1+\rho)}{d^2}\tilde{\hat{\boldsymbol{d}}}\cdot\boldsymbol{h} \tag{A.7}$$

We use a rotating frame oriented along the Sun-body line, pointing from the Sun to the Earth. Therefore, the vector $\hat{\boldsymbol{d}}$ rotates about the Earth's orbit normal $\hat{\boldsymbol{z}}$ as the body revolves around the Sun at the rate of change of the true anomaly, $\dot{f}$. The vector of the frame that makes it a right handed coordinate system is $\hat{\boldsymbol{t}} = \hat{\boldsymbol{z}} \times \hat{\boldsymbol{d}}$. The averaged Equations A.6 and A.7 are transformed into a rotating frame using the transport theorem, e.g., $\dot{\boldsymbol{e}} = \dot{\boldsymbol{e}}_{\boldsymbol{r}} + \dot{f}\hat{\boldsymbol{z}} \times \hat{\boldsymbol{e}}$ [92].

$$\dot{\boldsymbol{h}}_r + \dot{f}\tilde{\hat{\boldsymbol{z}}}\cdot\boldsymbol{h} = -\frac{3}{2}\sqrt{\frac{a}{\mu}}\frac{P_0\Sigma(1+\rho)}{d^2}\tilde{\hat{\boldsymbol{d}}}\cdot\boldsymbol{e} \tag{A.8}$$

$$\dot{\boldsymbol{e}}_r + \dot{f}\tilde{\hat{\boldsymbol{z}}}\cdot\boldsymbol{e} = -\frac{3}{2}\sqrt{\frac{a}{\mu}}\frac{P_0\Sigma(1+\rho)}{d^2}\tilde{\hat{\boldsymbol{d}}}\cdot\boldsymbol{h} \tag{A.9}$$

By using $\frac{df}{dt} = \frac{h}{r^2}$, the true anomaly can be used as the independent variable to simplify Equations A.8 and A.9 to Equation A.10.

$$\begin{bmatrix} \frac{d\boldsymbol{e}}{df} \\ \frac{d\boldsymbol{h}}{df} \end{bmatrix} = \begin{bmatrix} -\tilde{\hat{\boldsymbol{z}}} & \tan\Lambda\tilde{\hat{\boldsymbol{d}}} \\ \tan\Lambda\tilde{\hat{\boldsymbol{d}}} & -\tilde{\hat{\boldsymbol{z}}} \end{bmatrix} \begin{bmatrix} \boldsymbol{e} \\ \boldsymbol{h} \end{bmatrix} \tag{A.10}$$

with the SRP parameter defined by Equations 2.16.

The equations of motion, Equation A.10, can be solved in closed form as they are time invariant linear equations. To reduce the solution to elementary functions, it is helpful to define the scaled true anomaly.

Then the solution can be found as Equations 2.14 and 2.15 in the paper.

A.2 Lagrange Planetary Equations

The Lagrange equations in term of the Milaknovitch elements [12]

$$\dot{\boldsymbol{h}} = \boldsymbol{h} \times \frac{\partial \boldsymbol{\mathcal{R}}^*}{\partial \boldsymbol{h}} + \boldsymbol{e} \times \frac{\partial \boldsymbol{\mathcal{R}}^*}{\partial \boldsymbol{e}} \tag{A.11}$$

$$\dot{\boldsymbol{e}} = \boldsymbol{e} \times \frac{\partial \boldsymbol{\mathcal{R}}^*}{\partial \boldsymbol{h}} + \boldsymbol{h} \times \frac{\partial \boldsymbol{\mathcal{R}}^*}{\partial \boldsymbol{e}} \tag{A.12}$$

The typical formulation of the Lagrange equations taken from [101]

$$\frac{da}{dt} = \frac{2}{na}\frac{\partial R}{\partial M_0} \tag{A.13}$$

$$\frac{de}{dt} = \frac{1-e^2}{na^2 e}\frac{\partial R}{\partial M_0} - \frac{\sqrt{1-e^2}}{na^2 e}\frac{\partial R}{\partial \omega} \tag{A.14}$$

$$\frac{di}{dt} = \frac{1}{na^2\sqrt{1-e^2}\sin i}\left\{\cos i\frac{\partial R}{\partial \omega} - \frac{\partial R}{\partial \Omega}\right\} \tag{A.15}$$

$$\frac{d\omega}{dt} = \frac{\sqrt{1-e^2}}{na^2 e}\frac{\partial R}{\partial e} - \frac{\cot i}{na^2\sqrt{1-e^2}\sin i}\frac{\partial R}{\partial i} \tag{A.16}$$

$$\frac{dM_0}{dt} = -\frac{1-e^2}{na^2 e}\frac{\partial R}{\partial e} - \frac{2}{na}\frac{\partial R}{\partial a} \tag{A.17}$$

Appendix B

Additional Characterizing Graphs

The plots pertaining to distributions that were too small for the doubly-dynamics to match the singly dynamics are listed below. The first set is for the nominal area-to-mass ratio case, Figures B.1 and B.2. The second set is for the first HAMR case, Figure B.3 and B.4.

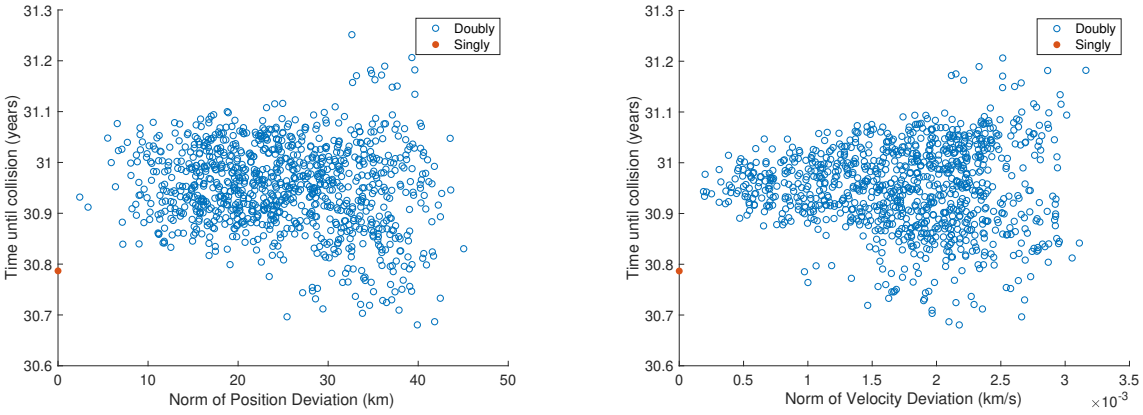

(a) Magnitude deviation of position vector

(b) Magnitude deviation of velocity vector

Figure B.1: The deviation of the initial conditions in terms of the magnitudes of the Cartesian coordinates as compared to the final reentry times for a 0.125% initial distribution.

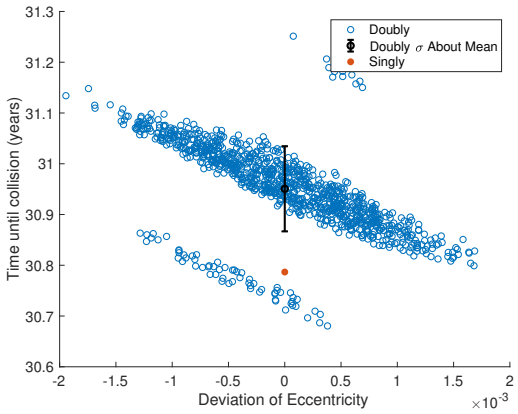

(a) eccentricity

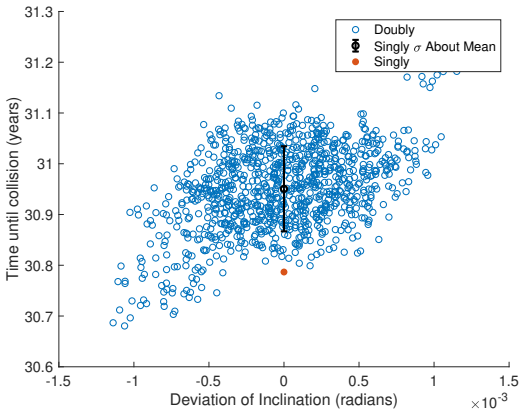

(b) inclination

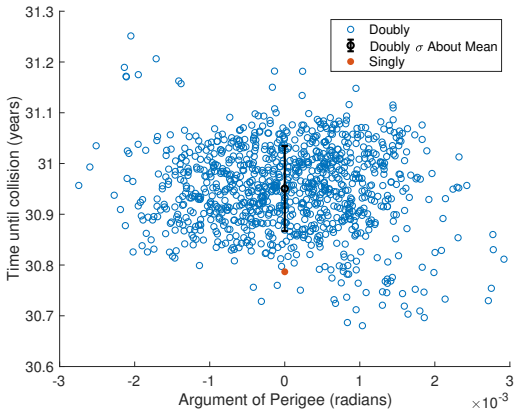

(c) argument of perigee

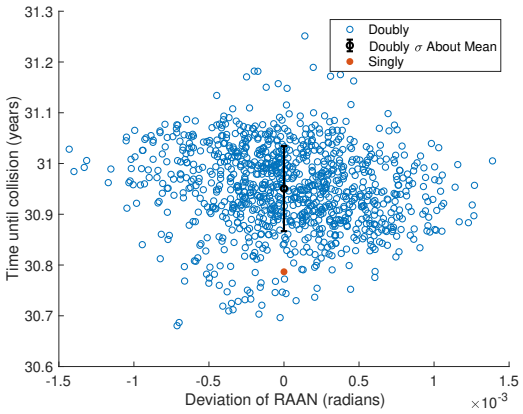

(d) right ascension of the ascending node

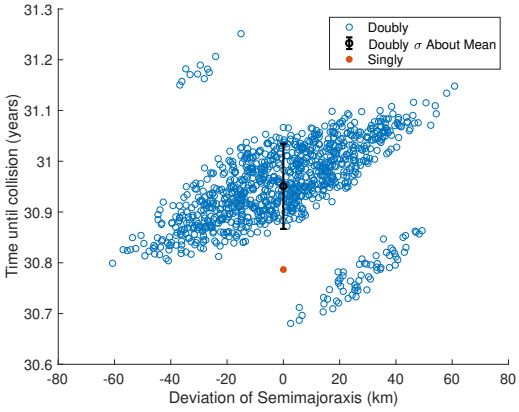

(e) semi-major axis

Figure B.2: The deviation of the initial conditions in terms of the orbital elements as compared to the final reentry times for a 0.125% initial distribution

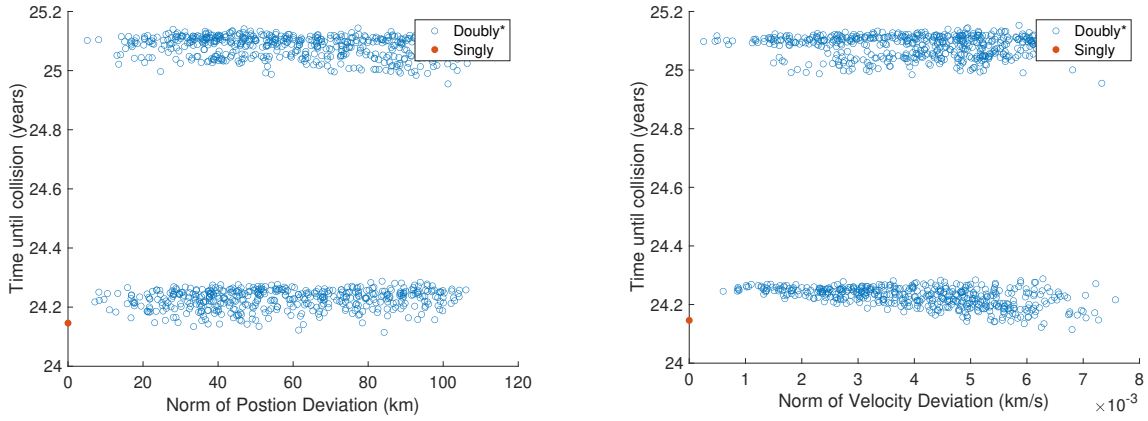

(a) Magnitude deviation of position vector

(b) Magnitude deviation of velocity vector

Figure B.3: The deviation of the initial conditions in terms of the magnitudes of the Cartesian coordinates as compared to the final reentry times for a 0.3% initial distribution

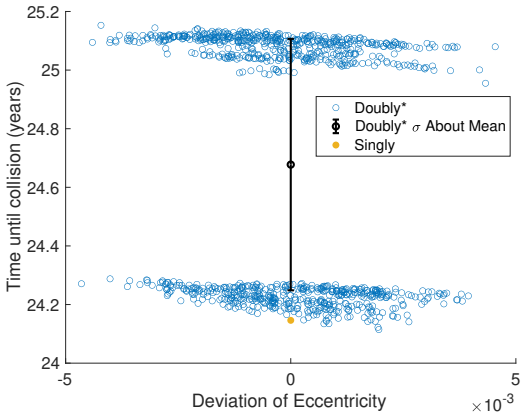

(a) eccentricity

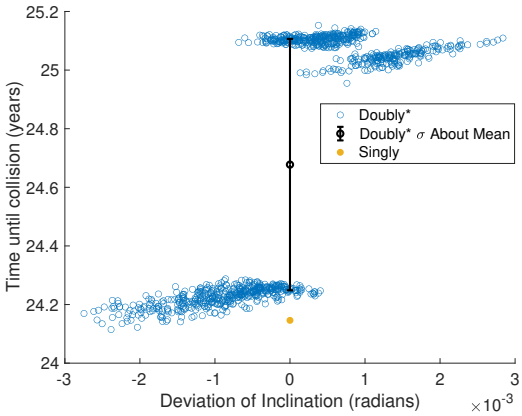

(b) inclination

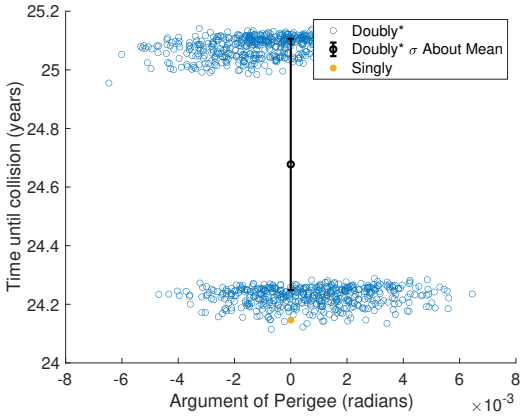

(c) argument of perigee

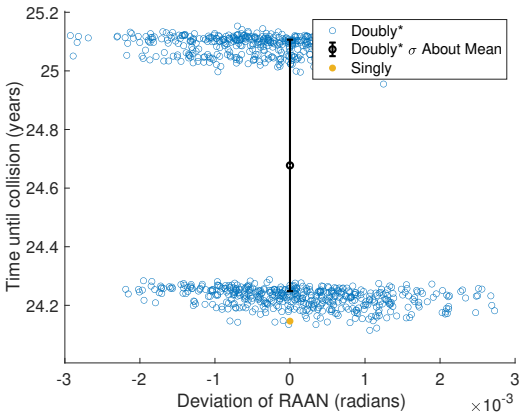

(d) right ascension of the ascending node

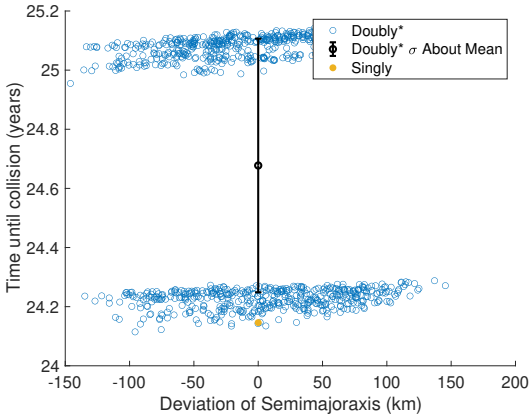

(e) semi-major axis

Figure B.4: The deviation of the initial conditions in terms of the orbital elements as compared to the final reentry times for a 0.3% initial distribution

Appendix C

Additional Fragment Cloud Distribution graphs

C.1 Varying RAAN

The fragment clouds were also analyzed for their reentry time distributions which are listed in this appendix. The impactor and parent sets were also separated in the violin plot distributions for the maximum eccentricities besides the additional reentry time distribution plots.

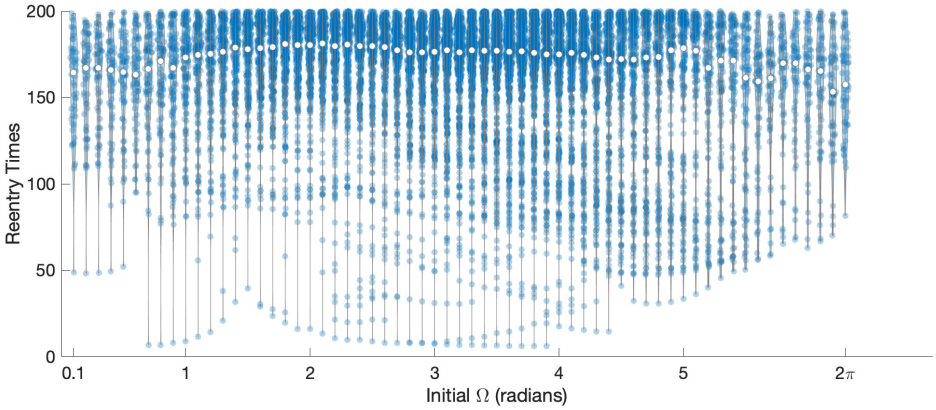

(a) GPS

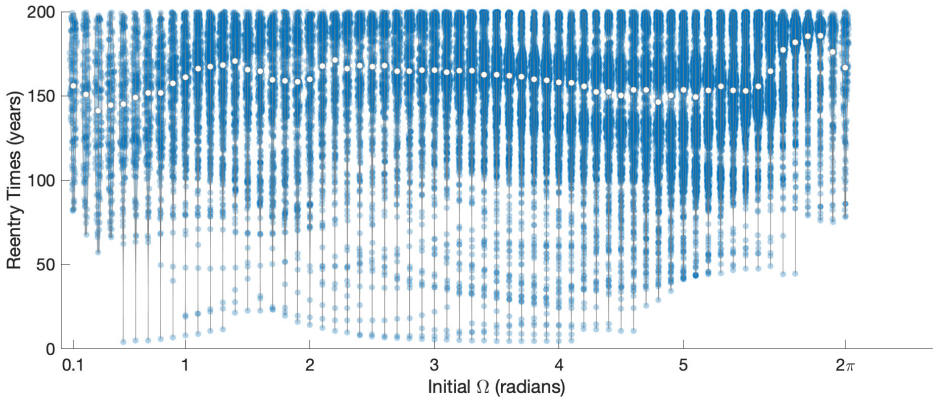

(b) Galileo

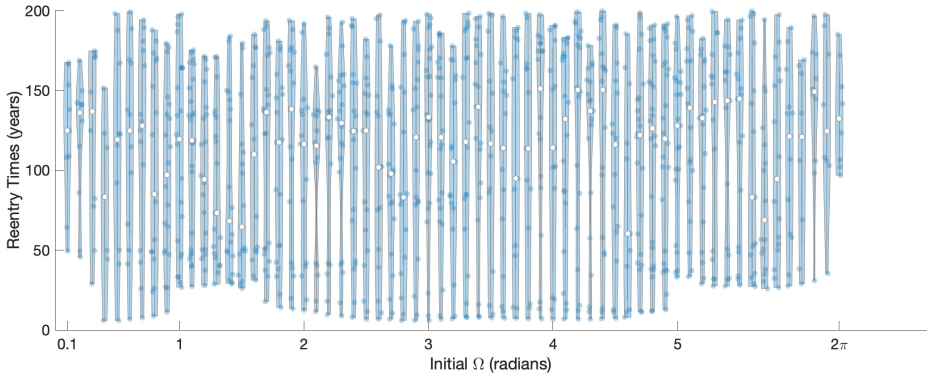

(c) GLONASS

Figure C.1: Reentry Times of objects produced in explosion event that have reentered after the simulation starts

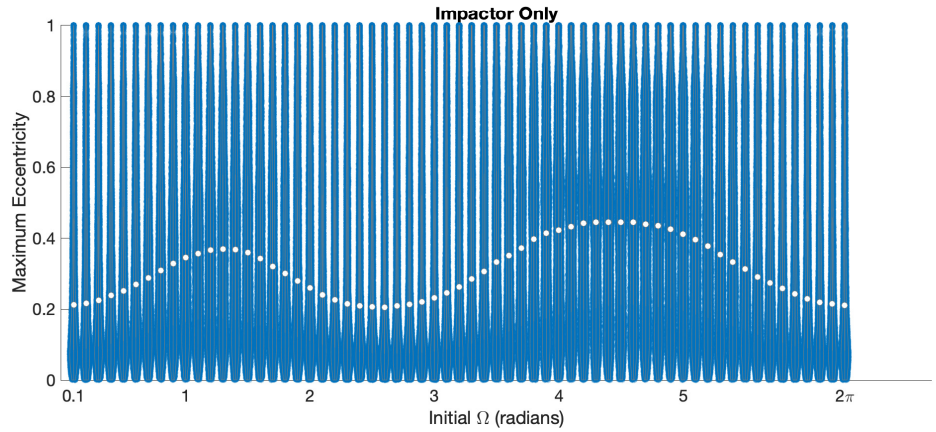

(a) GPS

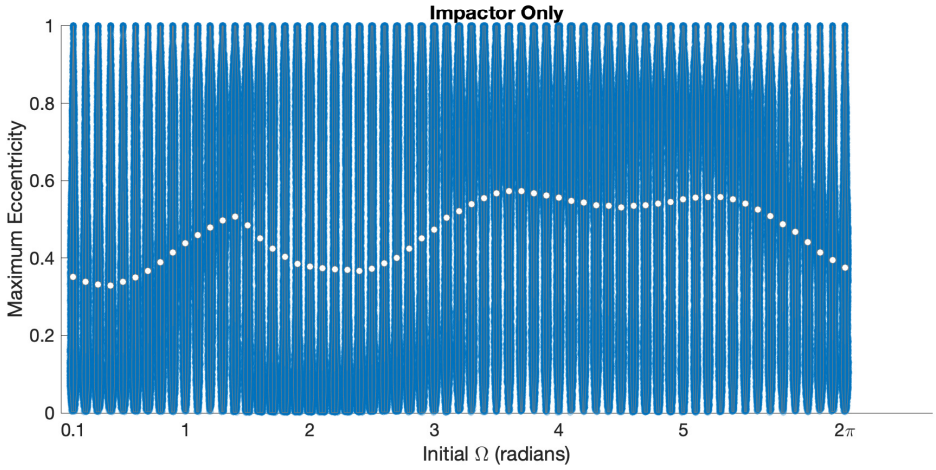

(b) Galileo

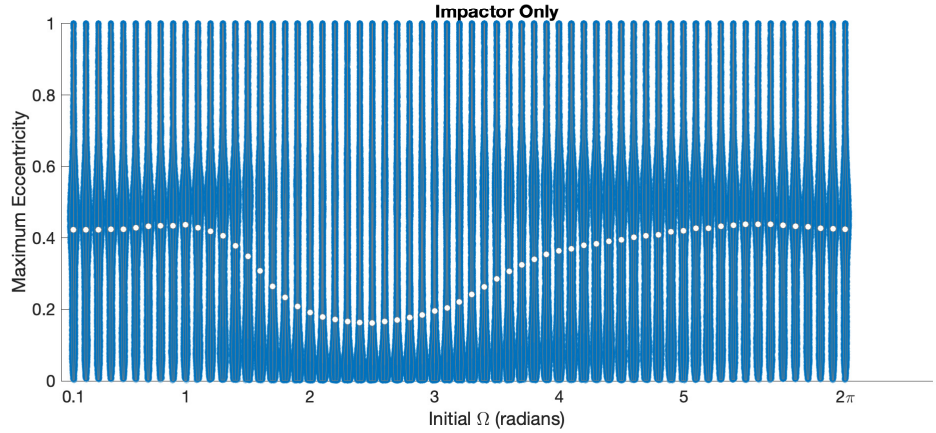

(c) GLONASS

Figure C.2: Maximum eccentricity of objects produced in by impactor object in a collision event

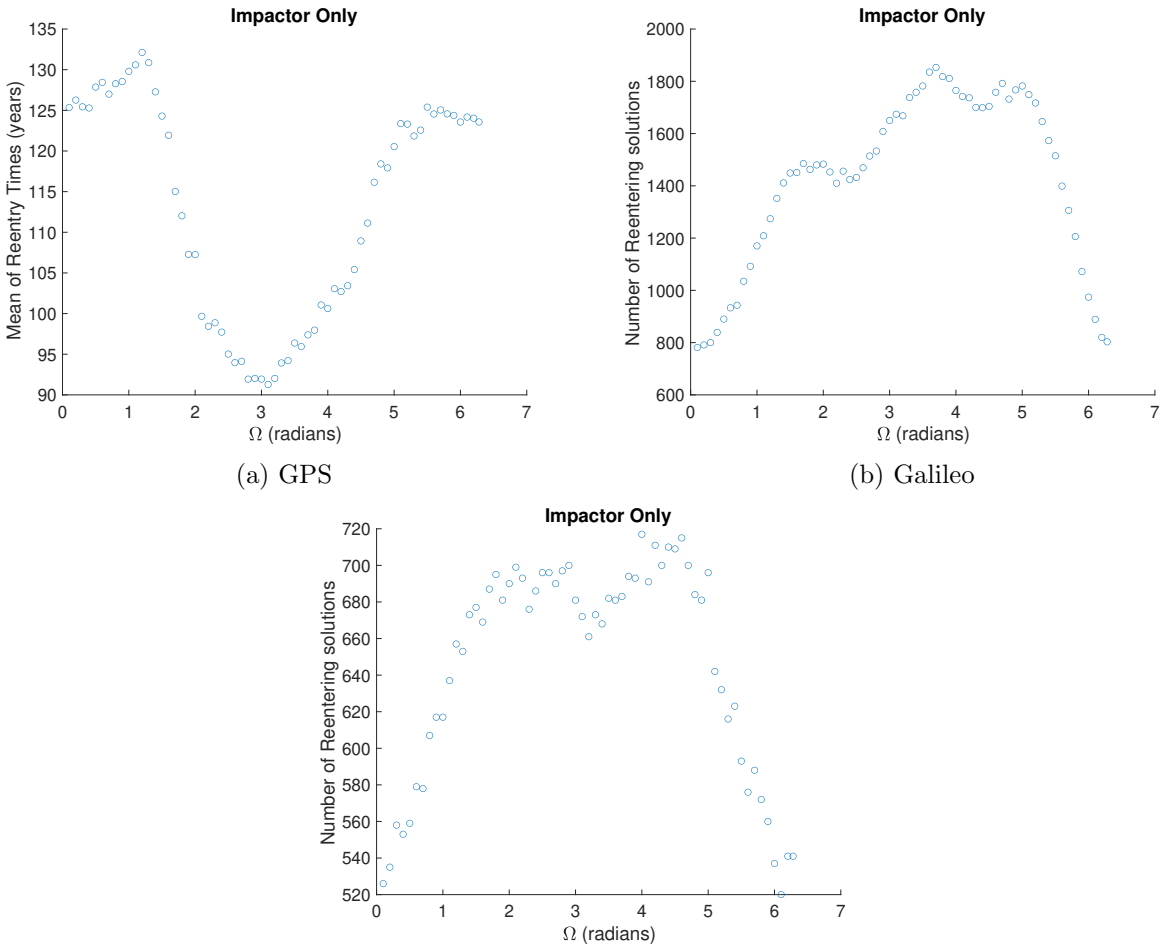

(a) GPS

(b) Galileo

(c) GLONASS

Figure C.3: Number of objects that reenter from impactor which were produced in ecollision event

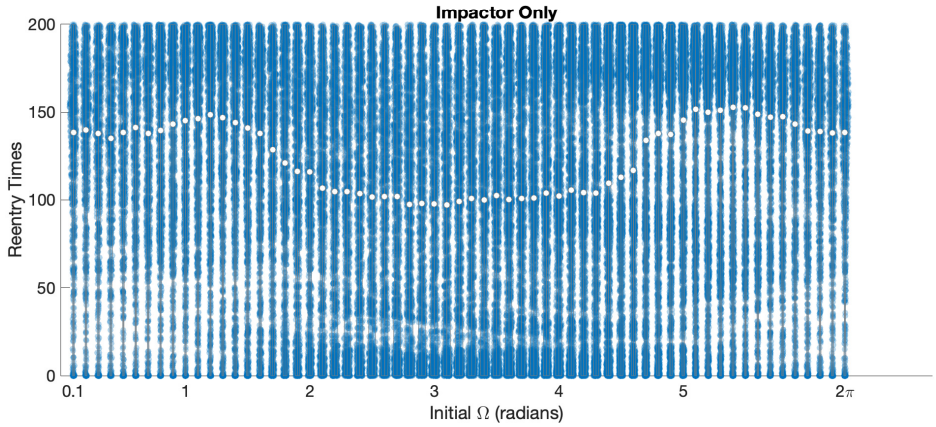

(a) GPS

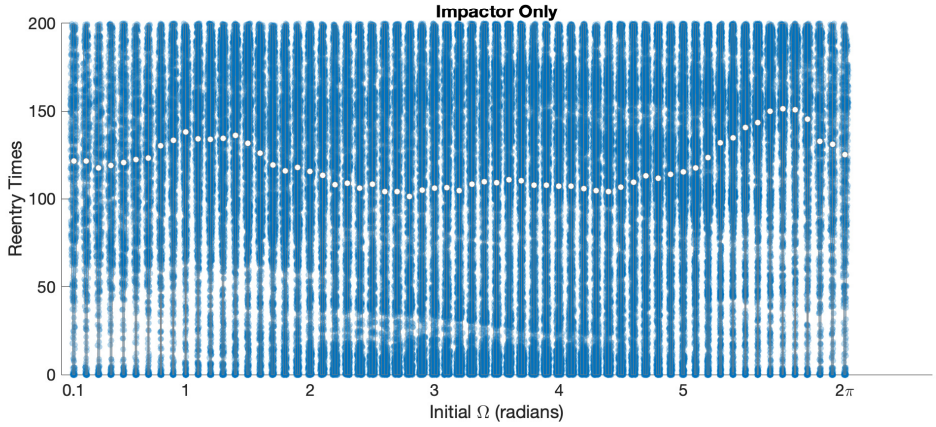

(b) Galileo

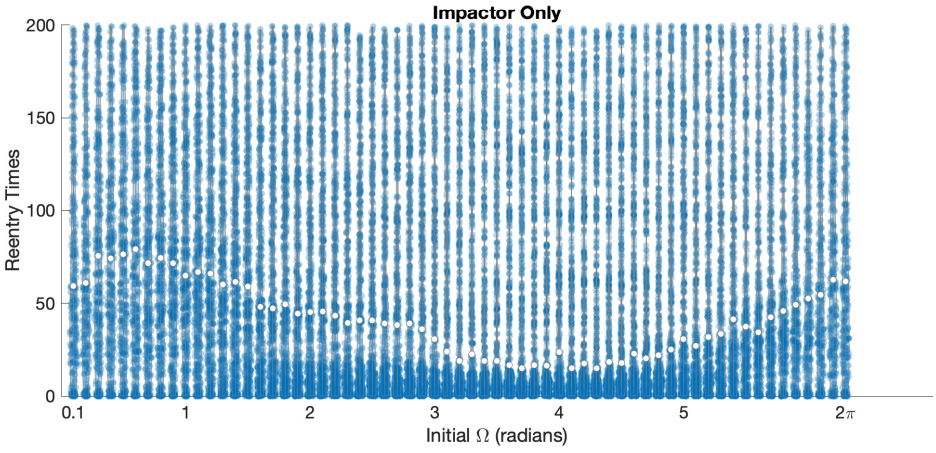

(c) GLONASS

Figure C.4: Reentry Times of objects produced in collision event that have reentered after the simulation starts

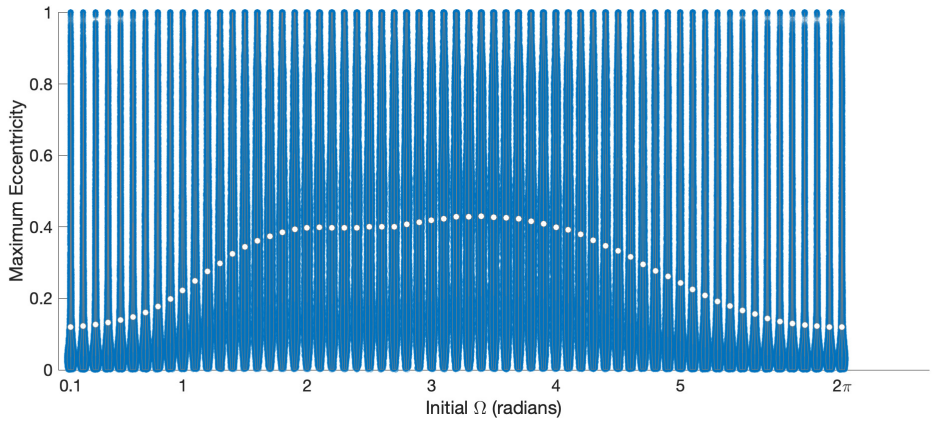

(a) GPS

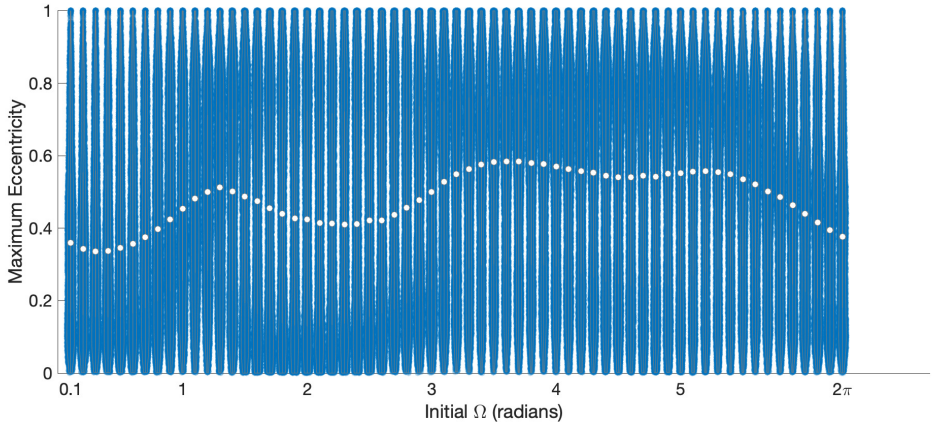

(b) Galileo

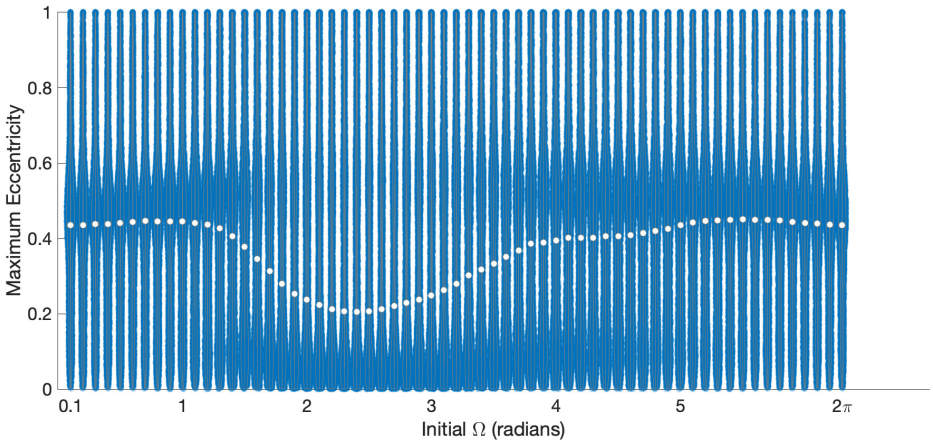

(c) GLONASS

Figure C.5: Maximum eccentricity of objects produced in by parent object in a collision event

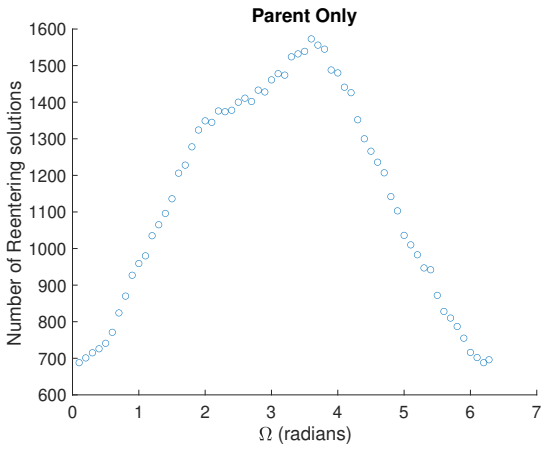

(a) GPS

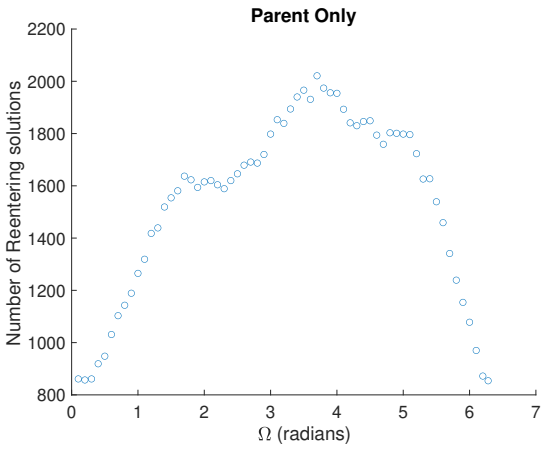

(b) Galileo

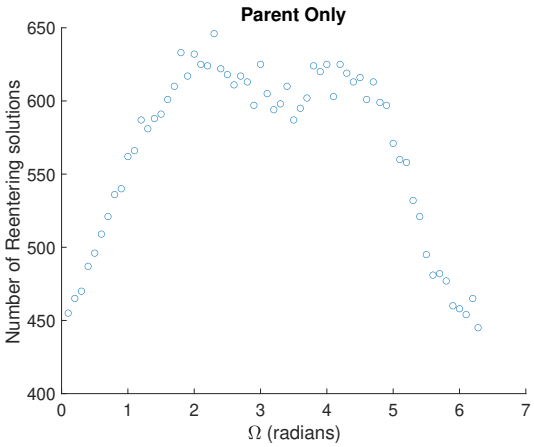

(c) GLONASS

Figure C.6: Number of objects that reenter from parent which were produced in collision event

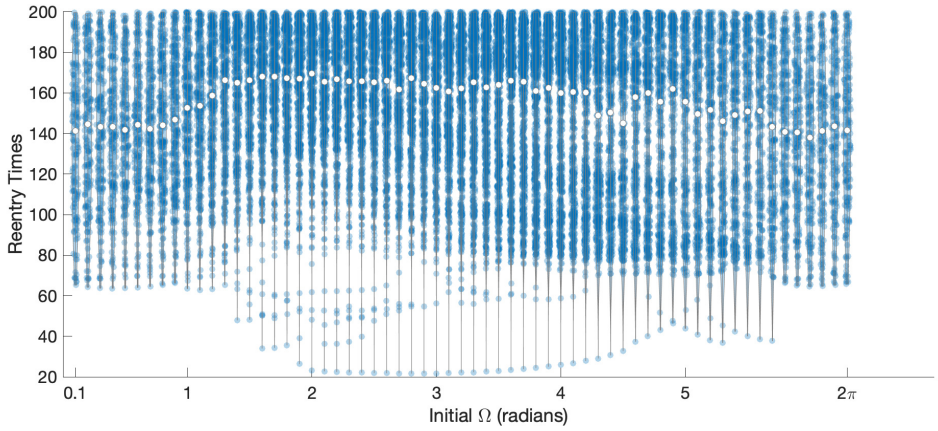

(a) GPS

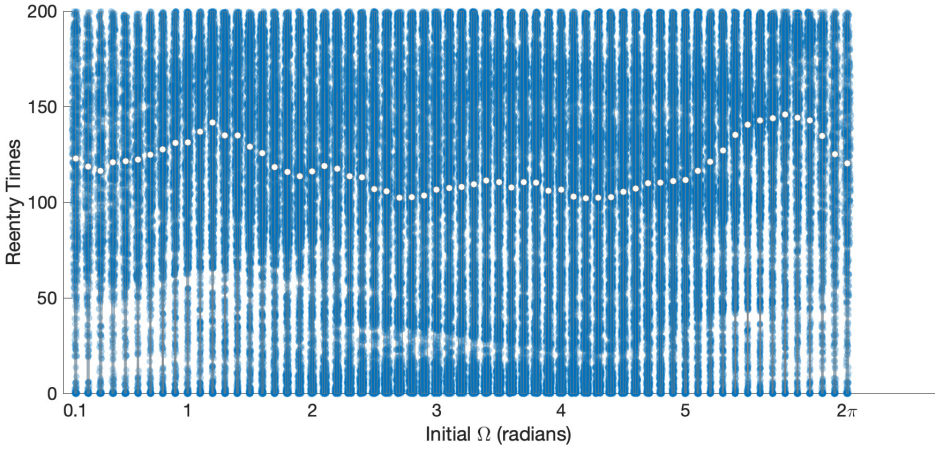

(b) Galileo

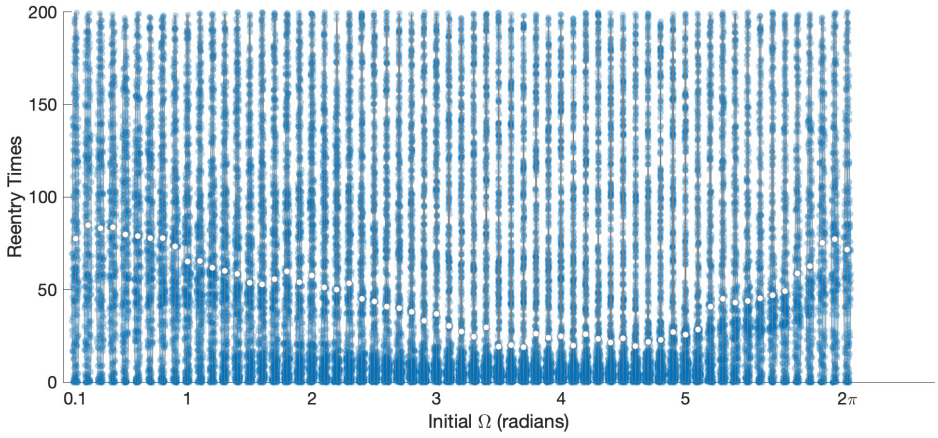

(c) GLONASS

Figure C.7: Reentry Times of objects produced in collision event that have reentered after the simulation starts

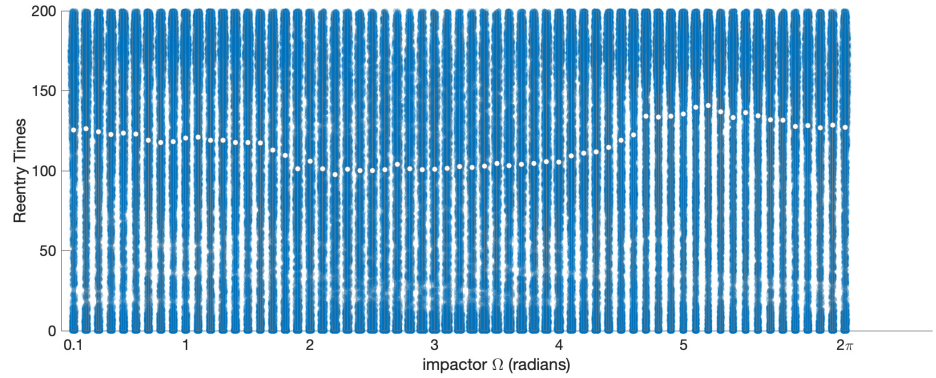

(a) GPS

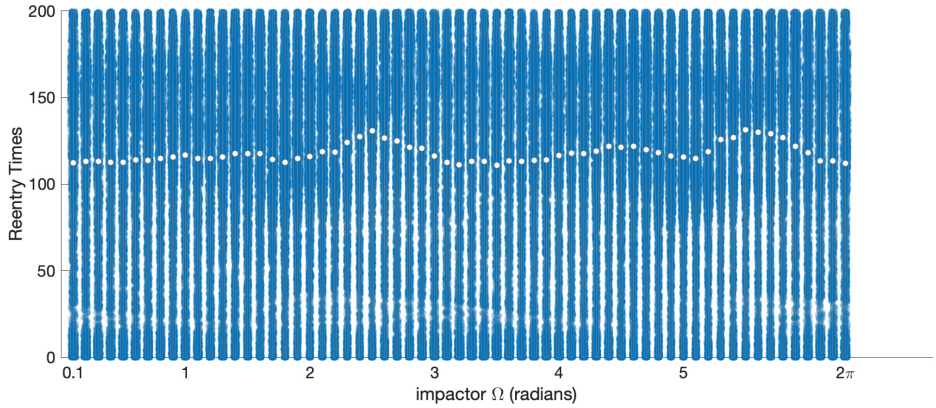

(b) Galileo

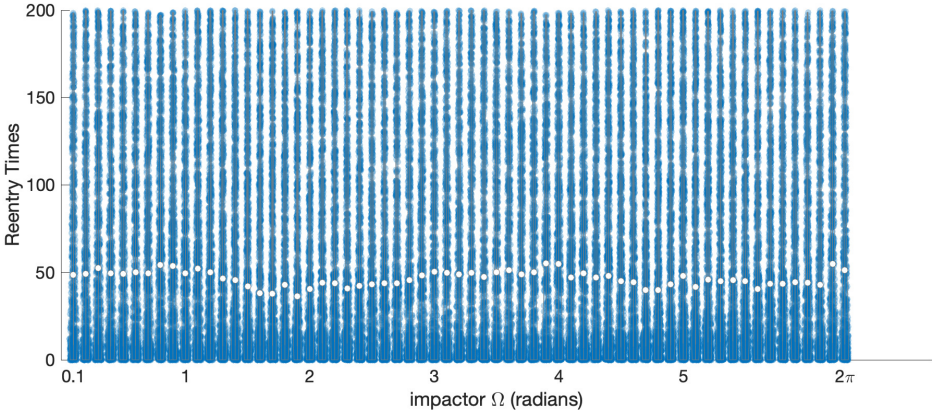

(c) GLONASS

Figure C.8: Reentry Times of objects produced in collision event that have reentered after the simulation starts

C.2 Varying Epoch

The same additional plots of reentry times for varying the initial epoch are listed below.

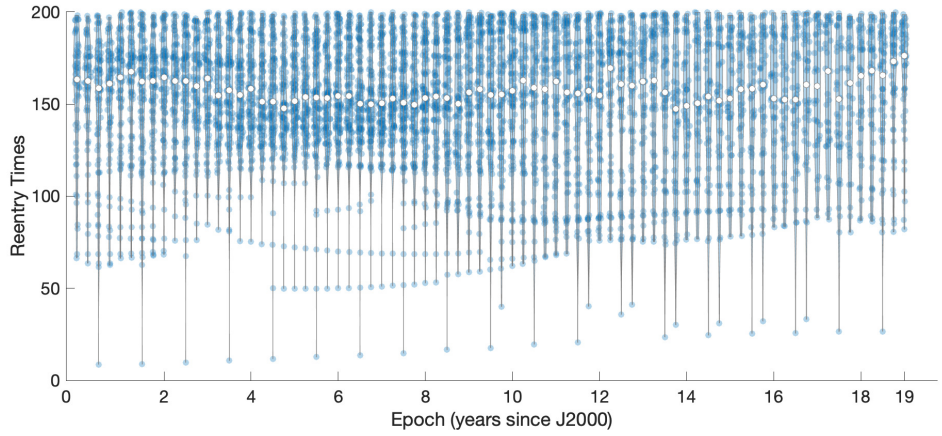

(a) GPS

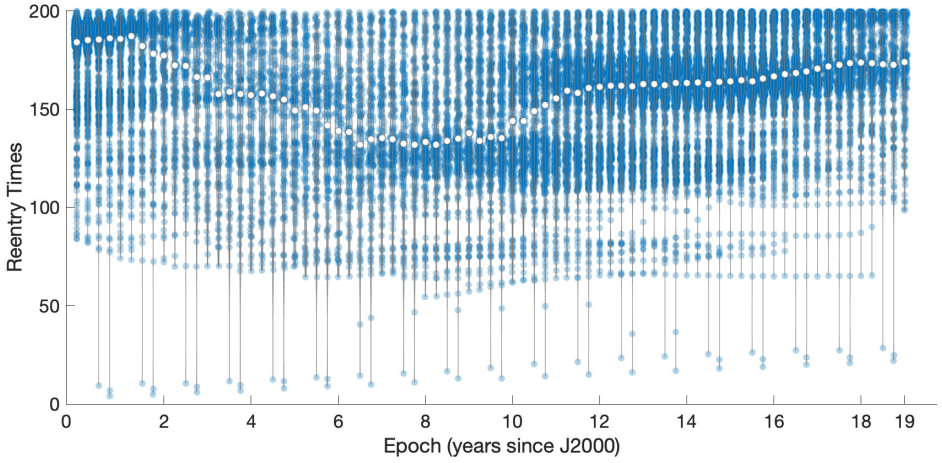

(b) Galileo

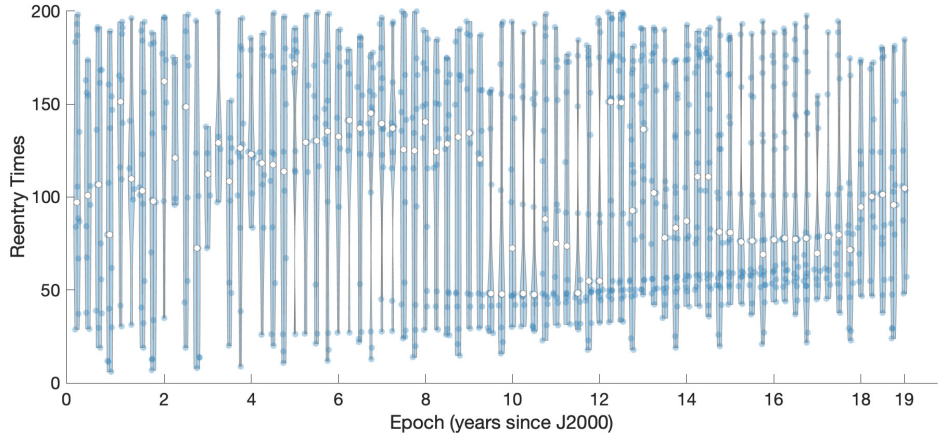

(c) GLONASS

Figure C.9: Reentry Times of objects produced in explosion event

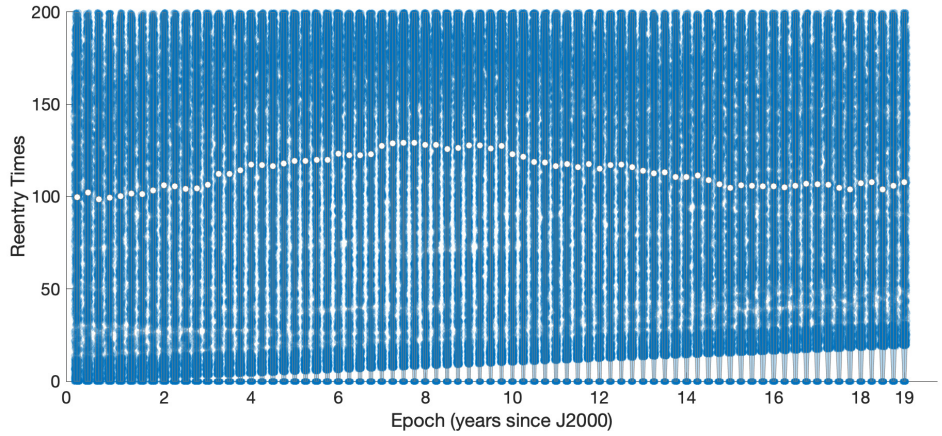

(a) GPS

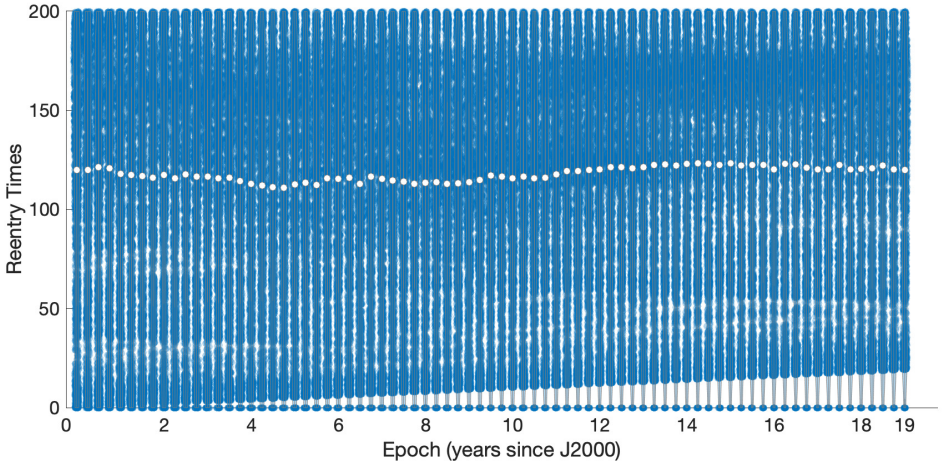

(b) Galileo

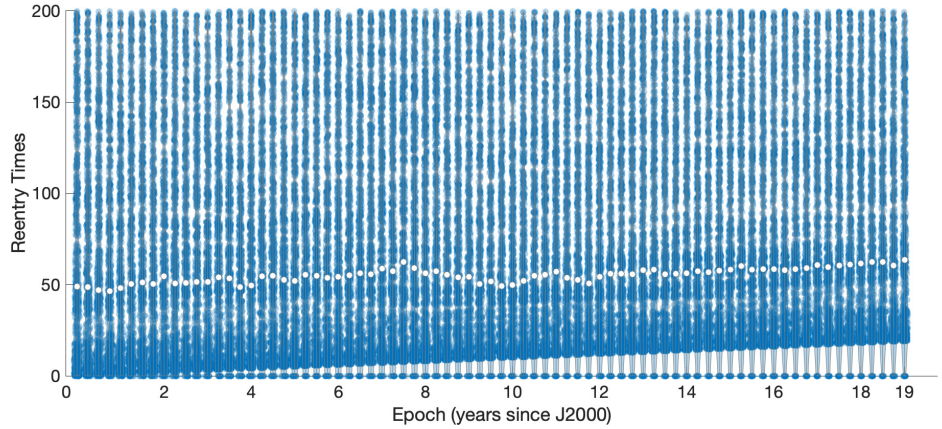

(c) GLONASS

Figure C.10: Maximum eccentricity of objects produced in collision event